

A Search in the Two-Photon Final State for Evidence of New Particle Production in
pp Collisions at $\sqrt{s} = 7$ TeV

Rachel Paula Yohay
Merrick, NY

B.S., California Institute of Technology, 2006

A Dissertation presented to the Graduate Faculty
of the University of Virginia in Candidacy for the Degree of
Doctor of Philosophy

Department of Physics

University of Virginia
August, 2012

1 Abstract

2 This thesis presents a search for evidence of new particle production in the two-
3 photon + jets + missing transverse energy final state using the 2011 Large Hadron
4 Collider proton-proton data, at a center-of-mass energy of 7 TeV, collected by the
5 Compact Muon Solenoid experiment. The distinctive signature of two photons, jets,
6 and a momentum imbalance in the plane transverse to the proton beam direction is
7 chiefly motivated by the theory of supersymmetry, which may provide a solution to
8 the hierarchy problem in particle physics. The instrumental background from ordinary
9 quantum chromodynamics and $W \rightarrow e\nu$ production dominates the total background
10 estimate, and is measured from the data. This background estimate, as well as the
11 high efficiency ($\sim 80\%$) to select and identify two high-energy photons in the data,
12 relies on the superior energy resolution of the lead tungstate crystal electromagnetic
13 calorimeter of the Compact Muon Solenoid as compared to the hadronic energy res-
14 olution. Signal efficiencies for gauge-mediated supersymmetric models, ranging from
15 a few percent to approximately 25%, are taken from Monte Carlo simulation. No
16 evidence of new particles is found in a dataset of 4.7 fb^{-1} of integrated luminosity.
17 Upper limits between 5 and 15 fb on the cross sections of various new physics models
18 are set at the 95% confidence level. The upper limits measured in this search are the
19 most stringent to date for gauge-mediated models of supersymmetry.

²⁰ Contents

²¹	List of Figures	v
²²	List of Tables	xix
²³	1 Introduction	1
²⁴	2 Motivation for Physics Beyond the Standard Model	4
²⁵	2.1 The Standard Model and Electroweak Symmetry Breaking	7
²⁶	2.2 Implications of the Higgs Mechanism	10
²⁷	2.3 Addressing Problems of the Standard Model with Supersymmetry .	12
²⁸	3 The Supersymmetric Extension to the Standard Model	16
²⁹	3.1 Supermultiplet Representation	16
³⁰	3.2 The Unbroken SUSY Lagrangian	17
³¹	3.3 Soft SUSY Breaking	23
³²	3.4 Gauge-Mediated SUSY Breaking	26
³³	3.5 Phenomenology of General Gauge Mediation	29
³⁴	3.6 Experimental Status of SUSY	32
³⁵	4 The Large Hadron Collider	38
³⁶	4.1 Design Considerations and Performance Limitations	39
³⁷	4.2 Beam Injection	42

38	4.3 Magnets and Cryogenics	46
39	4.4 Radiofrequency Cavities	48
40	5 The Compact Muon Solenoid Experiment	50
41	5.1 The Detectors and Their Operating Principles	54
42	5.1.1 Tracking System	54
43	5.1.2 Electromagnetic Calorimeter	63
44	5.1.3 Hadronic Calorimeter	74
45	5.1.4 Muon System	77
46	5.2 Triggering, Data Acquisition, and Data Transfer	82
47	5.2.1 Level 1 and High Level Trigger Systems	82
48	5.2.2 Data Acquisition System	86
49	5.2.3 Data Processing and Transfer to Computing Centers	89
50	6 Event Selection	92
51	6.1 Object Reconstruction	93
52	6.1.1 Photons	93
53	6.1.2 Electrons	106
54	6.1.3 Jets and Missing Transverse Energy	106
55	6.2 HLT	113
56	6.3 Event Quality	116
57	6.4 Photon Identification Efficiency	118
58	6.4.1 Tag and Probe Method	119
59	6.4.2 Photon Efficiency Scale Factor $\epsilon_e^{\text{data}}/\epsilon_e^{\text{MC}}$	126
60	7 Data Analysis	129
61	7.1 Control Samples	130
62	7.2 Modeling the QCD Background	133
63	7.2.1 Outline of the Procedure	133

64	7.2.2 Reweighting	134
65	7.2.3 Normalization	150
66	7.3 Modeling the Electroweak Background	153
67	7.4 Errors on the Background Prediction	157
68	7.5 Results	165
69	8 Interpretation of Results in Terms of GMSB Models	171
70	8.1 Simplified Models	171
71	8.2 Upper Limit Calculation and Model Exclusion	173
72	8.2.1 Signal Acceptance \times Efficiency	173
73	8.2.2 CL_s and the Profile Likelihood Test Statistic	177
74	8.3 Cross Section Upper Limits	185
75	8.4 Exclusion Contours	185
76	9 Conclusion	191
77	A Monte Carlo Samples	193
78	A.1 List of Samples	193
79	A.2 Explanation of Naming Conventions	194
80	Bibliography	196

⁸¹ List of Figures

82	2.1	Selected LEP measurements demonstrating its contribution to the precise understanding of the Standard Model. Reprinted from ref. [9]. . .	6
83			
84	2.2	Higgs potential (the sombrero) as a function of the real and imaginary parts of the complex scalar field. The movement of the balls shows that the symmetry $\phi = 0$ is spontaneously broken, the stable vacuum state of nature being somewhere along the circle of minimum potential. Reprinted from Fig. 1 of ref. [15].	10
85			
86			
87			
88			
89	2.3	Predicted evolution of the free parameters of supersymmetry as a function of renormalization scale for a representative set of SUSY parameters. Note the dash-dotted line marked “ H_u ” that goes negative at ~ 1 TeV; this indicates μ^2 running negative. Reprinted from Fig. 7.4 of ref. [20].	13
90			
91			
92			
93			
94	2.4	Inverse gauge couplings as a function of renormalization scale for the Standard Model assumption (dotted lines) and the SUSY assumption (solid lines; the double lines represent variations in SUSY parameters and in $\alpha_S(m_Z)$). Reprinted from Fig. 5.8 of ref. [20].	15
95			
96			
97			
98	3.1	Interactions in the unbroken SUSY Lagrangian.	24
99	3.2	Contributions to sfermion and gaugino masses from loop interactions with messenger particles in the GMSB framework.	27
100			

101	3.3 Possible contribution to $\mu \rightarrow e\gamma$ from $m_{\tilde{e}ij}$ soft term. Reprinted from	
102	Fig. 5.6(a) of ref. [20].	28
103	3.4 Typical LHC signatures of the bino and wino NLSP scenarios.	33
104	3.5 CMS limits on mSUGRA with $\tan \beta = 10$, corresponding to a model	
105	with third- generation squarks and sfermions somewhat lighter than	
106	their first- and second-generation counterparts. The limits set by in-	
107	dividual searches are shown as separate colored lines. Solid lines refer	
108	to 2011 searches (i.e. using an integrated luminosity of $\sim 1 \text{ fb}^{-1}$), while	
109	dashed lines refer to 2010 searches ($\sim 36 \text{ pb}^{-1}$). Reprinted from ref. [52].	34
110	3.6 ATLAS cross section upper limit on the SPS8 [53] model of mGMSB	
111	as a function of SUSY breaking scale Λ , lightest neutralino mass $m_{\tilde{\chi}_1^0}$,	
112	or lightest chargino mass $m_{\tilde{\chi}_1^\pm}$. Values of Λ , $m_{\tilde{\chi}_1^0}$, or $m_{\tilde{\chi}_1^\pm}$ below the	
113	intersection point between the blue (predicted SPS8 cross section) and	
114	black (observed cross section upper limit) curves are excluded. The	
115	model parameters listed above the plot are defined in Secs. 3.4 and 3.5,	
116	except for τ_{NLSP} , which is the neutralino lifetime. Reprinted from ref.	
117	[38].	35
118	3.7 CDF exclusion contour in the $\tau_{\tilde{\chi}_1^0}$ - $m_{\tilde{\chi}_1^0}$ plane, where $\tau_{\tilde{\chi}_1^0}$ is the lifetime	
119	of the neutralino. Reprinted from ref. [39].	36
120	4.1 Bird's-eye view of the LHC ring, showing the locations of the experi-	
121	ments and local landmarks. Arrows show the beam direction. ATLAS	
122	is located at Point 1, ALICE at Point 2, CMS at Point 5, and LHCb	
123	at Point 8. The ring figure is reprinted from Fig. 2.1 of ref. [60]. The	
124	CERN Globe of Innovation photo comes from ref. [63] and the airplane	
125	cartoon comes from ref. [64].	40
126	4.2 Overview of the LHC injector complex at CERN [68].	43
127	4.3 LHC injection scheme. Reprinted from Fig. 12.2 of ref. [60].	44

128	4.4	Cross-sectional view of septum magnet (beam direction is into or out of the page) showing the holes for the circulating beams and the separate gap for injected particles. Reprinted from Fig. 11.2 of ref. [60].	45
129	4.5	LHC injection kicker pulse shape. The <i>y</i> -axis measures percentage of maximum current. Reprinted from Fig. 11.7 of ref. [60].	45
130	4.6	Cross-sectional view of LHC dipole + cryostat. Reprinted from Fig. 3.3 of ref. [60].	46
131	4.7	Magnetic field lines of the dipole field. The beam direction is into the page. Reprinted from Fig. 4 of ref. [69].	47
132	4.8	Superconducting coils in a twin-bore dipole [70].	48
133	4.9	Cross section of the LHC tunnel, showing the cryogen delivery appa- ratus for a dipole. Reprinted from Fig. 7.1 of ref. [60].	49
134	5.1	CMS coordinate system.	51
135	5.2	Cutaway view of CMS. Reprinted from Fig. 1.1 of ref. [71].	52
136	5.3	Longitudinal quarter cross-sectional view of CMS. The nominal in- teraction point is at the lower right-hand corner of the drawing. The tracker is shown in purple diagonal hashing, the electromagnetic calorime- ter in green, the hadronic calorimeter in blue, and the muon stations in red. The solenoid is shown in black and white and labeled COIL, and the magnet return yoke is shown in yellow. Radial and longitudinal distances are measured in millimeters. Reprinted from Fig. CP 1 of ref. [72].	54
137	5.4	Longitudinal quarter view of the pixel detector. Reprinted from Fig. 3.6 of ref. [71].	56
138	5.5	BPix and FPix mechanical structures.	56
139	5.6	Pixel control and readout system. Reprinted from Fig. 3.9 of ref. [71].	58
140	5.7	Pixel detector performance highlights.	59

155	5.8 Longitudinal cross section of the silicon strip detector. Reprinted from	
156	Fig. 3.1 of ref. [71].	60
157	5.9 View of one tracker endcap, with the outline of a petal shown in blue.	
158	There are nine petals per wedge-shaped sector (one per TEC disk).	
159	Reprinted from Fig. 3.30 of ref. [71].	61
160	5.10 Exploded view of a strip module with two sensors. Reprinted from Fig.	
161	3.22 of ref. [71].	62
162	5.11 Block diagram of the strip readout architecture. Reprinted from Fig.	
163	3.20 of ref. [71].	62
164	5.12 Strip detector performance highlights.	64
165	5.13 Layout of the ECAL detector. Reprinted from Fig. 4.5 of ref. [71]. . .	65
166	5.14 Left: EB crystal with attached APD. Right: EE crystal with attached	
167	VPT. Reprinted from Fig. 4.2 of ref. [71].	66
168	5.15 Flow chart of the crystal readout, showing the 10-sample pulse shape.	
169	Reprinted from Fig. 4.9 of ref. [71].	66
170	5.16 Relative response of the crystals to blue laser pulses from February 1,	
171	2011 to January 1, 2012 [80]. Technical stops, during which the LHC is	
172	turned off for maintenance and development, are shown in gray. These	
173	periods of inactivity correspond to growth in the crystal response, as	
174	radiation damage recovery occurs.	68
175	5.17 Architecture of the laser monitoring system. Reprinted from Fig. 4.16	
176	of ref. [71].	69

177	5.18 Change in response of nine different VPTs in zero magnetic field vs.	
178	time. The response of each VPT is normalized to its response for the	
179	earliest data point taken. For times less than 0, no light pulsing is	
180	applied to the VPTs. For times between 0 and 20 minutes, pulsed	
181	LED light was applied to the VPTs. For times later than 20 minutes,	
182	the pulsing source was again removed.	69
183	5.19 VPT response in a 3.8 T laboratory magnetic field to blue LED light	
184	vs. integrated charge at photocathode [82]. The response is corrected	
185	for changes in the LED light output by PIN diode normalization. For	
186	integrated charge less than ~ 0.003 C, the average current draw at the	
187	photocathode is ~ 1 nA, delivered by blue LED triggered at 2 kHz. For	
188	integrated charge greater than ~ 0.003 C, the average current draw is	
189	~ 10 nA from a 20 kHz trigger rate.	70
190	5.20 Diagram of the LED inputs to a diffusing sphere and the fanout to the	
191	crystals. Adapted from Fig. 4.8 of ref. [71].	71
192	5.21 Hardware setup of the LED system.	72
193	5.22 Software control flow of the LED system.	73
194	5.23 Energy resolution vs. $ \eta $ for Z decay electrons for data (filled blue circles) and MC (empty red squares). The dotted lines show the locations	
195	of module gaps (three per SM).	74
196	5.24 Distribution of reconstructed times of Z decay electrons in EE [86]. .	75
197	5.25 Quarter longitudinal cross-sectional view of HCAL (and muon stations	
198	in purple). Reprinted from Fig. 5.1 of ref. [71].	76
199	5.26 Diagram of the optical readout of HB. Reprinted from Fig. 5.7 of ref.	
200	[71].	77
201	5.27 Cross-sectional view of one side of HF. The z -axis is horizontal. Reprinted	
202	from Fig. 5.28 of ref. [71].	78

204	5.28 Selected HCAL performance results.	79
205	5.29 View of the MB and ME layout in CMS.	80
206	5.30 Electric field lines within a drift tube as well as the contours of equal	
207	drift time. Reprinted from Fig. 7.5 of ref. [71].	81
208	5.31 CSC wedge, showing the cathode and wire planes. Reprinted from Fig.	
209	7.49 of ref. [71].	82
210	5.32 Muon p_T resolution as a function of muon p_T for tracker information	
211	only (blue), muon information only (black), and both tracker and muon	
212	information combined (red). Reprinted from Fig. 1.2 of ref. [71].	83
213	5.33 Di-muon invariant mass spectrum broken down by trigger path [90].	
214	The light(dark) gray regions show the contribution from high- p_T (low-	
215	p_T) di-muon triggers. Note that no $B_s \rightarrow \mu^+\mu^-$ decays have been	
216	observed [91]; the light blue region just shows the amount of triggers	
217	dedicated to the $B_s \rightarrow \mu^+\mu^-$ search.	83
218	5.34 Block diagram of the L1 trigger. Reprinted from Fig. 8.1 of ref. [71]. .	85
219	5.35 Geometry of an EM RCT candidate. Reprinted from Fig. 8.2 of ref. [71].	86
220	5.36 Diagram of the DAQ system. The identical event builder systems,	
221	shown as inputs and outputs to the boxes labeled ‘‘Readout Builder 1’’,	
222	‘‘Readout Builder 2’’, etc., represent the eight slices. Within one slice,	
223	data can flow from the detector front ends to the readout systems to	
224	the builder network (which assembles the event fragments) to the filter	
225	systems (HLT) independently of the other slices. Reprinted from Fig.	
226	9.8 of ref. [71].	87
227	5.37 Diagram of the WLCG tier system showing data archival and recon-	
228	struction at each tier along with data transfer between tiers. Reprinted	
229	from Fig. 11.2 of ref. [71].	91
230	6.1 Two gluinos each decay via $\tilde{\chi}_1^0 \rightarrow \gamma \tilde{G}$	93

231	6.2	Typical ECAL channel pulse shape. \hat{P} is the pedestal value, \hat{A} is the pulse amplitude, and \hat{T}_{\max} is the hit time. The red line is the assumed pulse shape from which the weights are derived. Reprinted from ref. [99].	94
232			
233			
234	6.3	Z peak reconstructed using pre-LHC calibration constants (red) or September 2011 π^0/η -derived intercalibration constants (blue). Reprinted from ref. [108].	97
235			
236			
237	6.4	Hybrid algorithm in EB. The shower extent is constant in η (five crys- tals), but spreads out in ϕ as the two sub-clusters (or basic clusters) are grouped into the same supercluster. The maximum extent in ϕ is 17 crystals. Reprinted from ref. [109].	99
238			
239			
240			
241	6.5	Z peak reconstructed in the dielectron channel for different kinds of clustering. The constituent hits were calibrated with the best available intercalibrations and laser calibrations as of December 2011. The light blue histogram shows the reconstruction using a 5×5 energy sum, the red histogram shows the reconstruction using the SC energy for crystals only (the dark blue histogram in the EE plot adds in the energy from ES), and the black histogram shows the reconstruction after the SCs are corrected using a multivariate method [110]. Reprinted from Fig. 30 of ref. [110].	100
242			
243			
244			
245			
246			
247			
248			
249			
250	6.6	ECAL, HCAL, and track isolation cones.	102
251			
252	6.7	ρ distribution for a sample of two-photon events, with at least one 40 GeV and one 25 GeV photon, passing the selection requirements in Table 6.1 and the trigger requirements in Table 6.3. This sample covers the full 2011 dataset of 4.7 fb^{-1}	103
253			
254			

255	6.8 S/\sqrt{B} (S and B defined in the text) vs. I_{comb} . “DR03” in the legend 256 indicates that this combined isolation was calculated in $\Delta R = 0.3$ 257 cones, as used throughout this analysis. Reprinted from Fig. 7 of ref. 258 [115].	104
259	6.9 Neyman’s χ^2 between the ff and $\gamma\gamma$ E_T distributions, truncated at 260 either 25 (red) or 50 (blue) GeV, vs. upper bound on fake combined 261 isolation. A jet is defined as in Table 6.2, but with the ΔR cleaning 262 criteria of Table 6.2 applied to the two primary EM objects and all 263 additional electrons, photons, and fake photons. The full reweighting 264 and normalization procedure is employed in the E_T calculation (see 265 Sec. 7.2). Reprinted from Fig. 9 of ref. [115].	105
266	6.10 Example event display showing jets clustered via the anti- k_T algorithm. 267 y is pseudorapidity. Reprinted from slide 85 of ref. [121].	109
268	6.11 Total jet energy correction factor $C_{\text{offset}}C_{\text{MC}}C_{\text{rel}}C_{\text{abs}}$ vs. η , including 269 uncertainty band, for jets reconstructed with the anti- k_T algorithm, 270 $R = 0.5$. Reprinted from Fig. 26 of ref. [119].	110
271	6.12 σ of a Gaussian fit to the x- and y-components of calibrated E_T vs. the 272 calibrated PF E_T sum in a sample of events containing at least two jets 273 with $p_T > 25$ GeV. σ is calibrated such that the E_T scale is equal for 274 all three algorithms. PF $\sum E_T$ is corrected, on average, to the particle 275 level using a Pythia v8 simulation [128]. The blue markers (data) and 276 line (MC) refer to PF jets. Reprinted from Fig. 13 of ref. [124].	112
277	6.13 Efficiency of HLT_Photon36_CaloIdL_IsoVL_Photon22_CaloIdL_IsoVL 278 for offline selected leading photon (left) and trailing photon (right) vs. 279 photon p_T . Reprinted from Fig. 2 of ref. [115].	115

280	6.14 $(TS4 - TS5)/(TS4 + TS5)$ vs. $TS4 + TS5$ for a minimum bias sample.	
281	HB/HE hits are considered noisy if they lie in the sparsely populated	
282	gray region labeled "NOISE" defined by the curved red lines. Adapted	
283	from ref. [132].	118
284	6.15 Tag and probe invariant mass fits for $15 \text{ GeV} \leq \text{probe } E_T < 20 \text{ GeV}$.	
285	Errors are statistical only. The tag-pass fit is shown in green in the	
286	upper-left-hand plot, the tag-fail fit in red in the upper-right-hand plot,	
287	and a fit to both samples in blue in the lower-left-hand plot. Dotted	
288	lines are the background components of the fits; solid lines are signal	
289	plus background.	124
290	6.16 Tag and probe invariant mass fits for $-0.25 \leq \text{probe } \eta < -0.5$. Errors	
291	are statistical only. The tag-pass fit is shown in green in the upper-	
292	left-hand plot, the tag-fail fit in red in the upper-right-hand plot, and	
293	a fit to both samples in blue in the lower-left-hand plot. Dotted lines	
294	are the background components of the fits; solid lines are signal plus	
295	background.	125
296	6.17 Dependence of the photon ID efficiency scale factor on some kinematic	
297	variables. Errors are statistical only.	126
298	6.18 Dependence of the photon ID efficiency scale factor on the number of	
299	primary vertices per event. Errors are statistical only.	127
300	7.1 Representative Feynman diagrams of some QCD backgrounds to the	
301	GGM SUSY search.	131
302	7.2 Representative Feynman diagrams of some electroweak backgrounds to	
303	the GGM SUSY search.	132

304	7.3	H_T , defined as the scalar sum of corrected jet E_T for jets defined as in Table 7.2. $\gamma\gamma$ is in black, ee ($81 \text{ GeV} \leq m_{ee} < 101 \text{ GeV}$) is in red, and ff is in blue. The ee and ff distributions are normalized to the number of events in the $\gamma\gamma$ distribution. Errors are statistical only.	135
305			
306			
307			
308	7.4	Number of jets per event for jets defined as in Table 7.2. $\gamma\gamma$ is in black, ee ($81 \text{ GeV} \leq m_{ee} < 101 \text{ GeV}$) is in red, and ff is in blue. The ee and ff distributions are normalized to the number of events in the $\gamma\gamma$ distribution. Errors are statistical only.	136
309			
310			
311			
312	7.5	\not{H}_T , defined as the magnitude of the negative vectorial sum of corrected jet E_T for jets defined as in Table 7.2. $\gamma\gamma$ is in black, ee ($81 \text{ GeV} \leq$ $m_{ee} < 101 \text{ GeV}$) is in red, and ff is in blue. The ee and ff distributions are normalized to the number of events in the $\gamma\gamma$ distribution. Errors are statistical only.	137
313			
314			
315			
316			
317	7.6	Corrected E_T for the jet with the largest corrected E_T per event, for jets defined as in Table 7.2 (excluding the p_T requirement). $\gamma\gamma$ is in black, ee ($81 \text{ GeV} \leq m_{ee} < 101 \text{ GeV}$) is in red, and ff is in blue. The ee and ff distributions are normalized to the number of events in the $\gamma\gamma$ distribution. Errors are statistical only.	138
318			
319			
320			
321			
322	7.7	ρ (average pileup energy density in the calorimeters per unit $\eta \cdot \phi$, cf. Sec. 6.1.1). $\gamma\gamma$ is in black, ee ($81 \text{ GeV} \leq m_{ee} < 101 \text{ GeV}$) is in red, and ff is in blue. The ee and ff distributions are normalized to the number of events in the $\gamma\gamma$ distribution. Errors are statistical only.	139
323			
324			
325			
326	7.8	Number of good reconstructed primary vertices per event according to the criteria of Sec. 6.3. $\gamma\gamma$ is in black, ee ($81 \text{ GeV} \leq m_{ee} < 101 \text{ GeV}$) is in red, and ff is in blue. The ee and ff distributions are normalized to the number of events in the $\gamma\gamma$ distribution. Errors are statistical only.	140
327			
328			
329			
330			

331	7.9 Cartoon showing the di-EM system in blue and the hadronic recoil in	
332	black. The di-EM p_T (dashed blue line) is used to reweight the control	
333	sample kinematic properties to match those of the candidate $\gamma\gamma$ sample.	142
334	7.10 E_T vs. di-EM p_T	143
335	7.11 E_T spectra of the reweighted ee ($81 \text{ GeV} \leq m_{ee} < 101 \text{ GeV}$) and	
336	ff control samples. Blue squares indicate di-EM p_T reweighting only;	
337	red triangles indicate di-EM $p_T +$ number of jets reweighting. PF p_T	
338	(cf. p. 143) is used to calculate the di-EM p_T . The full normalization	
339	procedure is employed, along with ee sideband subtraction (discussed	
340	at the end of this section). Error bars are statistical only.	144
341	7.12 Relative difference between the ECAL-only E_T measurement and the	
342	PF E_T measurement vs. EMF. PF E_T is defined in the text.	146
343	7.13 Average relative difference between the ECAL-only E_T measurement	
344	and the PF E_T measurement vs. EMF for the leading (filled marker)	
345	and trailing (open marker) electrons in ee events (red triangles), fakes	
346	in ff events (blue squares), and photons in $\gamma\gamma$ events (black circles).	
347	These are nothing more than profile histograms of Fig. 7.12. PF E_T is	
348	defined in the text. Error bars are statistical only.	147
349	7.14 E_T spectra of the reweighted ee ($81 \text{ GeV} \leq m_{ee} < 101 \text{ GeV}$) and ff con-	
350	trol samples. Blue squares indicate reweighting using the ECAL-only	
351	p_T estimate; red triangles indicate reweighting using the PF p_T esti-	
352	mate. The full reweighting and normalization procedure is employed,	
353	along with ee sideband subtraction (discussed at the end of this sec-	
354	tion). Error bars are statistical only.	148

355	7.15 \cancel{E}_T spectra of the ee ($81 \text{ GeV} \leq m_{ee} < 101 \text{ GeV}$) and ff control samples.	
356	Red triangles indicate full di-EM p_T + number of jets reweighting; blue	
357	squares indicate no reweighting. PF p_T (cf. p. 146) is used to calculate	
358	the di-EM p_T . The full normalization procedure is employed, along	
359	with ee sideband subtraction (discussed at the end of this section).	
360	Error bars are statistical only.	149
361	7.16 ee sideband di-EM p_T weights for events with 0, 1, or ≥ 2 jets (as in	
362	Table 6.2). Errors are statistical only.	151
363	7.17 \cancel{E}_T spectra of the ee sample for $71 \text{ GeV} \leq m_{ee} < 81 \text{ GeV}$ (red triangles),	
364	$81 \text{ GeV} \leq m_{ee} < 101 \text{ GeV}$ (black circles), and $101 \text{ GeV} \leq m_{ee} < 111$	
365	GeV (blue squares). The two sideband distributions (red and blue) and	
366	the Z signal distribution (black) are normalized to the total number of	
367	$\gamma\gamma$ events. Errors are statistical only.	151
368	7.18 ee ($81 \text{ GeV} \leq m_{ee} < 101 \text{ GeV}$) (red triangles), ff (blue squares), and	
369	$\gamma\gamma$ (black circles) di-EM p_T spectra for events with 0, 1, or ≥ 2 jets	
370	(as in Table 6.2). Errors are statistical only.	152
371	7.19 ee ($81 \text{ GeV} \leq m_{ee} < 101 \text{ GeV}$) and ff di-EM p_T weights for events	
372	with 0, 1, or ≥ 2 jets (as in Table 6.2). Errors are statistical only. . .	153
373	7.20 Fits to the ee and $e\gamma$ invariant mass spectra using the Crystal Ball	
374	RooCMSShape function described in the text and in Table 7.3. The total	
375	fit is shown in blue, while the background component is shown in red. . .	156
376	7.21 $f_{e \rightarrow \gamma}$ vs. electron p_T and η	156
377	7.22 \cancel{E}_T spectrum of the $e\gamma$ sample after scaling by $f_{e \rightarrow \gamma}$. The total error on	
378	$f_{e \rightarrow \gamma}$ is propagated to the total error on the electroweak background	
379	estimate.	157

380	7.23 E_T spectrum of the $e\gamma$ sample in 35 pb^{-1} of 2010 LHC data scaled by the 2010 measured $f_{e \rightarrow \gamma}$ (black dots), QCD and real Z predicted background from the 2010 ee sample (solid orange line), MC $W + \text{jet}$ estimate (dash-dotted purple line), and MC $W\gamma$ estimate (dashed blue line). The total $e\gamma$ prediction (red band) is the sum of the ee , $W + \text{jet}$, and $W\gamma$ predictions. Reprinted from Fig. 2 of ref. [140].	158
386	7.24 Average \cancel{E}_T vs. di-EM p_T for the ff (blue squares), ee (red triangles), and $\gamma\gamma$ (black circles) samples.	161
388	7.25 ee \cancel{E}_T distributions using the nominal sideband subtraction (black circles), low sideband only (red squares), and high sideband only (blue triangles). The bottom plot shows the ratio of the low sideband distribution to the nominal (red squares) and the ratio of the high sideband distribution to the nominal (blue triangles).	162
393	7.26 Comparison of \cancel{E}_T distributions for five different di-EM p_T bin definitions: uniform bins of width 10 GeV (red diamonds); uniform bins of width 50 GeV (blue downward-pointing triangles); bins with lower edges $\{0.0, 5.0, 10.0, 15.0, 20.0, 30.0, 40.0, 50.0, 60.0, 70.0, 80.0, 100.0, 750.0\}$ GeV for 0-jet events and $\{0.0, 5.0, 10.0, 15.0, 20.0, 30.0, 40.0, 50.0, 60.0, 70.0, 80.0, 100.0, 120.0, 150.0, 200.0, 700.0\}$ GeV for ≥ 1 -jet events (magenta upward-pointing triangles), i.e. a single wide bin at high di-EM p_T ; bins with lower edges $\{0.0, 5.0, 10.0, 15.0, 20.0, 30.0, 40.0, 50.0, 60.0, 70.0, 80.0, 100.0, 120.0, 150.0, 200.0\}$ GeV for 0-jet events and $\{0.0, 5.0, 10.0, 15.0, 20.0, 30.0, 40.0, 50.0, 60.0, 70.0, 80.0, 100.0, 120.0, 150.0, 200.0\}$ GeV for ≥ 1 -jet events (green squares), i.e. the bins used in ref. [59]; and the nominal bin definitions shown in Fig. 7.19 (black circles).	163
405	7.27 Agreement between $\gamma\gamma$, ee , and ff samples for uncorrected (red triangles) and corrected (blue squares) \cancel{E}_T	164

407	7.28 E_T distribution of the $\gamma\gamma$ search sample (black circles) along with the predicted E_T distributions of the QCD and electroweak backgrounds (small circle band for ee QCD prediction + electroweak prediction, slanted dashed band for ff QCD prediction + electroweak prediction). The electroweak background prediction is shown in the crosshatched band. The bottom plots show the ratio of the $\gamma\gamma E_T$ distribution to the $ee + e\gamma$ background distribution (open squares) and $ff + e\gamma$ background distribution (filled squares).	168
415	7.29 E_T distribution of the $\gamma\gamma + \geq 1$ jet search sample (black circles) along with the predicted E_T distributions of the QCD and electroweak backgrounds (small circle band for ee QCD prediction + electroweak prediction, slanted dashed band for ff QCD prediction + electroweak prediction). The electroweak background prediction is shown in the crosshatched band. The bottom plots show the ratio of the $\gamma\gamma E_T$ distribution to the $ee + e\gamma$ background distribution (open squares) and $ff + e\gamma$ background distribution (filled squares).	169
423	8.1 Next to leading order cross sections for the three different MC scenarios described in the text.	174
424		
425	8.2 Signal acceptance \times efficiency (defined in the text) for the three different scenarios described in Sec. 8.1.	176
426		
427	8.3 Cross section upper limits for the three different scenarios described in Sec. 8.1.	186
428		
429	8.4 Diagram of the points (red squares) used in the estimation of an upper limit when a computational failure occurs (middle white square).	187
430		
431	8.5 Exclusion contours for the three different scenarios described in Sec. 8.1.188	

432 List of Tables

452	3.2 Gauge supermultiplets of the supersymmetric Standard Model. Adapted from Table 1.2 of ref. [20].	19
453		
454	6.1 Selection criteria for photons and fakes. “Pixel seed,” I_{comb} , and $\sigma_{i\eta i\eta}$ are defined in the text.	101
455		
456	6.2 Definition of HB/HE hadronic jets.	111
457		
458	6.3 HLT paths triggered by the $\gamma\gamma$, $e\gamma$, ee , and ff samples, by run range. No triggers are prescaled.	114
459		
460	6.4 Candidate photon ID requirements.	120
461		
462	6.5 Tag and probe criteria. The superscript 0.4 indicates that the isolation variable was calculated in a cone of $\Delta R = 0.4$ around the photon candidate. The isolations without superscripts use the standard $\Delta R =$	
463	0.3 cones.	121
464		
465	6.6 Parameter values (parameter definitions are in the text) for the signal and background PDFs for the different samples. The background PDF applies to all efficiency bins except the four lowest E_T bins, which use	
466	a floating <code>RooCMSShape</code> background. When a bracketed range is given,	
467	the parameter is allowed to float within that range. When a constant	
468	is given, the parameter is fixed to that constant.	123
469		
470	7.1 Selection criteria for $\gamma\gamma$, $e\gamma$, ee , and ff events.	129
471		
472	7.2 Definition of HB/HE/HF hadronic jets.	141
473		
474	7.3 Parameter values for the signal and background PDFs for the ee and $e\gamma$ samples. When a bracketed range is given, the parameter is allowed	
475	to float within that range. When a constant is given, the parameter is	
476	fixed to that constant.	155
477		
478	7.4 Errors on the ee QCD background prediction as a fraction of the ee prediction.	165
479		

478	7.5 Errors on the ff QCD background prediction as a fraction of the ff	
479	prediction.	166
480	7.6 Errors on the $e\gamma$ electroweak background prediction as a fraction of	
481	the $e\gamma$ prediction.	166
482	7.7 Errors on the total QCD + electroweak background prediction as a	
483	fraction of the total prediction.	167
484	7.8 Observed numbers of two-photon events, ee and ff background esti-	
485	mates and their errors, and expected numbers of two-photon events	
486	from two representative GGM SUSY models (details of MC simulation	
487	given in Chapter 8) for the \cancel{E}_T bins used in the search. The ee estimate	
488	is shown for comparison; the ff estimate is the official result used in	
489	the interpretation. Errors on the background estimates are detailed in	
490	Tables 7.4, 7.5, 7.6, and 7.7. Errors on the expected numbers of GGM	
491	events are purely statistical.	167
492	7.9 Observed numbers of two-photon + ≥ 1 -jet events, ee and ff back-	
493	ground estimates and their errors, and expected numbers of two-photon	
494	+ ≥ 1 -jet events from two representative GGM SUSY models (details of	
495	MC simulation given in Chapter 8) for the \cancel{E}_T bins used in the search.	
496	The ee estimate is shown for comparison; the ff estimate is the official	
497	result used in the interpretation. Errors on the background estimates	
498	are detailed in Tables 7.4, 7.5, 7.6, and 7.7. Errors on the expected	
499	numbers of GGM events are purely statistical.	170

500 Chapter 1

501 Introduction

502 Although the Standard Model of particle physics has passed every experimental test
503 to date, it leaves some very fundamental questions unanswered. Why do particles have
504 mass? Why are their masses so different? Up to what energy scale is the Standard
505 Model a valid description of nature? Many competing theories have been proposed to
506 answer these questions. Establishing the existence of any one of them requires careful
507 searches for deviations from Standard Model predictions of particle production or
508 decay rates. The stellar performance of the Large Hadron Collider, the 7 TeV center-
509 of-mass energy proton collider located at the European Organization for Nuclear
510 Research (CERN) in Geneva, Switzerland, presents a golden opportunity to do such
511 a search for evidence of new physical phenomena.

512 One nearly universal prediction of theories of physics beyond the Standard Model
513 is that at a high enough collision energy, heavy particles introduced by the new theory
514 will be produced. The heavy particles will then decay, leading to distinctive signatures
515 in the hermetic detectors that completely surround the collision points. By comparing
516 the observed rate of processes with a particular signature to the expected rate from
517 the Standard Model alone, the existence of a particular theory of new physics can be
518 confirmed or ruled out.

519 This thesis presents a search for evidence of new heavy particles decaying to a final
520 state with two photons, jets, and a striking momentum imbalance that implies the
521 existence of a new kind of particle that can easily pass through matter without leaving
522 a trace. The signature is motivated by theories that incorporate supersymmetry, a new
523 symmetry of nature that predicts supersymmetric antiparticles to the known particles,
524 just as charge symmetry predicts a positively charged antiparticle for every negatively
525 charged particle and vice versa. Supersymmetry can provide answers to some of the
526 questions posed in the first paragraph: it predicts unification of all fundamental forces
527 at a specific energy scale and explains the Standard Model mechanism for endowing
528 particles with mass. Furthermore, it may also predict a source of astrophysical dark
529 matter. Besides its theoretical motivation, the choice of signature is also driven by
530 the low rate of expected Standard Model background.

531 The search is performed at the Compact Muon Solenoid experiment, a detector ca-
532 pable of identifying photons, electrons, muons, quark jets, τ leptons, and momentum
533 imbalances with high efficiency. The central feature of the experiment is a supercon-
534 ducting solenoid, which, at a length of 13 m and a diameter of 7 m [1], is one of the
535 largest superconducting magnets ever built. By bending the paths of charged parti-
536 cles in the final state under the Lorentz force, the magnetic field produced by the
537 solenoid allows charged particle momenta to be accurately measured. Highly granular
538 calorimeters sit inside the solenoid for the purpose of measuring the energy of neutral
539 final state particles.

540 This thesis is organized as follows. Chapters 2 and 3 motivate the search for physics
541 beyond the Standard Model and the specific signature of two photons, as well as give
542 an overview of the Standard Model and supersymmetric theoretical frameworks. A
543 description is given of the Large Hadron Collider in Chapter 4 and the Compact Muon
544 Solenoid detector in Chapter 5. Chapters 6 and 7 explain in detail the experimental
545 techniques used in the search. Chapter 6 shows how collisions that are likely to have

546 produced a new particle are selected from the enormous amount of data collected, then
547 Chapter 7 shows the data analysis in detail and presents the results. An interpretation
548 of the results in terms of new physics models is given in Chapter 8. Finally, the thesis
549 is concluded in Chapter 9.

550 **Chapter 2**

551 **Motivation for Physics Beyond the
552 Standard Model**

553 In the 1960s, Sheldon Glashow, Steven Weinberg, and Abdus Salam proposed a math-
554 ematical framework that unified the electromagnetic and weak forces at an energy
555 scale in the hundreds of GeV/c, as well as a mechanism for breaking the electroweak
556 symmetry at low energies [2–6]. At the same time, Murray Gell-Mann introduced the
557 concept of quarks to describe hadron spectroscopy, a concept that would later grow
558 into quantum chromodynamics (QCD), the full theory of the strong force [7, 8]. These
559 two key developments motivated the unified representation of particle physics as a set
560 of fields whose dynamics are invariant under the Standard Model (SM) gauge group

$$SU(3)_C \otimes SU(2)_L \otimes U(1)_Y \quad (2.1)$$

561 where $SU(3)_C$ describes the quark QCD interactions, $SU(2)_L$ describes the weak
562 interactions among quarks and leptons, and $U(1)_Y$ describes the electromagnetic in-
563 teraction.

564 The Standard Model has been an extremely successful predictor of particle pro-
565 duction mechanisms and the relationships between interaction cross-sections and de-

566 cay rates, as well as of the exact relationship between the masses of the electroweak
 567 force carriers and the electroweak couplings. The case for the validity of the Stan-
 568 dard Model was bolstered by the many precision QCD and electroweak measurements
 569 carried out at the Large Electron-Positron (LEP) collider, which ran from 1989-2000
 570 at center-of-mass energies between 65 and 104 GeV/ c [9]. Figure 2.1 shows some of
 571 the highlights of the LEP program. Figure 2.1(a) shows the decay width of the Z
 572 boson, which established with high precision the existence of only three families of
 573 quarks and leptons. Figure 2.1(b) shows the measured and predicted cross sections
 574 of $e^+e^- \rightarrow q\bar{q}$, $e^+e^- \rightarrow \mu^+\mu^-$, and $e^+e^- \rightarrow \tau^+\tau^-$. The data agree very well with
 575 the Standard Model prediction. This result confirms lepton universality (the $\mu^+\mu^-$
 576 and $\tau^+\tau^-$ cross sections are the same) and the expected amplitude of hadron pro-
 577 duction with respect to lepton production. Figure 2.1(c) shows the measured and
 578 predicted W^+W^- cross section. The fact that the data prefer the prediction that in-
 579 cludes the ZW^+W^- vertex lends further support to the correctness of the Standard
 580 Model. Finally, the running of the strong coupling constant with energy is shown in
 581 Figure 2.1(d), corroborating the predictions of SM renormalization.

582 However, there are still deep problems with the Standard Model, stemming from
 583 the introduction of the Higgs scalar into the theory to break electroweak symmetry
 584 [10–12]. Since the Higgs self-energy diagram diverges as the square of the ultraviolet
 585 cutoff scale, and assuming that there are no new important energy scales of physics
 586 between the weak scale ($\mathcal{O}(10^2 \text{ GeV}/c)$) and the Planck scale ($\mathcal{O}(10^{19} \text{ GeV}/c)$), in
 587 order to be consistent with experimental measurements, this diagram must include
 588 a remarkable 17-orders-of-magnitude cancellation that is otherwise poorly motivated
 589 [13]. The quest to find new physics at an intermediate energy scale between the weak
 590 and Planck scales, and thus extend the Standard Model, was the driving force behind
 591 the construction of the Large Hadron Collider (LHC) in 2009, the world’s highest
 592 energy particle accelerator to date.

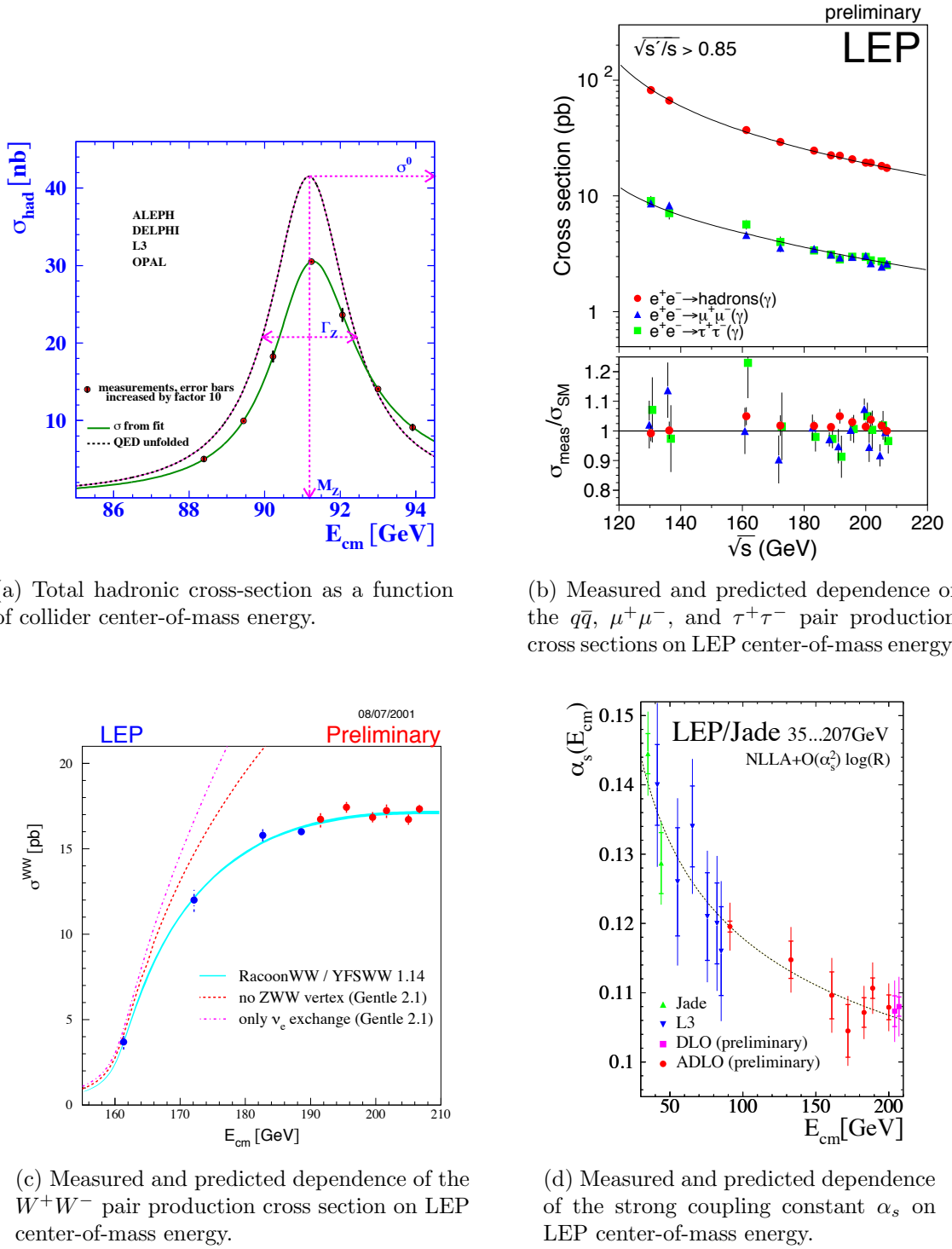


Figure 2.1: Selected LEP measurements demonstrating its contribution to the precise understanding of the Standard Model. Reprinted from ref. [9].

593 Section 2.1 of this chapter gives a brief overview of the Standard Model and
 594 electroweak symmetry breaking. Sections 2.2 and 2.3 examine the issues raised by
 595 electroweak symmetry breaking that the Standard Model is as yet ill-prepared to
 596 address.

597 **2.1 The Standard Model and Electroweak Symme-**
 598 **try Breaking**

599 All of the elementary matter particles (fermions)—quarks, charged leptons, and neutrinos—
 600 can be put in fundamental representations of the SM gauge groups. The fermion con-
 601 tent of the Standard Model is summarized in Table 2.1. The left-handed doublets are
 602 analogous to the spinors of non-relativistic quantum mechanics, with the z compon-
 603 ent of “weak isospin” I_3 equal to $+1/2(-1/2)$ for the upper(lower) component of the
 604 doublet.

605 There are two types of weak interactions: flavor-changing charged currents, in
 606 which an up-type and down-type quark or charged lepton and neutrino couple to
 607 a charged W , and neutral currents, in which a fermion couples to another of the
 608 same flavor and to a neutral Z . The charged current interaction is maximally parity
 609 violating—it only couples left-handed fermion doublets. The neutral current inter-
 610 action has a term coupling left-handed doublets and a term coupling right-handed
 611 singlets. There are no mass terms of the form $m_f^2(f_L\bar{f}_R + f_R\bar{f}_L)$ in the electroweak
 612 part of the Lagrangian, as these would violate gauge invariance [14]. The simplest
 613 way to link the left-handed and right-handed fermions is via a Yukawa interaction
 614 $-\xi [\bar{f}_R(\phi^\dagger f_L) + (\bar{f}_L\phi)f_R]$ where ϕ is a doublet of complex scalar fields [14].

615 The fermion interaction part of the Lagrangian is [14]

Table 2.1: Fermion content of the Standard Model. In the third column, the first number refers to the supermultiplet representation under $SU(3)_C$ (e.g. **3** means it has color charge and feels QCD), the second number refers to the representation under $SU(2)_L$ (e.g. **2** means it has weak isospin and feels the weak interaction), and the third number is the value of the hypercharge. A bar over a number refers to the adjoint representation. **1** means that the supermultiplet is not charged under that group, and thus does not feel the associated force (for example, the right-handed fermion singlets do not feel the weak interaction).

Type	Notation	Representation under $SU(3)_C \otimes SU(2)_L \otimes U(1)_Y$	Couples to
Left-handed quark doublet	$\begin{pmatrix} u_L \\ d_L \\ c_L \\ s_L \\ b_L \\ t_L \end{pmatrix}$	(3 , 2 , $\frac{1}{6}$)	g, W, Z, γ
Right-handed up-type quark singlet	$\begin{pmatrix} u_R^\dagger \\ c_R^\dagger \\ b_R^\dagger \end{pmatrix}$	($\bar{\mathbf{3}}$, 1 , $-\frac{2}{3}$)	g, γ
Right-handed down-type quark singlet	$\begin{pmatrix} d_R^\dagger \\ s_R^\dagger \\ t_R^\dagger \end{pmatrix}$	($\bar{\mathbf{3}}$, 1 , $\frac{1}{3}$)	g, γ
Left-handed lepton doublet	$\begin{pmatrix} \bar{\nu}_{eL} \\ e_L \\ \bar{\nu}_{\mu L} \\ \mu_L \\ \bar{\nu}_{\tau L} \\ \tau_L \end{pmatrix}$	(1 , 2 , $-\frac{1}{2}$)	W, Z, γ^a
Right-handed charged lepton singlet	$\begin{pmatrix} e_R^\dagger \\ \mu_R^\dagger \\ \tau_R^\dagger \end{pmatrix}$	($\bar{\mathbf{1}}$, 1 , 1)	γ

^aExcept for neutrinos, which have zero electric charge.

$$\begin{aligned}\mathcal{L}_{\text{int}} &= \bar{f}_R i\gamma^\mu (\partial_\mu + i\frac{g_Y}{2} A_\mu Y) f_R \\ &\quad + \bar{f}_L i\gamma^\mu (\partial_\mu + i\frac{g_Y}{2} A_\mu Y + i\frac{g_L}{2} \vec{\tau} \cdot \vec{b}_\mu) f_L\end{aligned}\quad (2.2)$$

616 where g_Y and g_L are the electromagnetic and weak coupling constants, respectively;
 617 Y is the weak hypercharge; A_μ is the EM gauge field; \vec{b}_μ is a three-component
 618 vector of weak gauge fields; and $\vec{\tau}$ is a three-component vector of the three Pauli
 619 matrices. Before electroweak symmetry breaking, the three weak gauge fields and the
 620 one EM gauge field are massless. The three weak gauge fields correspond to the three
 621 generators (the Pauli matrices) of $SU(2)_L$. The one EM gauge field corresponds to the
 622 one generator (the real scalar Y) of $U(1)_Y$, where $Y = 2(Q - I_3)$ (Q is electric charge).
 623 For the $SU(3)_C$ part of the Lagrangian, there are eight massless gauge fields (the
 624 gluons) corresponding to the eight generators of $SU(3)_C$ (the Gell-Mann matrices).

625 To break the electroweak symmetry implicit in the massless gauge bosons, a dou-
 626 blet of complex scalar fields (the Higgs) is introduced. It has a potential [14]

$$V(\phi^\dagger \phi) = \mu^2 \phi^\dagger \phi + |\lambda| (\phi^\dagger \phi)^2. \quad (2.3)$$

627 Since $\mu^2 < 0$, the potential has the shape of a sombrero, as shown in Figure 2.2.
 628 At the minimum of the potential, the scalar fields are not zero, but have some positive
 629 vacuum expectation value (VEV) (it can be chosen such that one component is zero
 630 and the other is $\sqrt{-\mu^2/2|\lambda|}$). Nature spontaneously chooses one of the infinitely many
 631 vacua along the circle of minimum V in $(\Re[\phi], \Im[\phi])$ space.

632 Expanding ϕ about its VEV v in the Lagrangian introduces one massive scalar, the
 633 Higgs, and new mass terms for the gauge bosons. However, the terms with positive
 634 mass are not the original b_1 , b_2 , b_3 , and A (spacetime indices dropped), but the

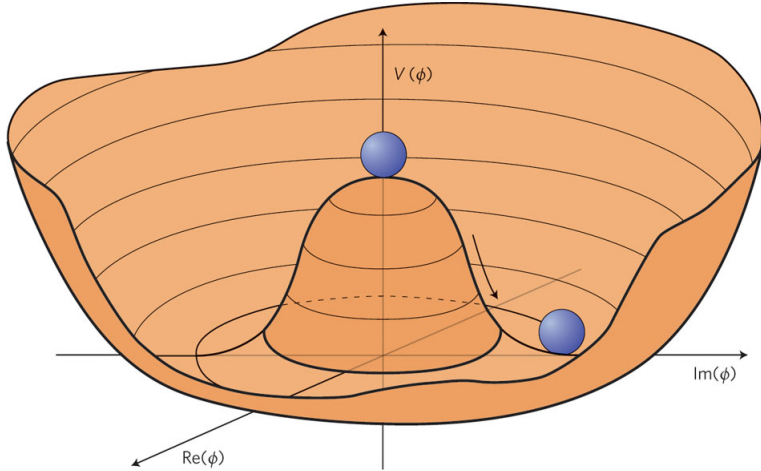


Figure 2.2: Higgs potential (the sombrero) as a function of the real and imaginary parts of the complex scalar field. The movement of the balls shows that the symmetry $\phi = 0$ is spontaneously broken, the stable vacuum state of nature being somewhere along the circle of minimum potential. Reprinted from Fig. 1 of ref. [15].

observable W^\pm and Z^0 . The W^\pm are linear combinations of b_1 and b_2 . The Z^0 is one of the linear combinations of b_3 and A , the other being the massless photon γ . After electroweak symmetry breaking (EWSB), the only remaining symmetry of the vacuum is electric charge, because the value of the electric charge operator acting on the Higgs VEV is zero. As expected, there is one massless photon in the SM to reflect this symmetry. The SM fermions can also acquire masses as a by-product of the Higgs mechanism via Yukawa terms.

2.2 Implications of the Higgs Mechanism

Before the formulation of the Higgs mechanism, physicists suspected that a heavy boson mediated the weak force from observations of β decay, but had no way of putting a mass term into the Lagrangian without breaking gauge symmetry. The Higgs mechanism of EWSB provided a way to generate masses for the $SU(2)_L$ gauge bosons. Furthermore, it predicted the W and Z masses in terms of g_L , g_Y , and v . g_L and g_Y could be measured in scattering experiments, and in 1983 the W and Z were

649 first observed at the Super Proton-Antiproton Synchrotron (Sp \bar{p} S) at the European
 650 Organization for Nuclear Research (CERN) in Geneva, Switzerland [16, 17]. Crucially,
 651 the values of the coupling constants and the gauge boson masses predict that the Higgs
 652 VEV should be 246 GeV, so the Higgs mass should not be too much different than
 653 that if λ is to remain small enough to do perturbation theory [18].

654 The Higgs mechanism raises some interesting questions that cannot be immedi-
 655 ately answered by SM physics. First of all, why should μ^2 be negative? The form of
 656 the Higgs potential given in Eq. 2.3 is about the simplest renormalizable form that
 657 can be written for a scalar field, but the choice of $\mu^2 < 0$ is completely arbitrary.
 658 Second, how can the hierarchy problem be avoided?

659 The Higgs mass squared receives one-loop corrections from all the particles it
 660 couples to; namely, all particles with mass. Because the Higgs is a scalar particle, one-
 661 loop corrections are proportional to Λ_{UV}^2 , where Λ_{UV} is the ultraviolet cutoff energy of
 662 the loop integral. Λ_{UV} can be interpreted as the energy at which the SM can no longer
 663 describe particle physics and non-SM physics takes over. Ideally, Λ_{UV} is something
 664 like the Planck scale. However, taking $\Lambda_{\text{UV}} = M_{\text{Planck}}$ implies that in order to keep the
 665 Higgs mass of order a few hundred GeV, as required by experimental tests of EWSB, a
 666 very large and precise counterterm must be applied at all orders in perturbation theory
 667 to the bare m_H^2 . The quadratic sensitivity of the Higgs mass to the cutoff scale and the
 668 extremely fine-tuned counterterms it necessitates is called the hierarchy problem. SM
 669 fermions do not experience this problem because chiral symmetry prevents explicit
 670 fermion mass terms at any order, so by dimensional analysis, fermion masses can only
 671 be sensitive to $\ln \frac{\Lambda_{\text{UV}}}{\Lambda_{\text{other}}}$.

672 One of the most elegant ways to address these problems is to incorporate *super-*
 673 *symmetry* (SUSY) into the SM. Supersymmetry is new fundamental symmetry of
 674 nature between bosons and fermions, and will be discussed more thoroughly in Chap-
 675 ter 3. The next section just briefly describes how supersymmetry can mitigate some

676 of the problems of the Higgs mechanism.

677 2.3 Addressing Problems of the Standard Model 678 with Supersymmetry

679 As in the ordinary Standard Model, the couplings and masses in supersymmetric
680 theory can be imposed at the supersymmetric scale and evolved down to the weak
681 scale by use of renormalization group equations. For many typical supersymmetric
682 scenarios (like the one shown in Figure 2.3), μ^2 is positive at the the supersymmetric
683 scale but runs negative at the weak scale, leading to precisely the conditions needed
684 for EWSB. This is a consequence of the fact that the evolution of m_H^2 depends on the
685 top quark Yukawa coupling, which, since the top is very heavy compared to the other
686 quarks ($m_t \sim 42m_b$, $m_t \sim 136m_c$ [19]), is large. In some sense, then, supersymmetry
687 not only provides the conditions for EWSB, but also explains why the top quark must
688 be so much heavier than the other quarks.

689 SUSY's greatest strength, however, comes from the way it elegantly solves the
690 hierarchy problem. The Higgs squared mass corrections from fermion loops take the
691 form [20]

$$\Delta m_H^2 = -\frac{|\lambda_F|^2}{8\pi^2} \Lambda_{UV}^2 + \dots \quad (2.4)$$

692 while the corrections from scalar loops would take the form [20]

$$\Delta m_H^2 = \frac{|\lambda_S|^2}{16\pi^2} \Lambda_{UV}^2 + \dots \quad (2.5)$$

693 where the ellipsis indicates terms proportional to $\ln \Lambda_{UV}$ that do not pose a prob-

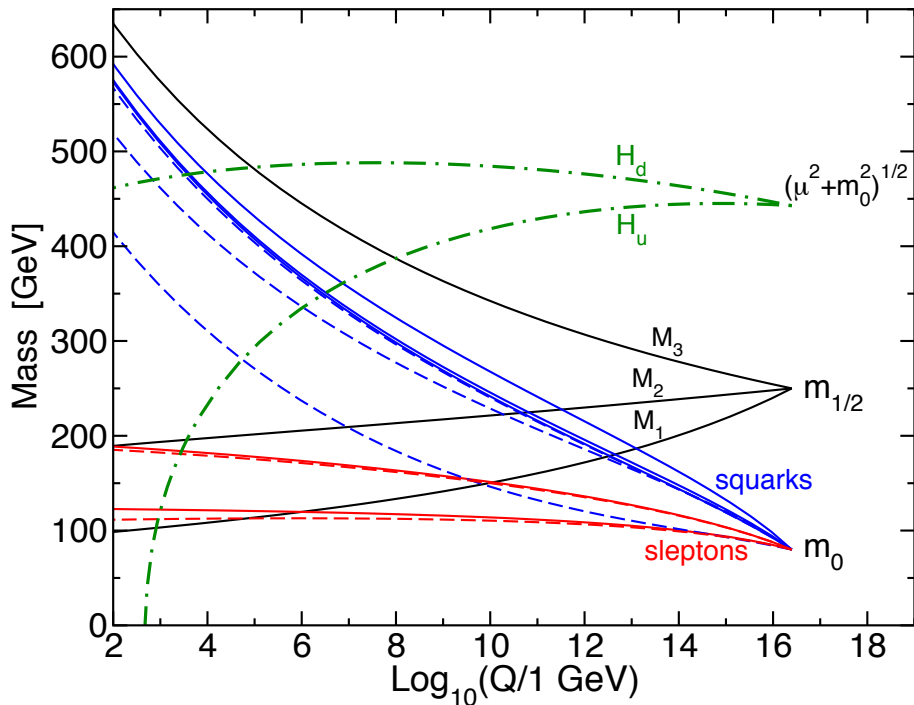


Figure 2.3: Predicted evolution of the free parameters of supersymmetry as a function of renormalization scale for a representative set of SUSY parameters. Note the dash-dotted line marked “ H_u ” that goes negative at ~ 1 TeV; this indicates μ^2 running negative. Reprinted from Fig. 7.4 of ref. [20].

694 lem for the validity of the SM up to the Planck scale. Since the fermion and scalar
 695 contributions have opposite signs, if each SM fermion were accompanied by two as-
 696 yet-undiscovered real scalar fields with $\lambda_S = |\lambda_F|^2$, then the problematic quadratic
 697 terms in Eqs. 2.4 and 2.5 would exactly cancel. This is precisely the foundation of
 698 supersymmetry: for each fermion, there is a supersymmetric partner complex scalar
 699 boson.¹ This would remove the hierarchy problem altogether, and is the main reason
 700 physicists are eager to find evidence for the existence of supersymmetry at the LHC.

701 In addition to providing some rationale for the Higgs mechanism, SUSY makes two
 702 other very desirable predictions. The first is that the strong, weak, and electromag-
 703 netic coupling constants will exactly unify at an energy scale of 10^{16} GeV/ c , as shown
 704 in Figure 2.4. Unification of forces is not required by any experimental consideration,
 705 but is an elegant result nonetheless. The second prediction of SUSY, explained in
 706 more detail in Sec. 3.5, is the existence of a new stable and electrically neutral parti-
 707 cle, undiscovered as of yet because of its extremely feeble (i.e. weak or gravitational)
 708 interactions with ordinary matter. This particle might be what astronomers have ob-
 709 served as dark matter. In fact, regardless of any theory, searches for evidence of dark
 710 matter at colliders are well motivated by suggestions from astronomy that some or
 711 all of the dark matter should have a mass at the weak scale [21].

712 Everything discussed in this chapter assumes that the Higgs mechanism is indeed
 713 the origin of EWSB. It is important to remember that no experimental observation
 714 to date unequivocally establishes the existence of the Higgs scalar, although some
 715 activity recently unearthed in the LHC data [22, 23] tentatively suggest a Higgs
 716 mass of ~ 125 GeV. The discovery of the Higgs scalar would place an important
 717 restriction on the types of SUSY theories that might be consistent with experiment.
 718 Operating at a 7 TeV center-of-mass energy, the LHC can thoroughly probe the scale
 719 of EWSB and the expected mass range of the Higgs, as well as the mass range of

¹The two real scalar fields combine to form one complex scalar field.

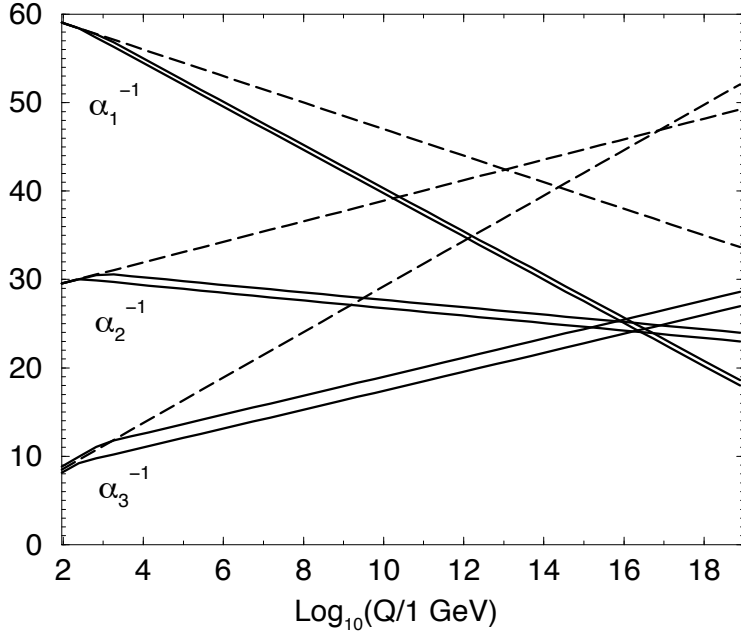


Figure 2.4: Inverse gauge couplings as a function of renormalization scale for the Standard Model assumption (dotted lines) and the SUSY assumption (solid lines; the double lines represent variations in SUSY parameters and in $\alpha_S(m_Z)$). Reprinted from Fig. 5.8 of ref. [20].

⁷²⁰ supersymmetric particles if SUSY is indeed the solution to the hierarchy problem
⁷²¹ and the light Higgs is found. Therefore, discovering or excluding SUSY is a key goal
⁷²² of the LHC physics program. The next chapter discusses SUSY more formally and
⁷²³ shows what phenomenological consequences it entails.

⁷²⁴ Chapter 3

⁷²⁵ ⁷²⁶ The Supersymmetric Extension to the Standard Model

⁷²⁷ The following introduction to SUSY focuses primarily on the aspects of the formalism that are relevant to phenomenology. In particular, most of the details of SUSY breaking (about which there is little theoretical consensus) are omitted, except where they are relevant to experiment. The notation is similar to that used in refs. [13] and [20], and much of the information presented is culled from those references.

⁷³² 3.1 Supermultiplet Representation

⁷³³ The Standard Model is extended to include supersymmetry by the introduction of a supersymmetry transformation that takes fermionic states to bosonic states and vice versa. The resulting model is called the *supersymmetric Standard Model*. In analogy with the known symmetries of the Standard Model, the SUSY transformation has associated generators that obey defining commutation and anticommutation relations, and a fundamental representation. All SM particles and their *superpartners* fall into one of two *supermultiplet* representations. Using the property of SUSY that

$$n_F = n_B, \quad (3.1)$$

740 where n_F is the number of fermionic degrees of freedom per supermultiplet and n_B is
 741 the number of bosonic degrees of freedom, the two types of supermultiplets are

- 742 1. *Chiral supermultiplets*: Weyl fermions (two helicity states $\Rightarrow n_F = 2$) associated
 743 with complex scalar fields (with two real components $\Rightarrow n_B = 2$)
- 744 2. *Gauge supermultiplets*: Spin-1 vector bosons (two helicity states $\Rightarrow n_B = 2$)
 745 associated with Weyl fermions (two helicity states $\Rightarrow n_F = 2$)

746 In the gauge supermultiplet, the vector boson is assumed massless (i.e. before
 747 EWSB generates a mass for it). Since the superpartners to the SM particles have not
 748 yet been discovered, they must be significantly heavier than their SM counterparts.
 749 Unbroken SUSY predicts that the SM particles and their superpartners must have
 750 exactly the same mass, so ultimately a mechanism for SUSY breaking, in addition to
 751 EWSB, must be introduced to generate masses for the superpartners (see Sec. 3.3).
 752 Tables 3.1 and 3.2 show the chiral and gauge supermultiplets of the supersymmetric
 753 Standard Model, respectively. Note that the scalar partners to the SM fermions are
 754 denoted by placing an “s” in front of their names, while the chiral fermion partners
 755 to the SM gauge bosons are denoted by appending “ino” to their names.

756 3.2 The Unbroken SUSY Lagrangian

757 The first piece of the full unbroken SUSY Lagrangian density consists of the kinetic
 758 and interacting terms related to the chiral supermultiplets. As explained in Sec. 3.1, a
 759 chiral supermultiplet consists of Weyl fermions ψ (the ordinary fermion) and complex
 760 scalars ϕ (the sfermion). For a collection of such chiral supermultiplets, the Lagrangian
 761 is

Table 3.1: Chiral supermultiplets of the supersymmetric Standard Model. In the last column, the first number refers to the supermultiplet representation under $SU(3)_C$ (e.g. **3** means it has color charge and feels QCD), the second number refers to the representation under $SU(2)_L$ (e.g. **2** means it has weak isospin and feels the weak interaction), and the third number is the value of the hypercharge. A bar over a number refers to the adjoint representation. **1** means that the supermultiplet is not charged under that group, and thus does not feel the associated force (for example, the right-handed fermion singlets do not feel the weak interaction). Adapted from Table 1.1 of ref. [20].

Type of supermultiplet	Notation	Spin-0 component	Spin-1/2 component	Representation under $SU(3)_C \otimes SU(2)_L \otimes U(1)_Y$
Left-handed quark/squark doublet ($\times 3$ families)	Q	$(\tilde{u}_L \tilde{d}_L)$	$(u_L d_L)$	$(\mathbf{3}, \mathbf{2}, \frac{1}{6})$
Right-handed up-type quark/squark singlet ($\times 3$ families)	\bar{u}	\tilde{u}_R^*	u_R^\dagger	$(\overline{\mathbf{3}}, \mathbf{1}, -\frac{2}{3})$
Right-handed down-type quark/squark singlet ($\times 3$ families)	\bar{d}	\tilde{d}_R^*	d_R^\dagger	$(\overline{\mathbf{3}}, \mathbf{1}, \frac{1}{3})$
Left-handed lepton/slepton doublet ($\times 3$ families)	L	$(\tilde{\nu}_{eL} \tilde{e}_L)$	$(\bar{\nu}_{eL} e_L)$	$(\mathbf{1}, \mathbf{2}, -\frac{1}{2})$
Right-handed lepton/slepton singlet ($\times 3$ families)	\bar{e}	\tilde{e}_R^*	e_R^\dagger	$(\overline{\mathbf{1}}, \mathbf{1}, 1)$
Up-type Higgs/Higgsino doublet	H_u	$(H_u^+ H_u^0)$	$(\tilde{H}_u^+ \tilde{H}_u^0)$	$(\mathbf{1}, \mathbf{2}, \frac{1}{2})$
Down-type Higgs/Higgsino doublet	H_d	$(H_d^0 H_d^-)$	$(\tilde{H}_d^0 \tilde{H}_d^-)$	$(\mathbf{1}, \mathbf{2}, -\frac{1}{2})$

Table 3.2: Gauge supermultiplets of the supersymmetric Standard Model. Adapted from Table 1.2 of ref. [20].

Type of supermultiplet	Spin-1/2 component	Spin-1 component	Representation under $SU(3)_C \otimes SU(2)_L \otimes U(1)_Y$
Gluon/gluino	\tilde{g}	g	(8, 1, 0)
W/wino	$\widetilde{W}^\pm \widetilde{W}^0$	$W^\pm W^0$	(1, 3, 0)
B/bino	\tilde{B}^0	B^0	(1, 1, 0)

$$\begin{aligned} \mathcal{L}_{\text{chiral}} = & -\partial^\mu \phi^{*i} \partial_\mu \phi_i - V_{\text{chiral}}(\phi, \phi^*) - i\psi^{\dagger i} \bar{\sigma}^\mu \partial_\mu \psi_i - \frac{1}{2} M^{ij} \psi_i \psi_j \\ & - \frac{1}{2} M_{ij}^* \psi^{\dagger i} \psi^{\dagger j} - \frac{1}{2} y^{ijk} \phi_i \psi_j \psi_k - \frac{1}{2} y_{ijk}^* \phi^{*i} \psi^{\dagger j} \psi^{\dagger k} \end{aligned} \quad (3.2)$$

where i runs over all supermultiplets in Table 3.1, $\bar{\sigma}^\mu$ are the negative of the Pauli matrices (except for $\sigma^0 = \bar{\sigma}^0$), M^{ij} is a mass matrix for the fermions, y^{ijk} are the Yukawa couplings between one scalar and two spinor fields, and $V_{\text{chiral}}(\phi, \phi^*)$ is the scalar potential

$$\begin{aligned} V_{\text{chiral}}(\phi, \phi^*) = & M_{ik}^* M^{kj} \phi^{*i} \phi_j + \frac{1}{2} M^{in} y_{jkn}^* \phi_i \phi^{*j} \phi^{*k} \\ & + \frac{1}{2} M_{in}^* y^{jkn} \phi^{*i} \phi_j \phi_k + \frac{1}{4} y^{ijn} y_{klm}^* \phi_i \phi_j \phi^{*k} \phi^{*l}. \end{aligned} \quad (3.3)$$

The Lagrangian can also be written as the kinetic terms plus derivatives of the *superpotential* W :

$$\begin{aligned} \mathcal{L}_{\text{chiral}} = & -\partial^\mu \phi^{*i} \partial_\mu \phi_i - i\psi^{\dagger i} \bar{\sigma}^\mu \partial_\mu \psi_i \\ & - \frac{1}{2} \left(\frac{\delta^2 W}{\delta \phi^i \delta \phi^j} \psi_i \psi_j + \frac{\delta^2 W^*}{\delta \phi_i \delta \phi_j} \psi^{\dagger i} \psi^{\dagger j} \right) - \frac{\delta W}{\delta \phi^i} \frac{\delta W^*}{\delta \phi_i} \end{aligned} \quad (3.4)$$

⁷⁶⁸ where

$$W = M^{ij} \phi_i \phi_j + \frac{1}{6} y^{ijk} \phi_i \phi_j \phi_k. \quad (3.5)$$

⁷⁶⁹ The second part of the Lagrangian involves the gauge supermultiplets. In terms
⁷⁷⁰ of the spin-1 ordinary gauge boson A_μ^a and the spin-1/2 Weyl spinor gaugino λ^a of
⁷⁷¹ the gauge supermultiplet, where a runs over the number of generators for the SM
⁷⁷² subgroup (i.e. 1-8 for $SU(3)_C$, 1-3 for $SU(2)_L$, and 1 for $U(1)_Y$), this part of the
⁷⁷³ Lagrangian is

$$\mathcal{L}_{\text{gauge}} = -\frac{1}{4} F_{\mu\nu}^a F^{\mu\nu a} - i \lambda^a \bar{\sigma}^\mu D_\mu \lambda^a + \frac{1}{2} D^a D^a \quad (3.6)$$

⁷⁷⁴ where

$$F_{\mu\nu}^a = \partial_\mu A_\nu^a - \partial_\nu A_\mu^a + g f^{abc} A_\mu^b A_\nu^c \quad (3.7)$$

⁷⁷⁵ (g is the coupling constant and f^{abc} are the structure constants for the particular SM
⁷⁷⁶ gauge group),

$$D_\mu \lambda^a = \partial_\mu \lambda^a + g f^{abc} A_\mu^b \lambda^c, \quad (3.8)$$

⁷⁷⁷ and D^a is an auxiliary field that is introduced as a bookkeeping tool to keep the
⁷⁷⁸ fermionic and bosonic degrees of freedom equal both on- and off-shell. There is no
⁷⁷⁹ kinetic term for D^a in the Lagrangian, so therefore it does not propagate or represent

⁷⁸⁰ any real particle. Its equation of motion, from $\delta\mathcal{L}/\delta D^a = 0$, yields a simple algebraic
⁷⁸¹ expression for D^a that can be used to eliminate it from the Lagrangian if desired.

⁷⁸² To build a fully supersymmetric and gauge-invariant Lagrangian, the ordinary
⁷⁸³ derivatives in $\mathcal{L}_{\text{chiral}}$ (Eq. 3.2) must be replaced by covariant derivatives

$$D_\mu \phi_i = \partial_\mu \phi_i - ig A_\mu^a (T^a \phi)_i \quad (3.9)$$

$$D_\mu \phi^{*i} = \partial_\mu \phi^{*i} + ig A_\mu^a (\phi^* T^a)^i \quad (3.10)$$

$$D_\mu \psi_i = \partial_\mu \psi_i - ig A_\mu^a (T^a \psi)_i. \quad (3.11)$$

⁷⁸⁴ This leads to the full Lagrangian

$$\begin{aligned} \mathcal{L} &= \mathcal{L}_{\text{chiral}} + \mathcal{L}_{\text{gauge}} \\ &\quad - \sqrt{2} g (\phi^{*i} T^a \psi_i) \lambda^a - \sqrt{2} g \lambda^{\dagger a} (\psi^{\dagger i} T^a \phi_i) + g (\phi^{*i} T^a \phi_i) D^a \\ &= -\partial^\mu \phi^{*i} \partial_\mu \phi_i - i \psi^{\dagger i} \bar{\sigma}^\mu \partial_\mu \psi_i + ig \partial^\mu \phi^{*i} A_\mu^a (T^a \phi)_i - ig \partial_\mu \phi_i A^{\mu a} (\phi^* T^a)^i \\ &\quad - g^2 A^{\mu a} (\phi^* T^a)^i A_\mu^a (T^a \phi)_i - g \psi^{\dagger i} \bar{\sigma}^\mu A_\mu^a (T^a \psi)_i - V_{\text{chiral}}(\phi, \phi^*) \\ &\quad - \frac{1}{2} M^{ij} \psi_i \psi_j - \frac{1}{2} M_{ij}^* \psi^{\dagger i} \psi^{\dagger j} - \frac{1}{2} y^{ijk} \phi_i \psi_j \psi_k - \frac{1}{2} y_{ijk}^* \phi^{*i} \psi^{\dagger j} \psi^{\dagger k} \\ &\quad - \frac{1}{4} F_{\mu\nu}^a F^{\mu\nu a} - i \lambda^{\dagger a} \bar{\sigma}^\mu \partial_\mu \lambda^a - ig \lambda^{\dagger a} \bar{\sigma}^\mu f^{abc} A_\mu^b \lambda^c + \frac{1}{2} D^a D^a \\ &\quad - \sqrt{2} g (\phi^{*i} T^a \psi_i) \lambda^a - \sqrt{2} g \lambda^{\dagger a} (\psi^{\dagger i} T^a \phi_i) + g (\phi^{*i} T^a \phi_i) D^a. \end{aligned} \quad (3.12)$$

⁷⁸⁵ Writing out $F_{\mu\nu}^a$ and $V_{\text{chiral}}(\phi, \phi^*)$ explicitly combining the D^a terms using the equation
⁷⁸⁶ of motion $D^a = -g \phi^{*i} T^a \phi_i$, and rearranging some terms, the final unbroken SUSY
⁷⁸⁷ Lagrangian is

$$\begin{aligned}
\mathcal{L} = & -\partial^\mu \phi^{*i} \partial_\mu \phi_i - i\psi^{\dagger i} \bar{\sigma}^\mu \partial_\mu \psi_i \\
& - \frac{1}{4} (\partial_\mu A_\nu^a - \partial_\nu A_\mu^a) (\partial^\mu A^{\nu a} - \partial^\nu A^{\mu a}) - i\lambda^{\dagger a} \bar{\sigma}^\mu \partial_\mu \lambda^a \\
& - M_{ik}^* M^{kj} \phi^{*i} \phi_j - \frac{1}{2} M^{ij} \psi_i \psi_j - \frac{1}{2} M_{ij}^* \psi^{\dagger i} \psi^{\dagger j} \\
& + ig \partial^\mu \phi^{*i} A_\mu^a (T^a \phi)_i - ig \partial_\mu \phi_i A^{\mu a} (\phi^* T^a)^i - g \psi^{\dagger i} \bar{\sigma}^\mu A_\mu^a (T^a \psi)_i \\
& - ig \lambda^{\dagger a} \bar{\sigma}^\mu f^{abc} A_\mu^b \lambda^c \\
& - \frac{1}{4} g f^{abc} [(\partial_\mu A_\nu^a - \partial_\nu A_\mu^a) A^{\mu b} A^{\nu c} + A_\mu^b A_\nu^c (\partial^\mu A^{\nu a} - \partial^\nu A^{\mu a})] \\
& - \frac{1}{2} M_{in}^* y^{jkn} \phi^{*i} \phi_j \phi_k - \frac{1}{2} M^{in} y_{jkn}^* \phi_i \phi^{*j} \phi^{*k} \\
& - \frac{1}{2} y^{ijk} \phi_i \psi_j \psi_k - \frac{1}{2} y_{ijk}^* \phi^{*i} \psi^{\dagger j} \psi^{\dagger k} \\
& - \sqrt{2} g (\phi^{*i} T^a \psi_i) \lambda^a - \sqrt{2} g \lambda^{\dagger a} (\psi^{\dagger i} T^a \phi_i) \\
& - g^2 A^{\mu a} (\phi^* T^a)^i A_\mu^a (T^a \phi)_i - \frac{1}{4} g^2 f^{abc} A_\mu^b A_\nu^c f^{abc} A^{\mu b} A^{\nu c} \\
& - \frac{1}{4} y^{ijn} y_{kln}^* \phi_i \phi_j \phi^{*k} \phi^{*l} - \frac{1}{2} g^2 (\phi^{*i} T^a \phi_i)^2.
\end{aligned} \tag{3.13}$$

788 The above Lagrangian applies to chiral supermultiplets interacting with one kind
789 of gauge supermultiplet (i.e. one SM gauge group). In the general case, there are
790 additional terms corresponding to interactions with all three SM gauge groups.

791 The following list gives a description of the terms in Eq. 3.13:

- 792 • First two lines: kinetic terms for the four types of fields ϕ_i , ψ_i , A_μ^a , and λ^a
- 793 • Third line: mass terms for the ϕ_i and ψ_i (see Figs. 3.1(a) and 3.1(b))
- 794 • Fourth and fifth lines: cubic couplings in which ϕ_i , ψ_i , or λ^a radiates an A_μ^a (see
 795 Figs. 3.1(c), 3.1(d), and 3.1(e))
- 796 • Sixth line: triple gauge boson couplings (see Fig. 3.1(f))
- 797 • Seventh line: triple sfermion couplings (see Fig. 3.1(g))

- 798 • Eighth line: cubic couplings in which ψ_i radiates a ϕ_i (see Fig. 3.1(h))
- 799 • Ninth line: ϕ_i - ψ_i - λ^a vertices (see Fig. 3.1(i))
- 800 • 10th line: A_μ^a - A_μ^a - ϕ_i - ϕ_i and quadruple gauge boson couplings (see Figs. 3.1(j)
801 and 3.1(k))
- 802 • 11th line: ϕ_i^4 vertices (see Figs. 3.1(l) and 3.1(m))

803 3.3 Soft SUSY Breaking

804 Since quadratic divergences in sfermion masses vanish to all orders in perturbation
805 theory in plain unbroken SUSY [20] due to the presence of gauge and Yukawa in-
806 teractions with the necessary relationships between coupling constants (i.e. chiral
807 symmetry inherited from the partner fermion protects the sfermion masses, as ex-
808 plained in Sec. 2.2), it is desirable that the terms that break SUSY not disturb this
809 property. In addition, SUSY should be broken spontaneously, as electroweak symme-
810 try is broken in the Standard Model, so that it is only made manifest at high energies.

811 To satisfy these constraints, SUSY-breaking terms are simply added to the unbroken
812 SUSY Lagrangian in Eq. 3.13 such that $\mathcal{L}_{\text{total}} = \mathcal{L}_{\text{unbroken}} + \mathcal{L}_{\text{breaking}}$. The coefficients
813 of terms in $\mathcal{L}_{\text{breaking}}$ must have positive mass dimension in order not to contribute
814 quadratically divergent loop corrections to the scalar masses (like the Higgs mass);
815 i.e. to not create a hierarchy problem (Sec. 2.2) for the scalars.¹ This form of SUSY

¹This point can be argued via dimensional analysis. Radiative corrections take the form Δm_S^2 , where m_S is the mass of the scalar particle in question. The dimensions of Δm_S^2 are mass². Δm_S^2 is proportional to some coupling constant or mass coefficient k multiplied by a function of Λ_{UV} , the high energy cutoff scale. The function of Λ_{UV} is determined by a loop integral, and thus typically takes the form Λ_{UV}^2 (quadratically divergent) or $\ln \frac{\Lambda_{\text{UV}}}{m_{\text{low}}}$ (logarithmically divergent, where m_{low} is some other lower-mass scale in the problem). Now, if k already contributes at least one power of mass to Δm_S^2 , then the high-energy behavior—the function of Λ_{UV} —can only contribute at most one power of the dimensionful parameter Λ_{UV} . However, there are typically no loop integrals that diverge linearly in Λ_{UV} , so by forcing k to have positive mass dimension, the form of the radiative corrections contributed by SUSY-breaking terms is limited to $\Delta m_S^2 \sim m_{\text{low}}^2 \ln \frac{\Lambda_{\text{UV}}}{m_{\text{low}}}$. In effect, the possibility of dangerous corrections proportional to Λ_{UV}^2 is excluded by dimensional analysis if the requirement that k contribute at least one power of mass is enforced.

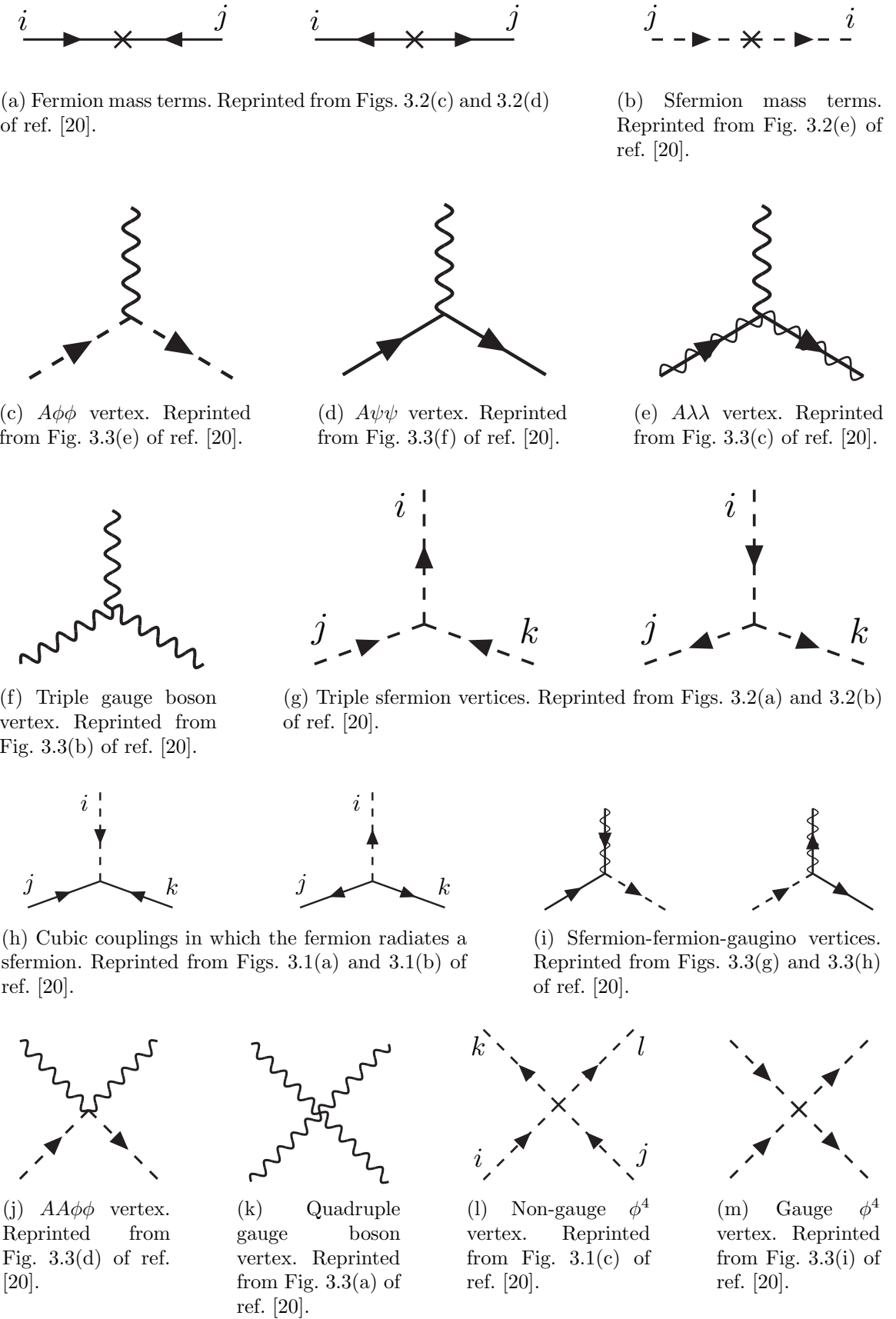


Figure 3.1: Interactions in the unbroken SUSY Lagrangian.

816 breaking is called *soft*, and all coefficients of soft SUSY breaking terms are expected
817 to be of order m_{soft} or m_{soft}^2 .

818 Soft SUSY breaking terms give masses to the sfermions and gauginos and introduce
819 a cubic sfermion vertex. The soft terms are given by

$$\begin{aligned} \mathcal{L}_{\text{soft}} = & -\frac{1}{2}(M_3\tilde{g}^a\tilde{g}^a + M_2\tilde{W}^a\tilde{W}^a + M_1\tilde{B}\tilde{B} + \text{h.c.}) \\ & - (a_u^{ij}\tilde{u}_{Ri}^*\tilde{Q}_j H_u - a_d^{ij}\tilde{d}_{Ri}^*\tilde{Q}_j H_d - a_e^{ij}\tilde{e}_{Ri}^*\tilde{L}_j H_d + \text{h.c.}) \\ & - m_{\tilde{Q}_{ij}}^2 \tilde{Q}_i^\dagger \tilde{Q}_j - m_{\tilde{L}_{ij}}^2 \tilde{L}_i^\dagger \tilde{L}_j \\ & - m_{\tilde{u}_{ij}}^2 \tilde{u}_{Ri} \tilde{u}_{Rj}^* - m_{\tilde{d}_{ij}}^2 \tilde{d}_{Ri} \tilde{d}_{Rj}^* - m_{\tilde{e}_{ij}}^2 \tilde{e}_{Ri} \tilde{e}_{Rj}^* \\ & - m_{H_u}^2 H_u^* H_u - m_{H_d}^2 H_d^* H_d - (b H_u H_d + \text{h.c.}) \end{aligned} \quad (3.14)$$

820 where a runs from 1-8 for \tilde{g}^a and from 1-3 for \tilde{W}^a , and i, j run over the three families.
821 The color indices are not shown. The first line of Eq. 3.14 contains the gaugino mass
822 terms. The second line contains cubic scalar couplings that contribute to mixing
823 between the left- and right-handed third generation sfermions (it is assumed in the
824 supersymmetric Standard Model that the a_u^{ij} , a_d^{ij} , and a_e^{ij} are negligible unless $i =$
825 $j = 3$). The third and fourth lines of Eq. 3.14 contain squark and slepton mass terms,
826 and finally the last line contains the Higgs mass terms.

827 Many viable models of achieving soft SUSY breaking have been studied over the
828 last 30 years. For an overview, see Sec. 6 of ref. [20]. However, this thesis will only cover
829 *gauge-mediated SUSY breaking* (GMSB), because the two-photon search performed
830 is far more sensitive to this model than to other models of SUSY breaking.

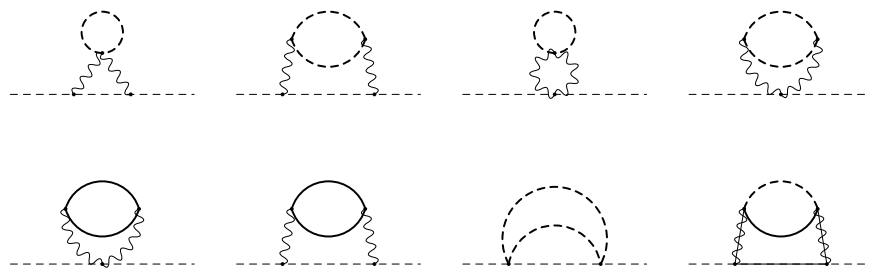
3.4 Gauge-Mediated SUSY Breaking

In gauge-mediated models [24–29], “hidden” fields spontaneously break the supersymmetry of very heavy chiral *messenger* supermultiplets. There are a number of competing models (see refs. [24–29]) that attempt to explain the precise mechanism of spontaneous SUSY breaking, but fortunately the details of those models mostly decouple from the phenomenology of GMSB. The messengers then communicate the SUSY breaking to the sparticles via self-energy loop diagrams of gauge interaction strength (i.e. via vertices like those shown in Figs. 3.1(c), 3.1(d), 3.1(i), 3.1(j), and 3.1(m), which are proportional to the SM gauge couplings constants). The messengers are very heavy, so they cannot be detected in current collider experiments. Feynman diagrams corresponding to gaugino and sfermion mass terms are shown in Figure 3.2.

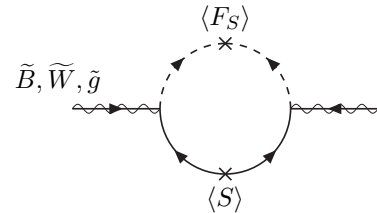
Historically, GMSB and gravity-mediated SUSY breaking, or mSUGRA [30–36], have been the two most thoroughly experimentally studied scenarios of SUSY breaking. One advantage of GMSB over mSUGRA is that it naturally suppresses flavor violation, a generic prediction of supersymmetry. Flavor violation is introduced in the scalar³ couplings and sfermion mass terms of $\mathcal{L}_{\text{soft}}$ (second, third, and fourth lines of Eq. 3.14). Since a_u^{ij} , a_d^{ij} , a_e^{ij} , $m_{\tilde{Q}ij}$, $m_{\tilde{L}ij}$, $m_{\tilde{u}ij}$, $m_{\tilde{d}ij}$, and $m_{\tilde{e}ij}$ are matrices in family space, any nonzero off-diagonal elements will lead to mixing between sfermions of different families. This can lead, for example, to contributions to the diagram $\mu \rightarrow e\gamma$ (Figure 3.3) exceeding the experimental bounds. To avoid this disaster, *universality* conditions are assumed:

$$\mathbf{m}_{\tilde{\mathbf{Q}}}^2 = m_{\tilde{Q}}^2 \mathbf{1}, \mathbf{m}_{\tilde{\mathbf{L}}}^2 = m_{\tilde{L}}^2 \mathbf{1}, \mathbf{m}_{\tilde{\mathbf{u}}}^2 = m_{\tilde{u}}^2 \mathbf{1}, \mathbf{m}_{\tilde{\mathbf{d}}}^2 = m_{\tilde{d}}^2 \mathbf{1}, \mathbf{m}_{\tilde{\mathbf{e}}}^2 = m_{\tilde{e}}^2 \mathbf{1} \quad (3.15)$$

i.e. all sfermion mass matrices arising from the soft terms are assumed to be proportional to the unit matrix $\mathbf{1}$, such that there can be no flavor mixing from these terms



(a) Sfermion mass terms. Heavy dashed lines denote messenger sfermions; solid lines denote messenger fermions. Reprinted from Fig. 6.4 of ref. [20].



(b) Gaugino mass term. The $\langle S \rangle$ part of the loop is a messenger fermion contribution; the $\langle F_S \rangle$ part is a messenger sfermion contribution. Reprinted from Fig. 6.3 of ref. [20].

Figure 3.2: Contributions to sfermion and gaugino masses from loop interactions with messenger particles in the GMSB framework.

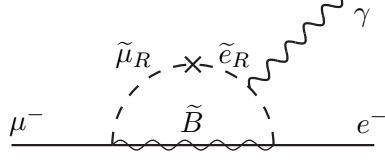


Figure 3.3: Possible contribution to $\mu \rightarrow e\gamma$ from $m_{\tilde{e}ij}$ soft term. Reprinted from Fig. 5.6(a) of ref. [20].

and contributions to flavor-changing processes are drastically reduced.² In mSUGRA models, universality is assumed from the beginning, while in GMSB it is a natural consequence of the fact that the sparticle-messenger vertices are the ordinary flavor-blind gauge couplings that prevent things like flavor-changing neutral currents.

In minimal GMSB (mGMSB), there are four messenger supermultiplets q, \bar{q}, l, \bar{l} providing the messenger (s)quarks and (s)leptons. There is one breaking scale Λ . The gaugino masses computed from diagrams like Fig. 3.2(b) are given by

$$M_a = \frac{\alpha_a}{4\pi} \Lambda \quad (3.16)$$

where a runs from 1-3 and the α_a are the SM gauge coupling constants. The sfermion masses computed from diagrams like Fig. 3.2(a) are given by

$$m_{\phi_i}^2 = 2\Lambda^2 \sum_{a=1}^3 \left(\frac{\alpha_a}{4\pi}\right)^2 C_a(i) \quad (3.17)$$

where $C_a(i)$ are group theory factors that are identical for all particles residing in the same type of supermultiplet (e.g. for all left-handed (s)quarks or left-handed (s)leptons). As explained in the previous paragraph, the gaugino and sfermion masses do not depend on fermion family.

²Universality also includes some assumptions about the form of a_{uij} , a_{dij} , and a_{eij} and the stipulation that the soft terms not introduce any CP-violating phases.

867 In recent years, much theoretical progress has been made in unifying models of
 868 gauge mediation and developing less restrictive models than mGMSB. *General gauge*
 869 *mediation* (GGM) [37] retains the essential features of mGMSB, such as flavor de-
 870 generacy and communication of SUSY breaking via messengers, but does not make
 871 assumptions about the specific messenger sector or SUSY breaking scale. Many dif-
 872 ferent collider final states can be interpreted in terms of GGM, and conversely, GGM
 873 implies a wealth of signatures, only a small fraction of which have been searched
 874 for at colliders [38–40]. The following section discusses the aspects of GGM collider
 875 phenomenology relevant to this thesis.

876 3.5 Phenomenology of General Gauge Mediation

877 The main distinguishing feature of all GMSB phenomenology is that the gravitino \tilde{G} is
 878 very light (eV-keV). In general, the gravitino mass is proportional to $\langle F \rangle / M_P$, where
 879 $\langle F \rangle$ is the vacuum expectation value (VEV) of a field F that spontaneously breaks
 880 SUSY in the vacuum state and M_P is the Planck mass. In GGM models, $\langle F \rangle \sim 10^8$
 881 GeV, leading to a very light gravitino. In contrast, mSUGRA predicts $\langle F \rangle \sim 10^{20}$
 882 GeV. The fact that the gravitino is so much lighter than any other particles in the
 883 supersymmetric Standard Model, and that it interacts only gravitationally (and thus
 884 extremely feebly), leads to two important phenomenological consequences:

- 885 1. All sparticle decay chains in GMSB end with the production of a gravitino.
- 886 2. The gravitino escapes 4π , hermetic collider detectors without interacting, leav-
 887 ing a signature of “missing” momentum transverse to the beam direction.

888 Even if the gravitino were lighter than any other sparticle, but heavier than an
 889 ordinary SM particle, it still could not decay to the SM particle due to *R-parity*. R-
 890 parity is a conserved quantity of the supersymmetric Standard Model introduced to

891 enforce baryon and lepton number conservation, which would otherwise be generically
 892 allowed at levels in conflict with experiment (e.g. the non-observation of baryon-
 893 and lepton-number-violating proton decay). All sparticles have R-parity -1, while all
 894 ordinary SM particles have R-parity +1, and R-parity conservation dictates that at
 895 any vertex, the product of the R-parities of each leg must be +1. This leads to two
 896 more important consequences:

- 897 1. Since conservation of energy only allows it to decay to ordinary SM particles,
 898 but R-parity prevents a sparticle-particle-particle vertex, the *lightest supersym-
 899 metric particle* (LSP) must be absolutely stable. All sparticle decays proceed
 900 through the *next-to-lightest supersymmetric particle* (NLSP), which in turn de-
 901 cays to the LSP. The fact that it is stable and only gravitationally interacting
 902 makes the gravitino a candidate dark matter particle (see Sec. 3.6).
- 903 2. In colliders, sparticles are produced in pairs (particle + particle \rightarrow sparticle +
 904 sparticle).

905 In GMSB, then, the gravitino is the LSP. If the NLSP is a gaugino,³ then the
 906 possible decays depend on mixing among the gauginos. The four neutral gauginos
 907 $\tilde{H}_u^0, \tilde{H}_d^0, \tilde{B}, \tilde{W}^0$ mix into four *neutralino* mass eigenstates $\tilde{\chi}_1^0, \tilde{\chi}_2^0, \tilde{\chi}_3^0, \tilde{\chi}_4^0$, and the four
 908 charged gauginos $\tilde{H}_u^+, \tilde{H}_d^-, \tilde{W}^+, \tilde{W}^-$ mix into two *chargino* mass eigenstates $\tilde{\chi}_1^\pm, \tilde{\chi}_2^\pm$
 909 (two mass eigenstates each with two possible charges = four particles). In the limit
 910 that EWSB effects are small, the neutralino and chargino masses can be written as
 911 the gauge eigenstate masses plus a small perturbation:

³In principle, the NLSP could be anything, but in most popular GGM models, it is either a gaugino or a stau. The stau NLSP search is not the subject of this thesis, so it will not be considered in this section.

$$m_{\tilde{\chi}_1^0} = M_1 - \frac{m_Z^2 \sin^2 \theta_W (M_1 + \mu \sin 2\beta)}{\mu^2 - M_1^2} + \dots \quad (3.18)$$

$$m_{\tilde{\chi}_2^0} = M_2 - \frac{m_W^2 (M_2 + \mu \sin 2\beta)}{\mu^2 - M_2^2} + \dots \quad (3.19)$$

$$m_{\tilde{\chi}_3^0} = |\mu| + \frac{m_Z^2 (\text{sgn}(\mu) - \sin 2\beta)(\mu + M_1 \cos^2 \theta_W + M_2 \sin^2 \theta_W)}{2(\mu + M_1)(\mu + M_2)} + \dots \quad (3.20)$$

$$m_{\tilde{\chi}_4^0} = |\mu| + \frac{m_Z^2 (\text{sgn}(\mu) + \sin 2\beta)(\mu - M_1 \cos^2 \theta_W - M_2 \sin^2 \theta_W)}{2(\mu - M_1)(\mu - M_2)} + \dots \quad (3.21)$$

$$m_{\tilde{\chi}_1^\pm} = M_2 - \frac{m_W^2 (M_2 + \mu \sin 2\beta)}{\mu^2 - M_2^2} + \dots \quad (3.22)$$

$$m_{\tilde{\chi}_2^\pm} = |\mu| + \frac{m_W^2 \text{sgn}(\mu)(\mu + M_2 \sin 2\beta)}{\mu^2 - M_2^2} + \dots \quad (3.23)$$

912 where $\tan \beta = \langle H_u^0 \rangle / \langle H_d^0 \rangle$.

913 The two scenarios studied in ref. [40] are the following:

914 • **Bino NLSP:** $M_1 \sim$ few hundred GeV, $M_2, |\mu| \gg M_1$. All but the lightest
 915 neutralino (Eq. 3.18) are effectively inaccessible at the LHC due to their large
 916 masses. The NLSP can always decay to $\gamma + \tilde{G}$, and if it is heavy enough, to
 917 $Z + \tilde{G}$ or $H + \tilde{G}$.

918 • **Wino NLSP:** $M_2 \sim$ few hundred GeV, $M_1, |\mu| \gg M_2$. The lightest neutralino
 919 (Eq. 3.18) and the lightest chargino (Eq. 3.22) are nearly degenerate in mass,
 920 and are the only two particles to play a role at the LHC. The decays described
 921 in the previous bullet point can happen, as well as chargino decays to $W + \tilde{G}$.

922 The search described in this thesis is optimized for the classic bino NLSP decay $\gamma + \tilde{G}$,
 923 but sensitivity to the wino co-NLSP scenario is also studied (see Chapter 8).

924 Since strong production of SUSY particles, for instance via $gg \rightarrow \tilde{g}\tilde{g}$, dominates
 925 over electroweak production, for instance via $q\bar{q} \rightarrow \tilde{\chi}_1^\pm \tilde{\chi}_1^\mp$, at the LHC due to the
 926 enhanced gg parton luminosity over the $q\bar{q}$ parton luminosity, early LHC searches are
 927 particularly sensitive to light squarks and gluinos. General gauge mediation makes no

928 a priori restrictions on the mass splitting between the strongly interacting sparticles
 929 and the weakly interacting sparticles, so models with light squarks and gluinos are
 930 viable. In fact, such models could not be probed as well at the Tevatron⁴ as they are
 931 at the LHC due to the aforementioned parton luminosities.

932 Typical LHC signatures of the bino and wino NLSP scenarios are shown in Fig-
 933 ure 3.4.

934 3.6 Experimental Status of SUSY

935 Collider searches for evidence of supersymmetry began in earnest in the 1980s [42–50]
 936 and continue to this day. Most recently, the LHC and Tevatron experiments have set
 937 the strictest limits on a variety of SUSY breaking scenarios, including GMSB and
 938 mSUGRA.

939 Figure 3.5 shows the current limits set by the CMS experiment on the mSUGRA
 940 model (with $\tan \beta = 10$) in the m_0 - $m_{1/2}$ plane. (Note that although the plot is trun-
 941 cated at $m_0 = 1000 \text{ GeV}/c^2$, some searches are sensitive out to $m_0 \sim 2000 \text{ GeV}/c^2$.)
 942 Although the LHC has pushed m_0 above $\sim 1 \text{ TeV}/c^2$ for $m_{1/2}$ up to $\sim 400 \text{ GeV}/c^2$,
 943 casting some doubt onto the theory’s prospects for solving the hierarchy problem,
 944 there is still a sizable chunk of mSUGRA parameter space that is not ruled out by
 945 collider experiments. Furthermore, parts of the CMS unexplored regions overlap with
 946 areas allowed by astrophysics experiments [51].

947 Figure 3.6 shows the most up-to-date limit (using 1 fb^{-1} of integrated luminosity
 948 collected by the ATLAS experiment [54] at the LHC) on the Snowmass Points and
 949 Slopes (SPS) model of mGMSB, dubbed SPS8 [53]. In general, the lifetime of the
 950 lightest neutralino in GMSB models can take on any value between hundreds of
 951 nanometers to a few kilometers depending on the mass of the lightest neutralino and

⁴Located on the Fermilab site in Batavia, Illinois, the Tevatron was a proton-antiproton collider operating at 1.96 TeV center-of-mass energy. The Tevatron ran from 1987 to 2011 [41].

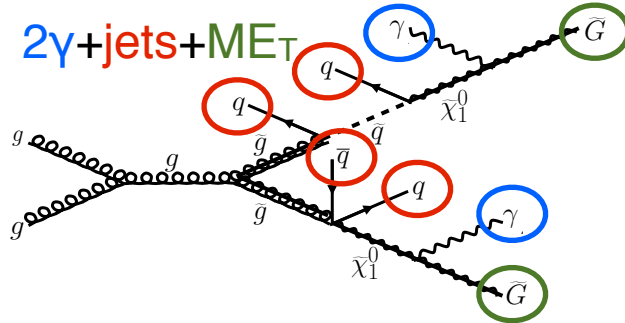
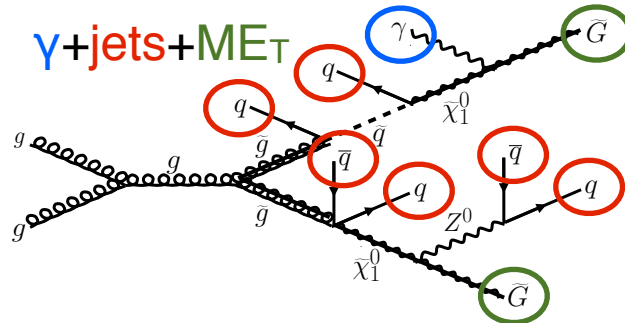
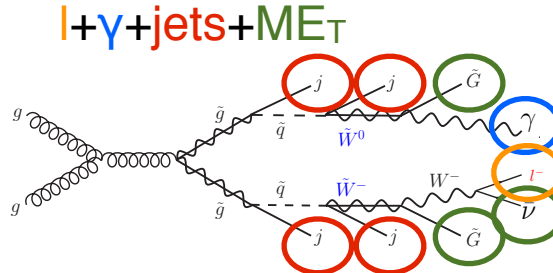
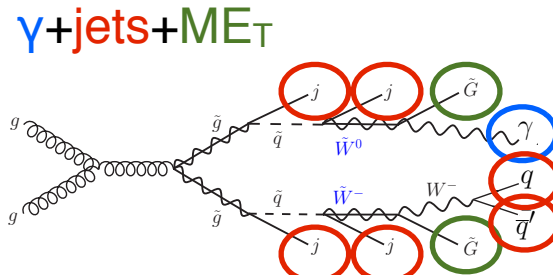
(a) Two gluinos each decay via $\tilde{\chi}_1^0 \rightarrow \gamma \tilde{G}$.(b) One gluino decays via $\tilde{\chi}_1^0 \rightarrow \gamma \tilde{G}$, the other via $\tilde{\chi}_1^0 \rightarrow Z(\rightarrow q\bar{q})\tilde{G}$.(c) One gluino decays via $\tilde{\chi}_1^0 \rightarrow \gamma \tilde{G}$, the other via $\chi_1^\pm \rightarrow W^\pm(\rightarrow l^\pm \nu_l)\tilde{G}$.(d) One gluino decays via $\tilde{\chi}_1^0 \rightarrow \gamma \tilde{G}$, the other via $\chi_1^\pm \rightarrow W^\pm(\rightarrow q\bar{q}')\tilde{G}$.

Figure 3.4: Typical LHC signatures of the bino and wino NLSP scenarios.

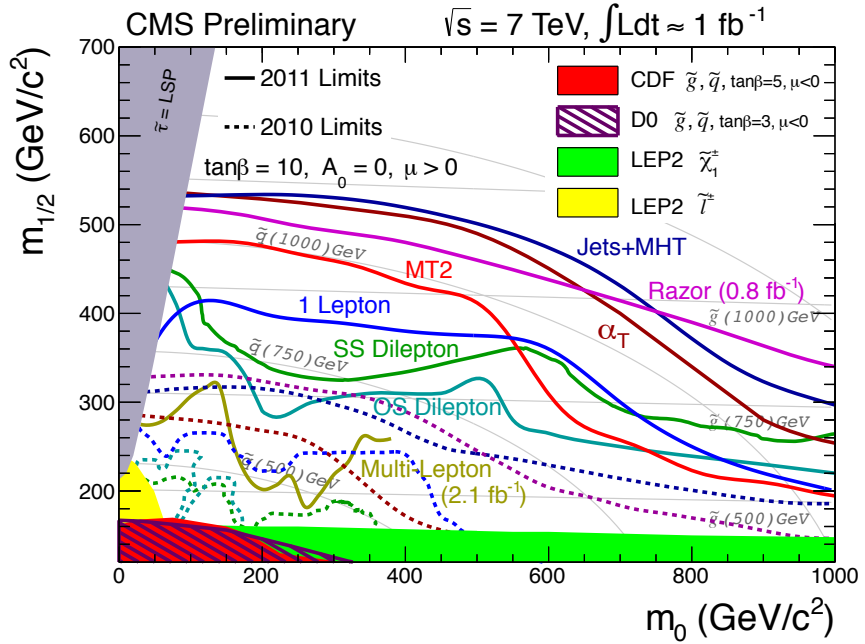


Figure 3.5: CMS limits on mSUGRA with $\tan\beta = 10$, corresponding to a model with third-generation squarks and sfermions somewhat lighter than their first- and second-generation counterparts. The limits set by individual searches are shown as separate colored lines. Solid lines refer to 2011 searches (i.e. using an integrated luminosity of ~ 1 fb $^{-1}$), while dashed lines refer to 2010 searches (~ 36 pb $^{-1}$). Reprinted from ref. [52].

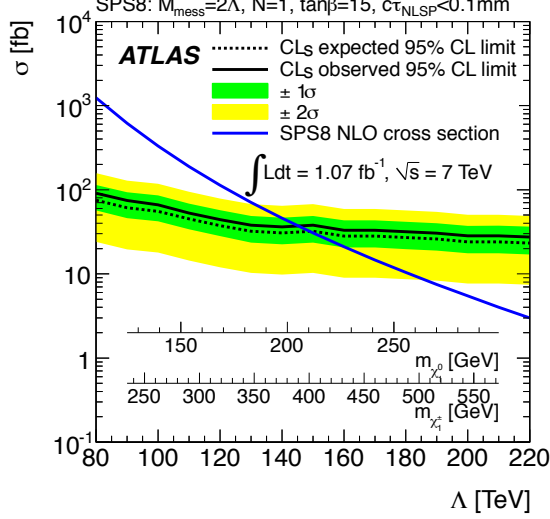


Figure 3.6: ATLAS cross section upper limit on the SPS8 [53] model of mGMSB as a function of SUSY breaking scale Λ , lightest neutralino mass $m_{\tilde{\chi}_1^0}$, or lightest chargino mass $m_{\tilde{\chi}_1^\pm}$. Values of Λ , $m_{\tilde{\chi}_1^0}$, or $m_{\tilde{\chi}_1^\pm}$ below the intersection point between the blue (predicted SPS8 cross section) and black (observed cross section upper limit) curves are excluded. The model parameters listed above the plot are defined in Secs. 3.4 and 3.5, except for τ_{NLSP} , which is the neutralino lifetime. Reprinted from ref. [38].

the SUSY breaking scale [20]. The search published in ref. [38] (from which Fig. 3.6 is culled) considers only *prompt* neutralino variants, i.e. with neutralino lifetime short enough that the distance traveled by the neutralino before decay cannot be resolved by the detector. The most recent limits on non-prompt SPS8-style neutralino models were set by the Collider Detector at Fermilab (CDF) collaboration with 570 pb^{-1} , and are shown in Figure 3.7 [39].

Finally, if the gravitino is to make up some or all of the dark matter, constraints on the form of gauge mediation must come from cosmological considerations and astronomical observations. The gravitino in gauge mediation models is usually very light ($\mathcal{O}(\text{eV-MeV})$) because it is proportional to the SUSY breaking scale divided by the Planck mass, and in GMSB the breaking scale is typically only of order a few hundred TeV ([20] and Sec. 3.5). A light, highly relativistic dark matter particle might have been produced, for instance, in the early, radiation-dominated period of the universe [55]. This *warm dark matter* (WDM) may be responsible for all of

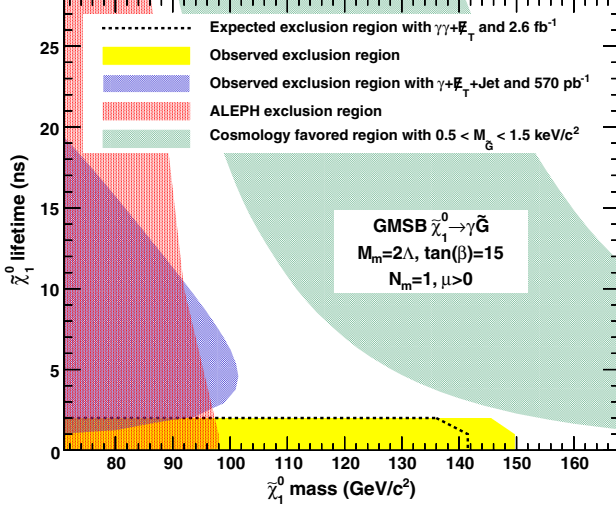


Figure 3.7: CDF exclusion contour in the $\tau_{\tilde{\chi}_1^0}$ - $m_{\tilde{\chi}_1^0}$ plane, where $\tau_{\tilde{\chi}_1^0}$ is the lifetime of the neutralino. Reprinted from ref. [39].

the dark matter needed to account for galactic structure, or it may share the duties with *cold dark matter* (CDM, weakly interacting particles with masses in the GeV range). In any viable model, the predicted relic density of the dark matter species must match the observed value of $\Omega h^2 \sim 0.1$ [56]. For many GMSB models, this measurement constrains the gravitino mass to the keV range [57]. This constraint, however, does not translate into a very strong bound on the lifetime of the lightest neutralino. Using the following equation (taken from [57]):

$$\tau_{\tilde{\chi}_1^0} \sim 130 \left(\frac{100 \text{ GeV}}{m_{\tilde{\chi}_1^0}} \right)^5 \left(\frac{\sqrt{\langle F \rangle}}{100 \text{ TeV}} \right)^4 \mu \text{m} \quad (3.24)$$

and applying the gravitino mass constraint $\sqrt{\langle F \rangle} \lesssim 3000 \text{ TeV}$ (cf. the first paragraph of Sec. 3.5 with $m_{\tilde{G}} \sim \text{keV}$) and $m_{\tilde{\chi}_1^0} = 100 \text{ GeV}$, the upper bound on the neutralino lifetime is 100 meters. For $\sqrt{\langle F \rangle} \sim 100 \text{ TeV}$, the neutralino lifetime is detectable on collider time scales.

Recently, a lower bound on the WDM particle mass in either pure warm or mixed warm and cold dark matter scenarios was set using observations of the Lyman- α forest. For pure WDM, $m_{\text{WDM}} > 8 \text{ keV}$, while for some mixed WDM-CDM scenarios,

980 $m_{\text{WDM}} > 1.1\text{-}1.5 \text{ keV}$ [55, 58]. These bounds and others have motivated the develop-
981 ment of more complicated gauge mediation models [58].

982 However, rather than focus on a specific GMSB model, of which there are many,
983 the search detailed in the following chapters is interpreted in a minimally model
984 dependent way. With this approach, the results can be applied to many competing
985 models. The remainder of this thesis is devoted to the experimental details of the
986 search, analysis strategy, and presentation of the results. The work described in this
987 thesis forms the basis for the CMS public result “Search for Supersymmetry in Events
988 with Photons and Missing Energy” [59], published in April 2012 (see Chapters 7 and 8
989 for results). Ref. [59] contains the best limits on bino-like NLSP and wino-like NLSP
990 GGM models to date.

⁹⁹¹ Chapter 4

⁹⁹² The Large Hadron Collider

⁹⁹³ At a 2010-2011 energy of 3.5 TeV/beam (7 TeV/beam design [60]) and maximum
⁹⁹⁴ instantaneous luminosity of $3.55 \times 10^{33} \text{ cm}^{-2} \text{ s}^{-1}$ [61] ($10^{34} \text{ cm}^{-2} \text{ s}^{-1}$ design [60]),
⁹⁹⁵ the CERN Large Hadron Collider (LHC) is the highest energy and highest intensity
⁹⁹⁶ proton-proton collider ever built. Its purpose is to allow the four LHC experiments to
⁹⁹⁷ explore TeV scale physics. For CMS and ATLAS, this implies examining the origins of
⁹⁹⁸ EWSB via searches for the SM Higgs boson and physical phenomena not predicted by
⁹⁹⁹ the SM that may explain the mass hierarchy in the SM. It also includes searches for
¹⁰⁰⁰ possible dark matter candidates that are often proposed to have masses at the weak
¹⁰⁰¹ scale. The LHC needs to provide high energy proton collisions because the masses
¹⁰⁰² of the sought-after particles are higher than those already incorporated into the SM.
¹⁰⁰³ It must also provide an unprecedented collision rate because signatures of the Higgs
¹⁰⁰⁴ boson and physics beyond the SM are very rare compared to SM processes.

¹⁰⁰⁵ The rest of this chapter is devoted to an overview of the LHC machine. Sec-
¹⁰⁰⁶ tion 4.1 gives the overall layout of the machine and design choices made in light of
¹⁰⁰⁷ energy and luminosity demands. Section 4.2 describes the LHC injection scheme. The
¹⁰⁰⁸ different types of magnets and their functions is illustrated in Section 4.3, and finally
¹⁰⁰⁹ the radiofrequency cavities are covered in Section 4.4. Unless otherwise noted, all

1010 information in this chapter comes from ref. [60].

1011 4.1 Design Considerations and Performance Lim- 1012 itations

1013 The layout of the 26.7-km long [62] LHC ring, located \sim 100 m underground on the
1014 border between France and Switzerland northwest of Geneva, is shown in Figure 4.1.
1015 The two circulating beams of protons travel in opposite directions, colliding only at
1016 the experimental points. There are eight straight sections, each \sim 528 m long, and
1017 eight arcs, each made of 23 106.9-m long arc cells. Beam crossings occur in four of
1018 the straight sections. The arcs contain six 14.3-m long dipole magnets, the cryogenics
1019 to cool the magnets, and short straight sections (SSS) with focusing and corrector
1020 magnets. The high luminosity experiments CMS and ATLAS are located diametrically
1021 opposite each other on the ring, ensuring that in principle each should receive the
1022 same integrated luminosity from the LHC. In Fig. 4.1, ATLAS is located at Point 1,
1023 ALICE at Point 2, CMS at Point 5, and LHCb at Point 8.

1024 To achieve a maximum energy per beam of 7 TeV, the peak magnetic field pro-
1025 duced by the dipole magnets must be 8.33 T, demanding the use of superconducting
1026 technology. Due to the like charges of the two beams, two separate magnet systems
1027 and evacuated beam pipes must be used to accelerate the protons in opposite di-
1028 rections. Space limitations in the LHC tunnel, which was previously used for the
1029 LEP e^+e^- collider, prevent the installation of two separate rings of magnets, so each
1030 dipole instead contains two beam pipe bores and two sets of superconducting coils to
1031 produce two fields in opposite directions. In order to safely operate the magnets at
1032 8.33 T, the cryogenic superfluid helium bath temperature is chosen to be 1.9 K (at a
1033 pressure of 0.13 MPa), colder than any other accelerator cryogen and well below the
1034 critical temperature of the niobium-titanium (NbTi) superconducting wires of 9.2 K

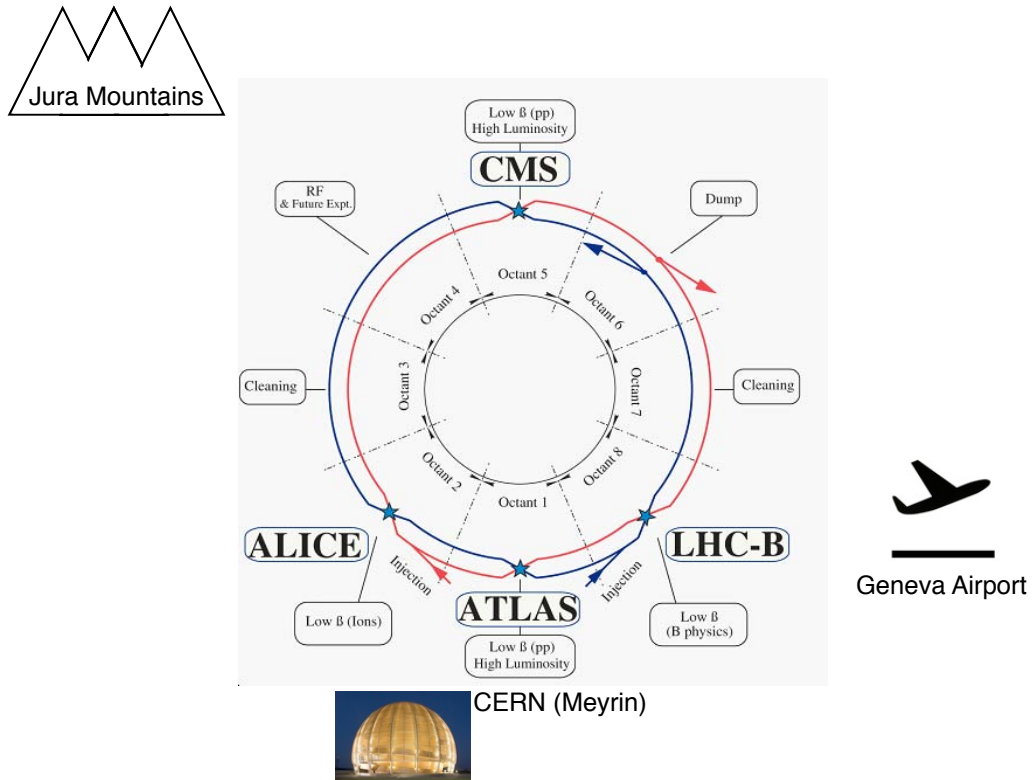


Figure 4.1: Bird's-eye view of the LHC ring, showing the locations of the experiments and local landmarks. Arrows show the beam direction. ATLAS is located at Point 1, ALICE at Point 2, CMS at Point 5, and LHCb at Point 8. The ring figure is reprinted from Fig. 2.1 of ref. [60]. The CERN Globe of Innovation photo comes from ref. [63] and the airplane cartoon comes from ref. [64].

[65]. The extremely low bath temperature leads to a lessened heat capacity in the wires and consequently a lower energy threshold for heating the wires above the temperature needed to maintain the superconducting state. In order to avoid a disastrous magnet quench caused by huge resistive losses if the wires were to transition to the normal conducting state, movements and heat dissipation within the cables must be controlled more tightly than in previous accelerators.

The LHC beams are arranged in bunches of protons, with each bunch separated by an integer multiple of the 25 ns minimum bunch spacing. The machine luminosity L is given by

$$L = \frac{N_b^2 n_b f_{\text{rev}} \gamma_r}{4\pi \epsilon_n \beta^*} F \quad (4.1)$$

where N_b is the number of protons per bunch (squared for the two beams), n_b is the number of bunches per beam, f_{rev} is the bunch revolution frequency, γ_r is the relativistic γ of the protons, ϵ_n is the normalized transverse beam emittance, β^* is the value of the β function at the collision point, and F is a geometrical factor less than one related to the *crossing angle* of the bunches with respect to the horizontal (ATLAS) or vertical (CMS) planes and the beam size. The normalized transverse beam emittance is a measure of the RMS spread of the beam in the plane transverse to its direction of motion, irrespective of its energy. A smaller emittance implies that particles are squeezed into a smaller area in phase space, leading to larger luminosity. The β function is defined as the square of the transverse beam size divided by the emittance. It describes the oscillations of the transverse beam size as a function of position in the ring. To achieve high luminosity, β^* is the minimum of the β function, and it is related to the focusing strength of the triplet magnets near the interaction points. In accelerating sections of the ring, the β function gets large so that the proton

1058 momenta may be more uniform. Each piece of Eq. 4.1 is limited by safety or design
 1059 considerations.

1060 Above some saturated bunch intensity, nonlinear beam-beam interactions experi-
 1061 enced by the protons during collisions cause the luminosity to scale as N_b , not N_b^2
 1062 [66]. The scale of these interactions is set by N_b/ϵ_n , and the size of the beam pipe and
 1063 maximum β function limit ϵ_n to 3.75 μm . Instabilities are also introduced through
 1064 interactions between the protons and the wall of the beam pipe that scale with the
 1065 beam current. Last but not least, the beam dump and magnet safety systems limit
 1066 the total stored energy in the ring. For these reasons, the maximum number of pro-
 1067 tons per bunch is limited to 1.15×10^{11} for a 25 ns bunch spacing. In bunches of this
 1068 proton multiplicity, the average number of proton-proton collisions per bunch cross-
 1069 ing, or *pileup*, in CMS and ATLAS is approximately 20. This unprecedented level of
 1070 pileup poses unique triggering, event reconstruction, and analysis challenges for the
 1071 experiments.

1072 n_b can range from zero to 2808 and had a maximum of ~ 1400 in 2011, corre-
 1073 sponding to 50 ns bunch spacing. f_{rev} is set by the circumference of the ring to 11.2
 1074 kHz [67]. γ_r is set by the beam energy, which was 3.5 TeV in 2011.

1075 The mechanical aperture of the triplet assemblies of quadrupole magnets limit
 1076 the minimum β^* to 0.55 [67] and maximum crossing angle to 285 μrad [67] at the
 1077 interaction points. The purpose of the crossing angle is to prevent parasitic collisions
 1078 in the 23-m length of shared beam pipe upstream and downstream of the interaction
 1079 points.

1080 4.2 Beam Injection

1081 The ultimate source of protons for the LHC is a bottle of hydrogen connected to the
 1082 CERN Linac2 linear accelerator, which accelerates the protons up to 50 MeV. From

The LHC injection complex

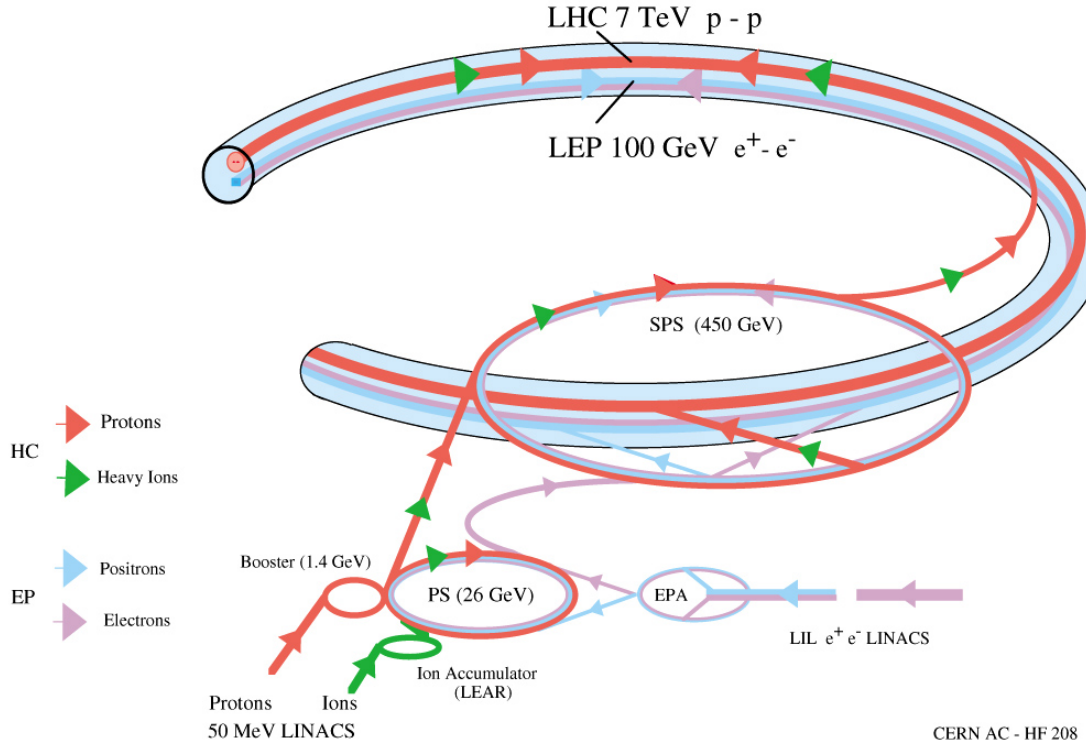


Figure 4.2: Overview of the LHC injector complex at CERN [68].

1083 there they enter the Proton Synchrotron Booster (PSB), which accelerates them to
 1084 1.4 GeV, and then the Proton Synchrotron (PS) itself, which brings them to 25 GeV.
 1085 The Super Proton Synchrotron (SPS) is the next stage, accelerating the protons to
 1086 an energy of 450 GeV. Finally, they leave the SPS and enter the LHC, where they are
 1087 accelerated to the desired beam energy (3.5 TeV in 2011). An overview of the LHC
 1088 injector complex is shown in Figure 4.2.

1089 The 25-ns spaced bunches (or 50 ns for 2011 operation) are produced in trains
 1090 of 72 in the PS via a process of splitting six initial bunches into 12 smaller bunches
 1091 at specified points along the ring. At the end of each train is a 300 ns (12 bunch)
 1092 gap, which is an artifact of the splitting process. The SPS is limited by its maximum
 1093 allowed bunch intensity to storing three or four PS trains at a time. There is an 220
 1094 ns (8 bunch) gap at the end of each train due to the SPS injection kicker rise time.

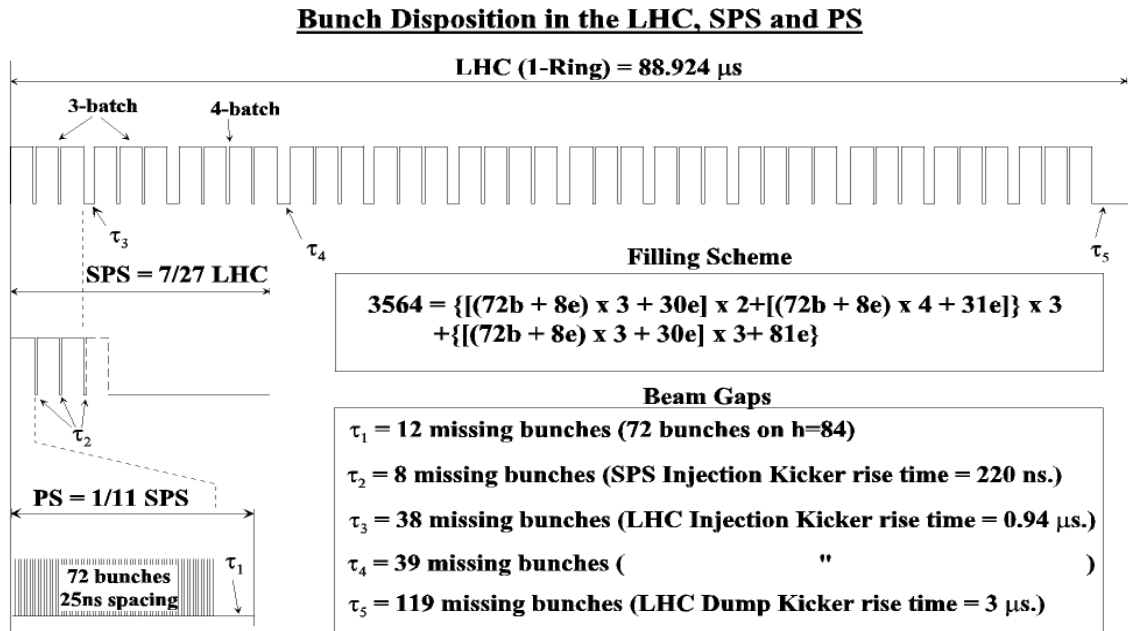


Figure 4.3: LHC injection scheme. Reprinted from Fig. 12.2 of ref. [60].

1095 The LHC is filled three or four trains at a time from the SPS. At the end of each
 1096 three-train and four-train group is a gap of $0.94 \mu s$ (38 or 39 bunches) due to the
 1097 LHC injection kicker rise time. Finally, at the end of an entire $88.924-\mu s$ long LHC
 1098 orbit is a gap of $3 \mu s$ (119 bunches), known as the *abort gap*, to allow for the LHC
 1099 dump kicker rise time. The injection scheme is shown in Figure 4.3.

1100 LHC injection occurs at points 2 and 8. At the intersection of the SPS-LHC
 1101 transfer line and the LHC beam pipe are five septum magnets that deflect the bunches
 1102 12 mrad horizontally into orbit. The septum magnets have a gap into which the
 1103 beam is injected as well as two separate holes for the circulating beams, as shown in
 1104 Figure 4.4. Four kicker magnets then deflect the bunches 0.85 mrad vertically into
 1105 orbit. The kicker magnets supply a pulsed magnetic field with a $0.94 \mu s$ rise time
 1106 (see Fig. 4.3) and a $5.84(7.86) \mu s$ flat top for three-train(four-train) injection (see
 1107 Figure 4.5). To limit emittance growth at injection due to over- or under-kicking the
 1108 injected bunches such that they miss the core of the LHC orbit, the kicker current is
 1109 limited to $< 0.5\%$ flat top ripple in any direction.

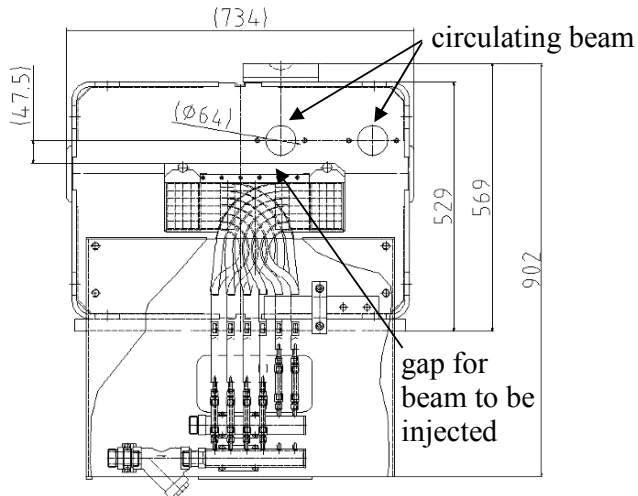


Figure 4.4: Cross-sectional view of septum magnet (beam direction is into or out of the page) showing the holes for the circulating beams and the separate gap for injected particles. Reprinted from Fig. 11.2 of ref. [60].

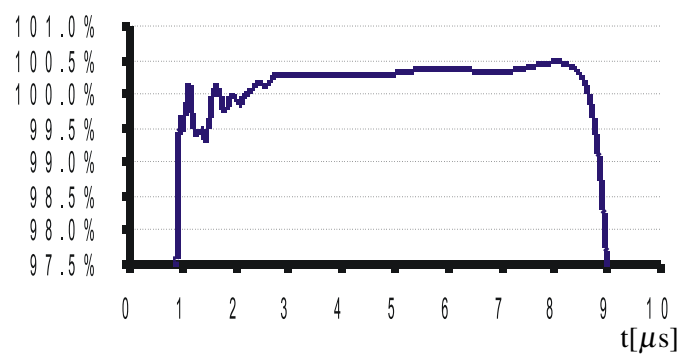


Figure 4.5: LHC injection kicker pulse shape. The y -axis measures percentage of maximum current. Reprinted from Fig. 11.7 of ref. [60].

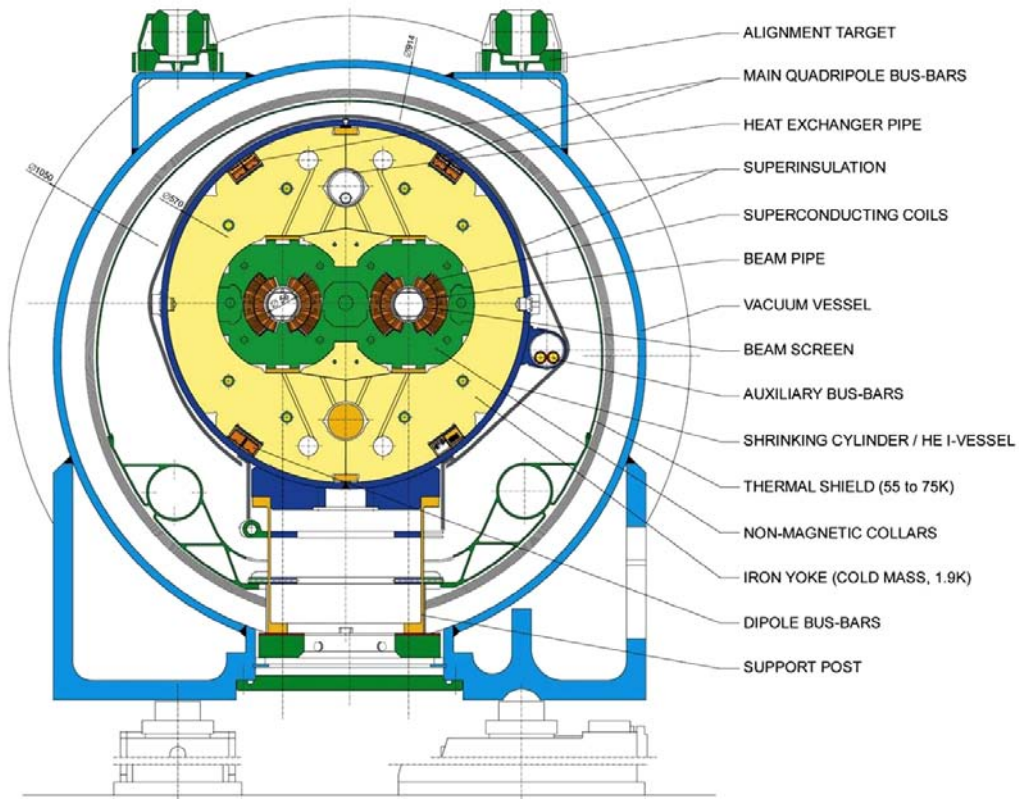


Figure 4.6: Cross-sectional view of LHC dipole + cryostat. Reprinted from Fig. 3.3 of ref. [60].

1110 4.3 Magnets and Cryogenics

1111 There are 1232 twin-bore dipole magnets along the LHC ring used for establishing
1112 the circular orbit of the protons. They consist of two evacuated beam pipes, each
1113 flanked by its own set of superconducting coils, inside an iron yoke which serves as
1114 the 1.9 K cold mass. The entire assembly sits inside a helium vessel, which is itself
1115 surrounded by a vacuum chamber thermally insulating the cold mass from the room
1116 temperature LHC cavern. The entire dipole + cryostat device is ~ 16.5 m long and
1117 weighs about 27.5 t. A cross-sectional view of the dipole is given in Figure 4.6.

1118 To provide a centripetal Lorentz force on the protons, the dipole field points verti-
1119 cally up or down, depending on the direction of the beam. The magnetic field lines for
1120 a single beam pipe are shown in Figure 4.7. Figure 4.8 shows the coil windings in two

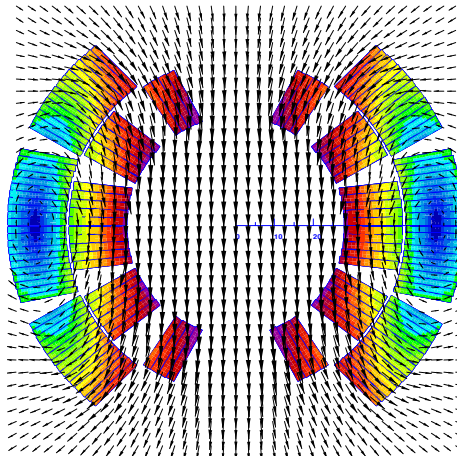


Figure 4.7: Magnetic field lines of the dipole field. The beam direction is into the page. Reprinted from Fig. 4 of ref. [69].

1121 bores. To provide the correct field direction, the coils are wound around blocks that
 1122 are ~ 14 m long (the length of the dipole), so that each winding has a circumference
 1123 of ~ 28 m.

1124 In addition to the dipoles, a number of different types of orbit corrector magnets
 1125 are installed throughout the ring. The main quadrupole magnets, as well as higher
 1126 order field corrector magnets, are located in the arcs and short straight sections. The
 1127 function of these magnets is to provide fine grained control over the magnetic field
 1128 in order to keep the bunches in the proper orbit and control the emittance and β
 1129 functions.

1130 In the straight sections, there are four specialized types of magnets related to SPS
 1131 extraction and bringing the beams into collision. Matching section quadrupoles near
 1132 the transfer lines help to match the injected bunch orbit to the circulating bunch orbit.
 1133 Dispersion suppressors, consisting of dipoles and quadrupoles, help to reduce beam
 1134 dispersion near the collision points due to off-momentum protons. Matching section
 1135 separation dipoles control the separation between the two beams near the collision
 1136 points. The magnets that perform the final squeeze of the beams before collision,
 1137 called the low- β inner triplets, must provide a very high field gradient of 215 T/m,

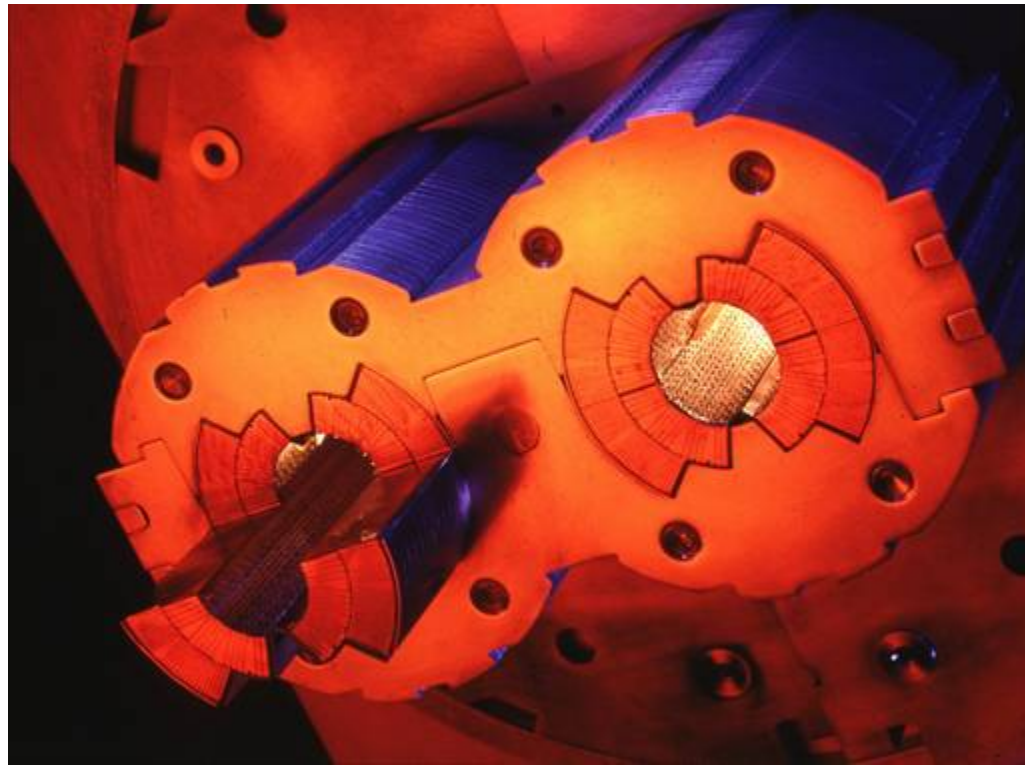


Figure 4.8: Superconducting coils in a twin-bore dipole [70].

₁₁₃₈ withstand a high radiation dose, and sustain high heat loads in the superconducting
₁₁₃₉ coils.

₁₁₄₀ The superfluid helium cryogen is delivered to the magnets via a distribution line
₁₁₄₁ from the main refrigerator. A cross section of the LHC tunnel, showing the cryogen
₁₁₄₂ delivery apparatus for a dipole, is shown in Figure 4.9.

₁₁₄₃ 4.4 Radiofrequency Cavities

₁₁₄₄ LHC bunches are captured and accelerated in 400 MHz superconducting radiofre-
₁₁₄₅ quency (RF) cavities. 400 MHz defines the bunch length of $\lesssim 2$ ns. As bunches pass
₁₁₄₆ through the cavities, the oscillating electric field is at its peak and accelerates the
₁₁₄₇ protons through a potential difference of 2 MV per cavity (16 MV per turn). The
₁₁₄₈ finite bunch length is due to particles that arrive out of phase with the electric field
₁₁₄₉ due to deviations in their momenta from the nominal. During a ramp of the beam

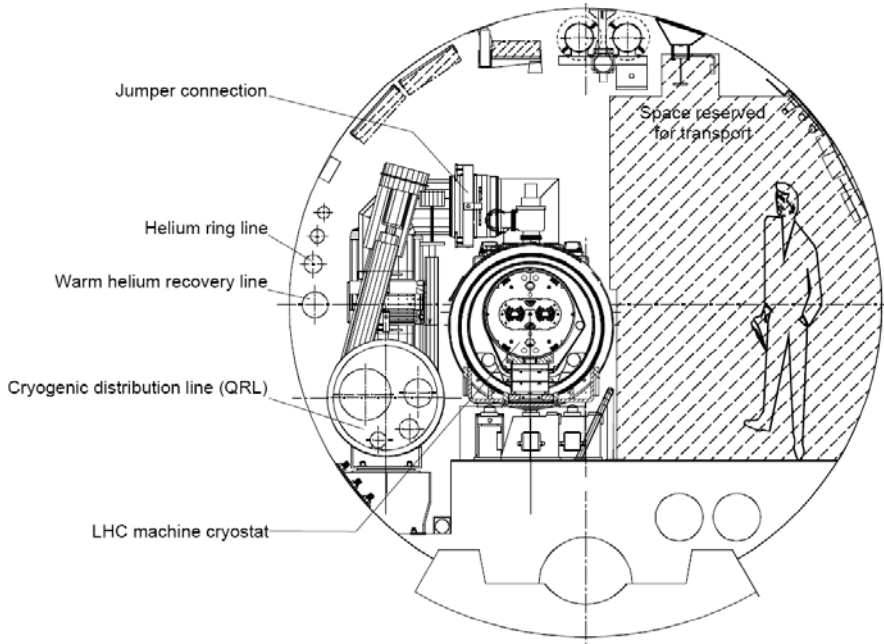


Figure 4.9: Cross section of the LHC tunnel, showing the cryogen delivery apparatus for a dipole. Reprinted from Fig. 7.1 of ref. [60].

1150 energy from 450 GeV to 3.5 or 7 TeV, bunches repeatedly travel around the ring, re-
 1151 ceiving an energy kick each time, until the desired energy is reached. Feedback from
 1152 the RF accelerating system causes an increase in magnet current to keep the bunches
 1153 in a fixed orbit.

1154 Superconducting material (niobium) coats the cylindrical walls of the cavity. RF
 1155 power is coupled to the cavity via a klystron. The RF electric field standing wave is set
 1156 up across the cavity in the beam direction. The transverse magnetic field dissipates
 1157 some energy into the walls, but much less than in a normal conducting cavity.

¹¹⁵⁸ **Chapter 5**

¹¹⁵⁹ **The Compact Muon Solenoid**
¹¹⁶⁰ **Experiment**

¹¹⁶¹ The Compact Muon Solenoid (CMS) detector sits at point 5 of the LHC ring, diamet-
¹¹⁶² rically opposite the ATLAS detector at point 1. It is a 4π hermetic general purpose
¹¹⁶³ detector, meaning that it has the capability to detect charged and neutral hadrons,
¹¹⁶⁴ photons, electrons, muons, taus, neutrinos, and non-Standard-Model particles with
¹¹⁶⁵ good efficiency over a large range of rapidity. Its main distinguishing feature is a su-
¹¹⁶⁶ perconducting solenoid that provides a 3.8T magnetic field parallel to the beam line.
¹¹⁶⁷ This strong magnetic field allows precise determination of the momentum and charge
¹¹⁶⁸ of muons and electrons up to a momentum of \sim 1 TeV.

¹¹⁶⁹ The origin of the CMS coordinate system is at the nominal interaction point. The
¹¹⁷⁰ y -axis points skyward, the x -axis points towards the center of the LHC ring, and
¹¹⁷¹ the z -axis points counterclockwise along the LHC ring. r denotes radial distances
¹¹⁷² from the beam line, ϕ is the azimuthal angle measured with respect to the positive
¹¹⁷³ x -axis, and θ is the polar angle measured with respect to the positive z -axis. The
¹¹⁷⁴ *pseudorapidity* η is defined as $\eta = -\ln \tan(\theta/2)$, and is a good approximation to
¹¹⁷⁵ rapidity $y = (1/2) \ln((E + p_z c)/(E - p_z c))$ for relativistic particles. The transverse

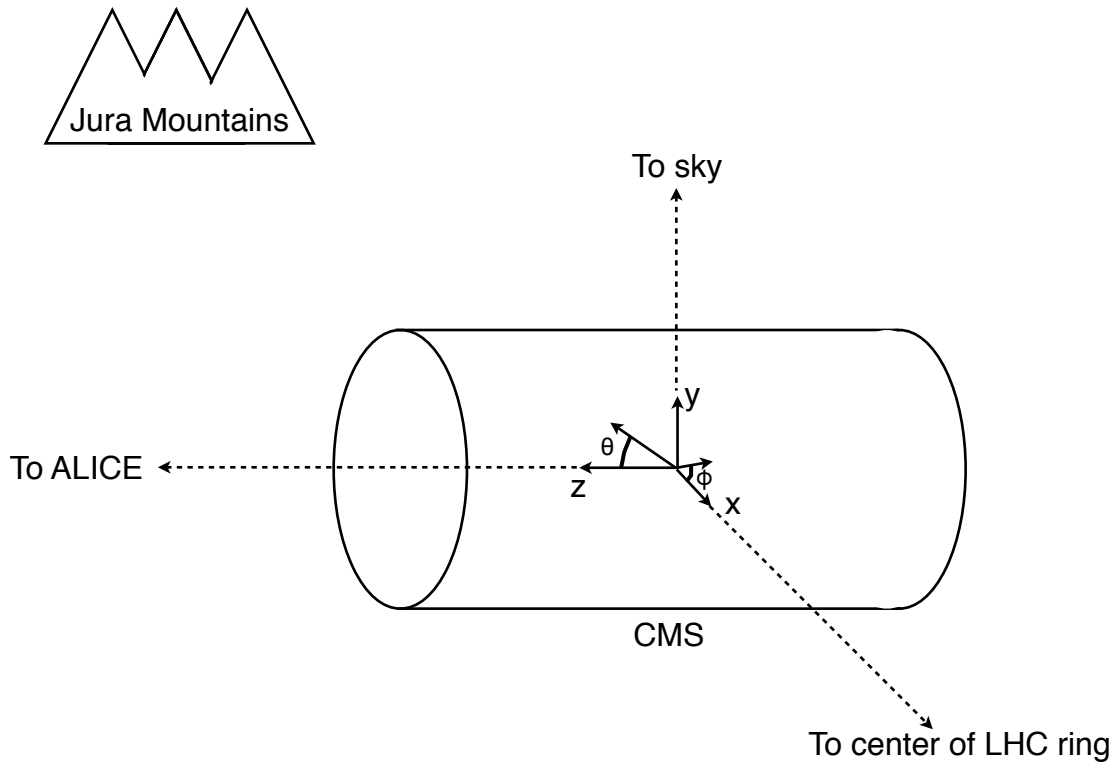


Figure 5.1: CMS coordinate system.

1176 momentum and energy (p_T and E_T) of a particle are defined as $p_T = p \cos \phi$ and
 1177 $E_T = E \cos \phi$, where p and E are the magnitude of the particle's momentum vector
 1178 and the particle's total energy, respectively. A depiction of the CMS coordinate system
 1179 is shown in Figure 5.1.

1180 The CMS sub-detectors are arranged in concentric cylindrical layers, plus “end-
 1181 caps,” around the beam line, as shown in Figure 5.2. Closest to the beam line are
 1182 three layers of silicon pixel detectors, with the innermost at radius 4.4 cm and out-
 1183 ermost at radius 10.2 cm [71]. Including the pixel endcaps, the total pixel coverage
 1184 extends to $\eta = 2.5$ [71]. The pixel detector plays an important role in determining the

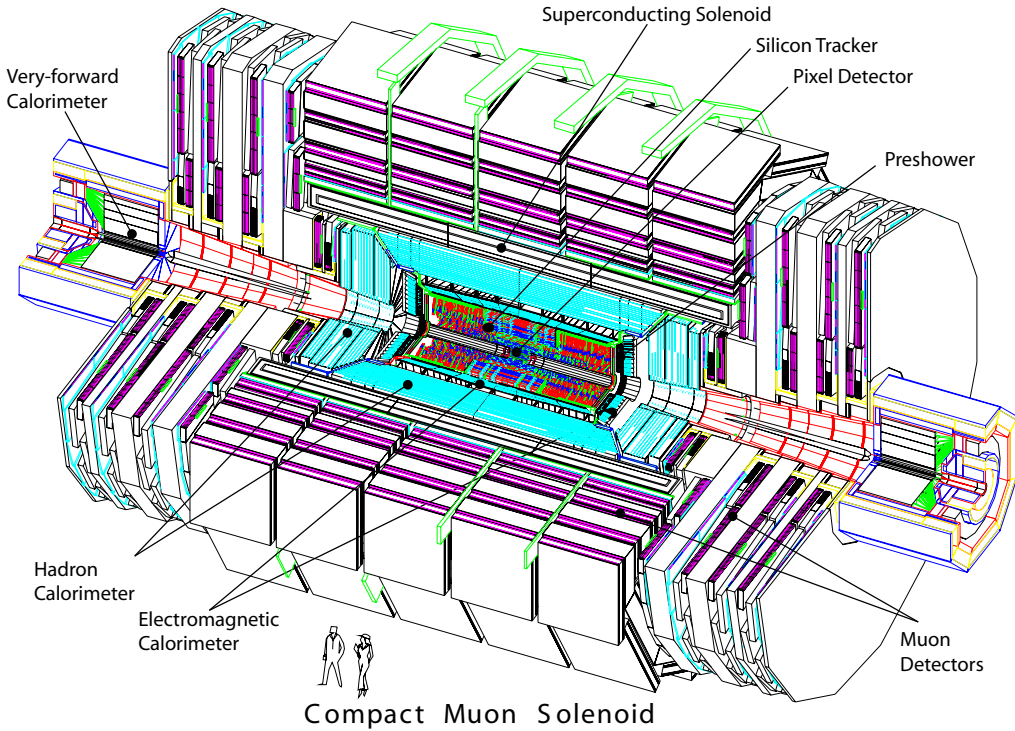


Figure 5.2: Cutaway view of CMS. Reprinted from Fig. 1.1 of ref. [71].

1185 proton-proton interaction position (*beam spot*) and the impact parameters of charged
 1186 particle trajectories, and is critical for the measurement of decay positions some dis-
 1187 tance from the beam spot (*displaced vertices*), such as those due to the showering and
 1188 hadronization of a b quark.

1189 The 10 next layers of CMS are comprised of silicon microstrip detectors, with the
 1190 outermost layer at a radius of 1.3 m from the beam line [71]. As for the pixel detectors,
 1191 the silicon strip endcaps extend tracking coverage to $\eta = 2.5$. The silicon microstrip
 1192 layers are the workhorse of the CMS tracking system, and provide excellent charged
 1193 particle momentum resolution and track finding efficiency.

1194 Outside the tracking detectors are the calorimeters, starting with the single-layer
 1195 lead tungstate crystal electromagnetic calorimeter at a radius of 1.3 m from the beam
 1196 line (location of crystal front faces) [71]. Each crystal is 23 cm long, corresponding
 1197 to 25.8 radiation lengths (X_0) [71]. The crystal dimensions are such that most of one

1198 electromagnetic shower, and no more, can be contained in a single crystal, leading to
 1199 excellent energy resolution for photons and electrons. The electromagnetic calorime-
 1200 ter radial and endcap layers cover a pseudorapidity range up to 3.0. A lead/silicon
 1201 sampling calorimeter sits in front of the crystal endcaps to provide better rejection
 1202 of neutral pions.

1203 The last layer of calorimetry inside the solenoid is the brass/scintillator sampling
 1204 hadronic calorimeter, which has a radial extent from 1.77-2.95 m [71]. The hadronic
 1205 barrel and endcap calorimeters cover up to $|\eta| = 3.0$, while the iron/quartz-fiber for-
 1206 ward hadronic calorimeter covers the region $3.0 \leq |\eta| \leq 5.2$.¹ There is one more
 1207 layer of hadronic calorimetry outside the solenoid in $|\eta| < 1.3$ which, together with
 1208 the layers inside the solenoid, provides approximately 12 hadronic interaction lengths
 1209 of instrumented absorber. Because of its large $|\eta|$ coverage and depth, the hadronic
 1210 calorimeter provides good missing transverse energy resolution and accurate measure-
 1211 ments of high energy jets.

1212 The iron return yoke of the solenoidal magnetic field is interleaved with muon
 1213 detectors from 4.1-7.4 m in r and 6.6-10.6 m in z , providing muon detection up to
 1214 $|\eta| = 2.4$ [71]. In the barrel region of $|\eta| < 1.2$, drift tubes are used to read out the
 1215 muon tracks, while in the endcaps cathode strip chambers are used. Due to their
 1216 speed, resistive plate chambers are used throughout the muon system to provide
 1217 an independent trigger and timing measurement. Combining the tracker and muon
 1218 system hits, the momenta and charge of muons up to $p_T = 1$ TeV can be precisely
 1219 reconstructed.

1220 A longitudinal quarter cross-sectional view of CMS is shown in Figure 5.3. The
 1221 remainder of this chapter is devoted to explaining the CMS subdetectors and readout
 1222 systems. Section 5.1 describes the subdetector technologies and performance bench-

¹The Centauro and Strange Object Research (CASTOR) and Zero Degree Calorimeter (ZDC) detectors provide additional calorimetry beyond $|\eta| = 5.2$. However, they are mainly used in the heavy ion and diffractive physics programs of CMS, and play no role in the detection of heavy SUSY particles. Therefore, they will not be discussed here.

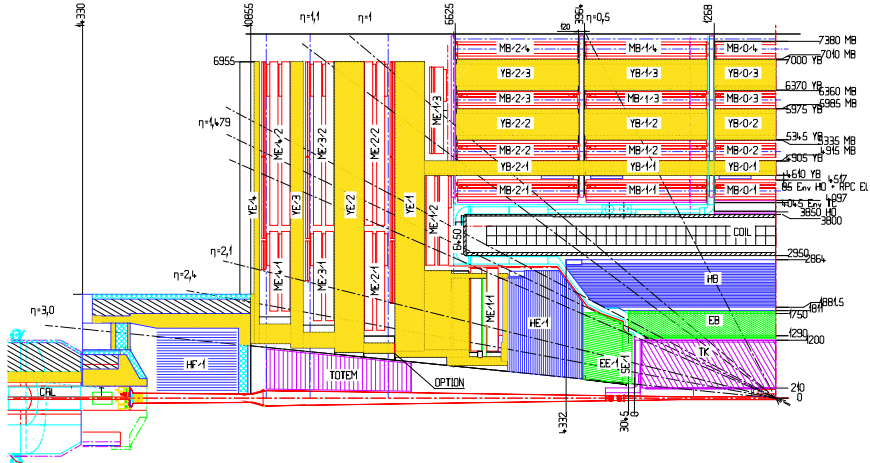


Figure 5.3: Longitudinal quarter cross-sectional view of CMS. The nominal interaction point is at the lower right-hand corner of the drawing. The tracker is shown in purple diagonal hashing, the electromagnetic calorimeter in green, the hadronic calorimeter in blue, and the muon stations in red. The solenoid is shown in black and white and labeled COIL, and the magnet return yoke is shown in yellow. Radial and longitudinal distances are measured in millimeters. Reprinted from Fig. CP 1 of ref. [72].

marks, while Section 5.2 details the CMS trigger and data acquisition systems and framework for promptly reconstructing and transferring data worldwide. For a thorough description of CMS, see ref. [71]. Unless otherwise noted, all information in this chapter comes from ref. [71].

5.1 The Detectors and Their Operating Principles

5.1.1 Tracking System

Given the LHC design instantaneous luminosity, efficient reconstruction of charged particle tracks from transverse momenta of 1 GeV up to 1 TeV can only be achieved with a low occupancy tracker. For $r < 10$ cm, the hit rate density is highest, leading to the choice of $100 \mu\text{m} \times 150 \mu\text{m}$ silicon pixel sensors for hit detection. For $20 \text{ cm} < r < 110 \text{ cm}$, the lower hit rate allows the use of silicon strips, with length along z of order centimeters and length along the $r \cdot \phi$ curve of order hundreds of microns. This

1235 design leads to a pixel hit occupancy of $\sim 10^{-4}$ /pixel/BX and a strip hit occupancy
 1236 of $\sim 10^{-2}$ /pixel/BX, where BX refers to 1 LHC bunch crossing.

1237 As radiation dose from hadrons accumulates over the lifetime of the tracker, silicon
 1238 leakage current through the semiconductor junctions increases, heating up the sensors.
 1239 Since the leakage current itself depends on temperature, this can lead to *thermal*
 1240 *runaway* that damages the detector. To avoid this, the tracker must be cooled to
 1241 approximately -10°C . Operating at this temperature, the signal:noise ratio in the
 1242 silicon sensors is 10:1, and should remain at that level over the 10-year lifetime of the
 1243 tracker.

1244 At its thickest ($|\eta| \sim 1.5$), the tracker depth (including services) is $\sim 1.8X_0$,
 1245 and the depth falls off to $\sim 1X_0$ in thinner areas. Unfortunately, the large mass of
 1246 the tracker degrades somewhat the performance of the electromagnetic calorimeter
 1247 behind it, as $\sim 50\%$ of photons will convert to e^+e^- pairs in the tracker.

1248 Pixel Detector

1249 A longitudinal quarter view of the three barrel pixel (BPix) layers and two forward
 1250 pixel (FPix) disks is shown in Figure 5.4. There are 768 BPix modules in total.
 1251 Each BPix layer is divided into 32 ϕ -wedges, with eight modules per wedge arranged
 1252 end-to-end in z . The ϕ -wedges operate nearly independently in terms of clock and
 1253 readout. Each FPix disk consists of 24 ϕ -wedges, with pie-shaped modules attached
 1254 to the front and back of the disk, for a total of 192 modules. The front- and back-side
 1255 modules of the FPix disks are constructed of different sized *plaquettes*, or multi-pixel
 1256 sensor chips, such that the gaps in the front-side module are covered by plaquette
 1257 area in the back-side module and vice versa. An illustration of the BPix and FPix
 1258 mechanical layouts is given in Figure 5.5.

1259 Since the electric field in the depletion region of the BPix sensors is perpendicular
 1260 (i.e. pointing along r) to the magnetic field of CMS (i.e. pointing along z), the charge

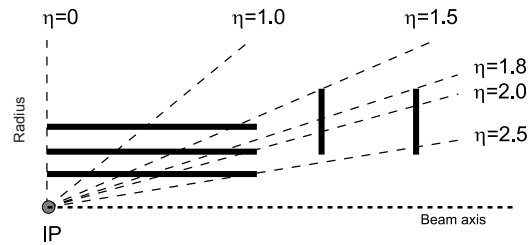
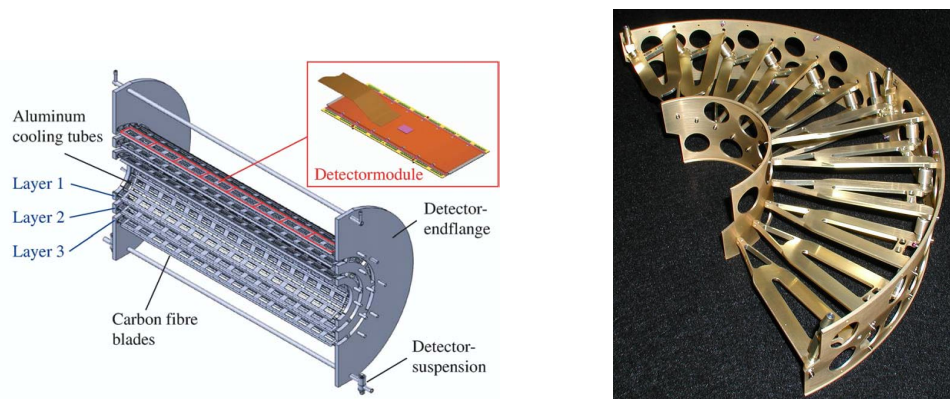


Figure 5.4: Longitudinal quarter view of the pixel detector. Reprinted from Fig. 3.6 of ref. [71].



(a) Cutaway view of the barrel pixel layers, showing the three layers and the eight end-to-end modules along z . Reprinted from Fig. 3.11 of ref. [71].

(b) Half-disk of the forward pixel detector, showing the 12 pie-shaped module mounts. Reprinted from Fig. 3.15 of ref. [71].

Figure 5.5: BPix and FPix mechanical structures.

carriers in the silicon experience a Lorentz drift along ϕ . The multi-pixel sensor pitch is such that this causes the charge from one particle hit to be shared among multiple pixels. Particle hits are reconstructed reading out the analog pixel signal and interpolating between signals in multiple pixels. This method achieves a 15-20 μm spatial resolution, which is comparable to the sensor pitch. To induce this effect in FPix, the sensor wedges are tilted by the approximate BPix Lorentz angle of 20° [73] with respect to the y -axis.

Each multi-pixel sensor consists of an array of 52×80 n-type pixels implanted onto an n-type substrate with 320 μm thickness. The other face of the substrate is covered with a thin layer of p-type semiconductor. Except for the outer edges, which are held at ground potential to prevent sparking between the sensor edges and the connected readout chip [74], the p-side is reverse biased at 150 V (BPix) or 300 V (FPix). The pixels are held at ground potential. A particle entering through the p-side will cause a burst of current to flow across the p-n junction. The charge will be collected by the pixels, which are bump-bonded to the readout. The BPix and FPix sensors employ slightly different technologies for electrically isolating the individual pixels, but both rely on the idea of surrounding the pixels with a p-type material to provide a p-n junction that acts as a barrier to current flow.

Each 52×80 pixel sensor is bump bonded to a readout chip (ROC). The ROCs provide zero suppression and amplify, buffer, and communicate the signals from the sensors. A single token bit manager (TBM) controls ~ 16 ROCs in the barrel or ~ 24 ROCs in the endcaps. Its purpose is to distribute the clock and trigger to the ROCs (the latter initiates a transmission of the signal further upstream to be assembled into the full event readout of CMS). The clock and trigger are supplied by the pixel front end controller (pFEC), which interfaces to the central clock and data acquisition systems. Analog signals that are collected from the pixel front ends are digitized by the pixel front end digitizer (pxFED). A diagram of the readout system is shown in

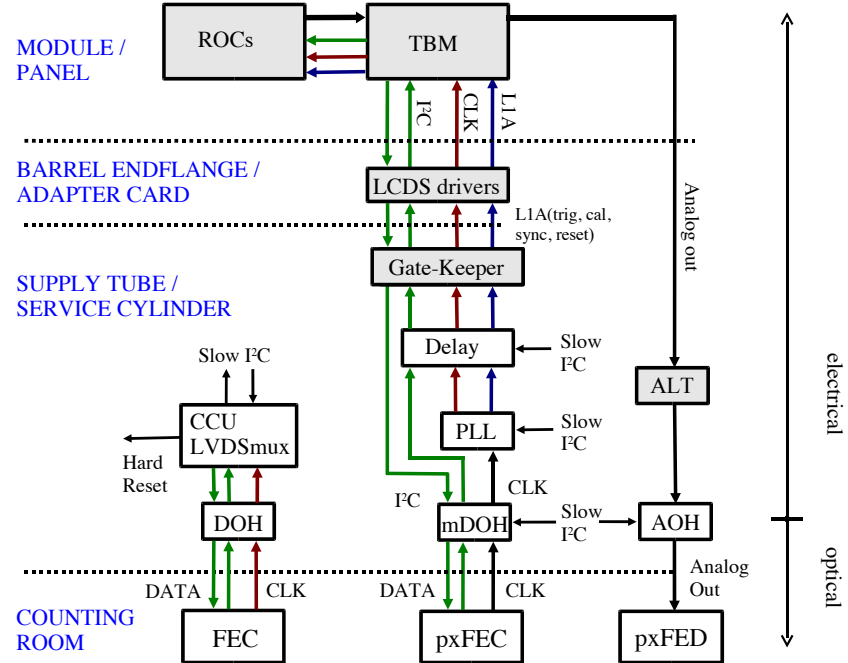


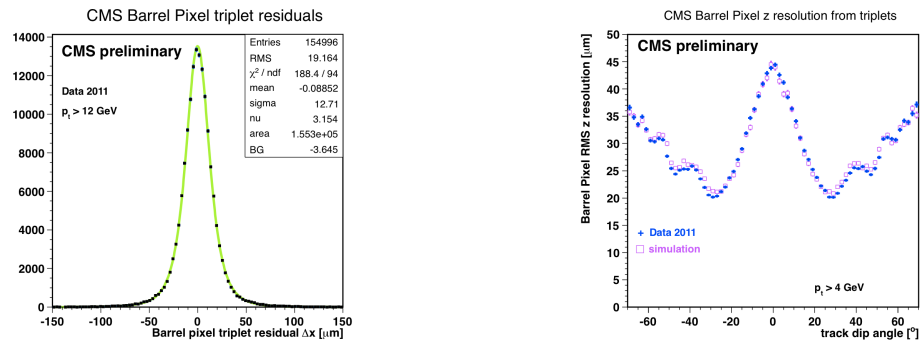
Figure 5.6: Pixel control and readout system. Reprinted from Fig. 3.9 of ref. [71].

1288 Figure 5.6.

1289 Figure 5.7 shows some results highlighting the performance of the pixel detector.

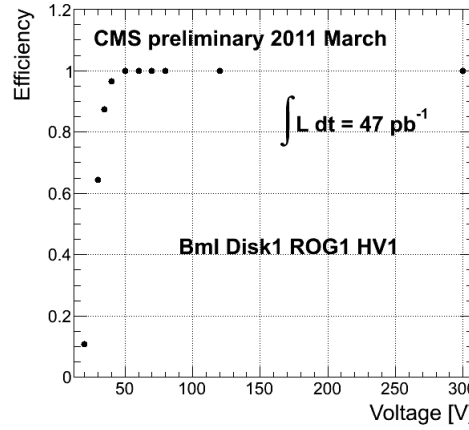
1290 Silicon Strip Tracker

1291 The silicon strip tracker is divided into four parts: the inner barrel (TIB) and inner
 1292 disks (TID), covering the radial extent $20 \text{ cm} < r < 55 \text{ cm}$ and z extent $80 \text{ cm} <$
 1293 $|z| < 90 \text{ cm}$; and the outer barrel (TOB) and endcap (TEC), covering the radial
 1294 extent $61 \text{ cm} < r < 108 \text{ cm}$ and z extent $124 \text{ cm} < |z| < 282 \text{ cm}$. A number of the
 1295 tracker layers and endcaps hold double-sided strip modules (shown as double lines
 1296 in Figure 5.8), with the rear module tilted at an angle of 100 mrad with respect to
 1297 the front module, to provide a measurement in two coordinates. There are a total of
 1298 15,148 modules in the tracker, arranged as shown in the longitudinal cross-sectional
 1299 view of Fig. 5.8. For the TIB and TOB, the modules are arranged in straight rows
 1300 end-to-end along z , with repeating rows covering the full 2π extent in ϕ . In each of the



(a) BPix hit resolution in the $r \cdot \phi$ coordinate [75].

(b) BPix hit resolution in the z coordinate vs. track dip angle, showing the effect of charge sharing on resolution [76].



(c) Pixel reconstruction efficiency vs. bias voltage for a group of three wedges in FPix [77].

Figure 5.7: Pixel detector performance highlights.

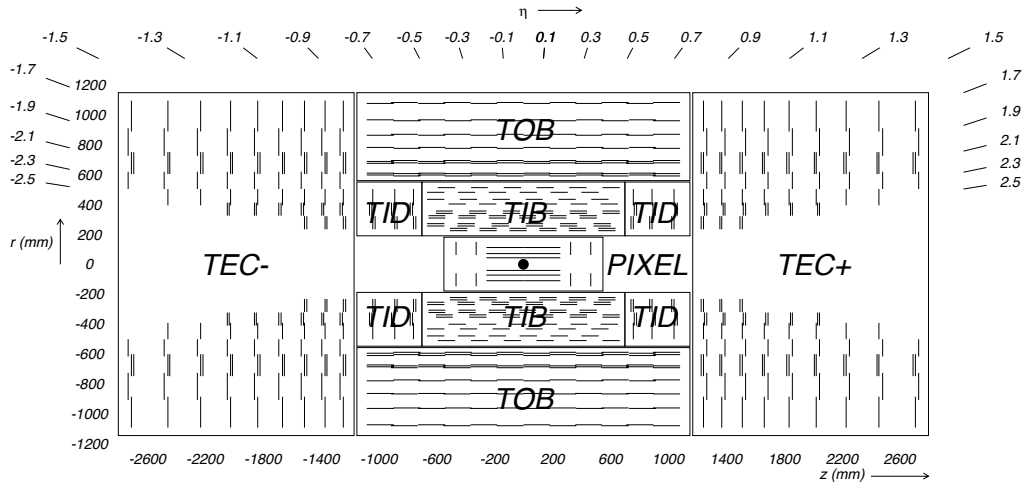


Figure 5.8: Longitudinal cross section of the silicon strip detector. Reprinted from Fig. 3.1 of ref. [71].

1301 TID disks, the modules are arranged into three concentric circular rings of increasing
 1302 r . In the TEC, the modules are affixed to ϕ -wedges called *petals*. One side of the TEC
 1303 and its petal structure is shown in Figure 5.9.

1304 Like the pixels, the strip sensors generate a signal when current flows across a
 1305 p-n junction in response to interaction with a charged particle. Whereas the pixels
 1306 are n-type implants on an n-type substrate, with a solid p-type rear layer to which
 1307 the high voltage is connected, the strips are p-type implants on an n-type substrate,
 1308 with a solid n-type rear layer connecting to the high voltage. The p-n junction in the
 1309 strip sensors is at the strip-substrate boundary, whereas in the pixel sensors it is at
 1310 the boundary between the rear layer and the substrate. Each sensor has either 512
 1311 or 768 electrically isolated strips, with pitch varying from 80-205 μm depending on
 1312 location. Strip lengths in z range from ~ 10 to ~ 25 cm. Thin (320 μm) sensors are
 1313 used in the TIB, TID, and inner four rings of the TEC, while thick (500 μm) sensors
 1314 are used in the TOB and the outer rings of the TEC. The thicker sensors compensate
 1315 for the increased strip capacitance (and hence electronics noise) of the longer strips
 1316 in the outer layers/disk of the tracker such that strip signal:noise is maintained above
 1317 10 everywhere.

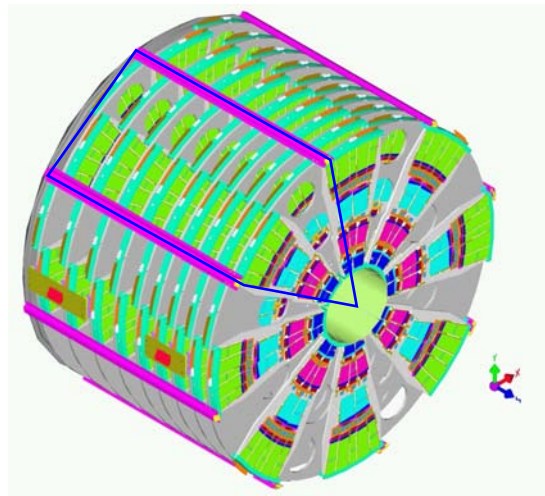


Figure 5.9: View of one tracker endcap, with the outline of a petal shown in blue. There are nine petals per wedge-shaped sector (one per TEC disk). Reprinted from Fig. 3.30 of ref. [71].

1318 The strips are wire bonded to a front end readout chip called the APV25. The
 1319 APV25 amplifies and shapes the strip signals before sending the full analog pulse
 1320 information to an APVMUX, which multiplexes the output of two APV25s. Then,
 1321 the electrical signal from the APVMUX is sent differentially a few centimeters to an
 1322 optical driver, where it is converted to an optical signal and sent to one of the 450
 1323 front end drivers (FEDs). The FEDs convert the signal back to an electrical pulse
 1324 and digitize it for use in the global event assembly. As for the pixels, analog readout
 1325 is used on detector so that hit reconstruction may benefit from charge sharing.

1326 Clock, trigger, and control signals are sent from the front end controllers (FECs)
 1327 to phase locked loop (PLL) chips on the front ends. The FECs interface to the global
 1328 clock and trigger system. Four or six APV25s, an APVMUX, and a PLL chip all sit on
 1329 a *hybrid*, two which one thin or two thick sensors are also affixed. The sensor-hybrid
 1330 combination and its frame form a module. Figure 5.10 shows a diagram of a module,
 1331 while Figure 5.11 shows a block diagram of the strip readout architecture.

1332 As an example of the strip capabilities, strip hit resolution and signal:noise mea-
 1333 surements are shown in Figure 5.12. The entire pixel + strip tracker has been used

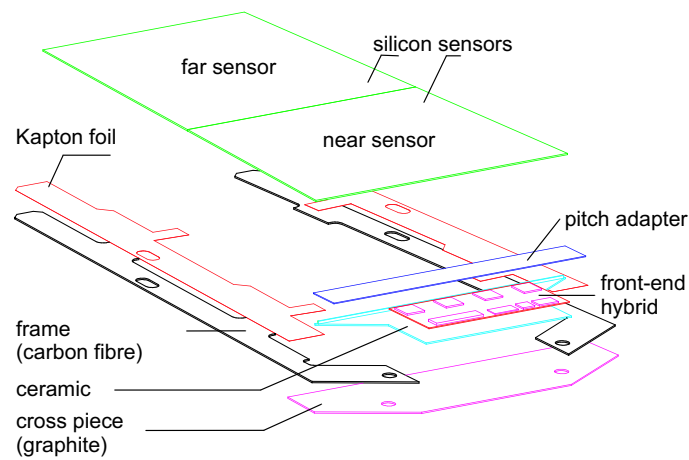


Figure 5.10: Exploded view of a strip module with two sensors. Reprinted from Fig. 3.22 of ref. [71].

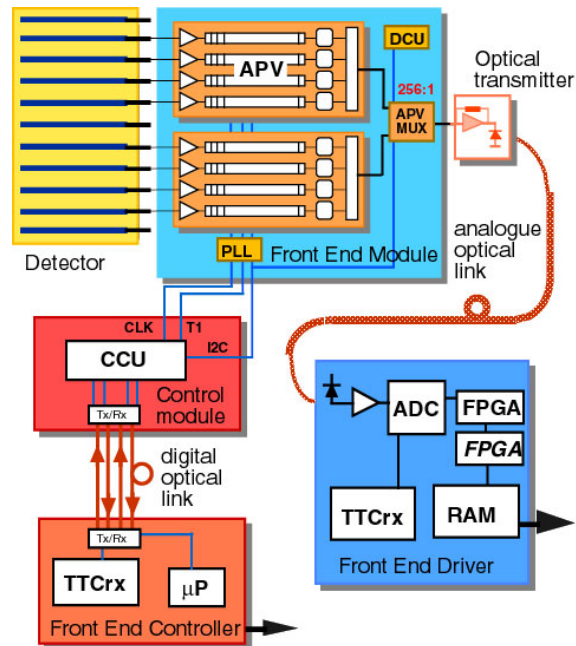


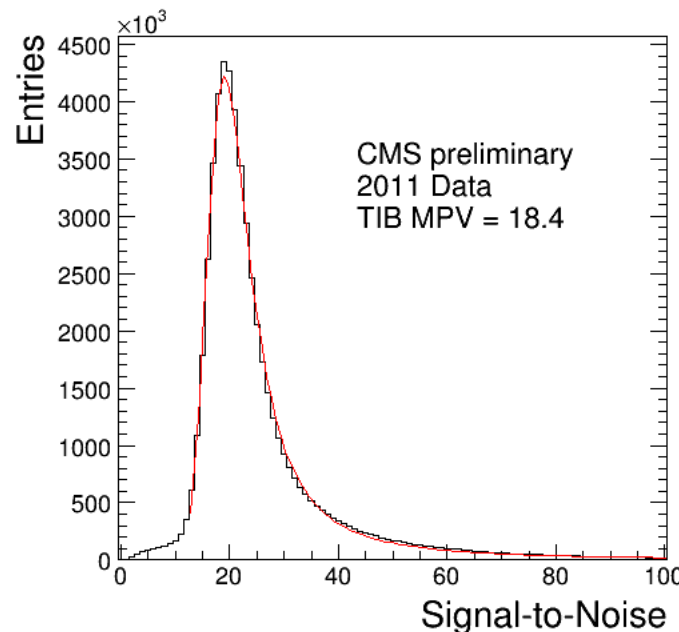
Figure 5.11: Block diagram of the strip readout architecture. Reprinted from Fig. 3.20 of ref. [71].

successfully in the reconstruction of primary and secondary vertices, electrons, muons, tau decays, and charm and bottom hadron decays. In addition, the superior performance of the tracker over the hadronic calorimeter for low energy charged hadrons has been exploited in the the particle flow jet and \cancel{E}_T reconstruction technique (see Sec. 6.1.3). The CMS silicon strips, as well as the pixels, are well aligned and operating at close to design performance.

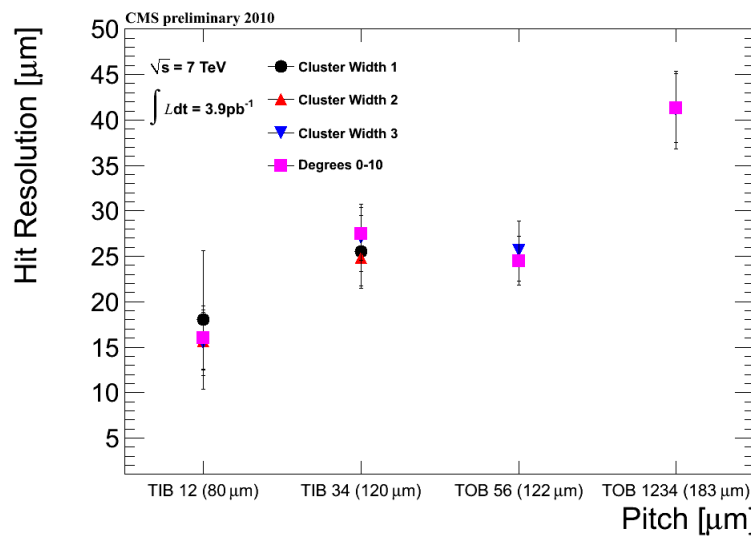
5.1.2 Electromagnetic Calorimeter

The electromagnetic calorimeter (ECAL) is composed of 75,848 lead tungstate (PbWO_4) crystals, divided into one barrel (EB) layer and two endcap (EE) disks. In EB, there are 1700 crystals per *supermodule* (SM), arranged in a 20×85 grid in $\phi \times \eta$. Two SMs are laid out end-to-end to form one row at fixed ϕ , with a total of 18 rows needed to cover the entire 2π extent in ϕ . The SMs may be operated independently. In EE, the independent unit is a wedge-shaped sector, with nine sectors covering each endcap side. The 14,648 EE crystals are divided approximately evenly between the 18 EE sectors. A two-layer preshower detector is placed in front of the EE disks, each layer consisting of a lead absorber followed by 1.9 mm pitch silicon strip detectors (the strips in the first layer are rotated 90° with respect to the second layer). The ECAL layout is shown in Figure 5.13.

The electromagnetic energy resolution can be parametrized as $(\sigma/E)^2 = (S/\sqrt{E})^2 + (N/E)^2 + (C)^2$, where S characterizes the size of photostatistical fluctuations, N characterizes the contribution from electronics noise, and C is a constant accounting for imperfect intercalibration between crystals, non-uniformity of crystal performance, and incomplete shower containment within one crystal. The design goal of the ECAL is to achieve $C = 0.5\%$. Therefore, fast, dense, and relatively radiation hard PbWO_4 was chosen as the crystal material. When a photon or electron strikes the crystal, it initiates an electromagnetic (EM) shower. Due to the density, short radiation length,



(a) TIB signal:noise [78].



(b) TIB and TOB hit resolution as a function of strip pitch [79].

Figure 5.12: Strip detector performance highlights.

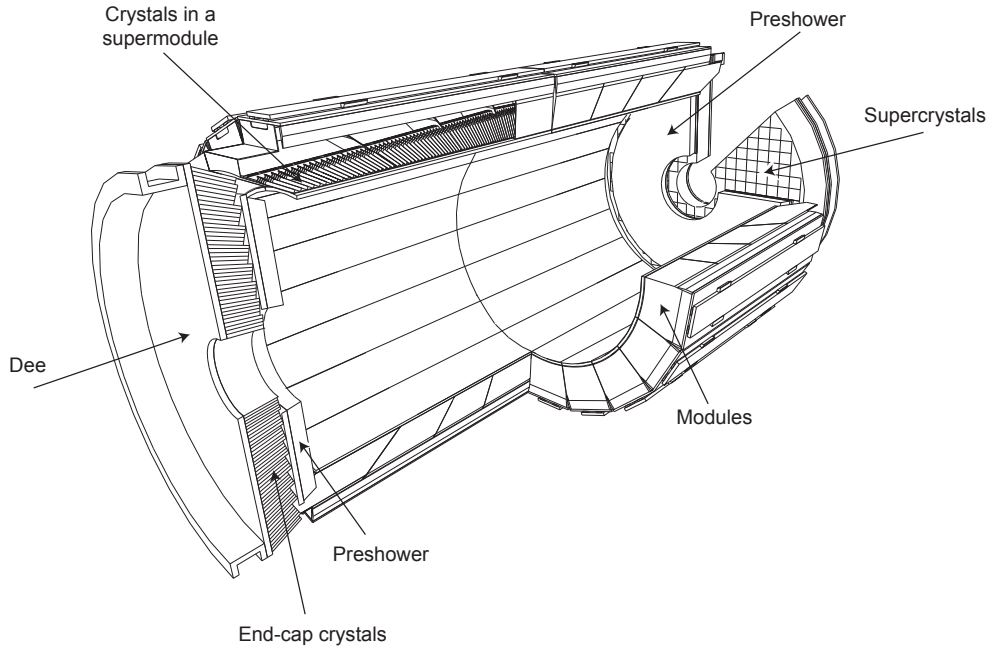


Figure 5.13: Layout of the ECAL detector. Reprinted from Fig. 4.5 of ref. [71].

and small Molière radius of PbWO_4 , nearly the entirety of an EM shower can be contained in a single 23-cm long crystal with front face dimensions $2.2 \text{ cm} \times 2.2 \text{ cm}$. The crystals scintillate in the blue-green part of the spectrum at 440 nm, emitting $\sim 80\%$ of the scintillation light within 25 ns. Light is transmitted along the length of the crystals and collected at the rear with avalanche photodiodes (APDs; semiconductor diodes) in EB or vacuum phototriodes (VPTs; conventional photomultipliers) in EE. Since the light output is low and varies with temperature, the crystals must be kept precisely at 18°C . The EB and EE crystals, which are slightly tapered to match the lateral shower development, are shown in Figure 5.14.

For each trigger, 10 samples, each separated by 25 ns, are read out. The 10-sample pulse is amplified and shaped by a multi-gain preamplifier (MGPA) residing on a very front end (VFE) card serving five crystals. The MGPA can switch between gains 1, 6, and 12 to avoid saturation of the electronics, and affords a dynamic range up to 3 TeV. The samples are digitized on the VFE card, then sent to the front end (FE)

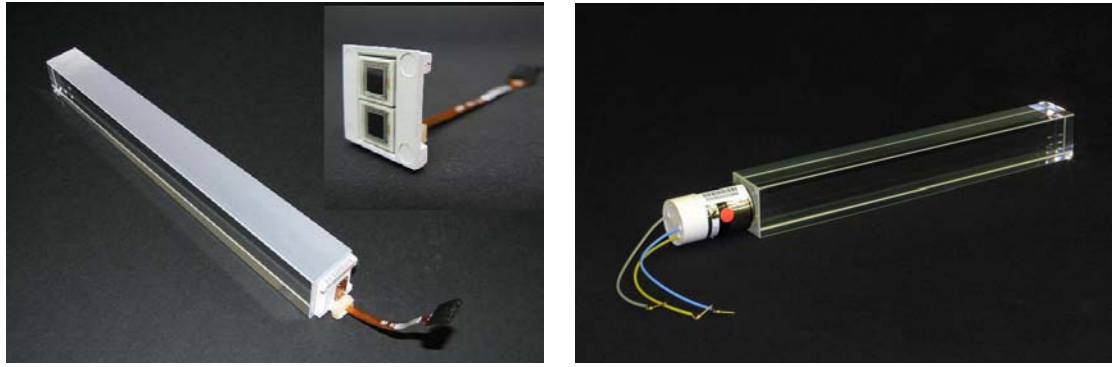


Figure 5.14: Left: EB crystal with attached APD. Right: EE crystal with attached VPT. Reprinted from Fig. 4.2 of ref. [71].

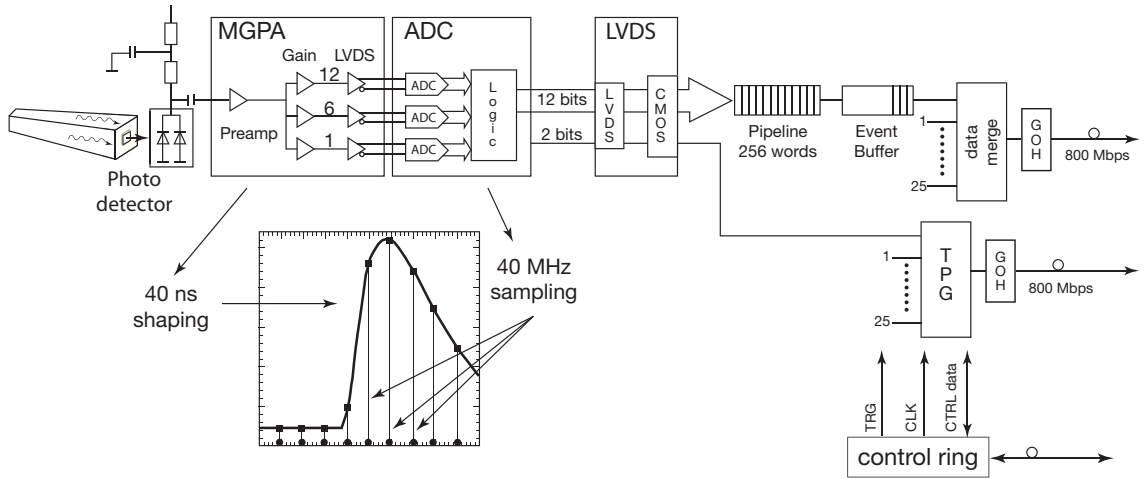


Figure 5.15: Flow chart of the crystal readout, showing the 10-sample pulse shape. Reprinted from Fig. 4.9 of ref. [71].

1374 card serving five VFEs. Digitized samples are buffered in the FE card until receipt
 1375 of a trigger, when they are sent over an optical link to the data concentrator card
 1376 (DCC) that interfaces to the global DAQ. The DCC interfaces to the *selective readout*
 1377 processor, which decides whether a crystal should be read out with or without zero
 1378 suppression based on its proximity to a high-energy hit. The clock is transmitted to
 1379 the FE cards from the Clock and Control System (CCS) boards. A flow chart of the
 1380 crystal readout is given in Figure 5.15.

1381 At each bunch crossing, the trigger concentrator cards (TCC) of the ECAL com-

1382 pute *trigger primitives* from 5×5 non-overlapping transverse energy sums (in the
 1383 endcaps the geometry is not always 5×5). This information, along with a special
 1384 bit in EB only characterizing the transverse shower profile that is used for rejection
 1385 of anomalous APD hits (see Sec. 6.1.1), is transmitted from the TCCs to the syn-
 1386 chronization and link boards (SLBs), and then on to the global trigger system. The
 1387 trigger decision is communicated to the DCCs, which request the buffered data from
 1388 the front ends if the decision is affirmative.

1389 Despite the radiation hardness of lead tungstate relative to other types of crystals,
 1390 it still suffers from transparency loss due to radiation-induced lattice damage, as
 1391 shown in Figure 5.16. In addition, any unforeseen change in the gains of the MGPAs
 1392 and VPTs, or in the pedestal levels, will degrade the energy resolution. For this
 1393 reason, a continuously running calibration system is installed with the ECAL. The
 1394 system makes use of the LHC abort gaps to read out the pedestal levels, test pulses
 1395 fired into the MGPAs, and laser (EB and EE) or LED (EE only) pulses fired into the
 1396 crystals at regular intervals. Laser and LED events are used to compute corrections
 1397 to the crystal gains for transparency loss, while the other types of calibration events
 1398 serve to monitor changes in the electronics performance due to magnetic field or high
 1399 voltage cycling. The mean time between transparency measurements is ~ 40 minutes.
 1400 Figure 5.17 shows the architecture of the laser monitoring system. The additional EE
 1401 light monitoring system consisting of LEDs serves to (a) stabilize the response of the
 1402 VPTs and (b) corroborate the laser calibration measurements. I describe it here in
 1403 some detail because it is my principal contribution to the CMS detector.

1404 VPT gains are known to be sensitive to the frequency and amplitude of incident
 1405 light [81]. In general, as the pulsing frequency increases the gain decreases and vice
 1406 versa, but some VPTs may exhibit a different dependence on rate changes. The gain
 1407 changes are most abrupt when a source of pulsed light (i.e. the LHC) is suddenly
 1408 turned on or off. Deviations of a few percent to over ten percent have been observed

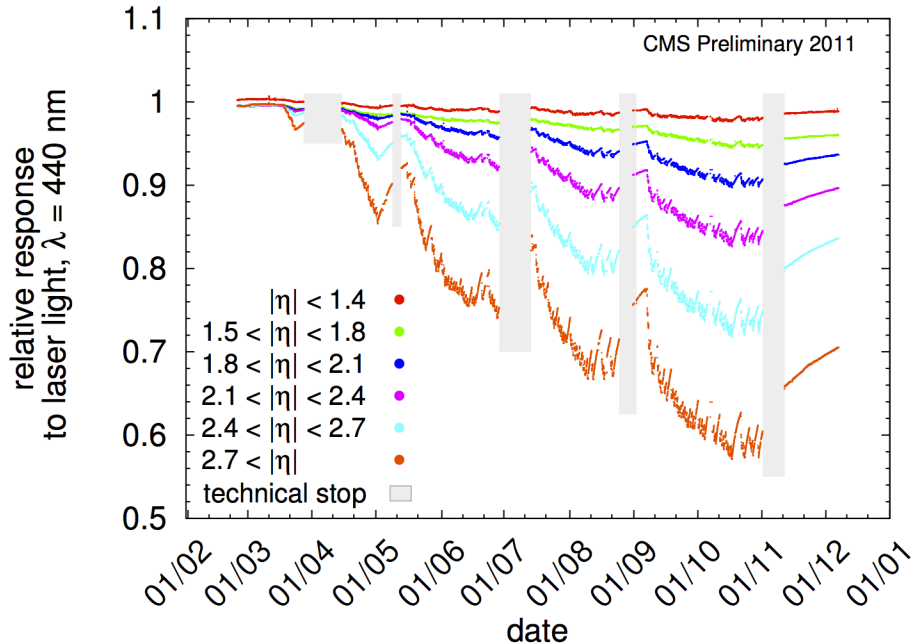


Figure 5.16: Relative response of the crystals to blue laser pulses from February 1, 2011 to January 1, 2012 [80]. Technical stops, during which the LHC is turned off for maintenance and development, are shown in gray. These periods of inactivity correspond to growth in the crystal response, as radiation damage recovery occurs.

in the lab (see Figure 5.18). The EE LED system mitigates the effects of LHC beam injections and dumps on the stability of the VPTs by continuously providing light pulses to the VPTs, irrespective of the state of the beam. VPTs are thus kept active by the LED light at all times, dampening the gain change at LHC on/off transitions. Note that although the VPT effect is strongly suppressed in the 3.8 T magnetic field of CMS, the LED system is still required in light of the stringent requirements on ECAL stability imposed by the $C = 0.5\%$ resolution goal. At present, there is no indication of a significant VPT effect discernible on top of the radiation damage, but in the future improved calibration precision will demand control over small effects like VPT gain fluctuations.

In addition to their stabilizing effect, the LED pulses are also read out as part of the ECAL calibration cycle and used to correct for crystal transparency loss and VPT gain loss due to aging. Figure 5.19 shows the decrease in response of a VPT in

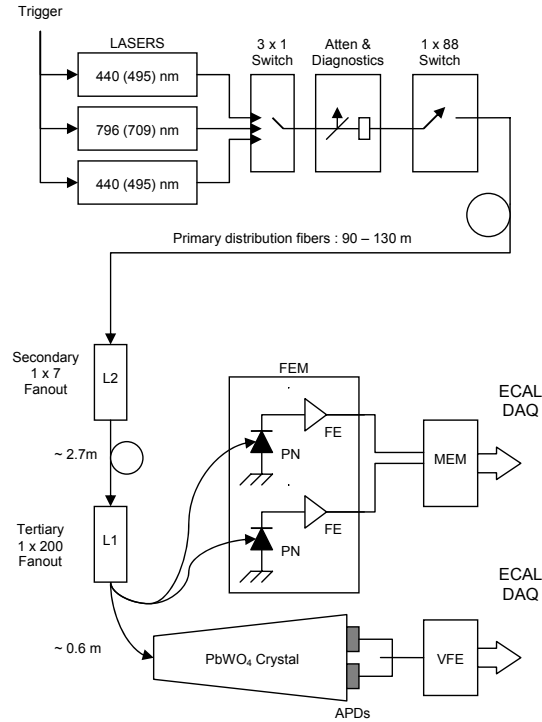


Figure 5.17: Architecture of the laser monitoring system. Reprinted from Fig. 4.16 of ref. [71].

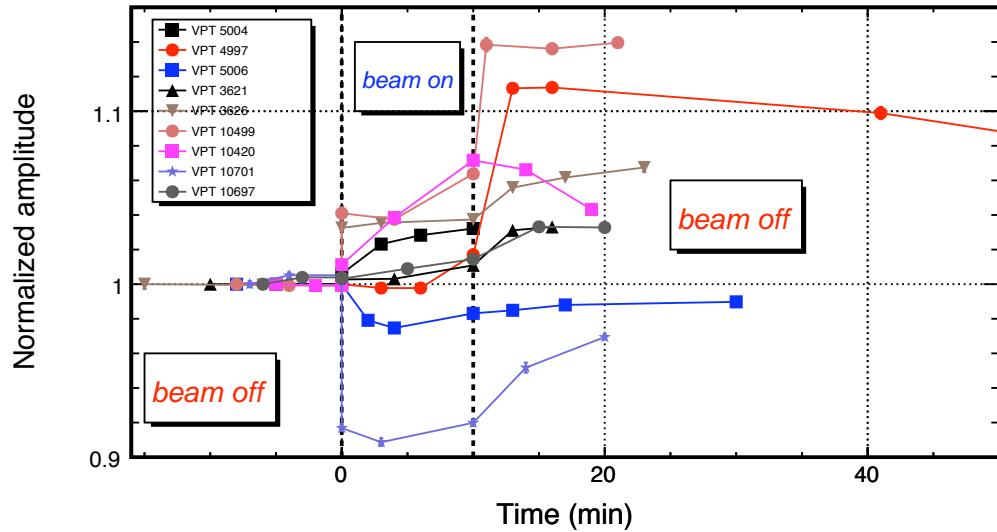


Figure 5.18: Change in response of nine different VPTs in zero magnetic field vs. time. The response of each VPT is normalized to its response for the earliest data point taken. For times less than 0, no light pulsing is applied to the VPTs. For times between 0 and 20 minutes, pulsed LED light was applied to the VPTs. For times later than 20 minutes, the pulsing source was again removed.

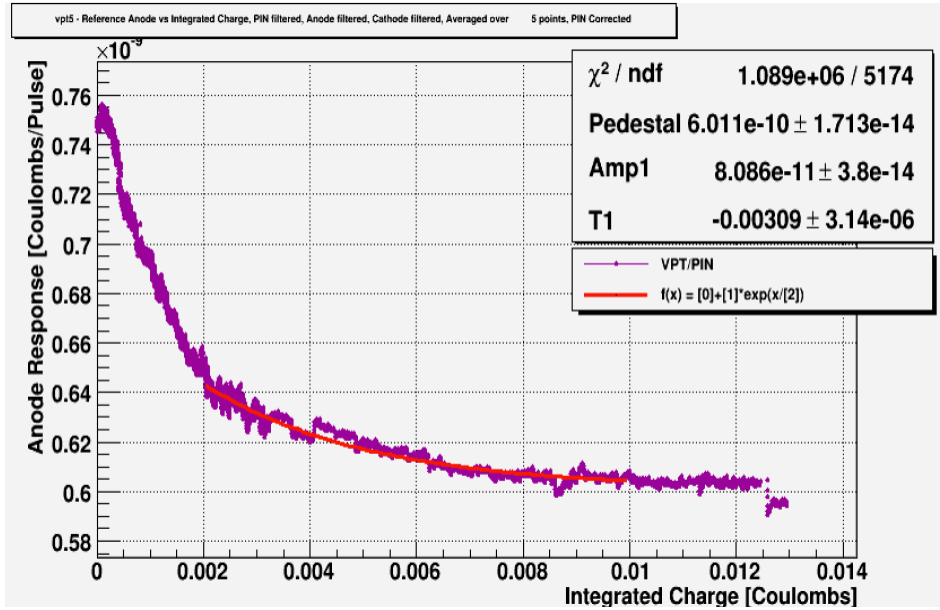


Figure 5.19: VPT response in a 3.8 T laboratory magnetic field to blue LED light vs. integrated charge at photocathode [82]. The response is corrected for changes in the LED light output by PIN diode normalization. For integrated charge less than ~ 0.003 C, the average current draw at the photocathode is ~ 1 nA, delivered by blue LED triggered at 2 kHz. For integrated charge greater than ~ 0.003 C, the average current draw is ~ 10 nA from a 20 kHz trigger rate.

1422 the lab at 3.8 T as a function of integrated charge at the VPT photocathode. The
 1423 loss of response due to photocathode aging differs from VPT to VPT, but a typical
 1424 value is $\sim X\%$ per Y C of integrated charge. The intrinsic time stability of LEDs
 1425 (sub-percent) over the laser (few percent) used for ECAL calibration makes the LED
 1426 information very useful despite the smaller light intensity delivered. LED data are
 1427 used to correct for transparency loss and VPT aging whenever laser data are missing
 1428 due to technical problems.

1429 The LED system utilizes two wavelengths. Blue LEDs, at 450 nm wavelength,
 1430 are near the peak of the crystal scintillation and VPT photocathode efficiency, and
 1431 therefore are ideal for transmitting the maximum amount of light to VPTs for stability
 1432 pulsing. Orange LED light, at 617 nm wavelength, is transparent to the crystals but
 1433 still somewhat efficient for the VPT photocathode, allowing loss of response from
 1434 crystal damage to be disentangled from VPT gain changes. In addition, the orange

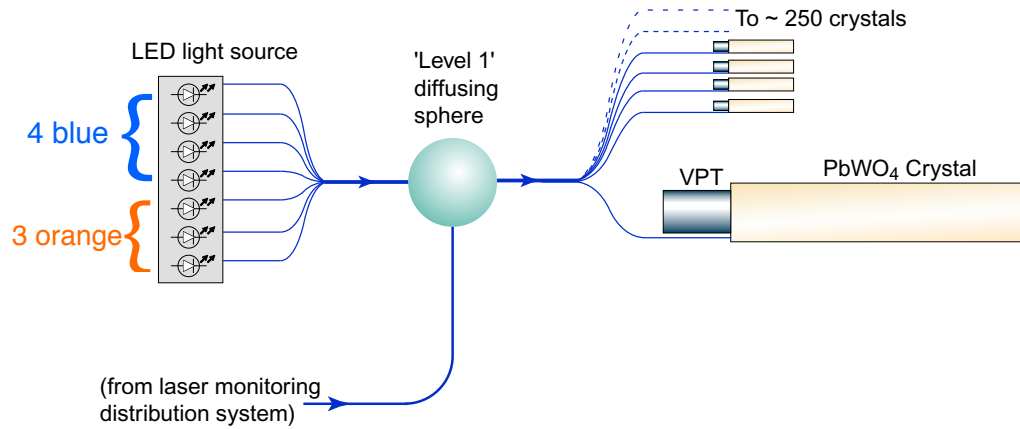


Figure 5.20: Diagram of the LED inputs to a diffusing sphere and the fanout to the crystals. Adapted from Fig. 4.8 of ref. [71].

wavelength serves as a second calibration wavelength in EE, where there is only a
 blue laser. Each endcap disk holds 38 LED circuits, with each circuit driving four
 blue and three orange LEDs. Each of the seven LEDs of a circuit is coupled to the
 same diffusing sphere by an optical fiber whose cleaved end is stuck inside a hole
 drilled into the LED surface. The light entering the diffusing sphere is fanned out
 to ~ 200 crystals + two PN diodes for tracking of the stability of the LED itself. A
 diagram of the inputs and outputs of a single diffusing sphere is shown in Figure 5.20.
 38 diffusing spheres cover a single endcap disk.

The LED driver circuits are grouped into boxes that serve six, four, or three
 diffusing spheres each, for a total of four boxes per half-endcap “dee” (eight per
 disk). Each box is powered from supplies residing in the underground control room
 at Point 5. One power supply channel feeds four LED boxes. The four boxes per
 dee receive a common clock signal and LED pulse trigger from a control box in the

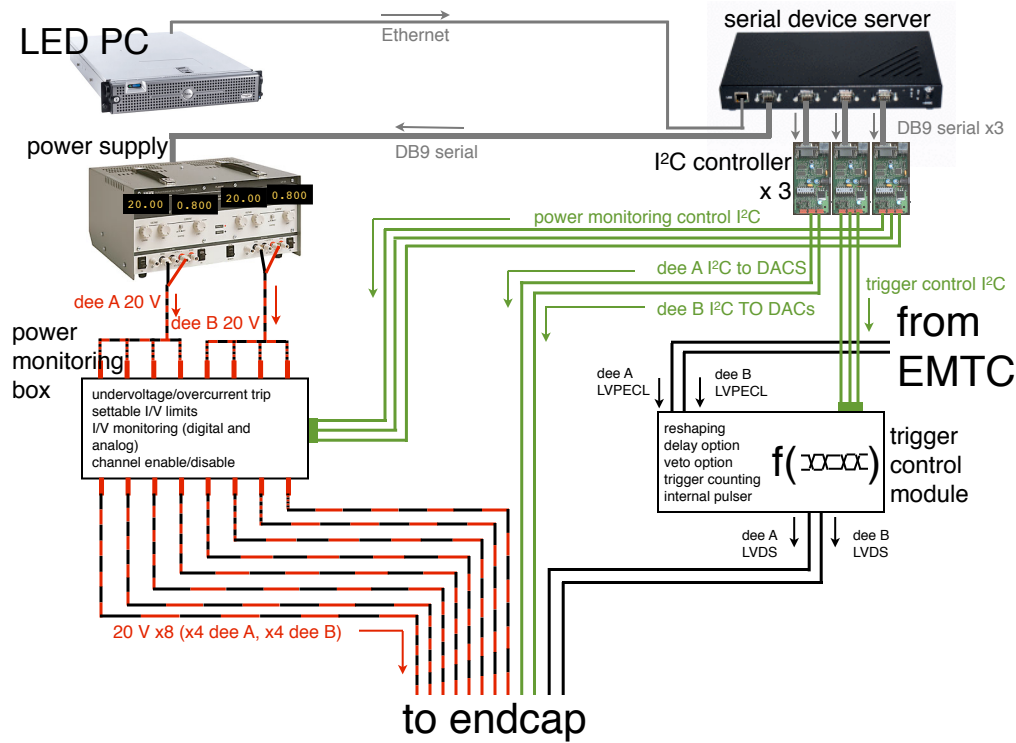


Figure 5.21: Hardware setup of the LED system.

1448 underground control room. The amplitude of a group of four blue or three orange
 1449 LEDs is controlled by a single digital-to-analog converter (DAC) chip. For the blue
 1450 LED groups, the amplitude ranges from zero to ~ 50 GeV equivalent. Due to the
 1451 lower photocathode efficiency for orange light, the amplitude of orange groups ranges
 1452 from zero to ~ 5 GeV equivalent. Power distribution, LED amplitudes, and pulse
 1453 widths and delays are set by a computer program that interfaces to the hardware via
 1454 an Ethernet-to-serial converter. The hardware setup of the LED system is shown in
 1455 Figure 5.21.

1456 The LED system has two modes: calibration, in which both blue and orange LED
 1457 pulses are read out and processed for calibration purposes; and stability, in which
 1458 blue LED pulses are fired continuously but not read out. During a calibration cycle,
 1459 the LED system is in stability mode except during the calibration mode readout
 1460 periods. For a given EE wedge, these calibration periods occur approximately every

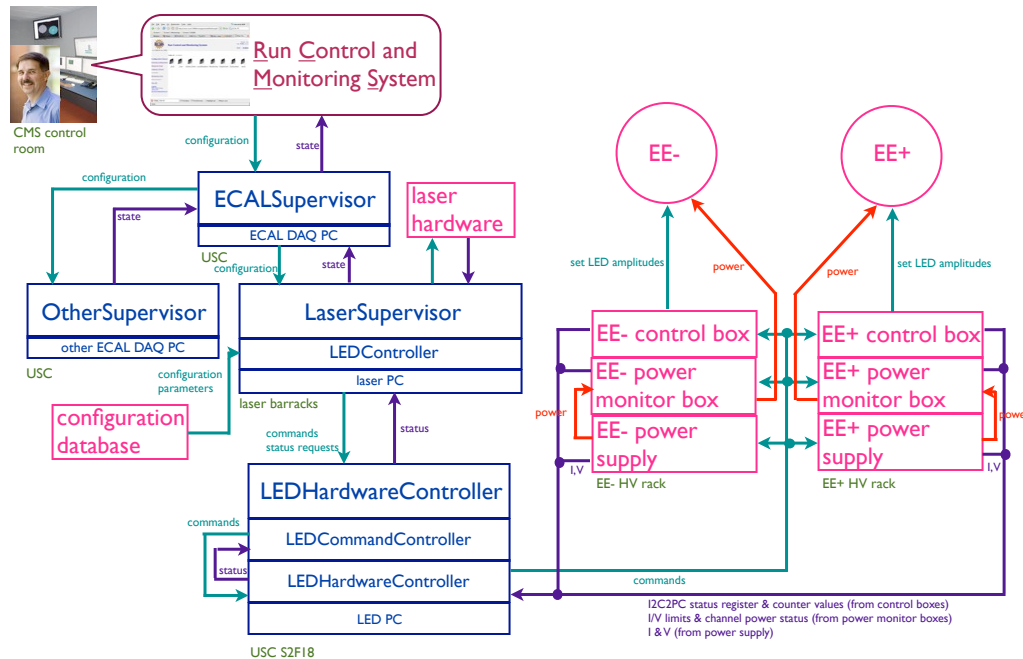


Figure 5.22: Software control flow of the LED system.

1461 40 minutes and last \sim 6 seconds. Orange or blue LED triggers are read out during the
 1462 calibration periods. Once they end, the EE wedge returns to stability mode. Critically,
 1463 stability pulsing occurs both inside and outside of a CMS data taking run, insuring
 1464 the stability of the VPTs. The calibration and stability pulsing rates, as well as the
 1465 overall health of the LED hardware, is monitored every ten minutes.

1466 Transitions between calibration and stability modes are executed by selectively
 1467 zeroing the amplitudes of certain LED groups and maximizing the amplitudes of
 1468 others. The computer program that controls the DACs of the LED system is itself
 1469 controlled by a server running on a dedicated PC at Point 5. This server listens to
 1470 commands from a program that coordinates the calibration cycles and consequently
 1471 dictates the state of the LEDs (on or off) at any given time. Status information is sent
 1472 back to the master program from the LED server. The master program is an XDAQ
 1473 executive (see Sec. 5.2.2) that itself interfaces to the top level CMS run control. A
 1474 diagram of the software control flow is given in Figure 5.22.

1475 The current ECAL energy resolution is somewhat worse than the design goal of

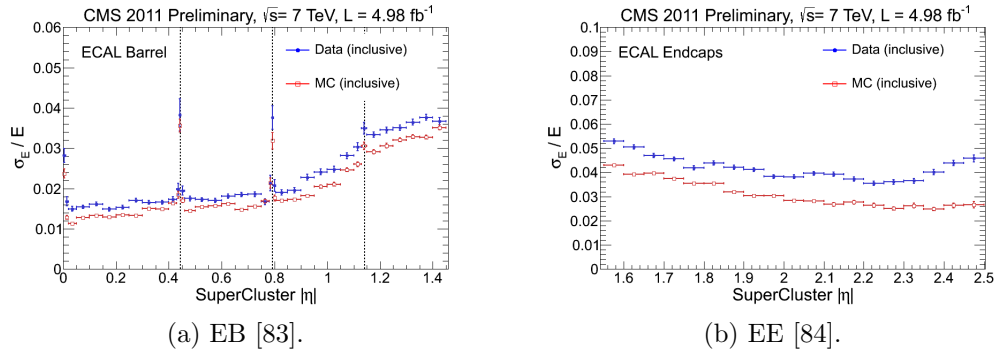


Figure 5.23: Energy resolution vs. $|\eta|$ for Z decay electrons for data (filled blue circles) and MC (empty red squares). The dotted lines show the locations of module gaps (three per SM).

1476 0.5%. An incomplete understanding of (a) the transparency loss and (b) the photon
 1477 conversion and electron bremsstrahlung processes in the $\sim 1X_0$ of tracker material in
 1478 front of the ECAL are the main limiting factors in improving the resolution. However,
 1479 as more data accumulate, more refined models of transparency loss and EM interac-
 1480 tions in the tracker can be built, leading to better resolution. Energy resolution vs.
 1481 $|\eta|$ can be seen in Figure 5.23.

1482 The 10-sample readout coupled with the fast scintillation time of lead tungstate
 1483 allows for a very precise reconstruction of the time of ECAL hits. ECAL timing is used
 1484 for searches for long-lived particles that decay to photons or jets, such as long-lived
 1485 neutralinos in GMSB [85]. Figure 5.24 shows the timing resolution in EE.

1486 5.1.3 Hadronic Calorimeter

1487 The CMS hadronic calorimeter (HCAL) has four parts: HCAL barrel (HB), HCAL
 1488 endcap (HE), and HCAL outer (HO), which all utilize the same brass absorber /
 1489 plastic scintillator sandwich technology; and HCAL forward (HF), which is a Čerenkov
 1490 detector made of quartz fibers. A quarter longitudinal cross-sectional view of HCAL
 1491 is shown in Figure 5.25. Like EB, HB is formed of 36 ϕ -wedges (18 cover 2π in positive
 1492 η , 18 cover 2π in negative η). Each wedge is divided into 16 along η and four along

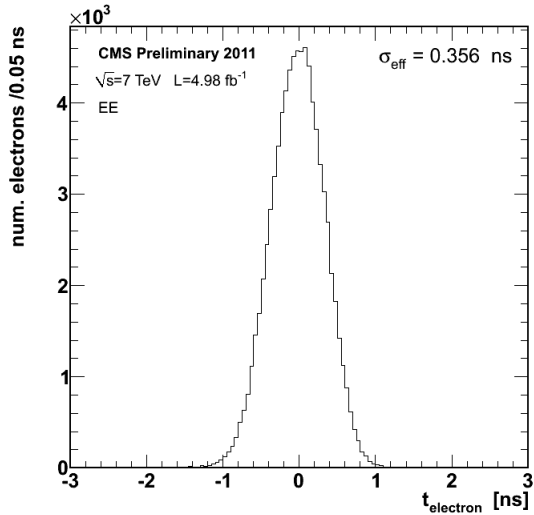


Figure 5.24: Distribution of reconstructed times of Z decay electrons in EE [86].

1493 ϕ , for a total of 64 readout towers per wedge (compare 1700 individually read out
 1494 crystals per EB wedge). HE is divided into 36 ϕ -wedges containing 38 readout towers
 1495 each. HO consists of five rings around HB and HE distributed symmetrically along z .
 1496 There are 72 ϕ -slices per ring, with each ϕ -slice further divided into 5, 6, or 8 along
 1497 z depending on ring. The HF fibers are distributed within the steel absorber. HF is
 1498 divided into 18 ϕ -wedges per endcap side, each containing 24 readout towers. All HB
 1499 towers have a single readout channel except for the two in each wedge at highest $|\eta|$,
 1500 which are segmented into two longitudinal layers for readout. In HE, all towers have
 1501 two longitudinal readout layers, except for the three rings of towers closest to the
 1502 beam line, which have three. There are also two longitudinal depths of HF fibers.

1503 HB, HE, and HO are all sampling calorimeters consisting of alternating layers of
 1504 brass absorber and plastic scintillator. The absorber initiates the hadronic shower,
 1505 and as shower particles travel through the scintillator the scintillation light is read
 1506 out by wavelength-shifting (WLS) fibers connected to the scintillator tiles.² The full
 1507 development of the shower is sampled by the layers of instrumented scintillator. The

²By contrast, in the ECAL, the crystal material acts as both absorber and scintillator, greatly reducing the contribution to energy resolution from sampling fluctuations.

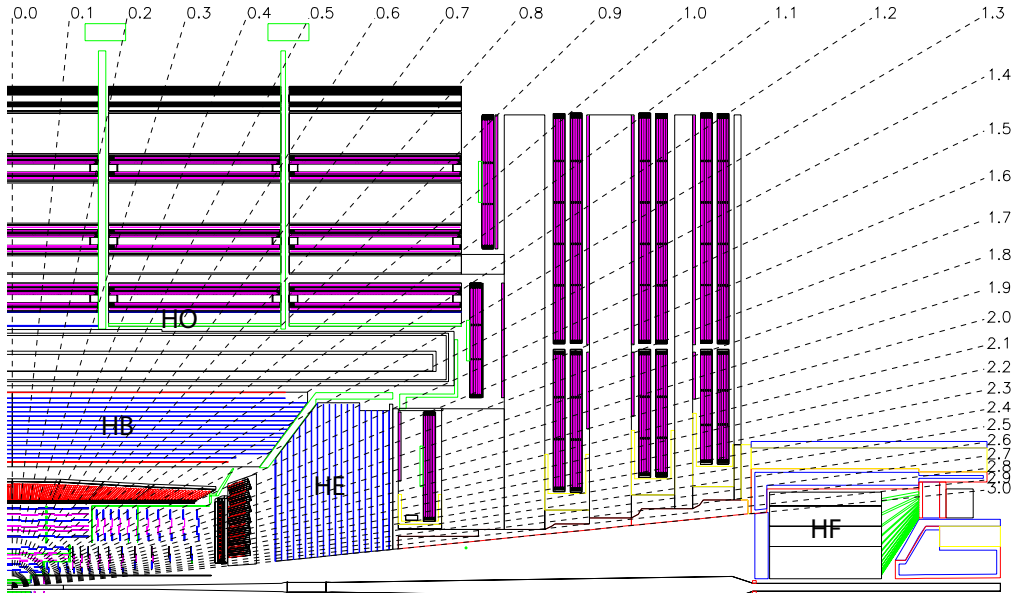


Figure 5.25: Quarter longitudinal cross-sectional view of HCAL (and muon stations in purple). Reprinted from Fig. 5.1 of ref. [71].

1508 scintillator tiles are staggered so that there are no cracks in coverage along the direc-
 1509 tion projected back to the beam spot. Light output from all tiles in a single readout
 1510 tower is collected via the WLS fibers and merged into a single signal that is amplified
 1511 by a hybrid photodiode (HPD). A diagram of the optical readout of HB (similar for
 1512 HE and HO) is shown in Figure 5.26.

1513 Due to the extremely harsh radiation environment near the beam line, HF is con-
 1514 structed of a 1.2-m thick, 1.7-m long ring of steel absorber with radiation hard quartz
 1515 fibers distributed within the steel and running parallel to the beam line. Hadronic
 1516 showers develop in the steel and are sampled in the quartz fibers when charged shower
 1517 particles hit the the fibers and emit Čerenkov light. The light is transmitted by to-
 1518 tal internal reflection down the fibers to a photomultiplier tube (PMT), where the
 1519 signals from all fibers in an HF tower are merged into one. Since only relativistic
 1520 particles emit Čerenkov light in these fibers, it is mostly the EM component of the
 1521 hadronic shower, consisting of neutral pions decaying to photons that interact electro-
 1522 magnetically with the absorber, that is sampled [87]. The charged hadrons produced

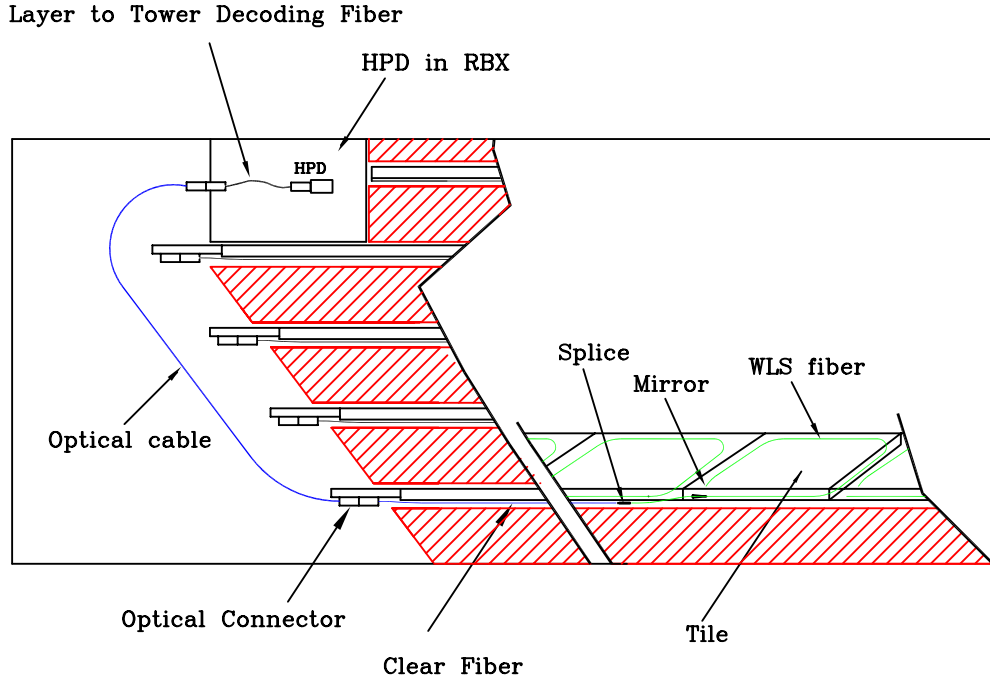


Figure 5.26: Diagram of the optical readout of HB. Reprinted from Fig. 5.7 of ref. [71].

in hadronic showers are typically too slow to generate Čerenkov light. Figure 5.27
shows a cross-sectional view of one side of HF.

Electrical signals from either HPDs (HB/HE/HO) or PMTs (HF) are digitized on
the front ends by means of a fast charge-integrating ADC. The digitized signals are
sent off-detector to the HCAL Trigger/Read-Out (HTR) boards, where they await a
trigger decision. If the trigger is accepted, the signals are sent on to the HCAL data
concentrator cards (DCCs), which interface to the global DAQ system. HCAL trigger
primitives, consisting of transverse energy sums over an entire tower, are calculated
in the HTR boards and sent to the global trigger system.

Selected HCAL performance results can be seen in Figure 5.28.

5.1.4 Muon System

Beginning at a radius of ~ 10 interaction lengths from the beam line, where all particles except muons should have been stopped by the HCAL, are the muon chambers,

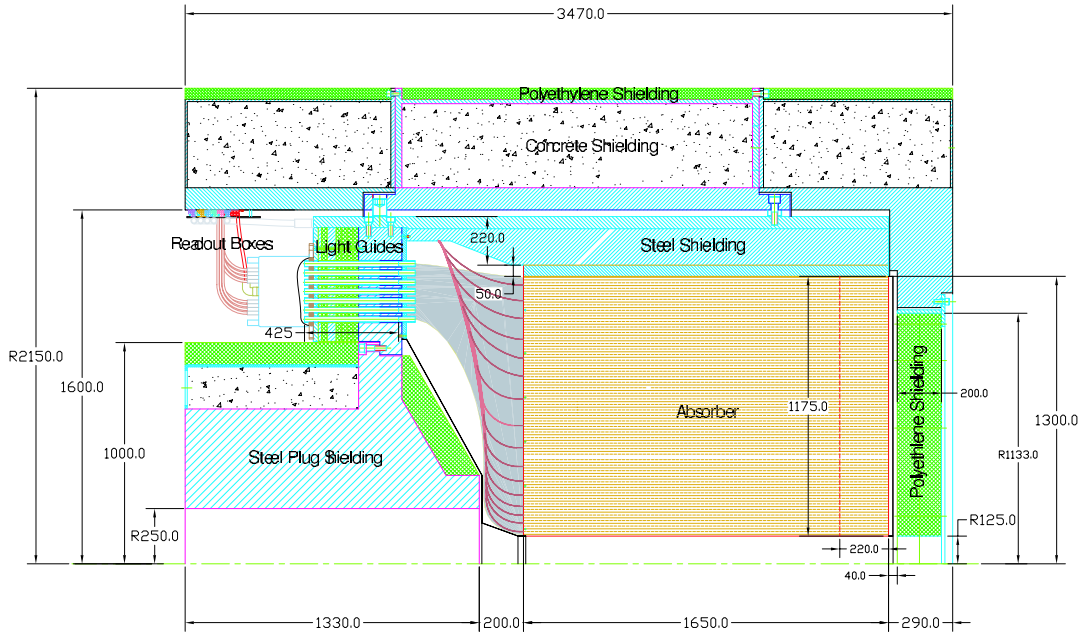
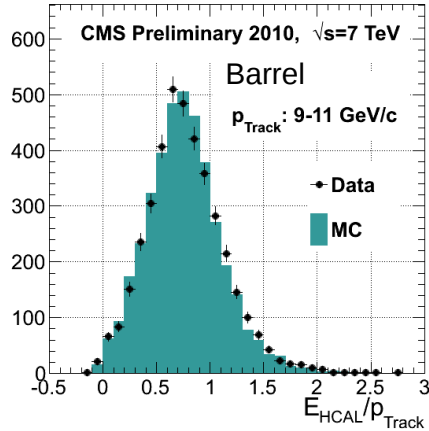


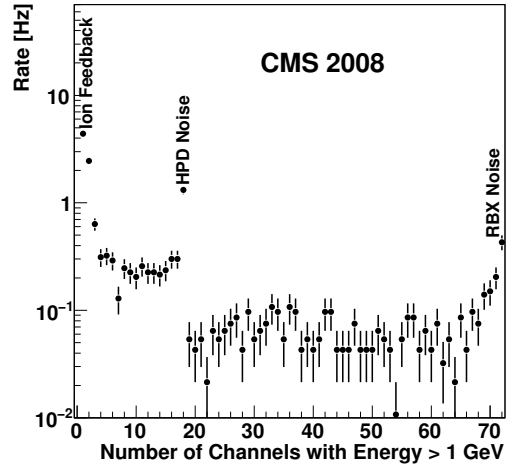
Figure 5.27: Cross-sectional view of one side of HF. The z -axis is horizontal. Reprinted from Fig. 5.28 of ref. [71].

1536 interspersed with the iron return yoke of the CMS magnetic field. Three technologies
 1537 are employed: drift tubes in the barrel section (MB), cathode strip chambers (CSCs)
 1538 in the endcap section (ME), and resistive plate chambers (RPCs) in both sections to
 1539 provide an independent trigger with superior time resolution. There are four barrel
 1540 layers of stations extending out to $|\eta| = 1.2$. Each endcap consists of five disks of
 1541 stations as shown in Figure 5.29(b), covering $1.4 < |\eta| < 2.4$. RPCs populate the
 1542 barrel and endcap muon systems alongside the DT chambers and CSCs. Since they
 1543 have time resolution much better than a few ns, they are used to assign the bunch
 1544 crossing of muon tracks and provide a p_T trigger with sharp turn-on.

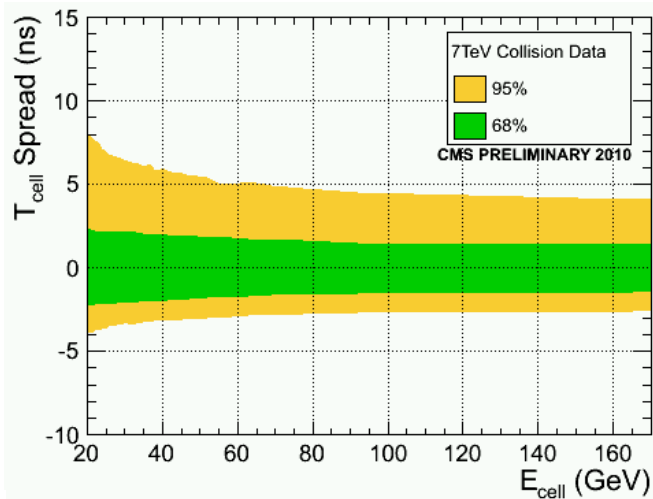
1545 Each DT chamber consists of two $r \cdot \phi$ superlayers (SLs) and optionally one z
 1546 SL (in all chambers except those in the fourth layer). The SLs contain four rows of
 1547 drift tubes, with the rows staggered such that there are no gaps in the coverage. The
 1548 $r \cdot \phi$ SLs have the tube axis parallel to the beam line, while the z SL is perpendicular
 1549 to the beam line. The tubes are ~ 2.4 m in length and $13 \text{ mm} \times 42 \text{ mm}$ in cross



(a) Data/MC comparison of HB response to charged tracks of 9-11 GeV/c momentum [88].

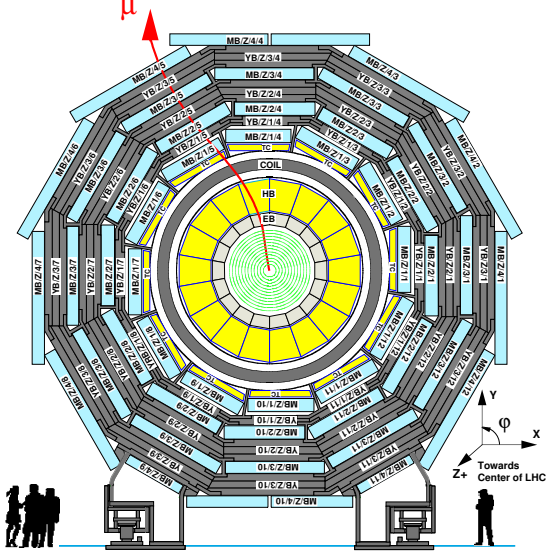


(b) Distribution of tower multiplicity, clearly showing three peaks in rate corresponding to noise sources (see Sec. 6.3) [89].

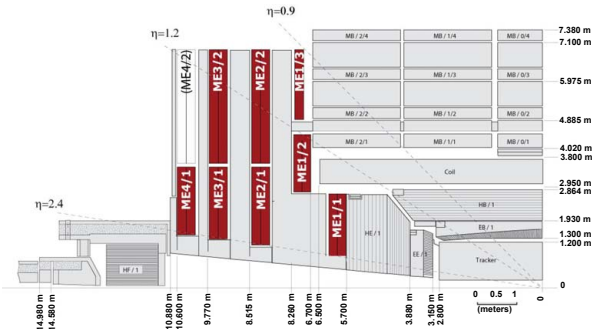


(c) Timing resolution vs. tower energy [88].

Figure 5.28: Selected HCAL performance results.



(a) One of the five wheels of MB, showing the four layers of muon stations. The five wheels are spaced symmetrically in z about $z = 0$. As a muon traverses the muon detectors, its curvature in the transverse plane changes direction and magnitude due to the magnetic field in the return yoke, which is of opposite sign and reduced strength relative to the field within the solenoid volume. Reprinted from Fig. 7.3 of ref. [71].



(b) Quarter longitudinal cross section of CMS highlighting the location of the ME disks. Reprinted from Fig. 7.47 of ref. [71].

Figure 5.29: View of the MB and ME layout in CMS.

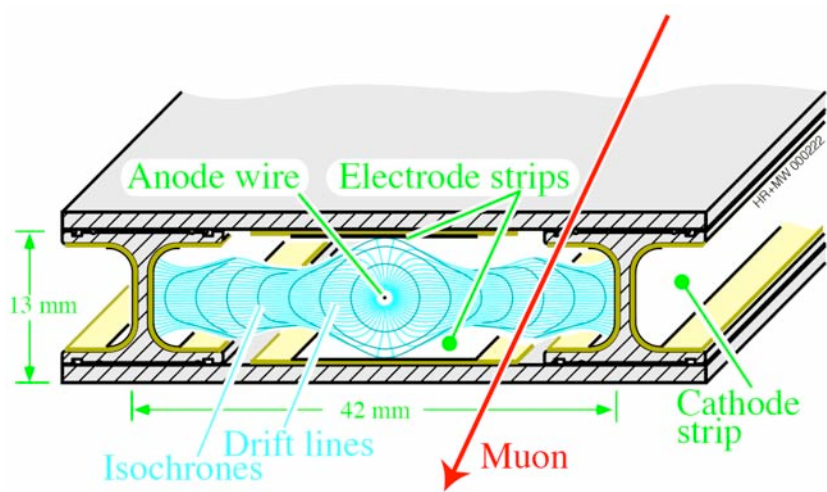


Figure 5.30: Electric field lines within a drift tube as well as the contours of equal drift time. Reprinted from Fig. 7.5 of ref. [71].

1550 section. Each chamber therefore records eight $r \cdot \phi$ tracking points and optionally four
 1551 z tracking points. The tubes are filled with an 85%Ar + 15% CO₂ gas mixture. An
 1552 anode wire at 3600 V runs the length of the tube, while the walls are covered with
 1553 electrodes held at 1800 V or -1200 V depending on wall. When a muon passes through
 1554 the tube, it ionizes the gas atoms. The liberated electrons drift along the electric field
 1555 lines created by the electrodes to the anode, which is read out. Figure 5.30 shows
 1556 the electric field lines within a drift tube as well as the contours of equal drift time.
 1557 The maximum drift time is 380 ns.

1558 CSCs consist of alternating layers of cathode strips (four planes oriented along r)
 1559 and anode wires (three planes oriented along ϕ). A 40%Ar + 50%CO₂ + 10%CF₄ gas
 1560 mixture fills the space between two successive planes, forming six gas gaps. When a
 1561 muon ionizes the gas atoms, the positive ions drift toward the anode and are read
 1562 out to provide a measurement of r , just as in the DTs. However, an image charge is
 1563 induced on the cathode strips, which is also read out to provide a measurement of ϕ .
 1564 The wires are spaced 3.2 mm apart. The cathode strips have pitch varying from 8.4
 1565 mm at the end closest to the beam line to 16 mm at the other end, and are spaced

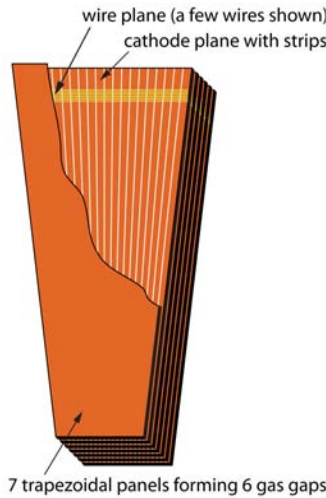


Figure 5.31: CSC wedge, showing the cathode and wire planes. Reprinted from Fig. 7.49 of ref. [71].

1566 0.5 mm apart. A trapezoidal CSC is shown in Figure 5.31.

1567 Track stubs from the muon system are combined with tracks from the tracking
1568 system to form more precise muon tracks than either system could form alone, as
1569 shown in Figure 5.32. This leads to extremely good di-muon invariant mass resolution
1570 (Figure 5.33) over a large p_T range.

1571 5.2 Triggering, Data Acquisition, and Data Trans- 1572 fer

1573 5.2.1 Level 1 and High Level Trigger Systems

1574 The Level-1 (L1) trigger system, which encompasses dedicated hardware processors
1575 to construct trigger objects (typically high p_T jets, electrons, photons, taus, and
1576 muons) out of the calorimeter and muon hits, distributes a L1 accept or reject to all
1577 subdetectors at the LHC bunch crossing frequency of 40 MHz. Further data filtering
1578 is performed by the High Level Trigger (HLT) system, a farm of ~ 1000 commercially

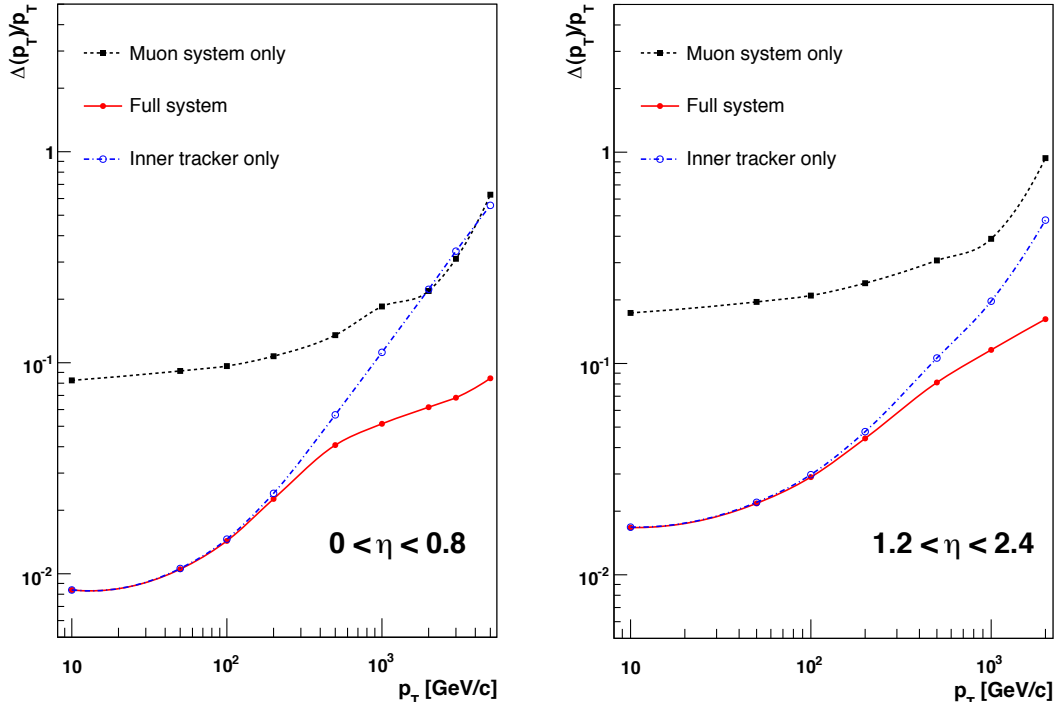


Figure 5.32: Muon p_T resolution as a function of muon p_T for tracker information only (blue), muon information only (black), and both tracker and muon information combined (red). Reprinted from Fig. 1.2 of ref. [71].

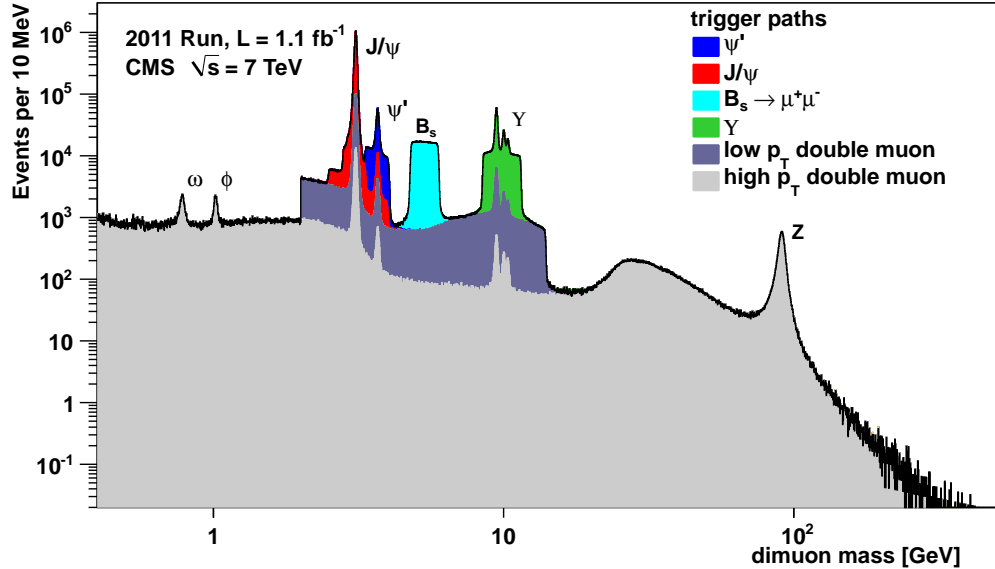


Figure 5.33: Di-muon invariant mass spectrum broken down by trigger path [90]. The light(dark) gray regions show the contribution from high- p_T (low- p_T) di-muon triggers. Note that no $B_s \rightarrow \mu^+\mu^-$ decays have been observed [91]; the light blue region just shows the amount of triggers dedicated to the $B_s \rightarrow \mu^+\mu^-$ search.

1579 available processors running a slimmed down version of the CMS event reconstruction
 1580 software CMSSW. The data rate received by the HLT is ~ 100 kHz; the output rate of
 1581 events permanently written to disk is ~ 100 Hz. An L1 trigger *latency* (time between
 1582 the collision and the distribution of the L1 decision to the subdetectors) of $3.2\ \mu\text{s}$ is
 1583 achieved via the use of fast electronics and sufficiently deep buffers to pipeline trigger
 1584 primitives waiting to be analyzed. This latency corresponds to the length of the LHC
 1585 abort gap, so in principle CMS may be operated with zero *dead time* (during which
 1586 LHC bunches are missed because the L1 system is blocked while processing other
 1587 triggers).

1588 At the bottom, the L1 trigger consists of trigger primitive generators (TPGs) in
 1589 the calorimeter and muon systems that send E_T sums or muon track stubs to the
 1590 regional calorimeter trigger (RCT) or muon track finders, respectively. The EB TPG
 1591 also sends a *fine grain veto bit* [92], which encodes information about the EM shower
 1592 pattern in the 5×5 array of crystals, and is used to reject anomalous signals (see
 1593 Sec. 6.1.1). The RCT, DT track finder (DTTF), and CSC track finder (CSCTF) sort
 1594 and rank the regional trigger primitives based on p_T and quality. The ranked RCT
 1595 candidates and muon track stubs are sent to the global calorimeter trigger (GMT)
 1596 and global muon trigger (GMT), respectively, where high-level objects like isolated
 1597 and non-isolated muons and EM candidates, jets, taus, and \cancel{E}_T are constructed from
 1598 all the regional inputs and ranked. Calorimeter isolation sums for muons are also
 1599 sent from the RCT to the GMT. The highest ranked global objects are sent to the
 1600 global trigger (GT), which sits at the top of the L1 trigger. The GT issues the final
 1601 L1 accept or reject to all subdetectors based on a comparison of the GMT and GCT
 1602 candidates with the requirements of its programmed trigger menu. A block diagram
 1603 of the L1 trigger is shown in Figure 5.34.

1604 A region in the RCT consists of a matrix of 4×4 trigger towers. A trigger tower
 1605 in EB/HB is one HCAL tower + the 5×5 matrix of ECAL crystals in front of it;

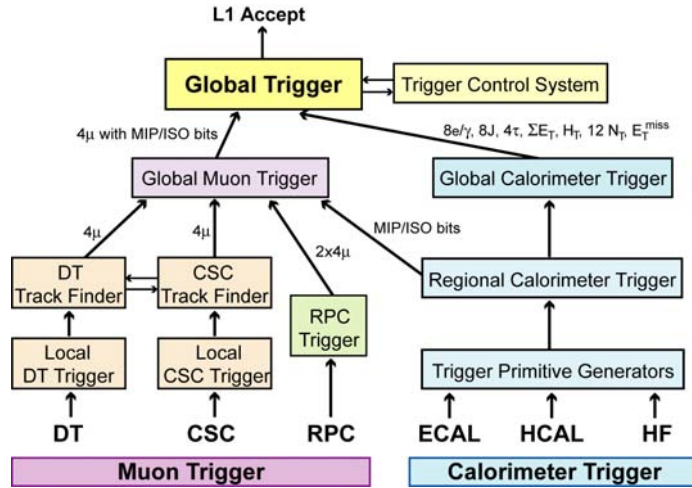


Figure 5.34: Block diagram of the L1 trigger. Reprinted from Fig. 8.1 of ref. [71].

in EE/HE the idea is similar but the counting of crystals and HE towers is slightly more complicated. An EM RCT candidate is built around a high E_T seed tower. The E_T of the candidate is the sum of the tower E_T and the E_T of its highest- E_T broad side neighbor (see Figure 5.35 for a definition of the broad side neighbors). Two isolation criteria are defined based on (a) the ratio of the EM energy to the HCAL energy in the tower and (b) the shower shape. For a non-isolated EM candidate, the highest- E_T broad side neighboring tower must pass these two isolation criteria; for an isolated EM candidate, all eight neighboring towers must pass the criteria, and there must also be at least one quiet corner with the E_T of all five towers in the corner below some threshold (see Fig. 5.35). The process is repeated until four isolated and four non-isolated EM candidates are found, starting with the highest- E_T tower in the region and moving down in tower E_T . An RCT region is flagged as consistent with tau decay only if the pattern of tower transverse energy sums defines at most a 2×2 matrix of energetic towers within the 4×4 RCT region.

From the tower transverse energy sums, eight EM candidates, and tau flag received from each RCT, the GCT computes the total E_T in the calorimeter (and the total E_T above some programmable threshold, called H_T), and the \cancel{E}_T . It also classifies the

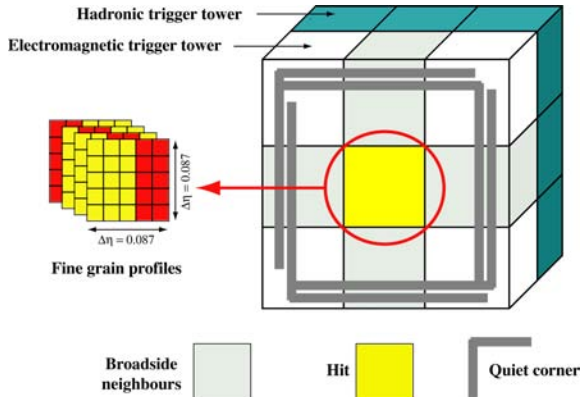


Figure 5.35: Geometry of an EM RCT candidate. Reprinted from Fig. 8.2 of ref. [71].

towers into jets and determines the globally highest ranked isolated and non-isolated EM candidates. The jet finding uses a clustering algorithm based on the energy of a sub-cluster with respect to its neighbors [93]. Jets are classified as tau decays if all of the RCT regions participating in the jet clustering had energy patterns consistent with tau decay. Counts of jets above 12 different programmable E_T thresholds are calculated. The jet counts, energy sums, E_T , and highest ranked EM candidates are sent to the GT, where the final L1 decision is taken and transmitted to the sub-detectors. The GT can execute a maximum of 128 trigger algorithms in parallel. If any one of these algorithms yields an accept, the event is accepted, and all trigger information is sent on to the HLT for further filtering. The double-photon HLT paths used in this analysis (see Sec. 6.2) require isolated L1 seeds (i.e. EM candidates built by the RCT) with $E_T > 12$ or 20 GeV, depending on path.

No muon triggers are used in the two-photon analysis. A description of the muon trigger system can be found in ref.[71].

5.2.2 Data Acquisition System

The CMS data acquisition (DAQ) system takes event fragments (calorimeter hits, track hits, etc.) from each of the 626 subdetector front end drivers (FEDs), assembles

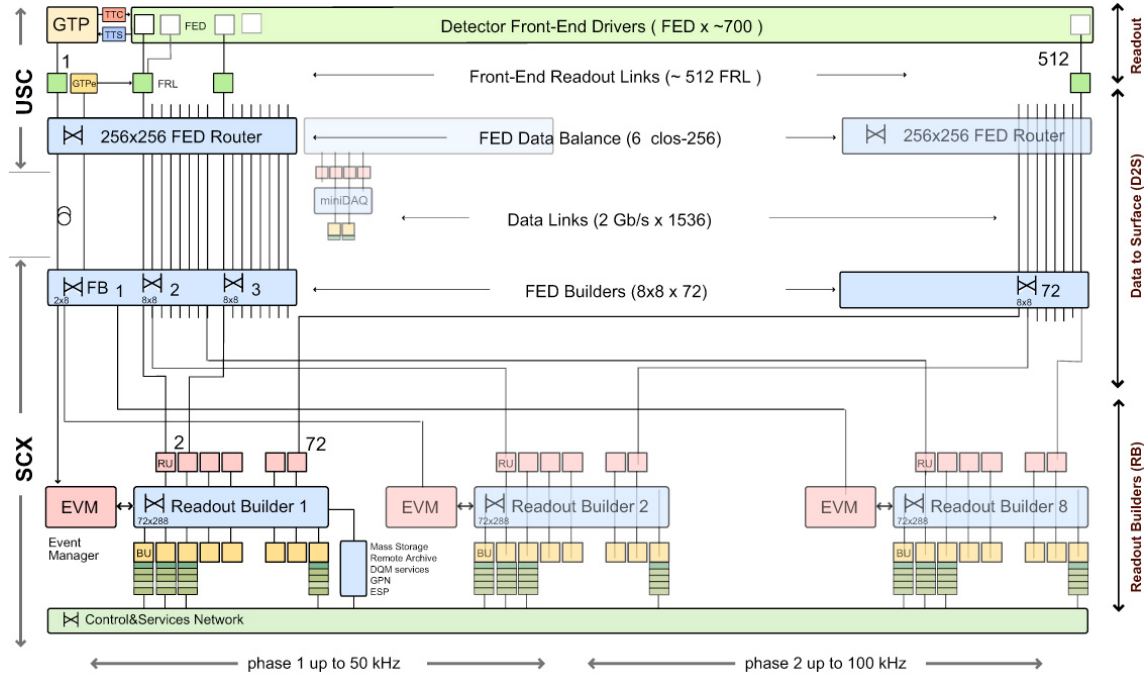


Figure 5.36: Diagram of the DAQ system. The identical event builder systems, shown as inputs and outputs to the boxes labeled “Readout Builder 1”, “Readout Builder 2”, etc., represent the eight slices. Within one slice, data can flow from the detector front ends to the readout systems to the builder network (which assembles the event fragments) to the filter systems (HLT) independently of the other slices. Reprinted from Fig. 9.8 of ref. [71].

them into a data structure representing the full event, and sends the event on to the HLT for further filtering. The DAQ must operate at an input rate of ~ 100 GB/s, corresponding to an input rate from the L1 trigger of ~ 100 kHz. To facilitate expansion of the system as the need arises, the DAQ is composed of eight nearly independent slices. Each slice functions as a smaller version of the whole DAQ that can handle an input event rate up to ~ 12.5 kHz. A diagram of the DAQ system, showing schematically the eight slices, is given in Figure 5.36.

Data from the front ends is collected by the FEDs and pushed to the front end readout links (FRLs), which may take inputs from up to two FEDs simultaneously. The FRLs check for transmission errors, generate event fragments with size ~ 2 kB, buffer the fragments in 64 kB memories, and finally send them to the FED builders.

1651 The FEDs, FRLs, and FED builders are located in the underground control room.
 1652 The 72 FED builders each construct one ~ 16 kB *super-fragment* from the input
 1653 event fragments, then send the super-fragment on to a readout unit (RU) located in
 1654 the surface control room ~ 80 m away. Super-fragments belonging to the same event
 1655 are sent to RUs in the same DAQ slice. There are 72 RUs per readout builder, one
 1656 for each super-fragment of an event, with each DAQ slice built around one readout
 1657 builder (see Fig. 5.36). Each readout builder hosts a number of builder units (BUs)
 1658 that perform the final integration of super-fragments into complete events.

1659 Resource brokers (RBs) in the HLT filter farm request complete events from the
 1660 BUs and distribute those events to the filter units (FUs) for HLT selection. If an
 1661 event passes any one of the HLT paths in the predefined menu, it is sent back to
 1662 the RB for transfer to the storage manager (SM). The SM nodes transfer accepted
 1663 events to the CERN Tier-0 prompt reconstruction facility for unpacking of the raw
 1664 data into ROOT [94] files that can be accessed by physicists wishing analyze the data.
 1665 The lag time between recording of an event in the DAQ and availability of the fully
 1666 reconstructed event for analysis is typically 48 hours.

1667 If the buffers of the upstream DAQ elements (the filter farm, readout builders,
 1668 FED builders, or FRLs) are full, those elements will not request new events from
 1669 downstream. This can lead to a buildup of events in the downstream element buffers,
 1670 *back-pressuring* all the way down to the FEDs themselves. The CMS trigger throttling
 1671 system (TTS) consists of dedicated lines between the FEDs and the GT for the
 1672 purpose of sending predefined signals to the GT about the state of the FED buffers.
 1673 If the buffer of a particular FED is getting full, it can alert the GT to reduce the
 1674 trigger rate so as to prevent FED buffer overflows and loss of time synchronization
 1675 between event fragments. The TTS latency is $\sim 1\mu\text{s}$. Causes of back-pressure (hence
 1676 dead time) include: problems with the FED electronics (in this case, the upstream
 1677 elements request events but the FEDs have trouble sending them), increases in the

1678 L1 accept rate (perhaps due to a noisy detector channel) beyond what the upstream
 1679 DAQ elements can handle, increases in the event size due to high pileup or a poor
 1680 quality beam that scrapes against the beam pipe, failures of the DAQ transmission
 1681 lines or DAQ hardware such that events are not requested from the FEDs fast enough,
 1682 or bottlenecks at the SM nodes or filter farm due to hardware failures or large event
 1683 sizes.

1684 All components of the DAQ, from the FEDs up to the SMs, are controlled by
 1685 cross-platform DAQ (XDAQ) [95] processes, or *executives*. The Simple Object Access
 1686 Protocol (SOAP) [96] protocol is used to transmit control and monitoring data be-
 1687 tween XDAQ-enabled devices and to the end user, who can view the running of a
 1688 XDAQ executive via a Web interface called HyperDAQ [97]. The Run Control and
 1689 Monitoring System (RCMS) handles the configuration and control of all XDAQ exec-
 1690 utives via a hierarchical structure. At the top of the hierarchy is the Level-0 *function*
 1691 *manager* (FM), controlling the Level-1 sub-detector FMs, which in turn control their
 1692 Level-2 system-specific XDAQ executives. The central DAQ and L1 trigger each have
 1693 their own Level-1 FM. A unit of data acquisition, called a *run*, may be configured,
 1694 started, and stopped by an end user interacting with the RCMS Web interface.

1695 5.2.3 Data Processing and Transfer to Computing Centers

1696 Data leaving the filter farm are grouped into datasets based on HLT path, i.e. there
 1697 are different datasets for events passing diphoton triggers, jet triggers, muon + elec-
 1698 tron triggers, etc. At the Tier-0 facility, the datasets go through three levels of
 1699 processing to create three *data tiers*. The first layer produces RAW data by unpack-
 1700 ing the detector byte streams sent from the DAQ and L1 trigger into data structures
 1701 holding the ADC counts recorded for each channel of the detector, digitized trigger
 1702 primitives, and the L1 decision. A single event has ~ 1.5 MB of RAW data. The next
 1703 layer of processing is the reconstruction, which forms channel energies in GeV, ap-

1704 plies calibrations, and creates high-level objects like photons, electrons, muons, taus,
 1705 jets, E_T , and charged tracks. The RECO data tier occupies ~ 0.5 MB per event.
 1706 Finally, analysis object data (AOD) is a subset of the RECO data, comprising the
 1707 high-level objects but usually excluding the individual channel hit information if it is
 1708 not associated to a physics object. This tier occupies ~ 0.1 MB per event. One copy
 1709 of the RAW data is stored permanently at CERN and another copy is distributed
 1710 amongst the Tier-1 facilities (see below) for permanent storage. Changes in the re-
 1711 construction algorithms periodically require reprocessing of the RAW data to form a
 1712 new RECO tier. In general, only the AOD tier is available to physicists wishing to
 1713 perform analyses due to the smaller size and faster replication and transfer time of
 1714 AOD with respect to RAW or RECO.

1715 There are three tiers of computing and data storage sites within the Worldwide
 1716 LHC Computing Grid (WLCG) [98]. The tier closest to CMS is Tier-0, which is
 1717 located at CERN and performs archiving of the RAW data, prompt reconstruction
 1718 of the data within ~ 48 hours of its being collected, and transferral of copies of the
 1719 RECO datasets to Tier-1 facilities. There are a few Tier-1 centers worldwide, hosted
 1720 by national computing facilities and laboratories. They store parts of the RAW dataset
 1721 and copies of the RECO datasets, participate in subsequent reconstruction passes
 1722 after the prompt reconstruction at Tier-0, and ship AOD datasets upon request to the
 1723 Tier-2 centers. Analysts interact primarily with the Tier-2 centers, which store AOD
 1724 datasets and run batch processing queues for running analysis jobs over the datasets.
 1725 Different layers of WLCG software control data transfer between sites, data storage,
 1726 and batch processing. A diagram of the WLCG tier system is given in Figure 5.37.

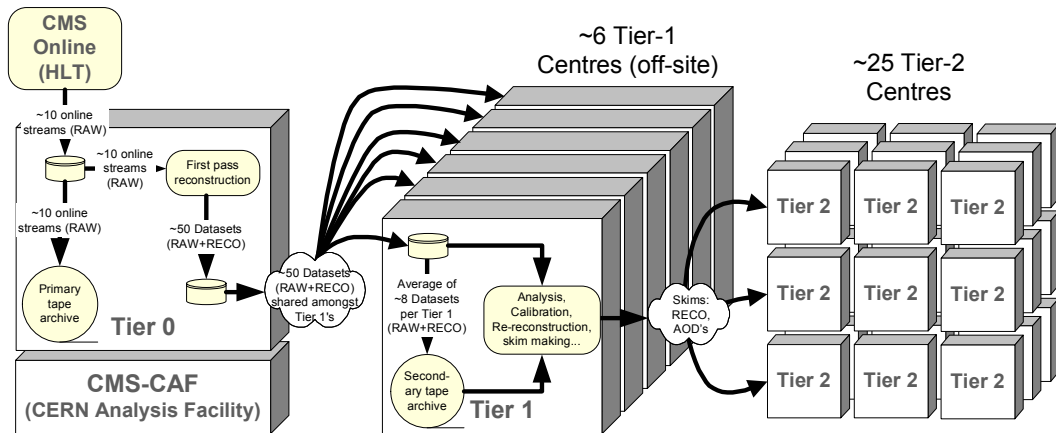


Figure 5.37: Diagram of the WLCG tier system showing data archival and reconstruction at each tier along with data transfer between tiers. Reprinted from Fig. 11.2 of ref. [71].

¹⁷²⁷ Chapter 6

¹⁷²⁸ Event Selection

¹⁷²⁹ In keeping with the phenomenology described in Sec. 3.5, the candidate GGM events
¹⁷³⁰ selected in this search consist of two high- E_T photons and a significant momentum
¹⁷³¹ imbalance transverse to the beam, indicating the production of an escaping gravitino.
¹⁷³² This momentum imbalance is usually referred to as *missing transverse energy* and is
¹⁷³³ denoted by the symbols \cancel{E}_T or ME_T . The GGM signature is shown in Figure 6.1.

¹⁷³⁴ However, in order to use real CMS data (as opposed to simulation) to derive
¹⁷³⁵ predictions for the backgrounds to the search, *control samples* that are not expected
¹⁷³⁶ to contain any GGM signal events and are distinct from the *candidate* two-photon
¹⁷³⁷ sample must be collected from the LHC data. These samples consist of different
¹⁷³⁸ numerical combinations of photons, electrons, and jets, and are explained in more
¹⁷³⁹ detail in Chapter 7. Since this search is performed in the high- E_T tail of the \cancel{E}_T
¹⁷⁴⁰ distribution, where adequate detector simulation is very difficult, it is advantageous
¹⁷⁴¹ to use *data-driven* background estimates, which capture the true detector response,
¹⁷⁴² over numbers derived from simulation.

¹⁷⁴³ In the following sections, the reconstruction of photons, electrons, jets, and \cancel{E}_T
¹⁷⁴⁴ is explained. Sec. 6.1 begins with an explanation of the high level reconstruction.
¹⁷⁴⁵ It is followed by Sec. 6.2, which describes the triggers used to collect the candidate

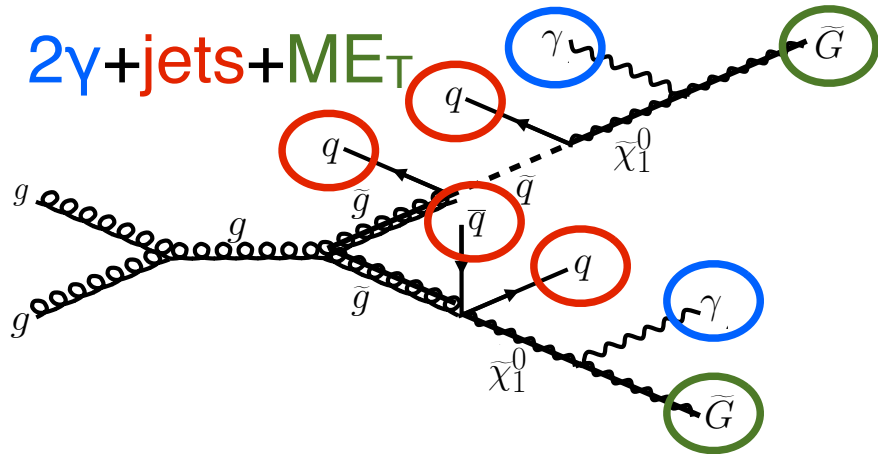


Figure 6.1: Two gluinos each decay via $\tilde{\chi}_1^0 \rightarrow \gamma \tilde{G}$.

1746 and control samples. Sec. 6.3 describes event cleaning cuts that are applied to the
1747 candidate and control samples. Finally, the chapter concludes with a measurement of
1748 the photon identification efficiency in Sec. 6.4.

1749 6.1 Object Reconstruction

1750 This section describes the *offline* object reconstruction, i.e. the reconstruction of par-
1751 ticle objects from events that have already been triggered and written to permanent
1752 storage, as opposed to the building of trigger objects explained in Secs. 5.2.1 and 6.2.

1753 6.1.1 Photons

1754 Uncalibrated EB/EE Hits

1755 Photon reconstruction begins with the ADC count value for each of the 10 recorded
1756 time samples per ECAL crystal per trigger. To construct an *uncalibrated hit*, the
1757 gain (1, 6, or 12; see Sec. 5.1.2) of each sample is determined and the ADC count
1758 value scaled appropriately. The pedestal is estimated from the average of the first
1759 three samples, which, for a properly timed in hit, should contain no signal. This

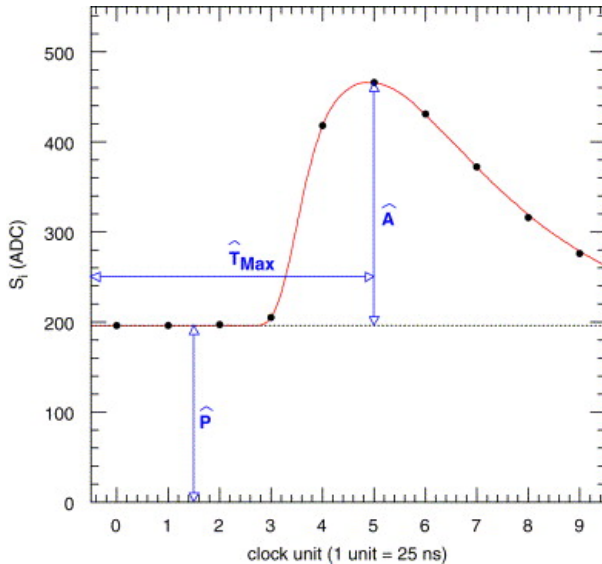


Figure 6.2: Typical ECAL channel pulse shape. \hat{P} is the pedestal value, \hat{A} is the pulse amplitude, and \hat{T}_{\max} is the hit time. The red line is the assumed pulse shape from which the weights are derived. Reprinted from ref. [99].

1760 pedestal value is subtracted from the rest of the samples. Finally, the amplitude of the
 1761 pulse is reconstructed using a predetermined weight for each sample [99]. The weights
 1762 correspond to the pulse shape expected from the MGPA and shaping circuit response.
 1763 The time of the hit is also reconstructed using the ratios between neighboring time
 1764 samples [100]. A typical ECAL channel pulse shape is shown in Figure 6.2.

1765 Calibrated EB/EE Hits

1766 In the next phase of the photon reconstruction, calibrations are applied to the un-
 1767 calibrated hits to form *calibrated hits* with energy measured in GeV. Channels are
 1768 excluded from seeding calibrated hits if

- 1769 • they are excessively noisy,
- 1770 • they are stuck in fixed gain (i.e. the MGPA gain does not change properly to
 1771 avoid saturation),
- 1772 • they are totally dead,

- 1773 • they have one or more neighboring dead channels, or
 1774 • they do not have good trigger primitives (i.e. trigger primitive is missing, satu-
 1775 rated, or *spike-like*; cf. Secs. 5.1.2 and 5.2.1).

1776 *ECAL spikes* are hits in which low energy protons and heavy ions from jets ionize
 1777 in the sensitive volume of the EB APD (Sec. 5.1.2), causing the APD to register a
 1778 fake large-amplitude hit. Because they are not the result of a real electromagnetic
 1779 shower, spikes tend to be isolated. They may also appear to arrive early or late with
 1780 respect to the nominal bunch crossing. Most spikes are reconstructed with a hit time
 1781 ~ 10 ns earlier than real EM hits because unlike real hits, whose pulse shapes include
 1782 the time constant associated with crystal scintillation, the reconstructed spikes only
 1783 involve the rise time of the electronics. There also is a long tail of late arriving spikes
 1784 due to slow neutrons from jets [101].

1785 Because of their particular timing and topological characteristics, cuts have been
 1786 developed to effectively identify and reject spike-like hits. This analysis utilizes both
 1787 the “Swiss cross” cut $1 - E_4/E_1 > 0.95$, where E_1 is the energy of the spike candidate
 1788 crystal and E_4 is the sum of the energies in the four crystals whose edges are next to
 1789 the four edges of the spike candidate crystal, and a timing cut $t \geq 3$ ns, to flag spikes.
 1790 More information about these cuts can be found in ref. [101]. A simpler algorithm
 1791 using the fine grain veto bit of the ECAL L1 TPG (Sec. 5.2.1) is used to reject spikes
 1792 at the trigger level.

1793 In addition to the trigger primitives, no uncalibrated hits that are spike-like are
 1794 eligible for calibration. The calibrations applied are corrections to account for crystal
 1795 transparency and VPT photocathode loss (leading to signal loss), measured continu-
 1796 ously by the laser/LED system; energy intercalibrations (relative energy calibration
 1797 between crystals); absolute scale calibrations between ADC counts and GeV;¹ and

¹The ADC-GeV scale factors (one for EB and one for EE) are defined such that the sum of fully calibrated and scaled hits in a particular 5×5 cluster of crystals (plus the associated energy deposited in ES) is 50 GeV for a 50 GeV incident unconverted photon [102].

1798 time intercalibrations (relative time calibration between crystals).

1799 The ECAL crystals were pre-calibrated before installation in CMS using labora-
 1800 tory light yield and photodetector gain measurements [103]. In addition, some EB
 1801 and EE crystals were intercalibrated using test beams [104], and all EB crystals were
 1802 intercalibrated with cosmic ray muons [105]. EE precalibrations were validated with
 1803 LHC *splash events* in 2009 [105, 106], in which the beam was dumped onto a col-
 1804 limitor approximately 150 meters upstream of CMS, causing a spray of muons to
 1805 enter CMS at one endcap and exit at the other. Splash events were also used to
 1806 derive time intercalibration constants. Before colliding beam operations commenced,
 1807 the intercalibration precision was estimated to be 0.5%-2.2% in EB and 1%-5% in EE
 1808 [107].

1809 Three calibration methods were employed once colliding beam operations began:

- 1810 • ϕ symmetry relative calibration between crystals, exploiting the azimuthal sym-
 1811 metry of CMS
- 1812 • π^0 and η relative calibration between crystals, using the diphoton decays of
 1813 these particles
- 1814 • E/p absolute calibration, comparing the momentum measured in the tracker p
 1815 to the energy measured in the ECAL E of a sample of electrons from Z decay

1816 By September 2011, the intercalibration precision in EB was measured to be between
 1817 0.3% and 1.1% using the π^0/η method [108]. Figure 6.3 shows the improvement in
 1818 Z reconstruction from pre-LHC calibration constants to the latest π^0/η -derived con-
 1819 stants.

1820 Calibrated ES Hits

1821 ES calibrated hits are formed from the three samples read out per sensor. Just as in the
 1822 case of EB/EE crystals, ES uncalibrated hits are gain-adjusted, pedestal-subtracted,

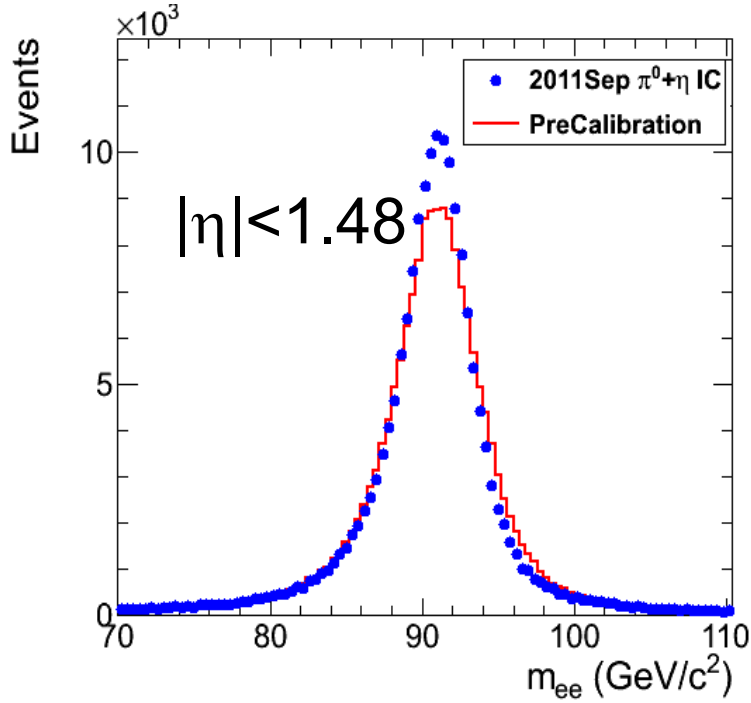


Figure 6.3: Z peak reconstructed using pre-LHC calibration constants (red) or September 2011 π^0/η -derived intercalibration constants (blue). Reprinted from ref. [108].

1823 and reconstructed using weights. To make a calibrated ES hit, intercalibration con-
 1824 stants, angle correction constants (for the non-uniformity of sensor angle with respect
 1825 to the vertical across ES), and a MIP-GeV absolute scale factor are applied.

1826 **Clustering**

1827 After calibrated ECAL hits are formed, they must be clustered into shapes that
 1828 represent the energy deposit from a single particle. *Basic clusters* are formed around
 1829 seed hits, defined as a hit that

- 1830 • has calibrated $E_T > 1(0.18)$ GeV in EB(EE),
- 1831 • does not originate from a dead channel or one with faulty hardware,
- 1832 • is not poorly calibrated,

- 1833 ● was reconstructed with the standard algorithm (i.e. not a special recovery algo-
- 1834 rithm for channels with subpar data integrity),
- 1835 ● is not saturated,
- 1836 ● is not spike-like, and
- 1837 ● is in time (EB).

1838 EB basic clusters are formed around the seeds via the *hybrid* algorithm, while EE
 1839 basic clusters are formed with the `multi5x5` algorithm [109]. In addition to handling
 1840 non-radiating electrons and unconverted photons, both algorithms are designed to also
 1841 recover all of the energy associated with electron bremsstrahlung deposits and photon
 1842 conversions. The geometry of the CMS magnetic field means that bremsstrahlung
 1843 and conversions will tend to spread the shower out in ϕ , not η . Both algorithms
 1844 work by forming basic clusters around seeds, then combining the basic clusters into
 1845 *superclusters* (SC) by searching in a window extended in the ϕ direction for all basic
 1846 clusters consistent with bremsstrahlung radiation from the primary electron, or with
 1847 a photon conversion. Figure 6.4 illustrates the hybrid algorithm in EB. In EE, the
 1848 energy deposited in ES must also be added into the total clustered energy sum.

1849 Figure 6.5 shows the effect of superclustering on $Z \rightarrow ee$ reconstruction.

1850 **Supercluster Corrections**

1851 The total clustered ECAL energy is defined as

$$E = F \times \sum_{i=1}^{n_{\text{crystal}}} G \times c_i \times A_i \quad (6.1)$$

1852 where G is the ADC-GeV or MIP-GeV scale factor, c_i are the intercalibration con-
 1853 stants, A_i is the uncalibrated hit amplitude in ADC counts, and F is a SC correction

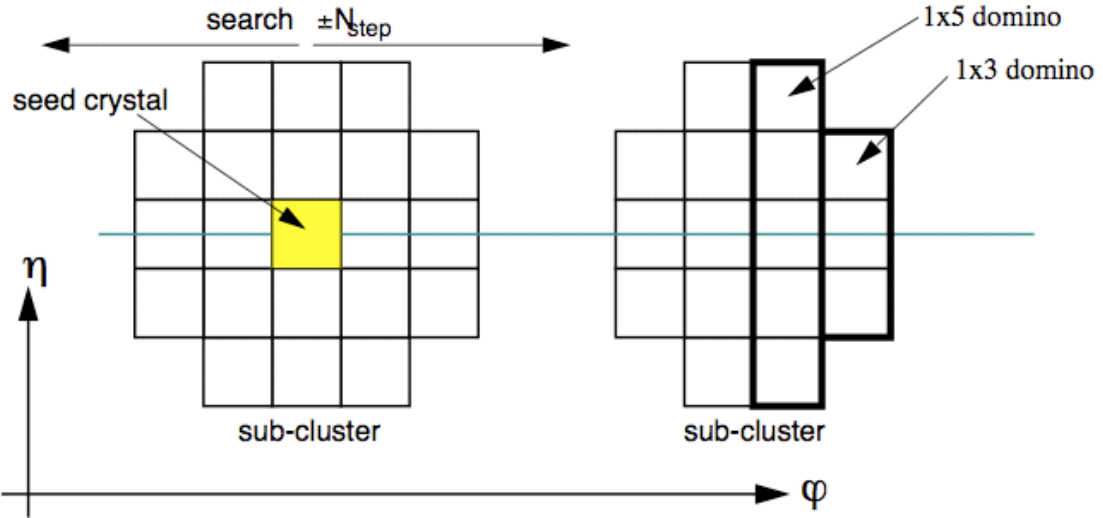


Figure 6.4: Hybrid algorithm in EB. The shower extent is constant in η (five crystals), but spreads out in ϕ as the two sub-clusters (or basic clusters) are grouped into the same supercluster. The maximum extent in ϕ is 17 crystals. Reprinted from ref. [109].

1854 factor. G and c_i were explained in Sec. 6.1.1. F is a product of three factors for hybrid
1855 SCs (two for `multi5x5` SCs in EE, items 2 and 3 below) [109]:

- 1856 1. $C_{\text{EB}}(\eta)$, which compensates for lateral energy leakage due to the crystal off-pointing in EB only. These corrections are taken from MC simulation [109] and
1857 were confirmed in test beams [104].
- 1859 2. $f(\text{brem})$, which corrects for biases in the clustering algorithms for showers characterized by differing amounts of bremsstrahlung. These corrections are taken
1860 from MC simulation [109].
- 1862 3. Residual correction $f(E_T, \eta)$, due to the variation in η of detector material
1863 traversed by a primary electron or photon, and to any residual E_T dependence
1864 of the reconstruction. These corrections are determined from MC and validated
1865 on $Z \rightarrow ee$ data samples [111].

1866 As a benchmark of ECAL calibration performance, the extra energy smearing in
1867 MC needed to achieve data/MC agreement in the Z width was between $\sim 0.9\%$ (in

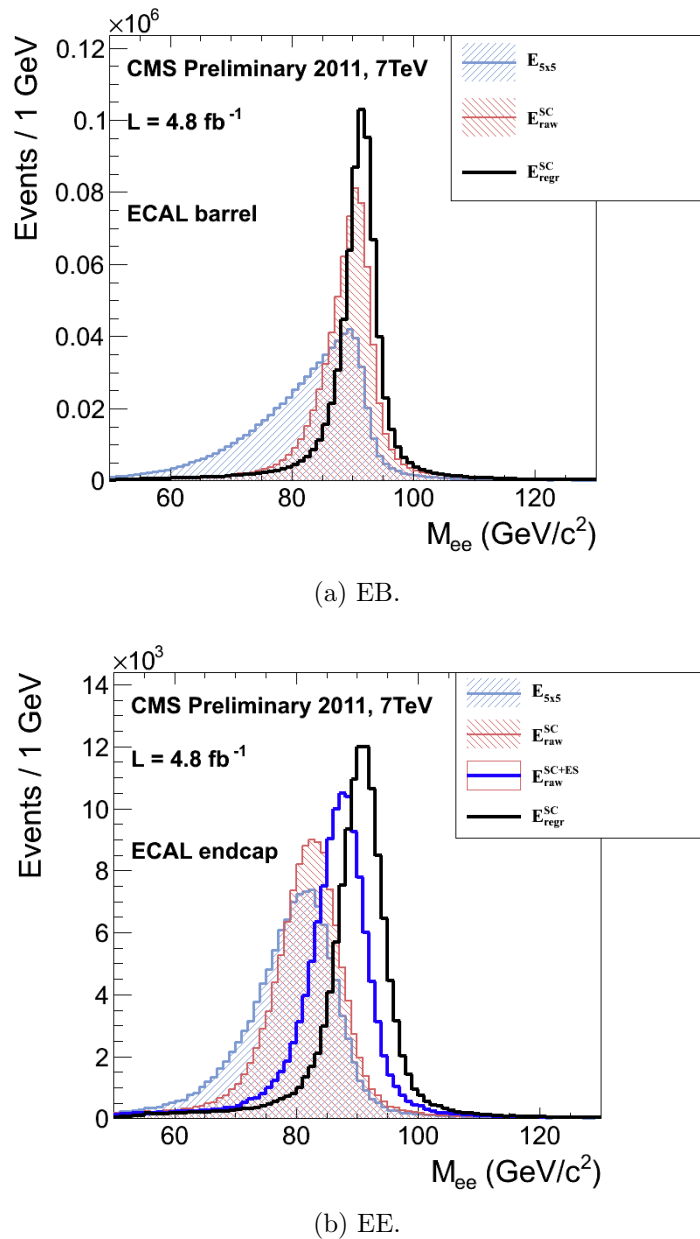


Figure 6.5: Z peak reconstructed in the dielectron channel for different kinds of clustering. The constituent hits were calibrated with the best available intercalibrations and laser calibrations as of December 2011. The light blue histogram shows the reconstruction using a 5×5 energy sum, the red histogram shows the reconstruction using the SC energy for crystals only (the dark blue histogram in the EE plot adds in the energy from ES), and the black histogram shows the reconstruction after the SCs are corrected using a multivariate method [110]. Reprinted from Fig. 30 of ref. [110].

1868 the central part of EB for electrons with little bremsstrahlung) and $\sim 3.3\%$ (in the
1869 outer part of EE for heavily radiating electrons) [110].

1870 **From Supercluster to Photon**

1871 The CMS photon object is any SC with $E_T > 10$ GeV and $H/E < 0.5$, unless the SC
1872 $E_T > 100$ GeV, in which case the H/E requirement is dropped. H/E is defined as the
1873 ratio of energy in the HCAL in a 0.15 cone around the SC centroid, directly behind
1874 the SC, to the SC energy. SCs with $R9 > 0.94(0.95)$ in EB(EE), where $R9$ is defined
1875 as the ratio of the energy in the central 3×3 cluster of crystals divided by the SC
1876 energy $E_{3 \times 3}/E_{\text{SC}}$, are the best calibrated and most accurate type of electromagnetic
1877 shower. Therefore, for these objects, the photon energy is defined as the energy sum
1878 of the fully calibrated hits in the central 5×5 cluster around the seed (with $C_{\text{EB}}(\eta)$
1879 applied for EB photons). For all other SCs, the photon energy is equal to the fully
1880 corrected SC energy (cf. Sec. 6.1.1).

1881 In this search, candidate photons and *fake photons* (f , “fakes”) are further selected
1882 according to the criteria listed in Table 6.1. Fakes are used in the determination of
1883 the QCD background, as explained in Chapter 7.

Table 6.1: Selection criteria for photons and fakes. “Pixel seed,” I_{comb} , and $\sigma_{i\eta i\eta}$ are defined in the text.

Variable	Cut (γ)	Cut (f)
SC $ \eta $	< 1.4442	< 1.4442
H/E	< 0.05	< 0.05
$R9$	< 1	< 1
Has pixel seed	No	No
$I_{\text{comb}}, \sigma_{i\eta i\eta}$	< 6 GeV AND < 0.011	$(\geq 6 \text{ AND } < 20 \text{ GeV}) \text{ OR } \geq 0.011$

1884 I_{comb} is defined as

$$I_{\text{comb}} = I_{\text{ECAL}} - 0.093\rho + I_{\text{HCAL}} - 0.0281\rho + I_{\text{track}} \quad (6.2)$$

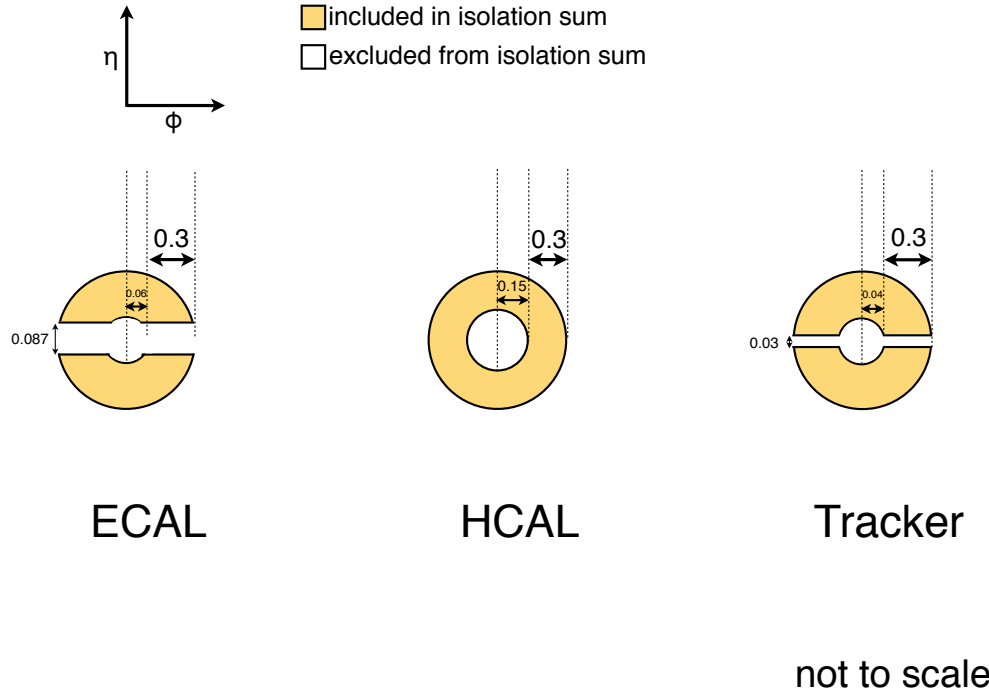


Figure 6.6: ECAL, HCAL, and track isolation cones.

1885 where I_{ECAL} , I_{HCAL} , and I_{track} are E_T sums in the annular regions defined in Figure 6.6
 1886 and ρ is the average pileup energy density in the calorimeters (per unit $\eta \cdot \phi$, or unit
 1887 calorimeter surface area) as measured with the Fastjet algorithm [112, 113]. ρ is
 1888 constant over the η range of the calorimeter. Note that the ECAL and track isolation
 1889 veto strips at constant η ensure that the isolation cuts are similarly efficient for
 1890 converted photons, radiating electrons, and unconverted photons.

1891 $\sigma_{i\eta i\eta}$ is the log energy weighted extent of the shower in η and is defined as

$$\sigma_{i\eta i\eta} = \frac{\sum_{i=1}^{25} w_i (\eta_i - \bar{\eta})^2}{\sum_{i=1}^{25} w_i} \quad (6.3)$$

1892 where the sums run over the 5×5 matrix of crystals surrounding the seed, $w_i =$
 1893 $\max(0, 4.7 + \ln(E_i/E))$, E_i is the energy of the i^{th} crystal, E is the total energy in the

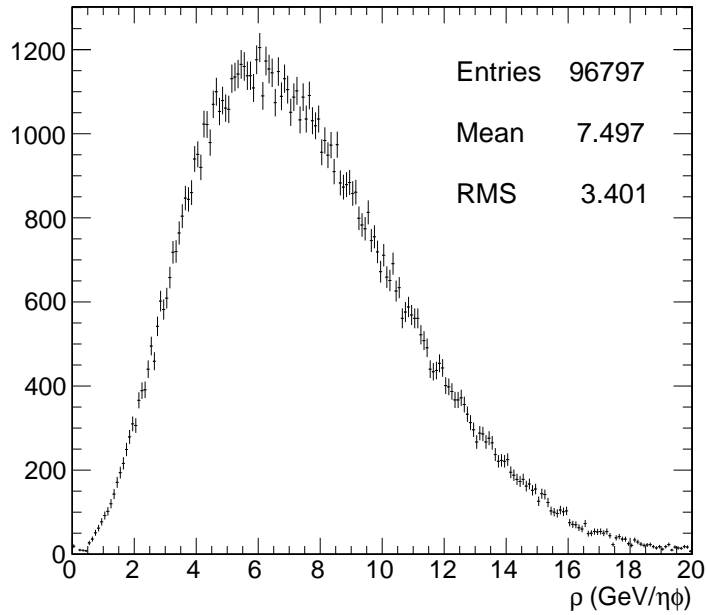


Figure 6.7: ρ distribution for a sample of two-photon events, with at least one 40 GeV and one 25 GeV photon, passing the selection requirements in Table 6.1 and the trigger requirements in Table 6.3. This sample covers the full 2011 dataset of 4.7 fb^{-1} .

1894 25 crystals, η_i is the offset in η of the i^{th} crystal from the seed, and $\bar{\eta}$ is the weighted
1895 average η of the 25 crystals (using the w_i as weights) [114].

1896 Figure 6.7 shows the ρ distribution for a sample of two-photon events, with at
1897 least one 40 GeV and one 25 GeV photon, passing the selection requirements in
1898 Table 6.1 and the trigger requirements in Table 6.3. This sample represents the full
1899 2011 dataset of 4.7 fb^{-1} . Since the average ρ is $\sim 7.5 \text{ GeV}$, and there is a long tail
1900 above this average value, it is necessary to subtract pileup energy from the ECAL
1901 and HCAL isolation cones to recover otherwise clean photons in events with large
1902 pileup. The ECAL and HCAL *effective areas* of 0.093 and 0.0281, respectively, are
1903 calculated by fitting the average ECAL or HCAL isolation energy vs. ρ in a sample
1904 of $Z \rightarrow ee$ events to a straight line. The slope of the line—which has the units of $\eta \cdot \phi$,
1905 or area—is the effective area.

1906 The cut on combined isolation of 6 GeV (Table 6.1) is the result of an S/\sqrt{B}

S \sqrt{B} Vs ComblsoDR03

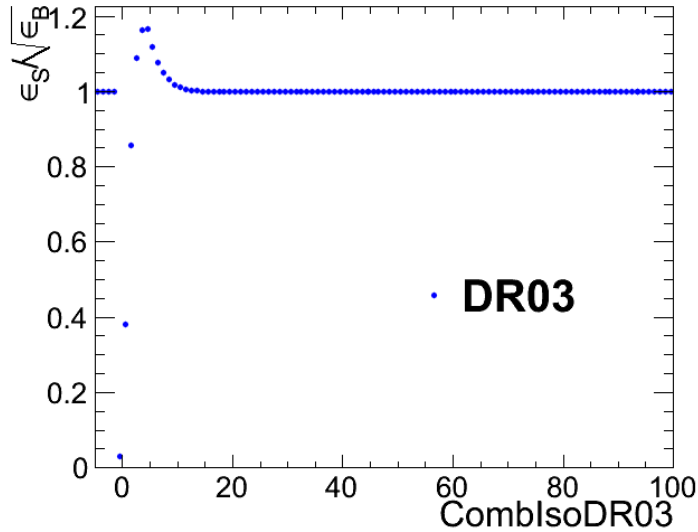


Figure 6.8: S/\sqrt{B} (S and B defined in the text) vs. I_{comb} . “DR03” in the legend indicates that this combined isolation was calculated in $\Delta R = 0.3$ cones, as used throughout this analysis. Reprinted from Fig. 7 of ref. [115].

optimization procedure [115]. S is a sample of photons in simulated GGM events that are products of neutralino decay, while B is a sample of photons matched to generated hadronic jets in simulated QCD events. Figure 6.8 shows the value of S/\sqrt{B} vs. combined isolation, in particular the pronounced peak around 6 GeV.

The upper bound on fake photon combined isolation guarantees that poorly isolated dijet events, with \cancel{E}_T resolution dissimilar to the candidate diphoton events, do not enter the ff sample. The exact value of 20 GeV (cf. Table 6.1) arises from a low- \cancel{E}_T $ff/\gamma\gamma \chi^2$ optimization procedure [115]. Figure 6.9 shows the value of the Neyman’s χ^2 between the ff and $\gamma\gamma \cancel{E}_T$ distributions, truncated at either 25 or 50 GeV, vs. upper bound on fake combined isolation. As shown in the figure, 20 GeV keeps the χ^2 small while also being large enough that a sufficient number of ff events may be collected.

Finally, a “pixel seed” is defined as a hit in the pixel detector consistent with a

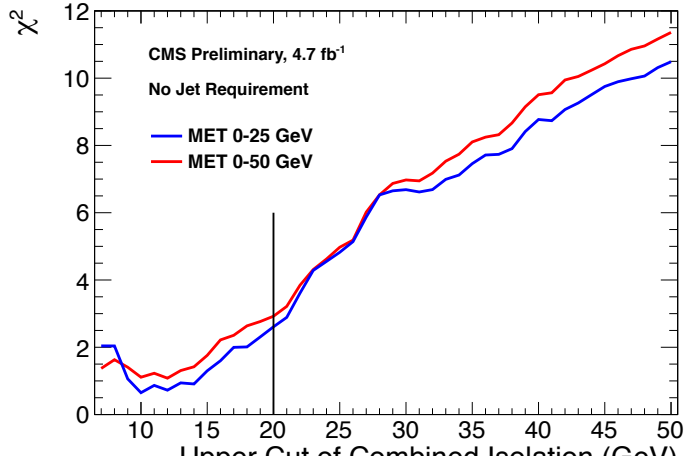
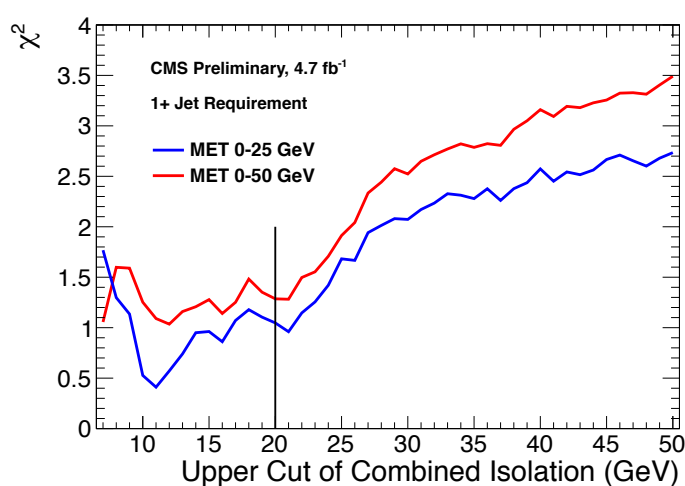
(a) Events with ≥ 0 jets.(b) Events with ≥ 1 jet.

Figure 6.9: Neyman's χ^2 between the ff and $\gamma\gamma$ \cancel{E}_T distributions, truncated at either 25 (red) or 50 (blue) GeV, vs. upper bound on fake combined isolation. A jet is defined as in Table 6.2, but with the ΔR cleaning criteria of Table 6.2 applied to the two primary EM objects and all additional electrons, photons, and fake photons. The full reweighting and normalization procedure is employed in the \cancel{E}_T calculation (see Sec. 7.2). Reprinted from Fig. 9 of ref. [115].

1920 track extrapolated from the position of the ECAL SC back to the primary vertex.
1921 Real photons, having no charge and therefore no bending in the magnetic field, should
1922 not have a pixel seed.

1923 6.1.2 Electrons

1924 Electrons are reconstructed identically to photons, except that in the electron case
1925 the presence of a pixel seed is enforced, rather than vetoed.² Photons and electrons
1926 are defined by very similar criteria so that $Z \rightarrow ee$ events can be used to model
1927 the QCD background in the two-photon sample without introducing any bias in the
1928 electron energy measurement (cf. Sec. 7.2).

1929 6.1.3 Jets and Missing Transverse Energy

1930 Particle Flow

1931 In this analysis, jets and E_T are formed from *particle flow* (PF) candidates. The
1932 particle flow algorithm [117, 118] uses information from all CMS subdetectors to
1933 reconstruct as accurately as possible the positions and momenta of all visible jet con-
1934 stituents, exploiting the fine granularity of the tracker and ECAL to achieve a greatly
1935 improved momentum resolution over calorimeter-only jets [119]. The PF algorithm is
1936 summarized below [117].

1937 1. Reconstruct the fundamental detector objects via iterative procedures

- 1938 • Tracks in the inner silicon layers
 - 1939 – High efficiency and low fake rate for charged hadrons in jets

²In many CMS analyses, electrons are reconstructed very differently from photons. In particular, a special tracking algorithm [116] is used to best follow a radiating electron. However, in this analysis, the electron tracking is not used.

- 1940 – Relaxed primary vertex constraint allows photon conversions, particles originating from nuclear interactions in the silicon, and long-lived particles to be reconstructed
- 1941
- 1942
- 1943 • Calorimeter clusters
- 1944 • Muon tracks in the outer muon layers
- 1945 2. Create a “block” of linked fundamental objects
 - 1946 • Link silicon tracks to calorimeter clusters via $\Delta R_{\text{track-cluster}}$ (account for electron bremsstrahlung)
 - 1947
 - 1948 • Link clusters in one calorimeter layer to clusters in a separate layer via $\Delta R_{\text{cluster-cluster}}$
 - 1949
 - 1950 • Link silicon tracks to muon tracks via global track χ^2
- 1951 3. ID the particles in the block
 - 1952 • If global (silicon + muon layers) muon p_T is compatible with silicon track p_T , ID as a muon and remove corresponding tracks from block
 - 1953
 - 1954 • ID electron tracks via special algorithm and removed all corresponding tracks and cluster from block
 - 1955
 - 1956 • Remove fake tracks from the block
 - 1957
 - 1958 • Allow multiple tracks to be associated to one HCAL cluster, but not multiple HCAL clusters to be associated to one track—for each track, keep only the HCAL cluster link that is closest in ΔR to the track
 - 1959
 - 1960 • If the cluster energy is significantly larger then the energy of the linked tracks, ID as a PF photon or PF neutral hadron
 - 1961
 - 1962 • If the cluster is not linked to a track, ID as a PF photon or PF neutral hadron
 - 1963

- 1964 • If the cluster energy is smaller than the energy of the linked tracks, ID
 1965 each track as a PF charged hadron

1966 **Jets**

1967 PF candidates are clustered into jets by means of the anti- k_T algorithm with $R = 0.5$
 1968 [120]. In this algorithm, all possible pairs of PF candidates i, j are looped over, and
 1969 the pairs that minimize the distance variable

$$d_{ij} = \frac{\Delta R_{ij}^2}{R^2 \max(k_{Ti}^2, k_{Tj}^2)} \quad (6.4)$$

1970 are clustered together, where k_{Ti} is the transverse momentum of PF candidate i . The
 1971 process is repeated, using the pairwise-clustered PF candidates as input objects to
 1972 the next round of clustering, until $d_{ij} > 1/k_{Ti}^2$ for all pairs of clustered PF candidates
 1973 [121]. An illustration is given in Figure 6.10. The anti- k_T algorithm is infrared and
 1974 collinear safe, leading to well-behaved theoretical predictions and ease of comparison
 1975 between data and MC simulation. It also tends to form circular jets, making it easy
 1976 for experimental effects such as expected out-of-cone energy and fiducial acceptance
 1977 to be measured or simulated. For these reasons, the anti- k_T jet clustering algorithm
 1978 was chosen for this analysis.

1979 Once jets are found, they must be corrected for biases in the energy measurement
 1980 due to non-compensation [122], invisible energy (lost to overcoming nuclear binding
 1981 energy, in neutrinos, or in unclustered muons, for example) [122], detector geometry
 1982 and cracks [123], zero suppression and trigger inefficiencies [124], pileup, and effects
 1983 of the clustering algorithm [123]. Four multiplicative correction factors are applied to
 1984 the raw jet four-momentum p_μ^{raw} [119]:

- 1985 • $C_{\text{offset}}(p_T^{\text{raw}})$, which accounts for extra energy due to noise, pileup, and the un-

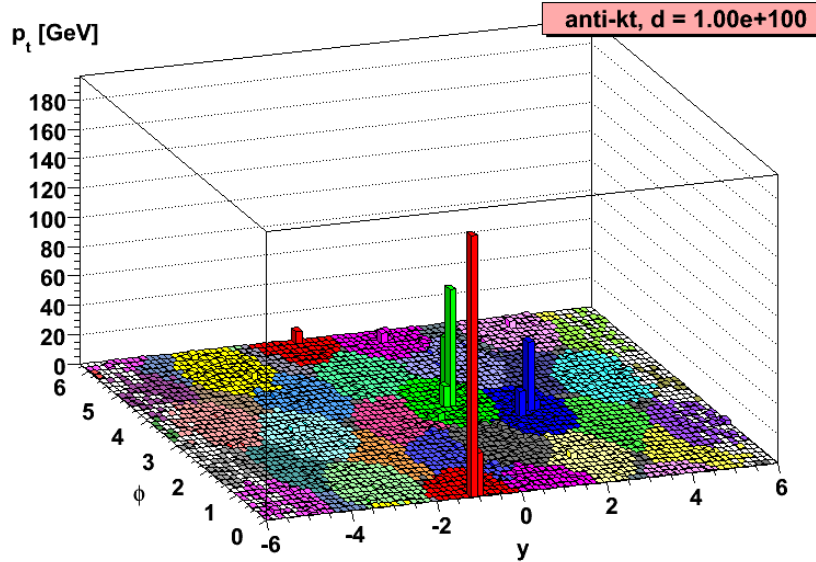


Figure 6.10: Example event display showing jets clustered via the anti- k_T algorithm. y is pseudorapidity. Reprinted from slide 85 of ref. [121].

- 1986 derlying event;
- 1987 • $C_{\text{MC}}(C_{\text{offset}}p_T^{\text{raw}}, \eta)$, which is derived from MC and accounts for most of the p_T
- 1988 and η dependence;
- 1989 • $C_{\text{rel}}(\eta)$, which accounts for the remaining differences in uniformity over the
- 1990 entire calorimeter between data and MC; and
- 1991 • $C_{\text{abs}}(C_{\text{rel}}C_{\text{MC}}C_{\text{offset}}p_T^{\text{raw}})$, which accounts for the remaining differences in linear-
- 1992 ity over the full p_T range between data and MC.

1993 Figure 6.11 shows the total jet energy correction factor $C_{\text{offset}}C_{\text{MC}}C_{\text{rel}}C_{\text{abs}}$ vs. η

1994 for jets reconstructed with the anti- k_T algorithm, $R = 0.5$. The PF jet corrections

1995 are more uniform across η than those of CALO jets (composed of simple calorimeter

1996 towers) or JPT jets (Jet Plus Tracks; composed of calorimeter energies replaced,

1997 where possible, with matching track p_T) [125]. In addition, for p_T in the range 30-200

1998 GeV and $|\eta|$ up to 2.0, the PF jet energy correction uncertainty is lower than that of

1999 the other two types of jets, and never exceeds $\sim 3\%$ [119]. The superior performance

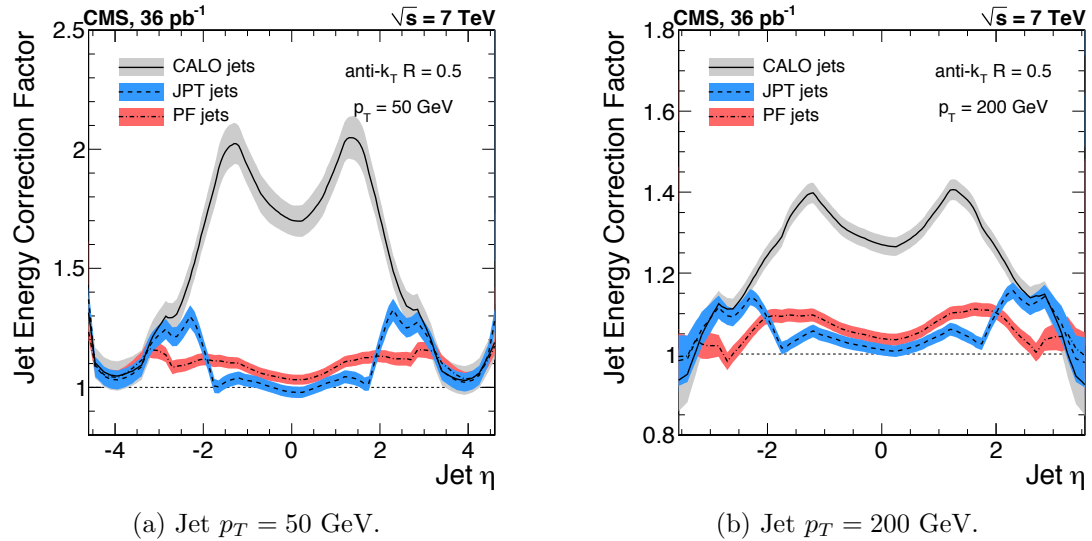


Figure 6.11: Total jet energy correction factor $C_{\text{offset}}C_{\text{MC}}C_{\text{rel}}C_{\text{abs}}$ vs. η , including uncertainty band, for jets reconstructed with the anti- k_T algorithm, $R = 0.5$. Reprinted from Fig. 26 of ref. [119].

of PF jets motivates their use in this search.

²⁰⁰¹ In this analysis, candidate and QCD control events are binned by number of jets
²⁰⁰² satisfying the criteria in Table 6.2.

2003 Missing Transverse Energy

²⁰⁰⁴ To be consistent with the jet reconstruction, E_T in this analysis is also reconstructed from PF candidates. Raw E_T is defined as

$$\mathcal{E}_{T\text{raw}} = \left| - \sum_{i=1}^{n_{\text{PF}}} \vec{p}_{Ti} \right| \quad (6.5)$$

where n_{PF} is the number of PF candidates in the event. $\cancel{E}_{T\text{raw}}$ may be corrected for the same effects that necessitate jet corrections, since $\cancel{E}_{T\text{raw}}$ is usually the result of jet mis-measurement (except, of course, in electroweak physics processes that include an energetic neutrino, or SUSY production). CMS *Type-I* E_T corrections simply involve

Table 6.2: Definition of HB/HE hadronic jets.

Variable	Cut
Algorithm	L1FastL2L3Residual corrected PF
p_T	$> 30 \text{ GeV}$
$ \eta $	< 2.6
Neutral hadronic energy fraction	< 0.99
Neutral electromagnetic energy fraction	< 0.99
Number of constituents	> 1
Charged hadronic energy	$> 0.0 \text{ GeV}$ if $ \eta < 2.4$
Number of charged hadrons	> 0 if $ \eta < 2.4$
Charged electromagnetic energy fraction	< 0.99 if $ \eta < 2.4$
ΔR to nearest PF electron ^a , muon ^b , or one of the two primary EM objects	> 0.5

^aA PF electron is defined as an electron reconstructed with the PF algorithm [126] with $p_T > 15 \text{ GeV}$, $|\eta| < 2.6$, and $(I_{\text{charged}} + I_{\text{photon}} + I_{\text{neutral}})/p_T < 0.2$, where $I_{\text{charged}}(I_{\text{photon}})(I_{\text{neutral}})$ is the sum of PF charged hadron(PF photon)(PF neutral hadron) momenta in a $\Delta R = 0.4$ cone around the PF electron.

^bMuons are reconstructed [127] from a combination of muon station and inner tracker hits. Here, a muon must have track $\chi^2 < 10$, at least one good muon station hit, inner track transverse impact parameter $< 0.02 \text{ cm}$, inner track longitudinal impact parameter $< 0.5 \text{ cm}$, $p_T > 15 \text{ GeV}$, $|\eta| < 2.6$, and $(I_{\text{ECAL}} + I_{\text{HCAL}} + I_{\text{track}})/p_T < 0.2$, where $I_{\text{ECAL}}(I_{\text{HCAL}})(I_{\text{track}})$ is the sum of ECAL(HCAL)(track) momenta in a $\Delta R = 0.3$ cone around the muon.

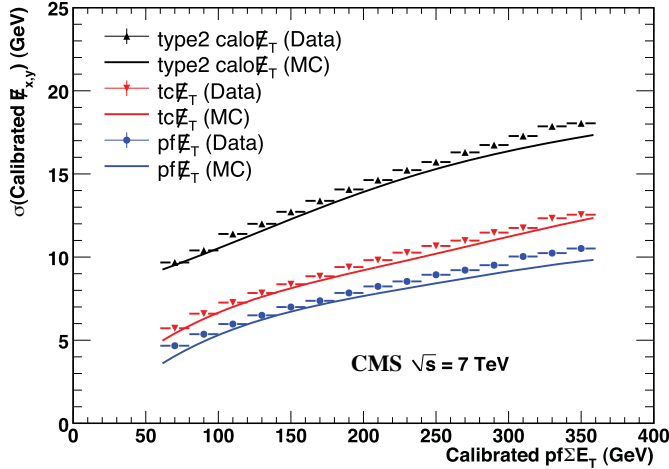


Figure 6.12: σ of a Gaussian fit to the x- and y-components of calibrated E_T vs. the calibrated PF E_T sum in a sample of events containing at least two jets with $p_T > 25$ GeV. σ is calibrated such that the E_T scale is equal for all three algorithms. PF $\sum E_T$ is corrected, on average, to the particle level using a Pythia v8 simulation [128]. The blue markers (data) and line (MC) refer to PF jets. Reprinted from Fig. 13 of ref. [124].

replacing the PF jets with their corrected energies (cf. Sec 6.1.3) and recalculating E_T . Only jets with electromagnetic fraction (EMF) below 90% and $p_T > 20$ GeV are replaced. This ensures that very electromagnetic jets (as well as isolated leptons, which also receive no correction), which consist chiefly of neutral pions and are measured accurately by the ECAL, do not receive a correction derived for jets with a large fraction of their energy in charged hadrons. In addition, the p_T cut guarantees that jet corrections are only applied where they are known to within a few percent. For this search, the level of agreement between the SM background estimate and the two-photon search sample in a low- E_T control region is the same regardless of whether the E_T is corrected or not, so for simplicity the Type-I E_T corrections are not used (see Sec. 7.4).

Figure 6.12 shows the σ of a Gaussian fit to the x- and y-components of calibrated E_T vs. the calibrated PF E_T sum in a sample of events containing at least two jets with $p_T > 25$ GeV. Again, PF E_T outperforms E_T constructed of calorimeter towers or track-corrected calorimeter deposits.

2025 **6.2 HLT**

2026 From the objects described in Sec. 6.1, four samples of events are formed:

- 2027 • $\gamma\gamma$ candidate sample, in which the two highest E_T objects are photons,
- 2028 • $e\gamma$ control sample, in which the two highest E_T objects are one electron and
2029 one photon,
- 2030 • ee control sample, in which the two highest E_T objects are electrons, and
- 2031 • ff control sample, in which the two highest E_T objects are fakes.

2032 In all samples, the leading EM object is required to have offline reconstructed $E_T > 40$
2033 GeV, while the trailing EM object is required to have offline reconstructed $E_T > 25$
2034 GeV. The high level triggers used to select the four samples, by run range, are listed
2035 in Table 6.3. No trigger is prescaled.

2036 Each piece of the HLT path name is defined as follows.

- 2037 • **Photon**: Energy deposit in the ECAL that fired an L1 trigger (cf. Sec. 5.2.1).
For Photon26_IsoVL_Photon18, the L1 seed E_T threshold is 12 GeV, while for
2038 2039 all other triggers in Table 6.3 it is 20 GeV (cf. Sec. 5.2.1).
- 2040 • Integer following the word **Photon**: E_T threshold in GeV for offline reconstructed
2041 photon, using the full photon reconstruction of Sec. 6.1.1 minus the laser cali-
2042 brations and assuming the primary vertex at (0, 0, 0).
- 2043 • **CaloIdL**: For EB photons, $H/E < 0.15$ and $\sigma_{i\eta i\eta} < 0.014$.
- 2044 • **IsoVL**: $I_{\text{ECAL}} < 0.012E_T + 6$ GeV, $I_{\text{HCAL}} < 0.005E_T + 4$ GeV, and $I_{\text{track}} <$
2045 $0.002E_T + 4$ GeV.
- 2046 • **R9Id**: $R9 > 0.8$.

Table 6.3: HLT paths triggered by the $\gamma\gamma$, $e\gamma$, ee , and ff samples, by run range. No triggers are prescaled.

Run range	$\gamma\gamma$	$e\gamma$	ee	ff
160404-163261	Photon26_ IsoVL_ Photon18	Photon26_ IsoVL_ Photon18	Photon26_ IsoVL_ Photon18	Photon26_ IsoVL_ Photon18
161216-166967	Photon36_ CaloIdL_ Photon22_ CaloIdL	Photon36_ CaloIdL_ Photon22_ CaloIdL	Photon36_ CaloIdL_ Photon22_ CaloIdL	Photon36_ CaloIdL_ Photon22_ CaloIdL
166347-180252	Photon36_ CaloIdL_ IsoVL_ Photon22_ CaloIdL_ IsoVL	Photon36_ CaloIdL_ IsoVL_ Photon22_ CaloIdL_ IsoVL	Photon36_ CaloIdL_ IsoVL_ Photon22_ CaloIdL_ IsoVL	Photon36_ CaloIdL_ IsoVL_ Photon22_ CaloIdL_ IsoVL Photon36_ CaloIdL_ IsoVL_ Photon22_ R9Id Photon36_ R9Id_ Photon22_ CaloIdL_ IsoVL Photon36_ R9Id_ Photon22_ R9Id

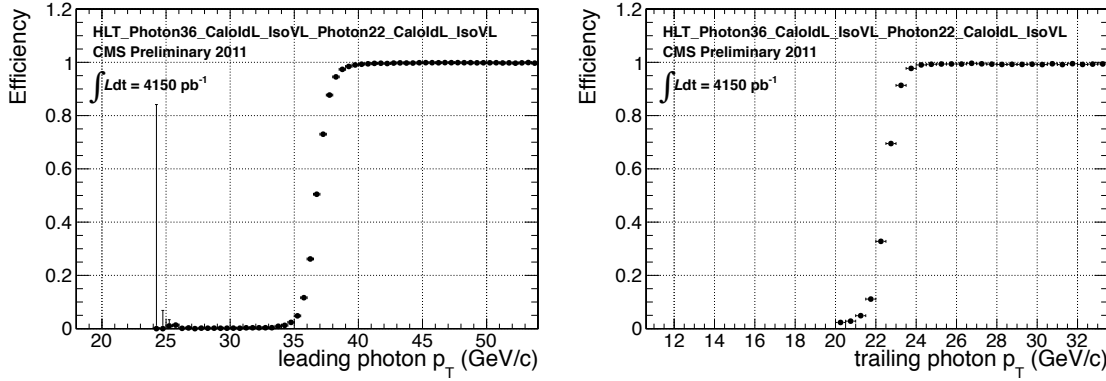


Figure 6.13: Efficiency of `HLT_Photon36_CaloIdL_IsoVL_Photon22_CaloIdL_IsoVL` for offline selected leading photon (left) and trailing photon (right) vs. photon p_T . Reprinted from Fig. 2 of ref. [115].

2047 In addition, the versions of `HLT_Photon26_IsoVL_Photon18` and
 2048 `Photon36_CaloIdL_Photon22_CaloIdL` that were active during runs 160404-163268
 2049 included a cut $E_{\max}/E_{5\times 5} < 0.98$ for spike rejection. E_{\max} is the energy in the highest
 2050 energy crystal of the EM cluster and $E_{5\times 5}$ is the energy in the 5×5 crystal matrix
 2051 around the seed crystal. For runs after 163268, Swiss cross spike rejection of individual
 2052 crystals from HLT quantities was performed (cf. Sec. 6.1.1). All information about the
 2053 evolution of the CMS HLT settings can be found in the HLT configuration browser
 2054 at <http://j2eeps.cern.ch/cms-project-confdb-hltdev/browser/>.

2055 As an example of the naming convention just described, the HLT path
 2056 `Photon36_CaloIdL_IsoVL_Photon22_R9Id` is fired if one photon is found with $E_T >$
 2057 36 GeV passing the CaloIdL and IsoVL requirements, and another is found with
 2058 $E_T > 22$ GeV passing the R9Id requirement.

2059 For the offline E_T cuts described in this section, the triggers are $> 99\%$ efficient,
 2060 as shown in Figure 6.13 [115]. The efficiencies are measured with respect to triggers
 2061 with lower E_T thresholds.

2062 6.3 Event Quality

2063 To suppress instrumental backgrounds, a set of event quality cuts are applied to the
 2064 $\gamma\gamma$, $e\gamma$, ee , and ff samples. First, all events are required to pass a good run selection,
 2065 as determined by the CMS Physics Validation Team [129]. The good run selection
 2066 excludes luminosity sections during which a sufficient part of the CMS detector was
 2067 unpowered or malfunctioning. Such conditions could occur if, for example, a high
 2068 voltage supply trips off in the middle of a run, or a DAQ error corrupts data quality
 2069 but is not spotted until after the data have been collected. The severity of a detec-
 2070 tor problem is judged by its effect on a wide range of analyses and reconstruction
 2071 algorithms. Of the $\sim 5 \text{ fb}^{-1}$ of integrated luminosity delivered by the LHC in 2011,
 2072 4.68 fb^{-1} passed the good run selection. This analysis is performed on the entire 2011
 2073 certified dataset.

2074 Second, all events must contain at least one good interaction vertex. The criteria
 2075 for a good vertex are:

- 2076 • $\chi^2 \neq 0$ OR $\text{ndof} \neq 0$ OR $N_{\text{tracks}} \neq 0$, where χ^2 and ndof are calculated for the
 2077 track fit to the vertex, and N_{tracks} is the number of tracks in the vertex fit
- 2078 • $\text{ndof} > 4$
- 2079 • $|z| < 24 \text{ cm}$, where z is the z -coordinate of the vertex position
- 2080 • $|\rho| < 2 \text{ cm}$, where ρ is the transverse displacement of the vertex position from
 2081 the beam line

2082 The good vertex requirement eliminates non-collision backgrounds such as beam
 2083 scraping, beam halo, cosmic muon interactions, and instrumental effects.

2084 Third, the two electromagnetic objects in the $\gamma\gamma$, $e\gamma$, ee , and ff events must
 2085 be separated in ϕ by at least 0.05. This requirement protects against beam halo
 2086 bremsstrahlung, in which a halo muon traveling parallel to the beam line radiates an

2087 energetic photon while itself depositing a large amount of energy in the ECAL. In
 2088 this case, the two ECAL hits would likely be at the same ϕ (and ρ).

2089 Fourth, the two EM objects must be separated in R by at least 0.6. Since the
 2090 isolation cone size used is 0.3, this ensures that the isolation energy of one EM object
 2091 cannot be in the veto strip (Fig. 6.6) of the other.

2092 Finally, the $\gamma\gamma$, $e\gamma$, ee , and ff events must pass an HCAL noise filter and ECAL
 2093 dead channel filter. The HCAL noise filter guarantees that all HCAL reconstructed
 2094 hits are inconsistent with any noise source. Noise sources [89] include:

- 2095 • Ion feedback in the HPDs absent any true incident photons, in which a thermal
 2096 electron ionizes a molecule in the HPD acceleration gap, faking a real signal
- 2097 • HPD discharge affecting nearly all channels in the same HPD [130], partially
 2098 explained by the effect of the 4 T CMS magnetic field on the flashover voltage
 2099 of the dielectric [131]
- 2100 • Concurrent signals in nearly all 72 channels of a single RBX, as yet unexplained
- 2101 • HF PMT window hits (as opposed to the usual quartz fiber hits)
- 2102 • ADC saturation

2103 Since HCAL noise may induce fake jets or E_T , events are rejected if any of the
 2104 following criteria are true:

- 2105 • Any HPD has > 17 hits
- 2106 • A single HPD has > 10 hits, but every other HPD has zero hits
- 2107 • An RBX has > 10 zero-ADC-count hits
- 2108 • Any HB/HE reconstructed hit corresponding to an RBX with > 50 GeV of
 2109 energy fails a two-dimensional cut defined by the variables $(TS4 - TS5)/(TS4 +$

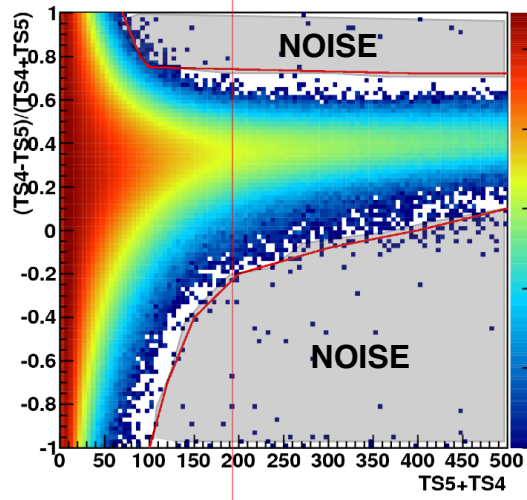


Figure 6.14: $(TS4 - TS5)/(TS4 + TS5)$ vs. $TS4 + TS5$ for a minimum bias sample. HB/HE hits are considered noisy if they lie in the sparsely populated gray region labeled "NOISE" defined by the curved red lines. Adapted from ref. [132].

2110 $TS5)$ vs. $TS4 + TS5$, where $TS4(TS5)$ is the hit amplitude in the fourth(fifth)
2111 time sample read out for that hit. The cut is defined in Fig. 6.14.

2112 The ECAL dead channel filter is designed to flag events in which significant EM
2113 energy was deposited in a masked region of the ECAL by using the trigger primitive
2114 information for the corresponding trigger tower. Energy deposited in a masked region
2115 of ECAL can cause fake \cancel{E}_T . Events are rejected if the trigger primitive E_T exceeds
2116 the maximum value of 63.75 GeV in any trigger tower that is masked in the readout.

2117 6.4 Photon Identification Efficiency

2118 In order to determine the cross section (or cross section upper limit) for a GGM
2119 signal, the photon identification efficiency is needed. Since no suitably large sample
2120 of $Z \rightarrow \mu\mu\gamma$ events in CMS exists yet, the efficiency calculation relies on the similarity
2121 between detector response to electrons and photons. A scale factor to correct the MC
2122 photon ID efficiency to the real photon efficiency for the data is obtained from the
2123 ratio of the electron efficiency from the data to the electron efficiency from MC.

2124 The different types of photon ID variables—calorimeter and track isolation, ratio of
 2125 hadronic to electromagnetic energy of the shower, and transverse shower shape—are
 2126 chosen so that their distributions for isolated electrons and photons are similar.³

2127 The photon selection efficiency is

$$\epsilon_\gamma = \epsilon_\gamma^{\text{MC}} \times \frac{\epsilon_e^{\text{data}}}{\epsilon_e^{\text{MC}}} \quad (6.6)$$

2128 where

- 2129 • ϵ_γ is the photon ID efficiency in data,
- 2130 • $\epsilon_\gamma^{\text{MC}}$ is the photon ID efficiency in MC,
- 2131 • ϵ_e^{data} is the electron ID efficiency obtained using $Z \rightarrow ee$ electrons in the data
 2132 that satisfy the photon ID cuts, and
- 2133 • ϵ_e^{data} is the electron ID efficiency obtained using $Z \rightarrow ee$ electrons in MC that
 2134 satisfy the photon ID cuts.

2135 The ratio $\epsilon_e^{\text{data}}/\epsilon_e^{\text{MC}}$ is defined as the scale factor by which the GGM signal MC
 2136 photon ID efficiency must be multiplied to give an estimate of the photon ID efficiency
 2137 in data. The photon ID requirements of Table 6.1 plus the IsoVL HLT requirement
 2138 described in Sec. 6.2 and Table 6.3 are repeated in Table 6.4.

2139 6.4.1 Tag and Probe Method

2140 A *tag and probe* method using Z events is utilized to measure the efficiency of the
 2141 photon ID cuts in Table 6.1. The tag is a well-identified electron. The probe, by
 2142 contrast, is as loosely identified as possible, and all tags must pass the probe criteria

³ $R9$ differs between photons and radiating electrons, but the requirement $R9 < 1$ is loose enough not to introduce problems with the use of electrons to measure the photon ID efficiency.

2143 in addition to the stringent tag criteria. The tag and probe criteria used in this study
2144 are shown in Table 6.5.

2145 The invariant mass of the tag and probe are required to be within a narrow window
2146 around Z mass. Assuming that the probabilities of the tag and probe legs of the Z
2147 decay to pass the photon ID cuts are uncorrelated, the efficiency can be estimated as

$$\epsilon = \frac{N_{\text{tag-pass}}}{N_{\text{tag-pass}} + N_{\text{tag-fail}}} \quad (6.7)$$

2148 where $N_{\text{tag-pass}}$ is the number of tag-probe pairs in which the probe leg passes the
2149 photon ID cuts under study and $N_{\text{tag-fail}}$ is the number of tag-probe pairs in which
2150 the probe leg fails the cuts. Implicit in these definitions is a double counting of pairs
2151 in which both electrons pass the tag and probe criteria [134]. In addition, in the rare
2152 circumstance (less than 1% in MC [134]) that two or more probes may be matched
2153 to one tag, the pair with invariant mass closest to the Z mass is chosen.

2154 In practice, $N_{\text{tag-pass}}$ and $N_{\text{tag-fail}}$ are returned by a simultaneous unbinned maxi-
2155 mum likelihood fit to the invariant mass distributions of tag-pass and tag-fail events,
2156 with appropriate signal and background PDF assumptions. The fit form used is

Table 6.4: Candidate photon ID requirements.

Variable	Cut
I_{ECAL}	$< 0.012E_T + 6 \text{ GeV}$
I_{HCAL}	$< 0.005E_T + 4 \text{ GeV}$
I_{track}	$< 0.002E_T + 4 \text{ GeV}$
H/E	< 0.05
$\sigma_{i\eta i\eta}$	< 0.011
$I_{\text{ECAL}} - 0.0792\rho + I_{\text{HCAL}} - 0.0252\rho + I_{\text{track}}$	$< 6 \text{ GeV}$
$R9$	< 1

Table 6.5: Tag and probe criteria. The superscript 0.4 indicates that the isolation variable was calculated in a cone of $\Delta R = 0.4$ around the photon candidate. The isolations without superscripts use the standard $\Delta R = 0.3$ cones.

Variable	Cut	
	Tag	Probe
RECO object	photon	photon
HLT	HLT_Ele17_CaloIdVT_CaloIsoVT_TrkIdT_TrkIsoVT_SC8_Mass30_v* (must have fired the 17 GeV leg)	—
H/E	< 0.05	< 0.15
$I_{\text{ECAL}}^{0.4}$	$< 0.006E_T + 4.2 \text{ GeV}$	—
$I_{\text{HCAL}}^{0.4}$	$< 0.0025E_T + 2.2 \text{ GeV}$	—
$I_{\text{track}}^{0.4}$	$< 0.001E_T + 2.0 \text{ GeV}$	—
E_T	$> 25 \text{ GeV}$	—
SC E_T	—	$> 15 \text{ GeV}$
SC $ \eta $	< 1.4442	< 1.4442
$\sigma_{i\eta i\eta}$	< 0.009	—
Has pixel seed	Yes	—
Track match type	General track ^a	—
Track match ΔR	< 0.04	—
Track match p_T	$> 15 \text{ GeV}$	—
Track match $ \eta $	< 1.479	—

^aA general track is reconstructed with the CMS standard combinatorial track finder [133].

$$\begin{aligned} f_{\text{tag-pass}}(m_{\text{tag-pass}}) &= \epsilon N_S f_S^{\text{pass}}(m_{\text{tag-pass}}) + N_B^{\text{pass}} f_B^{\text{pass}}(m_{\text{tag-pass}}) \\ f_{\text{tag-fail}}(m_{\text{tag-fail}}) &= (1 - \epsilon) N_S f_S^{\text{fail}}(m_{\text{tag-fail}}) + N_B^{\text{fail}} f_B^{\text{fail}}(m_{\text{tag-fail}}) \end{aligned} \quad (6.8)$$

where $f_{\text{tag-pass}}(m_{\text{tag-pass}})$ and $f_{\text{tag-fail}}(m_{\text{tag-fail}})$ are the tag-pass and tag-fail PDFs, respectively; ϵ is the efficiency; N_S is the total number of Z signal events summed over both samples; $f_S^{\text{pass}}(m_{\text{tag-pass}})$ and $f_S^{\text{fail}}(m_{\text{tag-fail}})$ are the tag-pass and tag-fail signal PDFs, respectively; N_B^{pass} and N_B^{fail} are the numbers of background events in the tag-pass and tag-fail samples, respectively; and $f_B^{\text{pass}}(m_{\text{tag-pass}})$ and $f_B^{\text{fail}}(m_{\text{tag-fail}})$ are the tag-pass and tag-fail background PDFs, respectively. This particular implementation of the tag and probe methodology is based on tag `CMSSW_4_2_5` of the CMSSW package `PhysicsTools/TagAndProbe`, and uses the MINUIT2 [135] library, as coded in RooFit [136], for the likelihood maximization. For this study, CMSSWv4.2.8 was used.

For both samples, the signal shape is assumed to be a Crystal Ball function [137] convoluted with the Z generated lineshape, while the background shape is a PDF that describes the falling background as well as the kinematic turn-on at low invariant mass. The background PDF, called `RooCMSShape` [134], is given by

$$f_{\text{RooCMSShape}}(x) = \begin{cases} 1e20 & \text{for } (x - \mu)\gamma < -70 \\ 0 & \text{for } (x - \mu)\gamma > 70 \\ \text{erfc}((\alpha - x)\beta) \exp(-(x - \mu)\gamma) & \text{otherwise} \end{cases} \quad (6.9)$$

where α , β , γ , and μ are parameters of the fit, most of which are held fixed. In the three lowest E_T bins, all parameters of the tag-pass and tag-fail background PDFs are left floating, because the effect of the relaxed E_T cuts has a significant effect on

the background shape. More details of the signal and background PDFs are given in Table 6.6. The fixed signal and background parameter values were determined by fitting a small sample ($0.0 \leq \eta < 0.25$) of Fall11 MC signal (DYJetsToLL) and background (QCD_Pt-20to30_BCtoE, QCD_Pt-30to80_BCtoE, QCD_Pt-80to170_BCtoE, GJet_Pt-20_doubleEMEnriched, WJetsToLNu, TTJets) with parameters left floating.⁴

Table 6.6: Parameter values (parameter definitions are in the text) for the signal and background PDFs for the different samples. The background PDF applies to all efficiency bins except the four lowest E_T bins, which use a floating `RooCMSShape` background. When a bracketed range is given, the parameter is allowed to float within that range. When a constant is given, the parameter is fixed to that constant.

PDF	Crystal Ball fit parameters				RooCMSShape fit parameters			
	μ	σ	α	n	μ	α	β	γ
Tag-pass signal	[-1.0, 1.0]	[1.0, 3.0]	0.87	97.0	N/A	N/A	N/A	N/A
Tag-fail signal	[-1.0, 1.0]	[1.0, 3.0]	0.73	134.9	N/A	N/A	N/A	N/A
Tag-pass background	N/A	N/A	N/A	N/A	65.0	61.949	0.04750	0.01908
Tag-fail background	N/A	N/A	N/A	N/A	α	[50.0, 100.0]	0.065	0.048

Some fit examples are shown in Figures 6.15 and 6.16. In Fig. 6.15, which shows fits to data and MC for $15 \text{ GeV} \leq \text{probe } E_T < 20 \text{ GeV}$, the kinematic turn-on is below the invariant mass range covered by the plot. The exponentially falling background is easily seen underneath the signal, and is especially pronounced in the background-dominated tag-fail sample.

⁴See Appendix A for a discussion of the MC samples.

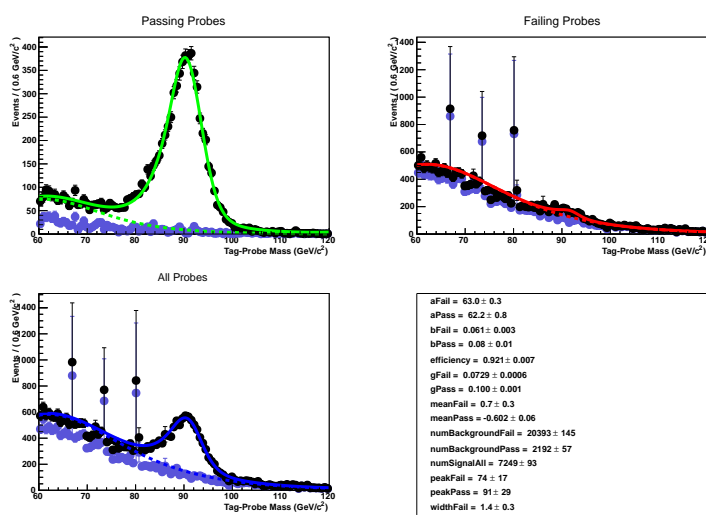
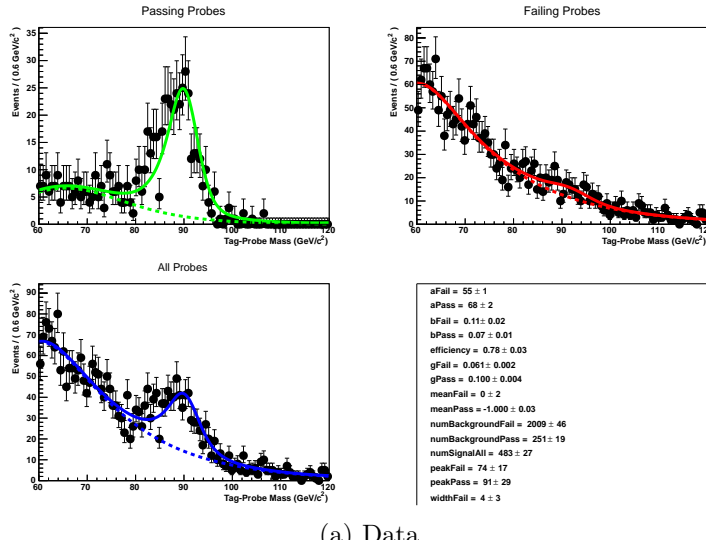


Figure 6.15: Tag and probe invariant mass fits for $15 \text{ GeV} \leq \text{probe } E_T < 20 \text{ GeV}$. Errors are statistical only. The tag-pass fit is shown in green in the upper-left-hand plot, the tag-fail fit in red in the upper-right-hand plot, and a fit to both samples in blue in the lower-left-hand plot. Dotted lines are the background components of the fits; solid lines are signal plus background.

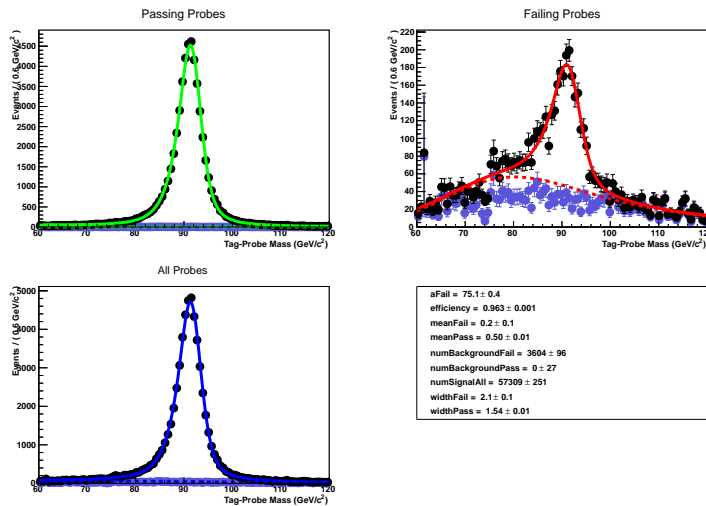
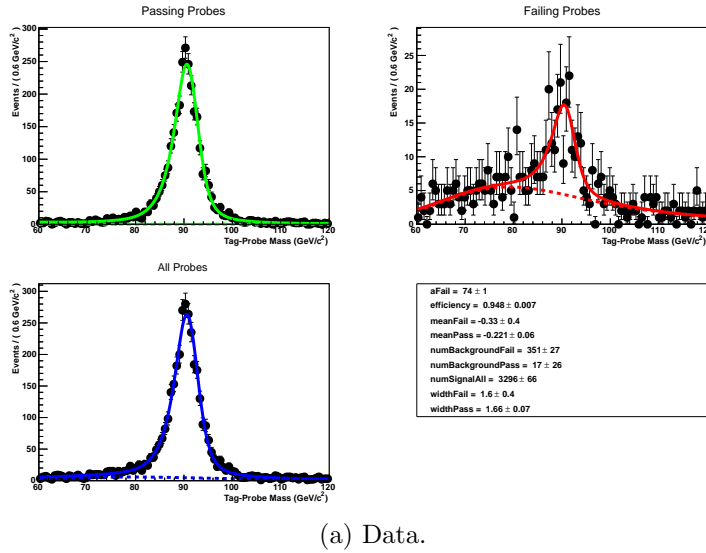


Figure 6.16: Tag and probe invariant mass fits for $-0.25 \leq \text{probe } \eta < -0.5$. Errors are statistical only. The tag-pass fit is shown in green in the upper-left-hand plot, the tag-fail fit in red in the upper-right-hand plot, and a fit to both samples in blue in the lower-left-hand plot. Dotted lines are the background components of the fits; solid lines are signal plus background.

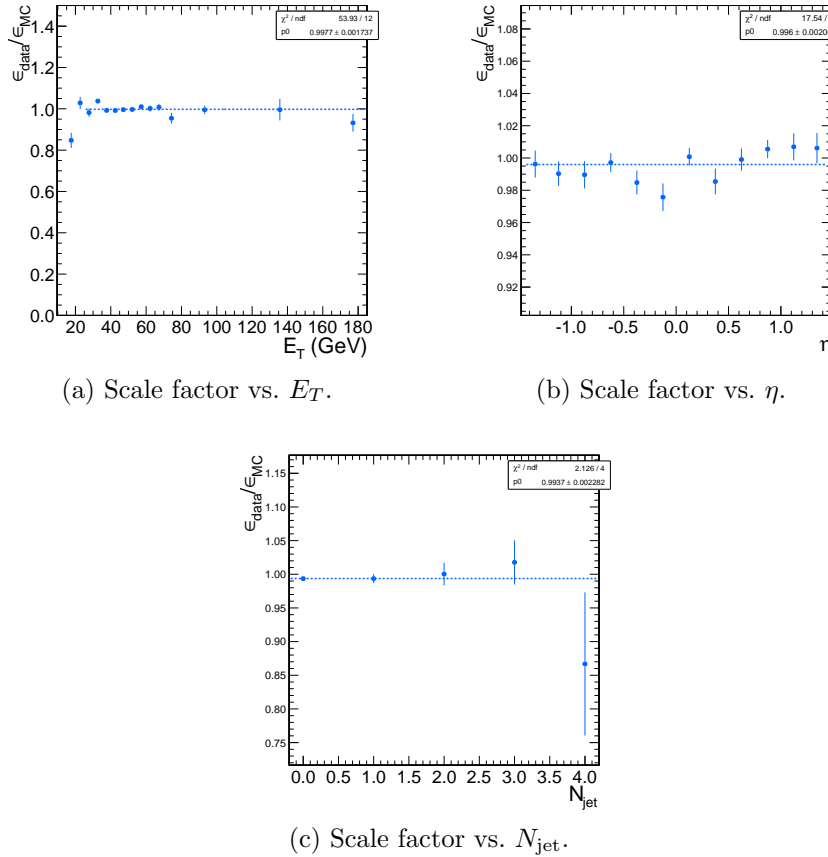


Figure 6.17: Dependence of the photon ID efficiency scale factor on some kinematic variables. Errors are statistical only.

2185 6.4.2 Photon Efficiency Scale Factor $\epsilon_e^{\text{data}} / \epsilon_e^{\text{MC}}$

2186 Figure 6.17 shows the dependence of the photon ID efficiency scale factor $\epsilon_e^{\text{data}} / \epsilon_e^{\text{MC}}$
2187 on E_T , η , and N_{jet} , where jets are defined as in Table 6.2, but with only the two
2188 Z electrons considered as candidates for overlap removal. Errors are statistical only.
2189 There no significant dependence of the scale factor on these variables, so only one
2190 scale factor is computed from the entire dataset.

2191 The effect of pileup is studied by comparing the efficiencies ϵ_e^{data} and ϵ_e^{MC} vs. the
2192 number of primary vertices (N_{PV}) in the event. The efficiency only drops a few percent
2193 for events with large N_{PV} after using pileup-corrected isolation cuts, as can be seen
2194 in Figure 6.18(a). The MC tracks the data, and the scale factor is flat vs. N_{PV} , as

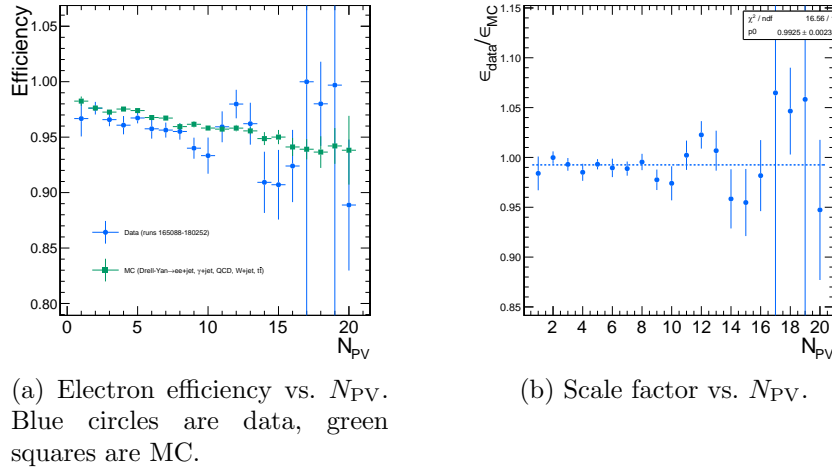


Figure 6.18: Dependence of the photon ID efficiency scale factor on the number of primary vertices per event. Errors are statistical only.

2195 shown in Fig. 6.18(b).

2196 The scale factor is measured to be $\epsilon_e^{\text{data}}/\epsilon_e^{\text{MC}} = 0.994 \pm 0.002(\text{stat.}) \pm 0.035(\text{syst.})$.

2197 Four main sources of systematic error, in addition to the statistical error of 0.2%, were
2198 studied.

2199 **Different behavior of electrons and photons in MC** Even though the photon
2200 ID cuts are designed to be similarly efficient for both electrons and photons,
2201 there might be a small difference in the performance between the two kinds
2202 of particles, e.g. because of electron bremsstrahlung. To check this effect, the
2203 MC electron ID efficiency was calculated using a $Z \rightarrow ee$ sample and the MC
2204 photon ID efficiency was calculated using a $\gamma + \text{jets}$ sample. Both samples were
2205 reconstructed in CMSSWv3.6. Half the difference between these two results,
2206 0.5%, was taken as an error on the scale factor.

2207 **Pileup** To account for the possibility that the MC simulation may not adequately
2208 reproduce the data in a high pileup environment, the data/MC scale factor
2209 for events with 1-4 good reconstructed primary vertices was calculated, along
2210 with the same for events with ≥ 5 good reconstructed primary vertices. The

2211 difference between the scale factors from both samples, 2.4%, was taken as an
 2212 error on the scale factor from pileup.

2213 **Signal fit over/underestimation** It was found that the signal fit slightly under-
 2214 estimates the data in the tag-pass sample, and slightly overestimates it in the
 2215 tag-fail sample. To cover this effect with a systematic error, the efficiencies in
 2216 data and MC, and then the scale factor, were recalculated using the background
 2217 (from fit) subtracted integrals of the tag-pass and tag-fail distributions, rather
 2218 than the fitted signal yields in those distributions. The difference between the
 2219 scale factor found in this way and the nominal scale factor, 1.9%, was taken as
 2220 an error on the scale factor.

2221 **Signal and background shape assumption** To assess the magnitude of the error
 2222 from the signal and background shape assumptions, the tag-pass and tag-fail
 2223 tail parameters (Crystal Ball α and n) were varied by $\pm 1\sigma$, and the background
 2224 shape was varied between `RooCMSShape`, exponential, power law, and quadratic.
 2225 All possible combinations of varied parameters were generated, and the data and
 2226 MC were refit and new scale factors generated according to those combinations.
 2227 The error was taken as the largest deviation of the scale factor from nominal,
 2228 1.8%.

2229 Finally, the pixel veto efficiency was estimated from MC to be 0.96 ± 0.005 (syst.),
 2230 with error due to varying assumptions of the tracker material distribution [138]. In
 2231 general, the photon ID selection used in this analysis is very efficient for GGM photons
 2232 and robust to pileup, and its efficiency is fairly well measured.

²²³³ Chapter 7

²²³⁴ Data Analysis

²²³⁵ The signature of GGM SUSY particle production in this search is an excess of two-
²²³⁶ photon events with high E_T above the Standard Model background. E_T is recon-
²²³⁷ structed using the particle flow algorithm as described in Sec. 6.1.3. Candidate two-
²²³⁸ photon events, as well as control events, are selected according to the offline object
²²³⁹ criteria presented in Secs. 6.1.1, 6.1.2, and 6.1.3; the event quality criteria in Sec. 6.3;
²²⁴⁰ and the trigger requirements in Sec. 6.2. These are summarized in Table 7.1.

Table 7.1: Selection criteria for $\gamma\gamma$, $e\gamma$, ee , and ff events.

Variable	Cut			
	$\gamma\gamma$	$e\gamma$	ee	ff
HLT match	IsoVL	IsoVL	IsoVL	IsoVL R9Id
E_T	$> 40/\text{GeV}$ $> 25 \text{ GeV}$			
SC $ \eta $	< 1.4442	< 1.4442	< 1.4442	< 1.4442
H/E	< 0.05	< 0.05	< 0.05	< 0.05
$R9$	< 1	< 1	< 1	< 1
Pixel seed	No/No	Yes/No	Yes/Yes	No/No
I_{comb} , $\sigma_{i\eta i\eta}$	$< 6 \text{ GeV} \&\&$ < 0.011	$< 6 \text{ GeV} \&\&$ < 0.011	$< 6 \text{ GeV} \&\&$ < 0.011	$< 20 \text{ GeV} \&\&$ $(\geq 6 \text{ GeV} \parallel$ $\geq 0.011)$
JSON	Yes	Yes	Yes	Yes
No. good PVs	≥ 1	≥ 1	≥ 1	≥ 1
ΔR_{EM}	> 0.6	> 0.6	> 0.6	> 0.6
$\Delta\phi_{\text{EM}}$	≥ 0.05	≥ 0.05	≥ 0.05	≥ 0.05

2241 This search utilizes 4.7 fb^{-1} of CMS data collected during the period April-
2242 December 2011, corresponding to the following datasets [139]:

- 2243 • `/Photon/Run2011A-05Jul2011ReReco-ECAL-v1/AOD`
- 2244 • `/Photon/Run2011A-05Aug2011-v1/AOD`
- 2245 • `/Photon/Run2011A-03Oct2011-v1/AOD`
- 2246 • `/Photon/Run2011B-PromptReco-v1/AOD`

2247 The search strategy is to model the backgrounds to the GGM SUSY signal using
2248 \cancel{E}_T shape templates derived from the control samples, and then to look for a high- \cancel{E}_T
2249 excess above the estimated background in the $\gamma\gamma$ sample. There are two categories of
2250 backgrounds: QCD processes with no real \cancel{E}_T and electroweak processes with real \cancel{E}_T
2251 from neutrinos. The relevant QCD background processes are multijet production with
2252 at least two jets faking photons, photon + jet production with at least one jet faking
2253 a photon, and diphoton production. The relevant electroweak background processes,
2254 which are small compared to the QCD background, involve $W \rightarrow e\nu$ decay with a
2255 recoiling jet that fakes a photon or a real radiated photon (the W may come from
2256 the decay of a top quark in $t\bar{t}$ events). In both cases, the electron is misidentified
2257 as a photon due to a small inefficiency in reconstructing the electron pixel seed.
2258 The main diagrams contributing to the QCD(electroweak) backgrounds are shown in
2259 Figure 7.1(7.2).

2260 7.1 Control Samples

2261 Data control samples are used to model all of the backgrounds. The primary control
2262 sample used to model the QCD background is the ff sample, which is similar to the
2263 candidate $\gamma\gamma$ sample but with combined isolation or $\sigma_{inj\eta}$ cuts inverted. The cuts

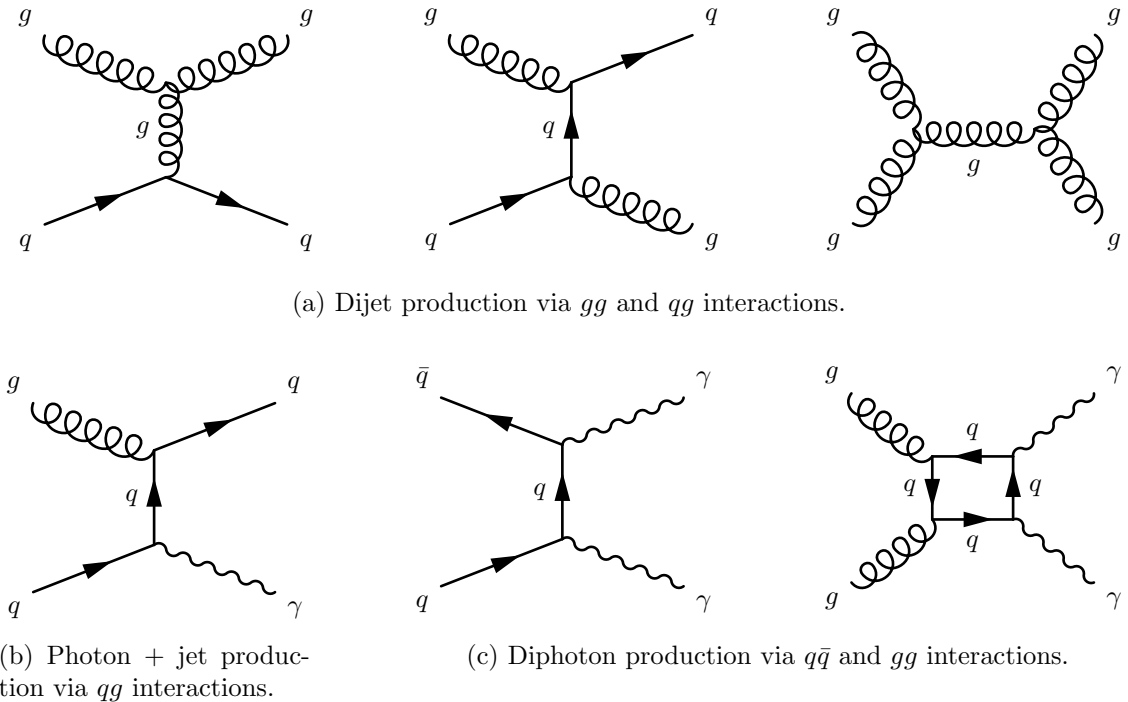


Figure 7.1: Representative Feynman diagrams of some QCD backgrounds to the GGM SUSY search.

2264 on these variables are used to distinguish between photons and jets, so by inverting
 2265 those cuts, the resulting ff sample becomes enriched with QCD dijets. Because the
 2266 fake photons are still required to pass a tight cut on H/E , they are guaranteed to be
 2267 very electromagnetic jets, with an EM energy scale and resolution similar to that of
 2268 the candidate photons. This insures that the resulting estimate of the \cancel{E}_T shape does
 2269 not have too long of a tail from severe HCAL mis-measurements that are actually
 2270 rare in the $\gamma\gamma$ sample.

2271 As a cross-check, the ee sample is also used to model the QCD background. This
 2272 sample of Z decays should have no true \cancel{E}_T , just like the ff sample, and the electron
 2273 definition (differing from the photon definition only in the presence of a pixel seed)
 2274 insures that the electron energy scale and resolution is similar to that of the photon.

2275 Finally, the $e\gamma$ sample is used to model the electroweak background from $W \rightarrow e\nu$
 2276 decays. The $e\gamma$ \cancel{E}_T distribution is scaled by the electron \rightarrow photon misidentification

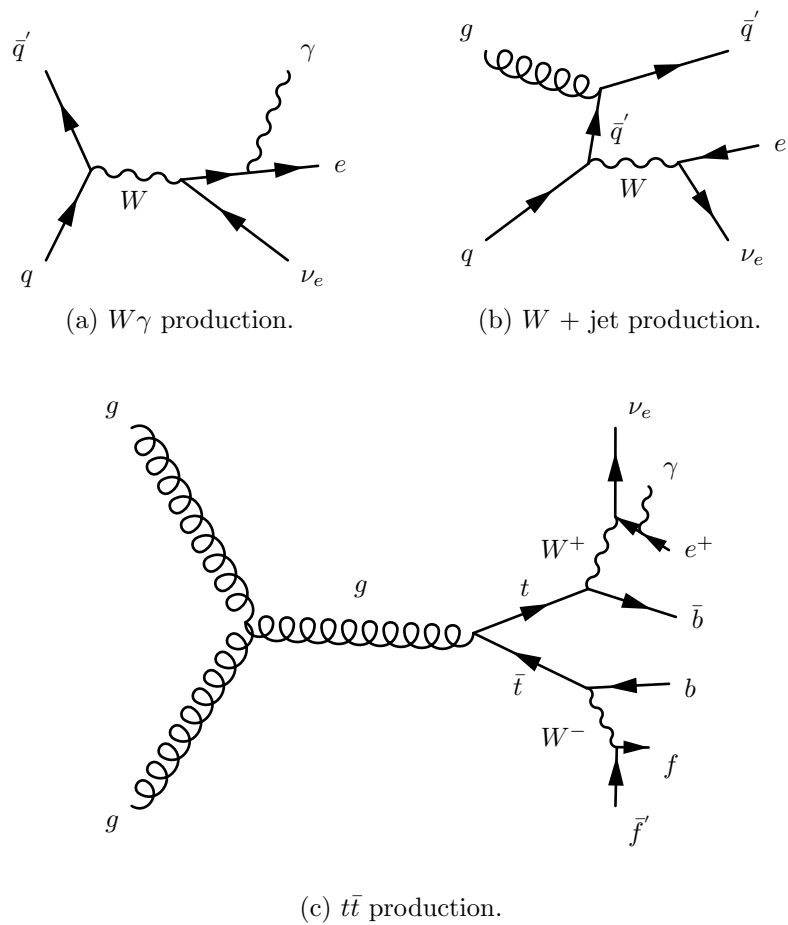


Figure 7.2: Representative Feynman diagrams of some electroweak backgrounds to the GGM SUSY search.

2277 rate to predict the number of $W\gamma$, $W + \text{jet}$, and $t\bar{t}$ events in the $\gamma\gamma$ sample.

2278 The remainder of this chapter describes the data analysis procedures and the final
 2279 results of the search. Sec. 7.2 addresses the QCD background estimation. Sec. 7.3
 2280 addresses the electroweak background estimation. The chapter concludes with a dis-
 2281 cussion of systematic errors in Sec. 7.4 and a presentation of the final results in
 2282 Sec. 7.5.

2283 7.2 Modeling the QCD Background

2284 7.2.1 Outline of the Procedure

2285 Due to the fact that the CMS ECAL energy resolution is much better than the
 2286 HCAL energy resolution, the energies of the two candidate photons in the events of
 2287 the $\gamma\gamma$ sample are typically measured to far greater accuracy and precision than the
 2288 energy of the hadronic recoil in those events. Therefore, fake \cancel{E}_T in the $\gamma\gamma$ sample
 2289 is almost entirely the result of hadronic mis-measurement in QCD dijet, photon +
 2290 jet, and diphoton events. The strategy employed to model this background is to find
 2291 a control sample in data consisting of two well-measured EM objects, just like the
 2292 candidate $\gamma\gamma$ sample, and assign each event a weight to account for the underlying
 2293 kinematic differences between the control and candidate samples. Once the reweighted
 2294 \cancel{E}_T spectrum of the control sample is created, it is then normalized in the low- \cancel{E}_T
 2295 region, the assumption being that GGM SUSY does not predict a significant amount
 2296 of events at low \cancel{E}_T . There are three aspects of this QCD background estimation
 2297 procedure that bear highlighting:

2298 **Choice of control sample** Since the underlying cause of \cancel{E}_T in the candidate sam-
 2299 ple is mis-measured hadronic activity, a control sample with similar hadronic
 2300 activity to the candidate sample should be chosen. Hadronic activity refers to
 2301 number of jets, jet E_T , pileup, etc.

2302 **Reweighting** The control sample is reweighted so that its \cancel{E}_T spectrum appears as it
 2303 would if the control sample had the same kinematic properties as the candidate
 2304 $\gamma\gamma$ sample (i.e. particle p_T and η distributions, etc.). By choosing an appropriate
 2305 control sample and reweighting it, the control \cancel{E}_T distribution should now match
 2306 both the hadronic activity and the kinematics of the candidate sample.

2307 **Normalization** Finally, the control E_T distribution is normalized in a region of
 2308 low \cancel{E}_T , where contamination from the expected GGM SUSY signal is small.
 2309 This implies an extrapolation of the low- \cancel{E}_T QCD background prediction to the
 2310 high- \cancel{E}_T signal region.

2311 As explained in the beginning of this chapter, the ff sample is used as the primary
 2312 QCD control sample, while the ee sample is used as a cross-check. Both samples have
 2313 two well-measured EM objects per event, no real \cancel{E}_T , and similar hadronic activity to
 2314 the $\gamma\gamma$ sample. Figures 7.3- 7.8 show a comparison of the shapes of some distributions
 2315 relevant to hadronic activity between the $\gamma\gamma$, ee , and ff samples. In general, the
 2316 ee sample has less hadronic activity than the $\gamma\gamma$ and ff samples, as shown by the
 2317 more steeply falling ee distributions in Figs. 7.3, 7.4, 7.5, and 7.6. In addition to the
 2318 kinematic reweighting, there is also a reweighting by number of jets per event, which
 2319 attempts to correct for this difference (see Sec. 7.2.2).

2320 7.2.2 Reweighting

2321 To reweight the control sample events to match the kinematics of the candidate sample
 2322 events, a weight based on the p_T of the di-EM-object system and the number of jets
 2323 in the event is used. As explained in Sec. 7.2.1, E_T in the $\gamma\gamma$, ff , and ee samples
 2324 is due to the poorly measured hadronic recoil off the well-measured di-EM system.
 2325 Therefore, the p_T of the di-EM system is a good handle on the true magnitude of
 2326 the hadronic recoil, which affects the measured \cancel{E}_T . The di-EM system is depicted

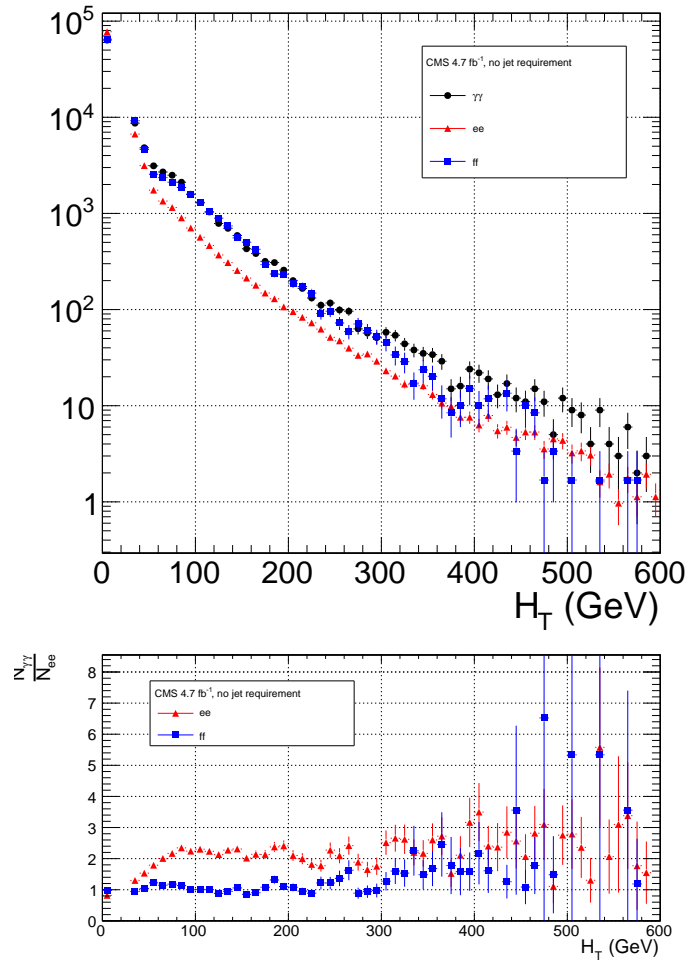


Figure 7.3: H_T , defined as the scalar sum of corrected jet E_T for jets defined as in Table 7.2. $\gamma\gamma$ is in black, ee ($81 \text{ GeV} \leq m_{ee} < 101 \text{ GeV}$) is in red, and ff is in blue. The ee and ff distributions are normalized to the number of events in the $\gamma\gamma$ distribution. Errors are statistical only.

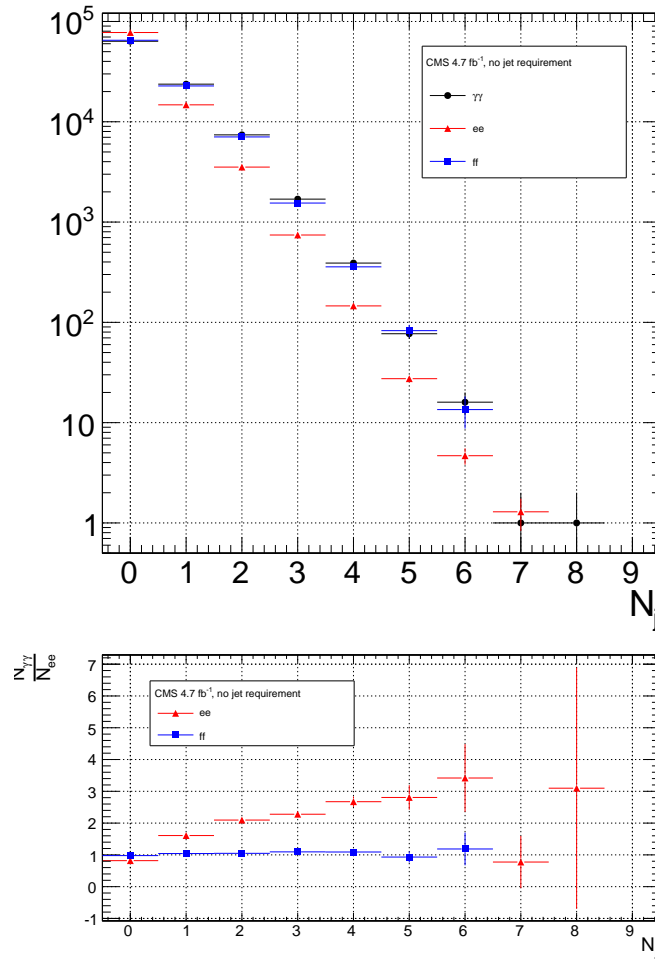


Figure 7.4: Number of jets per event for jets defined as in Table 7.2. $\gamma\gamma$ is in black, ee ($81 \text{ GeV} \leq m_{ee} < 101 \text{ GeV}$) is in red, and ff is in blue. The ee and ff distributions are normalized to the number of events in the $\gamma\gamma$ distribution. Errors are statistical only.

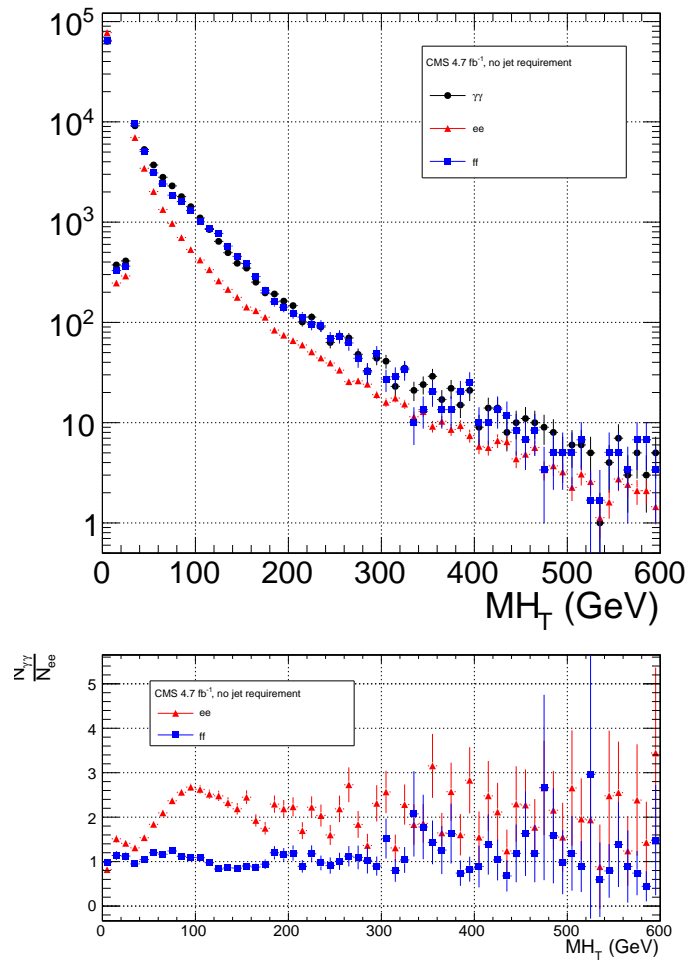


Figure 7.5: H_T , defined as the magnitude of the negative vectorial sum of corrected jet E_T for jets defined as in Table 7.2. $\gamma\gamma$ is in black, ee ($81 \text{ GeV} \leq m_{ee} < 101 \text{ GeV}$) is in red, and ff is in blue. The ee and ff distributions are normalized to the number of events in the $\gamma\gamma$ distribution. Errors are statistical only.

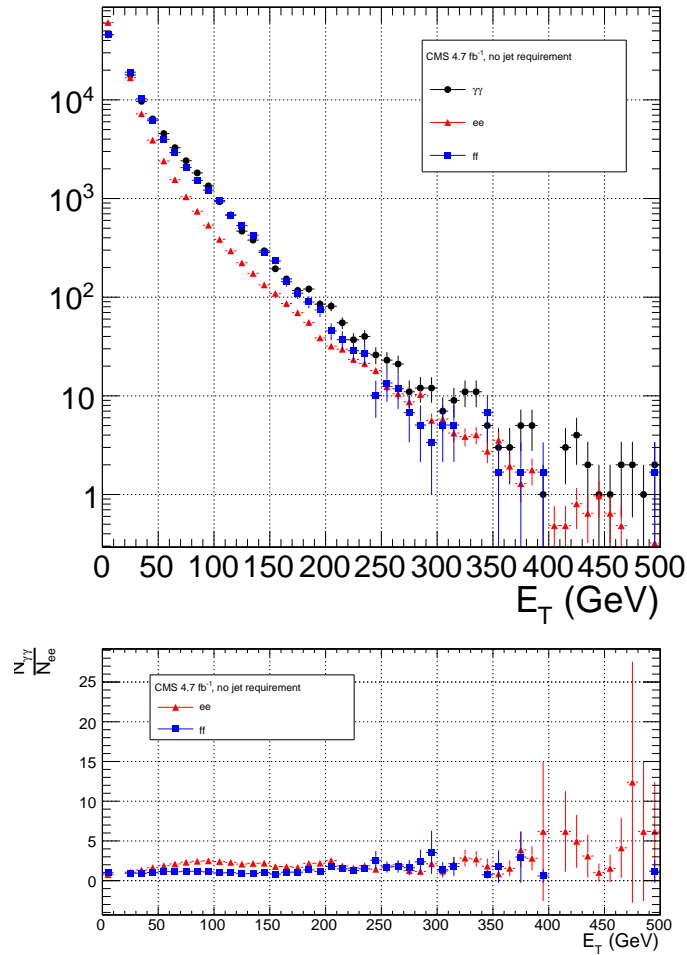


Figure 7.6: Corrected E_T for the jet with the largest corrected E_T per event, for jets defined as in Table 7.2 (excluding the p_T requirement). $\gamma\gamma$ is in black, ee ($81 \text{ GeV} \leq m_{ee} < 101 \text{ GeV}$) is in red, and ff is in blue. The ee and ff distributions are normalized to the number of events in the $\gamma\gamma$ distribution. Errors are statistical only.

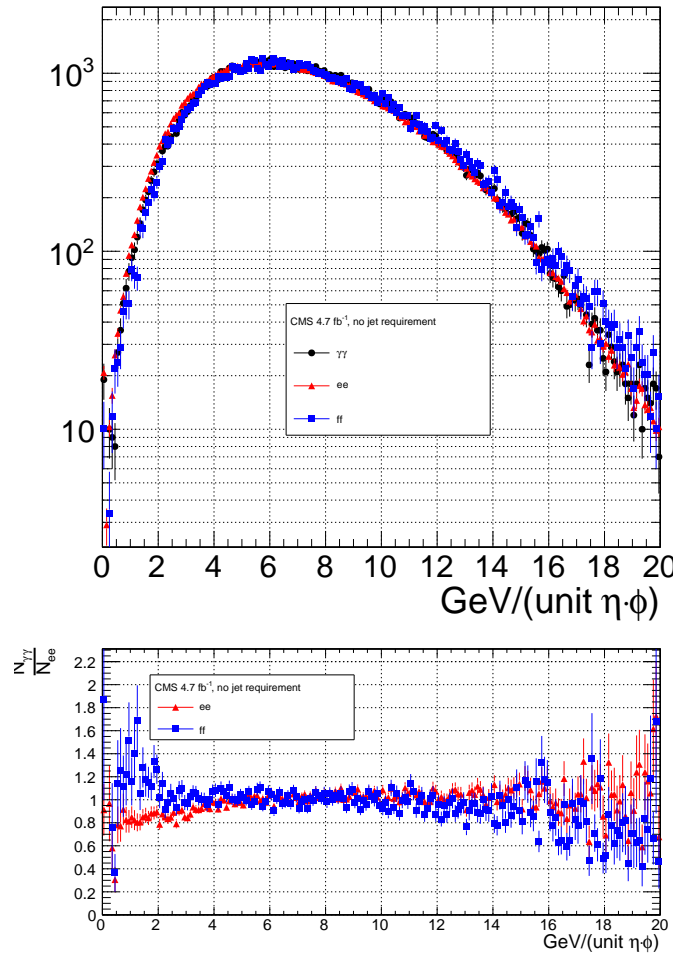


Figure 7.7: ρ (average pileup energy density in the calorimeters per unit $\eta \cdot \phi$, cf. Sec. 6.1.1). $\gamma\gamma$ is in black, ee ($81 \text{ GeV} \leq m_{ee} < 101 \text{ GeV}$) is in red, and ff is in blue. The ee and ff distributions are normalized to the number of events in the $\gamma\gamma$ distribution. Errors are statistical only.

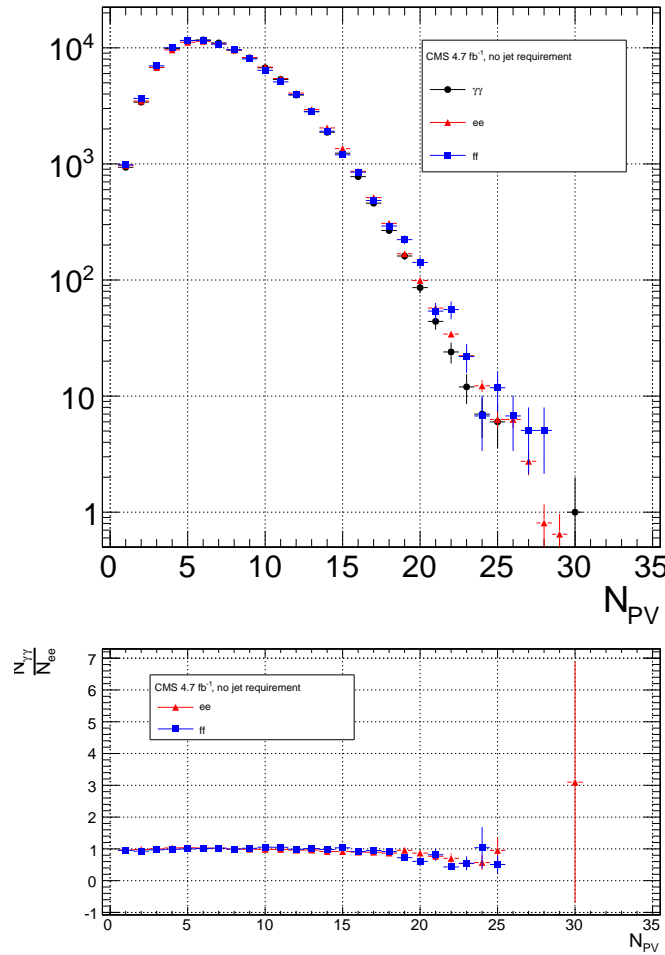


Figure 7.8: Number of good reconstructed primary vertices per event according to the criteria of Sec. 6.3. $\gamma\gamma$ is in black, ee ($81 \text{ GeV} \leq m_{ee} < 101 \text{ GeV}$) is in red, and ff is in blue. The ee and ff distributions are normalized to the number of events in the $\gamma\gamma$ distribution. Errors are statistical only.

Table 7.2: Definition of HB/HE/HF hadronic jets.

Variable	Cut
Algorithm	L1FastL2L3Residual corrected PF (cf. Sec. 6.1.3)
p_T	$> 30 \text{ GeV}$
$ \eta $	< 5.0
Neutral hadronic energy fraction	< 0.99
Neutral electromagnetic energy fraction	< 0.99
Number of constituents	> 1
Charged hadronic energy	$> 0.0 \text{ GeV}$ if $ \eta < 2.4$
Number of charged hadrons	> 0 if $ \eta < 2.4$
Charged electromagnetic energy fraction	< 0.99 if $ \eta < 2.4$
ΔR to nearest PF electron ^a , muon ^b , or one of the two primary EM objects	> 0.5

^aA PF electron is defined as an electron reconstructed with the PF algorithm [126] with $p_T > 15 \text{ GeV}$, $|\eta| < 2.6$, and $(I_{\text{charged}} + I_{\text{photon}} + I_{\text{neutral}})/p_T < 0.2$, where $I_{\text{charged}}(I_{\text{photon}})(I_{\text{neutral}})$ is the sum of PF charged hadron(PF photon)(PF neutral hadron) momenta in a $\Delta R = 0.4$ cone around the PF electron.

^bMuons are reconstructed [127] from a combination of muon station and inner tracker hits. Here, a muon must have track $\chi^2 < 10$, at least one good muon station hit, inner track transverse impact parameter $< 0.02 \text{ cm}$, inner track longitudinal impact parameter $< 0.5 \text{ cm}$, $p_T > 15 \text{ GeV}$, $|\eta| < 2.6$, and $(I_{\text{ECAL}} + I_{\text{HCAL}} + I_{\text{track}})/p_T < 0.2$, where $I_{\text{ECAL}}(I_{\text{HCAL}})(I_{\text{track}})$ is the sum of ECAL(HCAL)(track) momenta in a $\Delta R = 0.3$ cone around the muon.

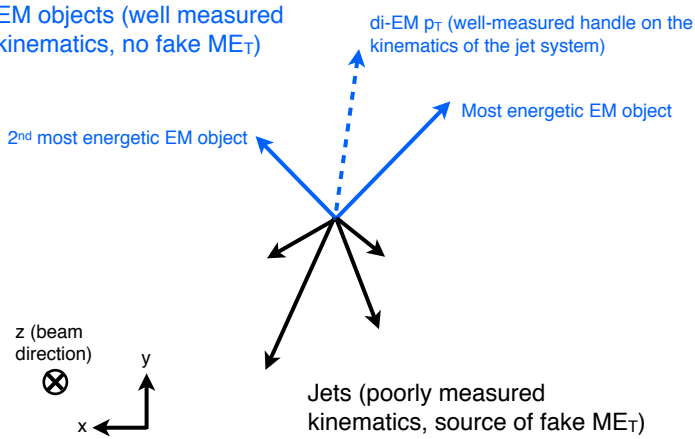
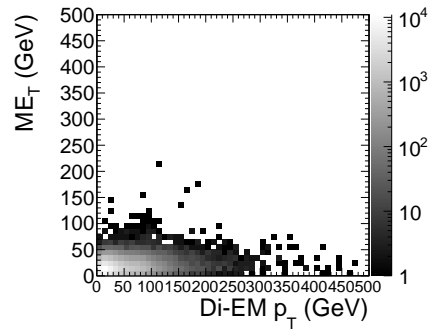
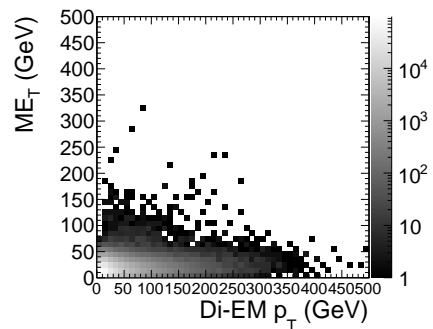
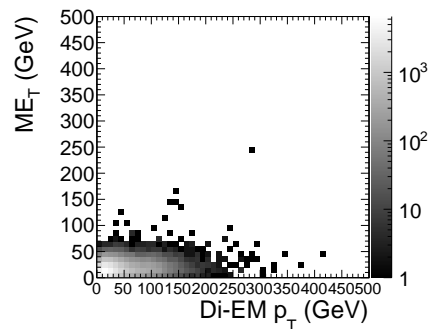


Figure 7.9: Cartoon showing the di-EM system in blue and the hadronic recoil in black. The di-EM p_T (dashed blue line) is used to reweight the control sample kinematic properties to match those of the candidate $\gamma\gamma$ sample.

in Figure 7.9. As shown in Figure 7.10, E_T is largely uncorrelated with di-EM p_T , so there is little danger of reweighting away a true signal excess.

Whereas the di-EM p_T reweighting accounts for differences in production kinematics between the control and $\gamma\gamma$ samples, a simultaneous reweighting based on the number of jets in the event accounts for differences in hadronic activity between the samples, especially between ee and $\gamma\gamma$ (cf. Figs. 7.3- 7.8). Jets are defined as in Table 6.2. Figure 7.11 shows the effect of reweighting by number of jets per event, which is to increase(decrease) the tail of the ee (ff) E_T spectrum.

Although the electron and photon energies are well measured by the ECAL, the ECAL-only measurement of the fake photon energy (cf. Sec 6.1.1) is biased slightly low due to the fact that fakes (which are really jets) tend to deposit some energy in the HCAL. This can be seen in Figs. 7.12 and 7.13, which show the relative difference between the ECAL-only E_T measurement and the PF E_T measurement vs. EMF for electrons, photons, and fakes. PF E_T is defined as the L1Fast-corrected E_T of the nearest PF jet with $p_T \geq 20$ GeV (i.e., the E_T of the PF jet object reconstructed from the same ECAL shower as the fake photon). On average, the high-EMF fakes, which

(a) $\gamma\gamma$.(b) ee .(c) ff .Figure 7.10: E_T vs. di-EM p_T .

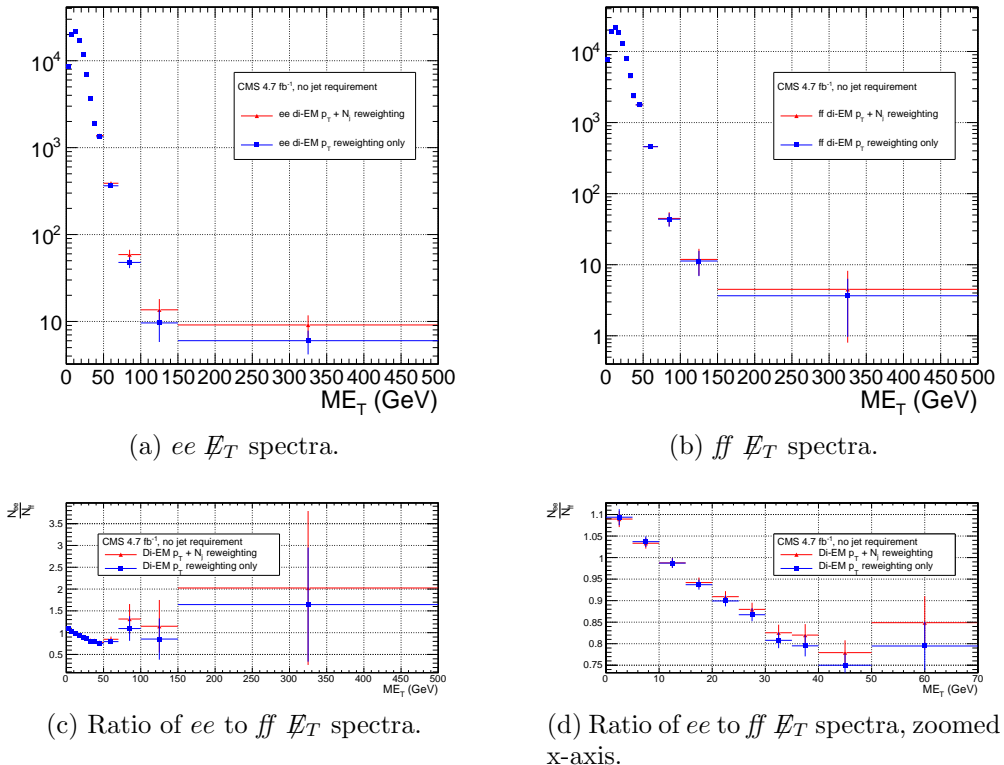


Figure 7.11: \cancel{E}_T spectra of the reweighted ee ($81 \text{ GeV} \leq m_{\text{ee}} < 101 \text{ GeV}$) and ff control samples. Blue squares indicate di-EM p_T reweighting only; red triangles indicate di-EM $p_T + \text{number of jets}$ reweighting. PF p_T (cf. p. 143) is used to calculate the di-EM p_T . The full normalization procedure is employed, along with ee sideband subtraction (discussed at the end of this section). Error bars are statistical only.

make up the bulk of the sample, tend to deposit a few percent more energy in the HCAL than the electrons or photons. This energy is recovered by the PF algorithm. For this reason, the PF p_T is used in the calculation of di-EM p_T rather than the ECAL-only p_T .¹ This leads to a modest improvement in the agreement between the ee and ff \cancel{E}_T spectra, as shown in Figure 7.14.

The control sample event weights are defined as

$$w_{ij} = \frac{N_{\text{control}}}{N_{\gamma\gamma}} \frac{N_{\gamma\gamma}^{ij}}{N_{\text{control}}^{ij}} \quad (7.1)$$

where i runs over the number of di-EM p_T bins, j runs over the number of jet bins, N_{control} is the total number of events in the control sample, $N_{\gamma\gamma}$ is the total number of events in the $\gamma\gamma$ sample, $N_{\gamma\gamma}^{ij}$ is the number of $\gamma\gamma$ events in the i^{th} di-EM p_T bin and j^{th} jet bin, and N_{control}^{ij} is the number of control sample events in the i^{th} di-EM p_T bin and j^{th} jet bin. The effect of the reweighting is more significant for the ee sample than for the ff sample, as shown in Figure 7.15.

The ee sample contains a non-negligible background of $t\bar{t}$ events in which both W bosons decay to electrons. These events have significant real \cancel{E}_T from the two neutrinos (unlike the $\gamma\gamma$ events), and therefore inflate the background estimate at high \cancel{E}_T . In order to remove the $t\bar{t}$ contribution from the ee sample, a sideband subtraction method is employed.

Only events in the ee sample with $81 \text{ GeV} \leq m_{ee} < 101 \text{ GeV}$, where m_{ee} is the di-electron invariant mass, are used in the QCD background estimate. This choice maximizes the ratio of Z signal to background. The sidebands used to estimate the background contribution within the Z window are defined such that $71 \text{ GeV} \leq m_{ee} < 81 \text{ GeV}$ and $101 \text{ GeV} \leq m_{ee} < 111 \text{ GeV}$.

¹In the few events ($\mathcal{O}(10^{-3})$) in which two PF jet objects, corresponding to the two electrons or fakes, are not found, the ECAL-only p_T is used.

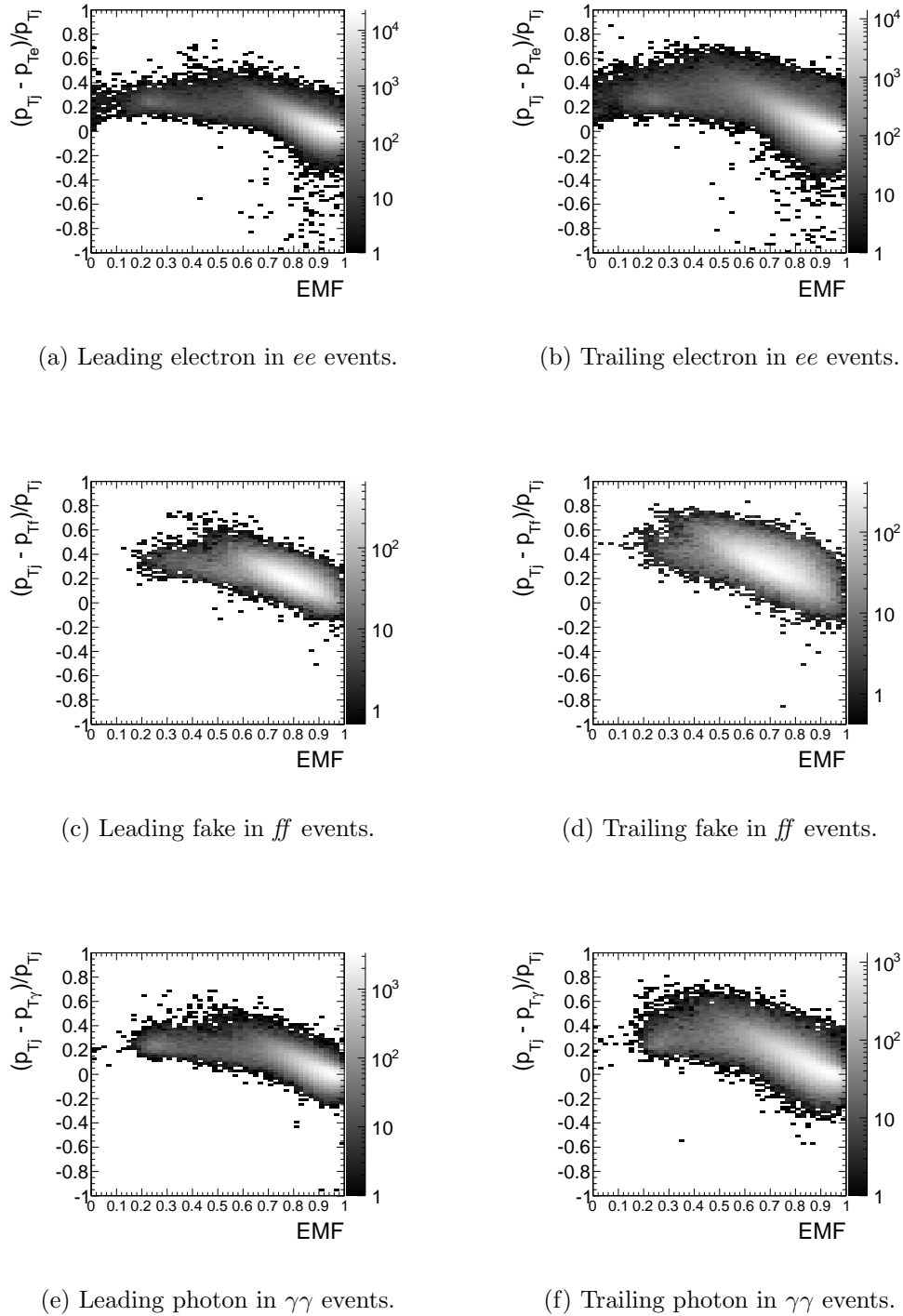


Figure 7.12: Relative difference between the ECAL-only E_T measurement and the PF E_T measurement vs. EMF. PF E_T is defined in the text.

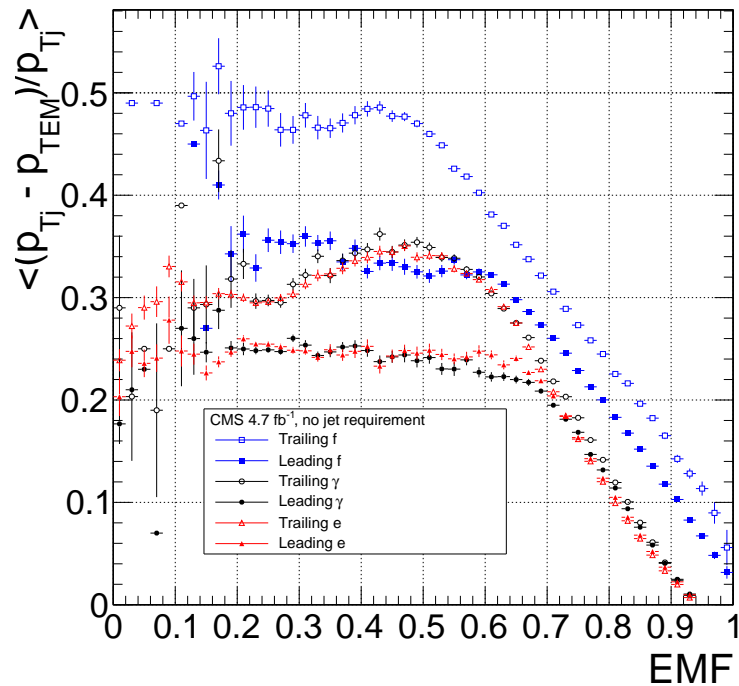


Figure 7.13: Average relative difference between the ECAL-only E_T measurement and the PF E_T measurement vs. EMF for the leading (filled marker) and trailing (open marker) electrons in ee events (red triangles), fakes in ff events (blue squares), and photons in $\gamma\gamma$ events (black circles). These are nothing more than profile histograms of Fig. 7.12. PF E_T is defined in the text. Error bars are statistical only.

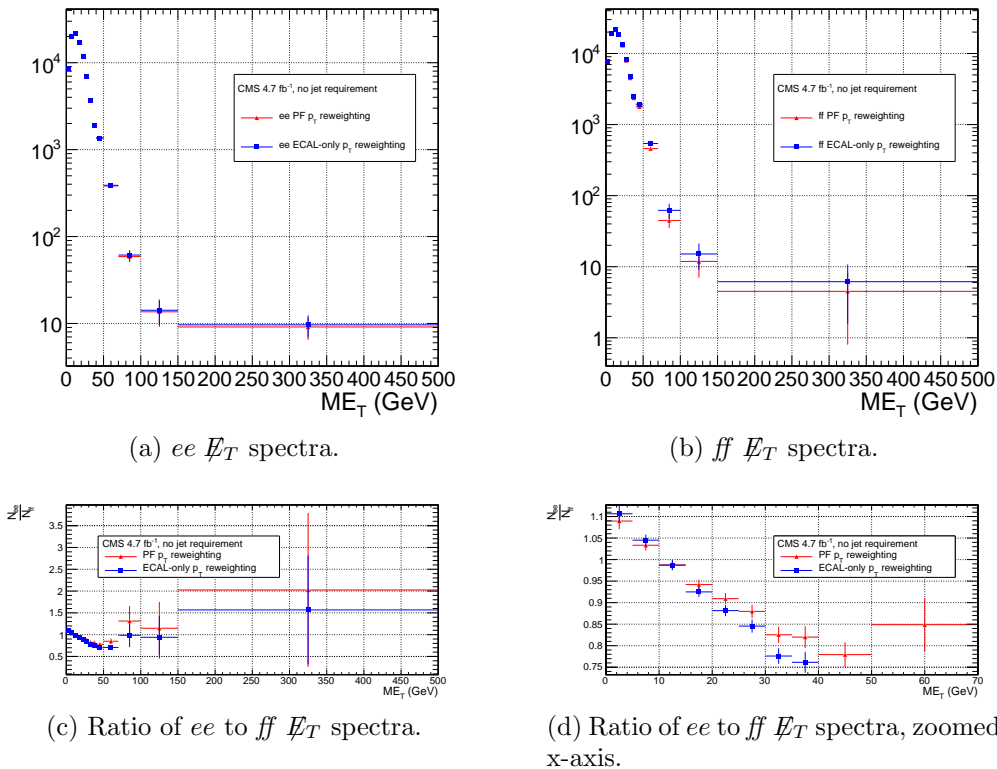


Figure 7.14: \cancel{E}_T spectra of the reweighted ee ($81 \text{ GeV} \leq m_{ee} < 101 \text{ GeV}$) and ff control samples. Blue squares indicate reweighting using the ECAL-only p_T estimate; red triangles indicate reweighting using the PF p_T estimate. The full reweighting and normalization procedure is employed, along with ee sideband subtraction (discussed at the end of this section). Error bars are statistical only.

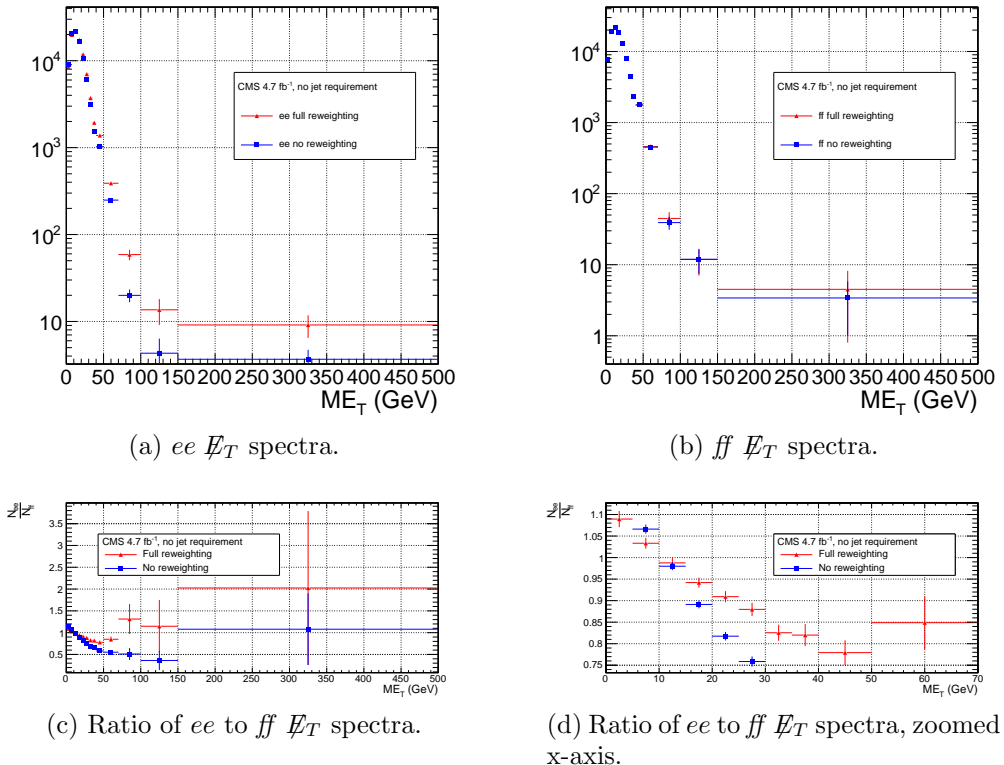


Figure 7.15: \cancel{E}_T spectra of the ee ($81 \text{ GeV} \leq m_{ee} < 101 \text{ GeV}$) and ff control samples. Red triangles indicate full di-EM $p_T +$ number of jets reweighting; blue squares indicate no reweighting. PF p_T (cf. p. 146) is used to calculate the di-EM p_T . The full normalization procedure is employed, along with ee sideband subtraction (discussed at the end of this section). Error bars are statistical only.

2365 The full reweighting procedure is applied to the Z signal region and the two
 2366 sideband regions independently. Only Z signal events are used in the calculation of
 2367 the di-EM p_T weights for the Z signal region, and likewise only the events within
 2368 a given sideband region are used in the calculation of the weights for that region.
 2369 Assuming a constant $t\bar{t}$ background shape, the resulting reweighted sideband \cancel{E}_T
 2370 distributions are added together and subtracted from the reweighted Z signal \cancel{E}_T
 2371 distribution. The sideband subtracted Z signal \cancel{E}_T distribution is then normalized
 2372 as discussed in Secs. 7.2.1 and 7.2.3. The statistical and reweighting error from the
 2373 sideband regions is propagated to the error on the final ee QCD \cancel{E}_T estimate.

2374 The di-EM p_T weights for the two ee sideband regions are shown in Figure 7.16.
 2375 The overall scale of the weights, as well as the trend with di-EM p_T , is similar for
 2376 the two regions (except at high di-EM p_T , where the statistics are poor anyway).
 2377 Figure 7.17 shows the \cancel{E}_T spectra for the two sideband regions and the Z signal
 2378 region after subtraction. The shapes of the spectra indicate that the high- \cancel{E}_T tail,
 2379 present in the sideband distributions, was successfully subtracted from the Z signal
 2380 distribution.

2381 The ee ($81 \text{ GeV} \leq m_{ee} < 101 \text{ GeV}$), ff , and $\gamma\gamma$ di-EM p_T spectra for events with
 2382 0, 1, or ≥ 2 jets (as in Table 6.2) are shown in Figure 7.18. Broad humps in the ff
 2383 and $\gamma\gamma$ spectra are due to kinematic ΔR and p_T turn-ons that are suppressed in the
 2384 ee sample due to the invariant mass cut. Figure 7.19 shows the weights applied to
 2385 the ee ($81 \text{ GeV} \leq m_{ee} < 101 \text{ GeV}$) and ff \cancel{E}_T spectra as a function of di-EM p_T and
 2386 number of jets per event.

2387 7.2.3 Normalization

2388 After reweighting, the \cancel{E}_T distributions of the QCD control samples are normalized
 2389 to the $\cancel{E}_T < 20 \text{ GeV}$ region of the candidate $\gamma\gamma$ \cancel{E}_T spectrum, where signal con-
 2390 tamination is low. The normalization factor is $(N_{\gamma\gamma}^{\cancel{E}_T < 20 \text{ GeV}} - N_{e\gamma}^{\cancel{E}_T < 20 \text{ GeV}})/N_{\text{control}}^{\cancel{E}_T < 20 \text{ GeV}}$,

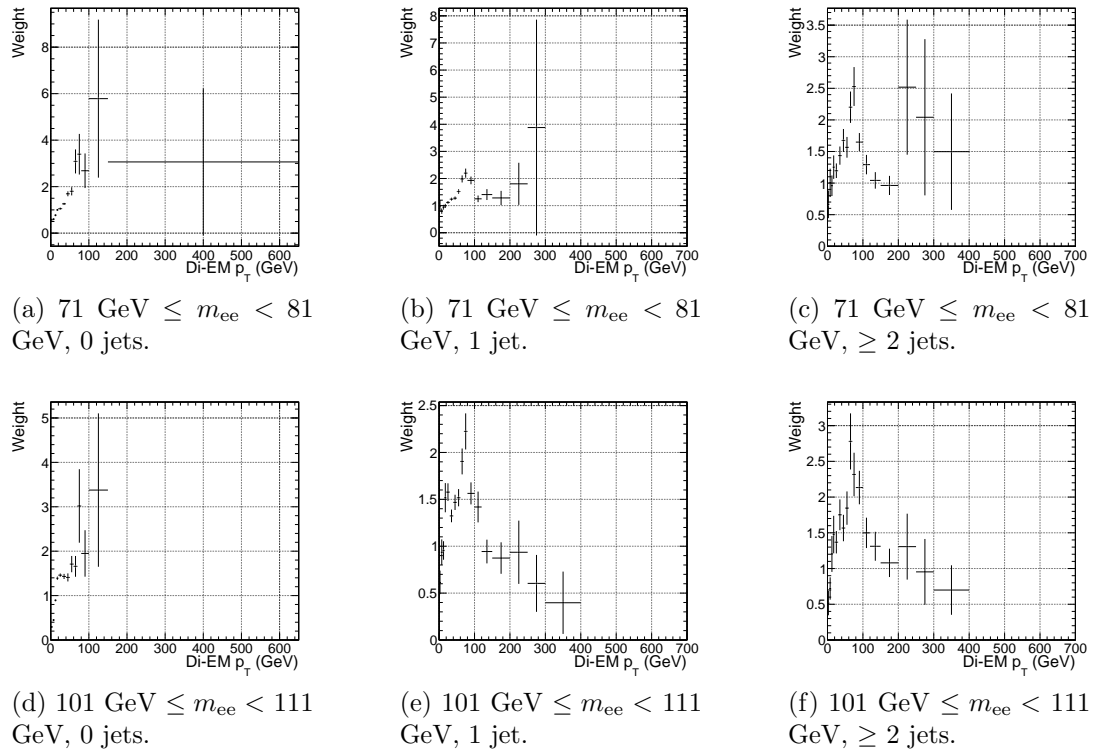


Figure 7.16: ee sideband di-EM p_T weights for events with 0, 1, or ≥ 2 jets (as in Table 6.2). Errors are statistical only.

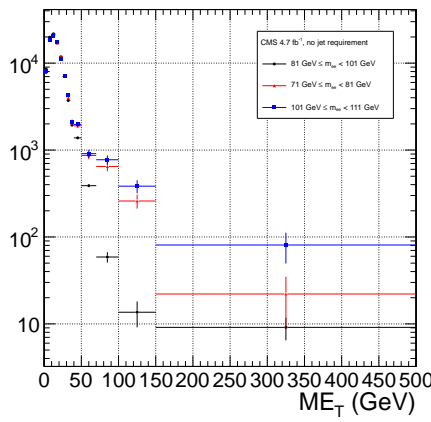
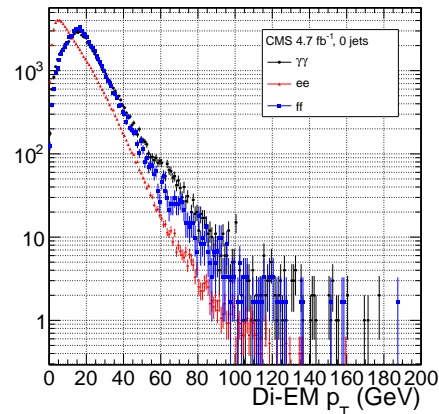
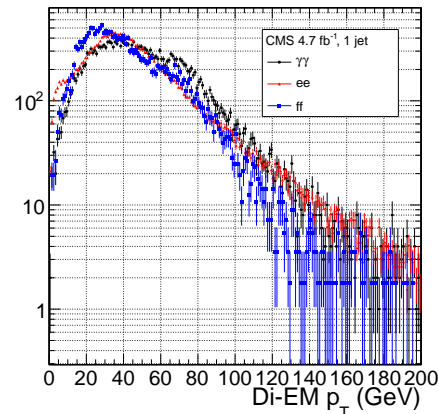


Figure 7.17: E_T spectra of the ee sample for $71 \text{ GeV} \leq m_{ee} < 81 \text{ GeV}$ (red triangles), $81 \text{ GeV} \leq m_{ee} < 101 \text{ GeV}$ (black circles), and $101 \text{ GeV} \leq m_{ee} < 111 \text{ GeV}$ (blue squares). The two sideband distributions (red and blue) and the Z signal distribution (black) are normalized to the total number of $\gamma\gamma$ events. Errors are statistical only.



(a) 0 jets.



(b) 1 jet.

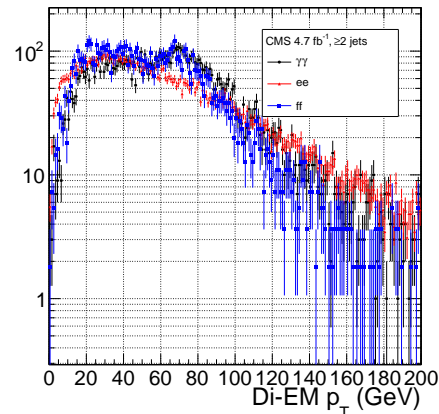
(c) ≥ 2 jets.

Figure 7.18: ee ($81 \text{ GeV} \leq m_{ee} < 101 \text{ GeV}$) (red triangles), ff (blue squares), and $\gamma\gamma$ (black circles) di-EM p_T spectra for events with 0, 1, or ≥ 2 jets (as in Table 6.2). Errors are statistical only.

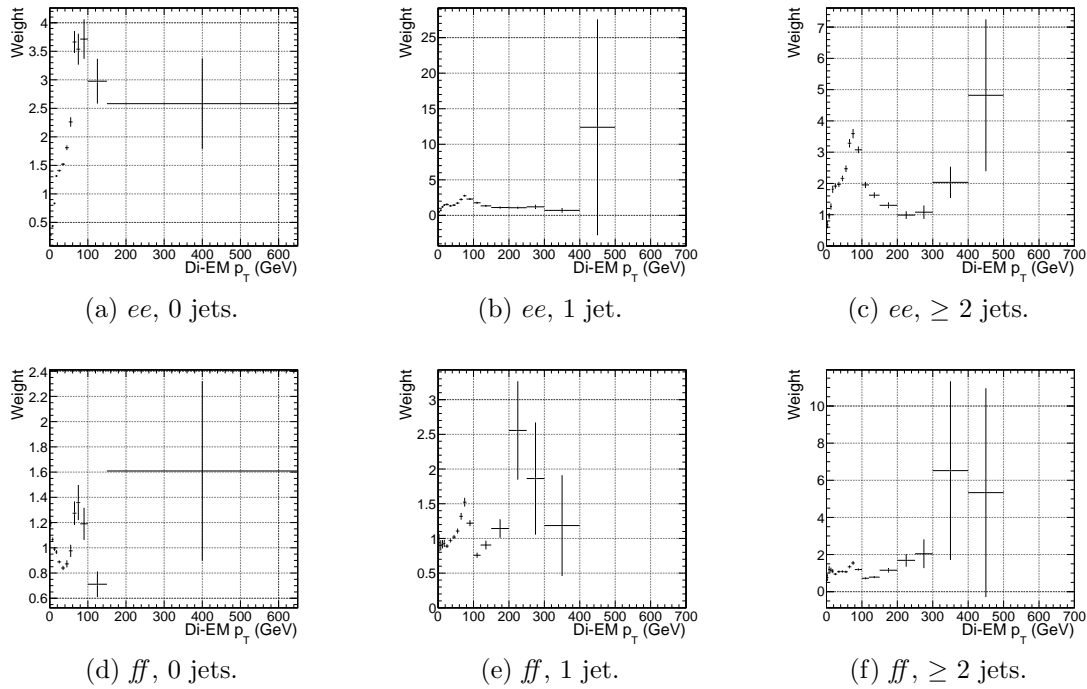


Figure 7.19: ee ($81 \text{ GeV} \leq m_{ee} < 101 \text{ GeV}$) and ff di-EM p_T weights for events with 0, 1, or ≥ 2 jets (as in Table 6.2). Errors are statistical only.

2391 where $N_{e\gamma}^{E_T < 20 \text{ GeV}}$ is the expected number of electroweak background events with E_T
 2392 $< 20 \text{ GeV}$ (discussed in Section 7.3). The error on the QCD background prediction
 2393 introduced by normalization is discussed in Sec. 7.4.

2394 7.3 Modeling the Electroweak Background

2395 $W\gamma$, $W + \text{jet}$, and $t\bar{t}$ processes in which the W decay electron is misidentified as a
 2396 photon (due to a failure to properly associate a pixel seed to the electron candidate)
 2397 can contribute significantly to the high- E_T tail of the $\gamma\gamma E_T$ spectrum. To estimate
 2398 this background, the $e\gamma$ sample, which is enriched in $W \rightarrow e\nu$ decays, is scaled by
 2399 $f_{e \rightarrow \gamma}/(1 - f_{e \rightarrow \gamma})$, where $f_{e \rightarrow \gamma}$ is the rate at which electrons are misidentified as photons.
 2400 The derivation of this scaling factor comes from the two equations

$$N_{e\gamma}^W = f_{e \rightarrow e} N_W \quad (7.2)$$

$$N_{\gamma\gamma}^W = (1 - f_{e \rightarrow e}) N_W \quad (7.3)$$

where $N_{e\gamma}^W$ is the number of W events in the $e\gamma$ sample in which the electron was correctly identified, $f_{e \rightarrow e}$ is the probability to correctly identify an electron, N_W is the true number of triggered $W \rightarrow e\nu$ events, and $N_{\gamma\gamma}^W$ is the number of W events in the $\gamma\gamma$ sample in which the electron was misidentified as a photon. The contribution from $Z \rightarrow ee$ can be neglected (i.e. $f_{e \rightarrow \gamma}$ is small and the Z contribution involves $f_{e \rightarrow \gamma}^2$, since both electrons have to be misidentified). Since $f_{e \rightarrow e} = 1 - f_{e \rightarrow \gamma}$, solving for $N_{\gamma\gamma}^W$ gives

$$N_{\gamma\gamma}^W = \frac{f_{e \rightarrow \gamma}}{1 - f_{e \rightarrow \gamma}} N_{e\gamma}^W \quad (7.4)$$

$f_{e \rightarrow \gamma}$ is measured by fitting the Z peaks in the ee and $e\gamma$ samples. The number of Z events fitted in the ee and $e\gamma$ samples, respectively, is given by

$$N_{ee}^Z = (1 - f_{e \rightarrow \gamma})^2 N_Z \quad (7.5)$$

$$N_{e\gamma}^Z = 2f_{e \rightarrow \gamma}(1 - f_{e \rightarrow \gamma}) N_Z \quad (7.6)$$

where N_Z is the true number of triggered $Z \rightarrow ee$ events. Solving for $f_{e \rightarrow \gamma}$ gives

$$f_{e \rightarrow \gamma} = \frac{N_{e\gamma}^Z}{2N_{ee}^Z + N_{e\gamma}^Z} \quad (7.7)$$

2411 A Crystal Ball function is used to model the Z signal shape in both the ee and
 2412 $e\gamma$ samples, while an exponential convoluted with an error function (`RooCMSShape`,
 2413 see Sec. 6.4.1) is used to model the background shape. The fixed fit parameters are
 2414 identical for the two samples, but the other parameters are allowed to float indepen-
 2415 dently. Table 7.3 shows the values and ranges of the fixed and floating fit parameters,
 2416 respectively.

Table 7.3: Parameter values for the signal and background PDFs for the ee and $e\gamma$ samples. When a bracketed range is given, the parameter is allowed to float within that range. When a constant is given, the parameter is fixed to that constant.

PDF	Crystal Ball fit parameters				<code>RooCMSShape</code> fit parameters			
	μ	σ	α	n	μ	α	β	γ
ee sig- nal	[86.2, 96.2]	[1.0, 5.0]	1.063	143.16	N/A	N/A	N/A	N/A
$e\gamma$ sig- nal	[86.2, 96.2]	[1.0, 5.0]	1.063	143.16	N/A	N/A	N/A	N/A
ee back- ground	N/A	N/A	N/A	N/A	58	97.0	0.0922	0.191
$e\gamma$ back- ground	N/A	N/A	N/A	N/A	56	72.02	0.098	0.0375

2417 Fits to the ee and $e\gamma$ invariant mass spectra are shown in Figure 7.20. Fig-
 2418 ure 7.21(a) indicates that there is some dependence of $f_{e \rightarrow \gamma}$ on the electron p_T , but
 2419 since the the bulk of the electrons have $p_T \sim 45$ GeV, applying a p_T -dependent mis-
 2420 identification rate has a negligible effect on the final background estimate. (Note that
 2421 all fit parameters are floating in the p_T -dependent fits.) The dependence on η is small,
 2422 as shown in Figure 7.21(b). Therefore, a constant misidentification rate (derived from
 2423 all ee and $e\gamma$ events), rather than a p_T - and η -dependent misidentification rate, is
 2424 used in the final electroweak background estimate, with the difference between the
 2425 constant rate and the rate for electrons with p_T between 25 and 40 GeV (the range
 2426 in which the bulk of the trailing photons in the $\gamma\gamma$ sample lie) taken as a systematic
 2427 error.

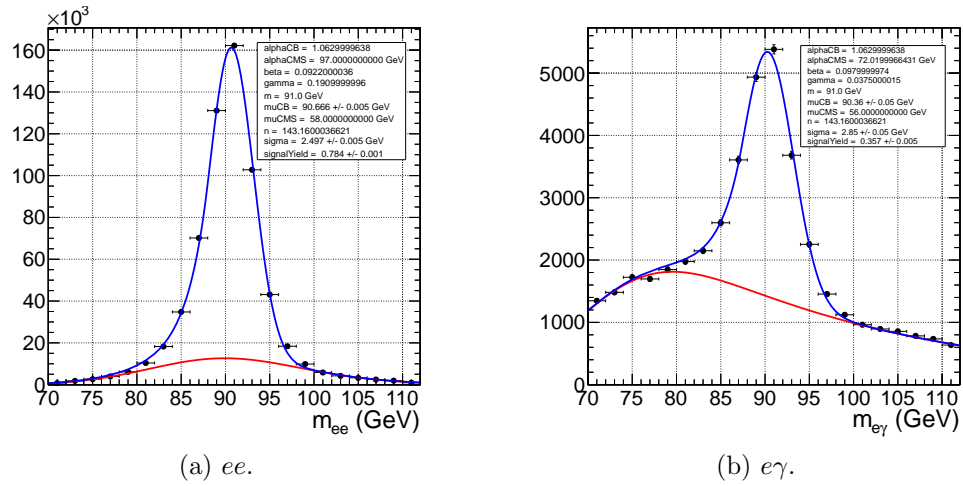
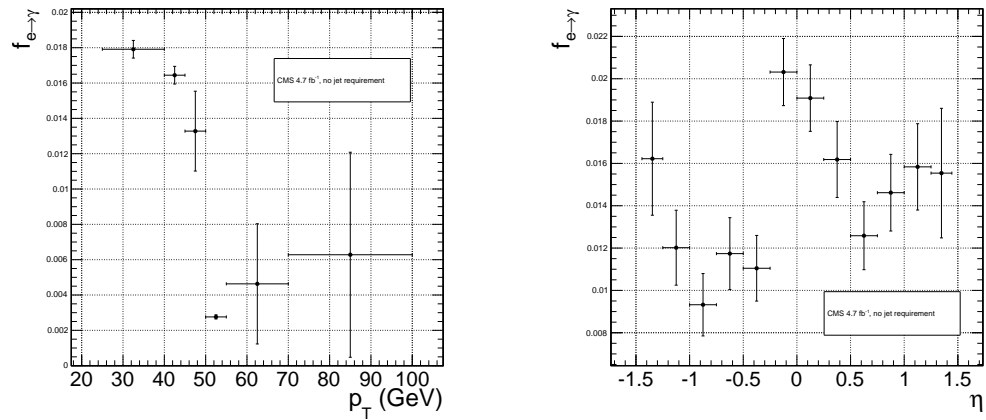


Figure 7.20: Fits to the ee and $e\gamma$ invariant mass spectra using the Crystal Ball RooCMSShape function described in the text and in Table 7.3. The total fit is shown in blue, while the background component is shown in red.



(a) $f_{e\rightarrow\gamma}$ vs. electron p_T . For the lowest p_T bin, the fit to the $e\gamma$ spectrum does not converge well, so the Z signal fraction is fixed to the value in Fig. 7.20(b).

(b) $f_{e\rightarrow\gamma}$ vs. electron η .

Figure 7.21: $f_{e\rightarrow\gamma}$ vs. electron p_T and η .

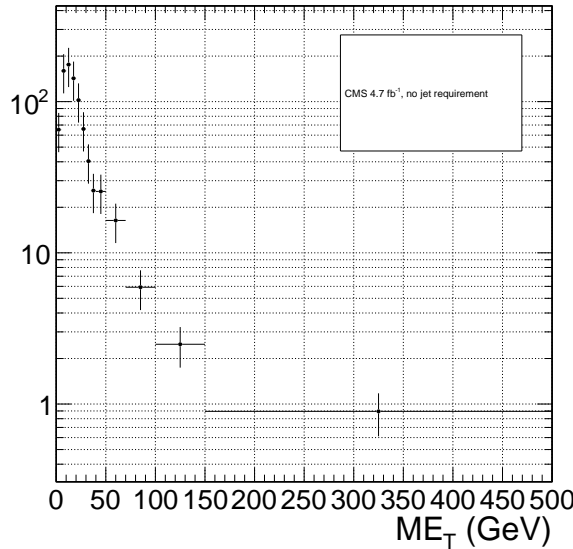


Figure 7.22: \cancel{E}_T spectrum of the $e\gamma$ sample after scaling by $f_{e \rightarrow \gamma}$. The total error on $f_{e \rightarrow \gamma}$ is propagated to the total error on the electroweak background estimate.

Using the integrals of the Z fits shown in Fig. 7.20, Eq. 7.7, and the p_T systematic discussed above, $f_{e \rightarrow \gamma}$ is calculated to be $0.014 \pm 0.000(\text{stat.}) \pm 0.004(\text{syst.})$. The scaled $e\gamma$ MET distribution is shown in Figure 7.22.

In the 36 pb^{-1} version of this analysis [140], it was shown that the ee sample could accurately predict the QCD and real Z contribution to the $e\gamma$ sample at low \cancel{E}_T , and that the expectation from $W \rightarrow e\nu$ MC accounted for the remaining W contribution at high \cancel{E}_T . A plot of the \cancel{E}_T distributions of the 2010 $e\gamma$ sample and the predicted components is shown in Figure 7.23. This exercise helps to validate both the QCD and electroweak background prediction methods.

7.4 Errors on the Background Prediction

The statistical error on the final background estimate in a particular \cancel{E}_T bin comes from three sources: the number of control sample events collected in that bin, the statistical error on the weights applied to events in that bin, and the statistics of the normalization region. In the case of the ee control sample, there are contributions

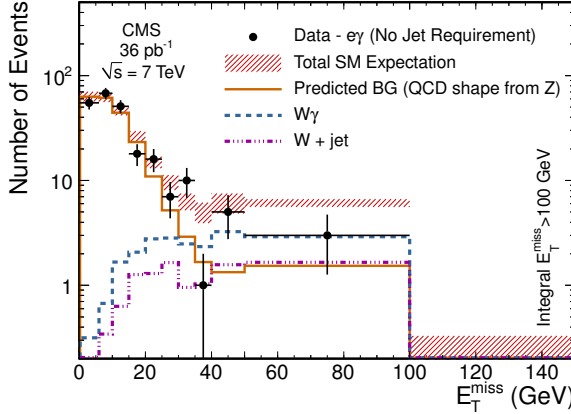


Figure 7.23: E_T spectrum of the $e\gamma$ sample in 35 pb^{-1} of 2010 LHC data scaled by the 2010 measured $f_{e \rightarrow \gamma}$ (black dots), QCD and real Z predicted background from the 2010 ee sample (solid orange line), MC $W + \text{jet}$ estimate (dash-dotted purple line), and MC $W\gamma$ estimate (dashed blue line). The total $e\gamma$ prediction (red band) is the sum of the ee , $W + \text{jet}$, and $W\gamma$ predictions. Reprinted from Fig. 2 of ref. [140].

from the statistics of the m_{ee} sidebands as well.

In order to propagate the statistical error due to the reweighting procedure to the shape of the final QCD E_T distribution, 1000 toy sets of weights are generated. Each set includes a weight for each (di-EM p_T , N_j) bin, with the values picked from a Gaussian distribution with mean and standard deviation equal to the observed weight for that bin and its statistical error. The effect of reweighting error is not correlated between E_T bins. For each of the 1000 experiments, the control sample data are reweighted according to the generated weights, and the background estimates are calculated for each E_T bin. Since the distribution of the toy background estimates follows a Gaussian distribution in each E_T bin, the RMS spread of the estimates is taken as the statistical error due to reweighting. This procedure is carried out for the ff , ee , low sideband ee , and high sideband ee samples.

The total statistical error on the background estimate per E_T bin is given by

$$\sigma_{\text{stat}}^2 = \sigma_{\text{stat}, \text{QCD}}^2 + \sigma_{\text{stat}, \text{EW}}^2 \quad (7.8)$$

2455 where $\sigma_{\text{stat,QCD}}^2$ is the square of the total statistical error on the QCD prediction in
 2456 the \cancel{E}_T bin

$$\sigma_{\text{stat,QCD}}^2 = \sigma_{\text{stat},s}^2 + \sigma_{\text{Poisson,QCD}}^2 + \sigma_{\text{reweight},s}^2 + \sigma_{\text{reweight,QCD}}^2 \quad (7.9)$$

2457 and $\sigma_{\text{stat,EW}}$ is the Poisson error on the number of $e\gamma$ events in the \cancel{E}_T bin ($= \sqrt{N_{e\gamma}}$,
 2458 where $N_{e\gamma}$ is the prediction in the \cancel{E}_T bin after scaling by $f_{e\rightarrow\gamma}$). The contributions
 2459 to $\sigma_{\text{stat,QCD}}^2$ are discussed below.

- 2460 • $\sigma_{\text{stat},s}^2$ is the statistical error contributed by the normalization factor s (i.e. from
 2461 Poisson error in the normalization region $\cancel{E}_T < 20$ GeV):

$$\begin{aligned} \sigma_{\text{stat},s}^2 = & \frac{N_{\text{control}}^2}{(N_{\gamma\gamma}^{\text{norm}} - N_{e\gamma}^{\text{norm}})^2} ([\sigma_{\text{Poisson},\gamma\gamma}^{\text{norm}}]^2 + [\sigma_{\text{Poisson},e\gamma}^{\text{norm}}]^2) + \\ & \frac{N_{\text{control}}^2}{(N_{\text{control}}^{\text{norm}})^2} (\sigma_{\text{Poisson,control}}^{\text{norm}})^2 \end{aligned} \quad (7.10)$$

2462 where N_{control} is the number of reweighted, normalized events in the \cancel{E}_T bin,
 2463 $N_{\gamma\gamma}^{\text{norm}}$ is the number of $\gamma\gamma$ events in the normalization region, $N_{e\gamma}^{\text{norm}}$ is the num-
 2464 ber of $e\gamma$ events in the normalization region (after scaling by $f_{e\rightarrow\gamma}$), $\sigma_{\text{Poisson},\gamma\gamma}^{\text{norm}}$
 2465 is the Poisson error on the number of $\gamma\gamma$ events in the normalization region
 2466 ($= \sqrt{N_{\gamma\gamma}^{\text{norm}}}$), $\sigma_{\text{Poisson},e\gamma}^{\text{norm}}$ is the Poisson error on the number of $e\gamma$ events in the
 2467 normalization region ($= \sqrt{N_{e\gamma}^{\text{norm}}}$), $N_{\text{control}}^{\text{norm}}$ is the number of QCD control (ee
 2468 or ff) events in the normalization region, and $\sigma_{\text{Poisson,control}}^{\text{norm}}$ is the Poisson error
 2469 on the number of QCD control (ee or ff) events in the normalization region
 2470 ($= \sqrt{\sum_{i=1}^{N_{\text{control}}^{\text{norm}}} w_i^2}$, where w_i is the di-EM p_T weight applied to event i). For
 2471 the ee control region, N_{control} and $N_{\text{control},\text{norm}}$ are sideband subtracted, and
 2472 $\sigma_{\text{Poisson,control}}^{\text{norm}}$ includes the Poisson error on the number of sideband events.

- 2473 • $\sigma_{\text{Poisson,QCD}}$ is the Poisson error due to the number of QCD control (ee or ff)
2474 events in the \cancel{E}_T bin, equal to $\sqrt{\sum_{i=1}^{N_{\text{control}}} w_i^2}$, where w_i is the di-EM p_T weight
2475 applied to event i . For the ee control region, $\sigma_{\text{Poisson,QCD}}$ includes the Poisson
2476 error on the number of subtracted sideband events.

- 2477 • $\sigma_{\text{reweight},s}$ is the error contributed by the control sample reweighting in the nor-
2478 malization region ($= \frac{N_{\text{control}}^2}{(N_{\text{control}}^{\text{norm}})^2} \sigma_{\text{reweight,control}}^{\text{norm}}$). $\sigma_{\text{reweight,control}}^{\text{norm}}$ is the quadrature
2479 sum of the RMS of the 1000 toy reweighting experiments for each \cancel{E}_T bin in the
2480 normalization region. For the ee control sample, it also includes (in quadrature)
2481 the RMS of the toys in the sideband samples.

- 2482 • $\sigma_{\text{reweight,QCD}}$ is the error contributed by the control sample reweighting in the \cancel{E}_T
2483 bin ($= s \sigma_{\text{reweight,control}}$). $\sigma_{\text{reweight,control}}$ is the RMS of the 1000 toy reweighting
2484 experiments for the E_T bin. For the ee control sample, it also includes (in
2485 quadrature) the RMS of the toys in the sideband samples.

2486 The difference in hadronic activity between the ee , ff , and $\gamma\gamma$ samples results in
2487 a small bias (~ 1 GeV) of the ee \cancel{E}_T distribution towards lower values with respect
2488 to the ff and $\gamma\gamma$ samples, as shown in Figure 7.24. Therefore, the ff sample is used
2489 as the primary QCD background estimator, and the difference between the ee and ff
2490 predictions is assigned as an error on the knowledge of the hadronic activity. For \cancel{E}_T
2491 > 100 GeV, this error amounts to 43% of the total QCD + electroweak background
2492 estimate, and is the dominant source of systematic error.

2493 The second largest source of systematic error comes from the p_T dependence of the
2494 $e \rightarrow \gamma$ misidentification rate (see 7.3). For $\cancel{E}_T > 100$ GeV, the expected electroweak
2495 background is 3.4 ± 1.0 events, so this error amounts to 4.8% of the total QCD +
2496 electroweak background estimate.

2497 The assumption of a constant $t\bar{t}$ and $W + \text{jets}$ background shape under the Z
2498 peak in the ee sample induces a systematic error on the ee sideband-subtracted back-

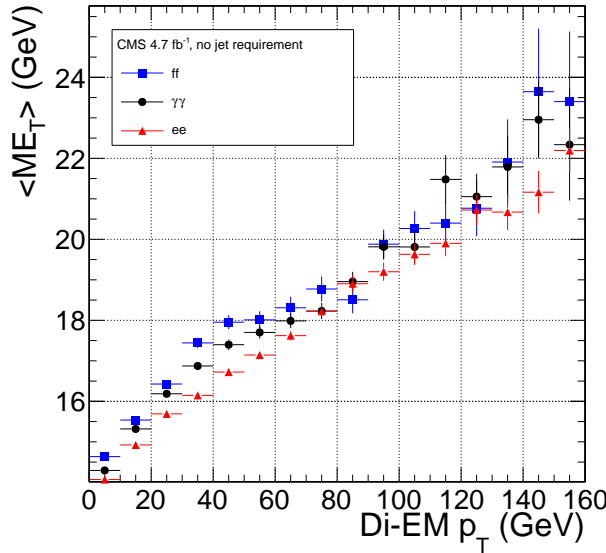


Figure 7.24: Average \cancel{E}_T vs. di-EM p_T for the ff (blue squares), ee (red triangles), and $\gamma\gamma$ (black circles) samples.

ground prediction. To assess the magnitude of this error, the sideband subtraction (see Sec. 7.2.2) is performed once using only the prediction from the high sideband, and once using only the prediction from the low sideband. In each of these cases, the prediction is weighted by a factor of two, to account for the fact that the sideband regions are only half as wide (10 GeV) as the signal region (20 GeV). The maximum variation from the nominal ee estimate is taken as the error, which amounts to 11% for $\cancel{E}_T > 100$ GeV. \cancel{E}_T distributions using the nominal ee sideband subtraction, the low-sideband-only subtraction, and the high-sideband-only subtraction are shown in Figure 7.25.

Finally, the few percent error on the jet energy correction factors introduces an error on the final background estimate through (a) the use of the PF p_T to measure the di-EM p_T , (b) the counting of jets passing a 30 GeV p_T threshold for placement of the event in an N_j bin for reweighting, and (c) the counting of jets above threshold for the ≥ 1 -jet version of the selection. To estimate this error, 100 pseudo-experiments are generated with identical properties as the true data sample, except with corrected jet energies (in all events) all shifted by an amount $r\sigma(p_T, \eta)$. r is a random number

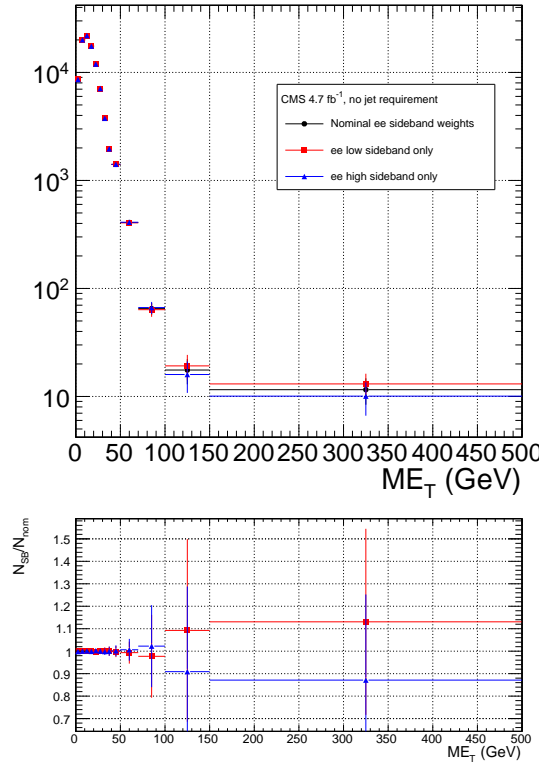


Figure 7.25: ee \cancel{E}_T distributions using the nominal sideband subtraction (black circles), low sideband only (red squares), and high sideband only (blue triangles). The bottom plot shows the ratio of the low sideband distribution to the nominal (red squares) and the ratio of the high sideband distribution to the nominal (blue triangles).

2515 drawn from a Gaussian distribution with mean 0 and width 1, and $\sigma(p_T, \eta)$ is the
 2516 uncertainty on the jet energy correction factor (which, like the correction factor itself,
 2517 is a function of p_T and η). The same factor r is applied to all jets in all events in the
 2518 pseudo-experiment because the jet energy correction errors are correlated from jet to
 2519 jet (they result from e.g. uncertainties in MC simulation or uncertainties in ECAL
 2520 energy scale [119]). The standard error of the mean of the 100 resulting background
 2521 estimates in each relevant \cancel{E}_T bin is taken as the error. The error in each \cancel{E}_T bin is
 2522 assumed to be uncorrelated. This process is repeated for both the inclusive and ≥ 1 -
 2523 jet selections. For $\cancel{E}_T \geq 100$ GeV, the jet energy correction uncertainty is 1.5% (2.2%)
 2524 of the total background for the inclusive (≥ 1 -jet) selection.

2525 The uncertainty in how to define the (di-EM p_T , N_j) bins, especially at high di-

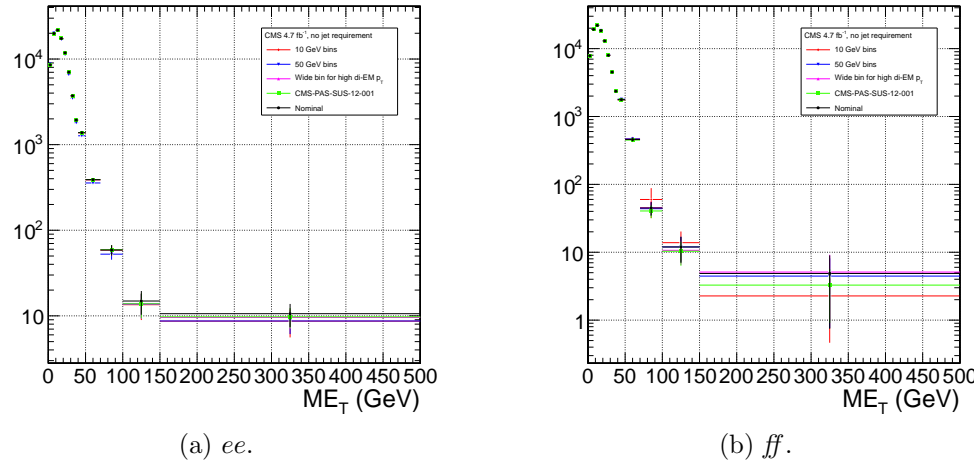


Figure 7.26: Comparison of \cancel{E}_T distributions for five different di-EM p_T bin definitions: uniform bins of width 10 GeV (red diamonds); uniform bins of width 50 GeV (blue downward-pointing triangles); bins with lower edges $\{0.0, 5.0, 10.0, 15.0, 20.0, 30.0, 40.0, 50.0, 60.0, 70.0, 80.0, 100.0, 750.0\}$ GeV for 0-jet events and $\{0.0, 5.0, 10.0, 15.0, 20.0, 30.0, 40.0, 50.0, 60.0, 70.0, 80.0, 100.0, 150.0\}$ GeV for ≥ 1 -jet events (magenta upward-pointing triangles), i.e. a single wide bin at high di-EM p_T ; bins with lower edges $\{0.0, 5.0, 10.0, 15.0, 20.0, 30.0, 40.0, 50.0, 60.0, 70.0, 80.0, 100.0, 150.0\}$ GeV for 0-jet events and $\{0.0, 5.0, 10.0, 15.0, 20.0, 30.0, 40.0, 50.0, 60.0, 70.0, 80.0, 100.0, 120.0, 150.0, 200.0, 700.0\}$ GeV for ≥ 1 -jet events (green squares), i.e. the bins used in ref. [59]; and the nominal bin definitions shown in Fig. 7.19 (black circles).

2526 EM p_T where the statistics are low, is covered by the 1000-toys procedure as long as
 2527 the bins are not too coarse. This is shown in Figure 7.26. If the bins are too coarse,
 2528 the details of the shape of the di-EM p_T spectra are lost, and the reweighting has a
 2529 smaller effect.

2530 The use of uncorrected instead of corrected PF \cancel{E}_T (see Sec. 6.1.3) makes no
 2531 difference in the agreement of the background predictions and the search sample in
 2532 a control region at low \cancel{E}_T , as shown in Figure 7.27. Since the control samples are
 2533 derived from the same data as the search sample, any biases in the \cancel{E}_T reconstruction
 2534 due to jet energy scale are present equally in both samples.

2535 Tables 7.4 and 7.5 list all the errors on the ee and ff QCD background predictions,
 2536 respectively, for the \cancel{E}_T bins used in the search. Table 7.6 lists the errors on the

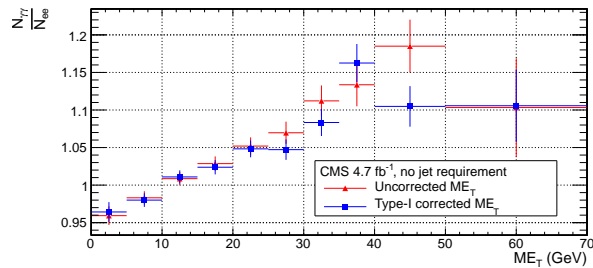
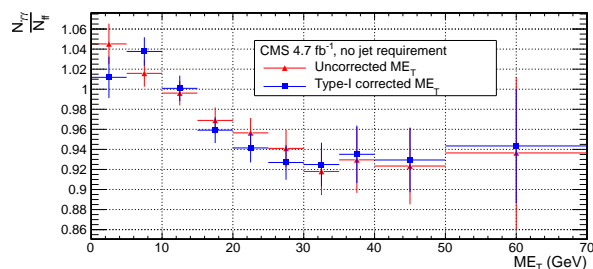
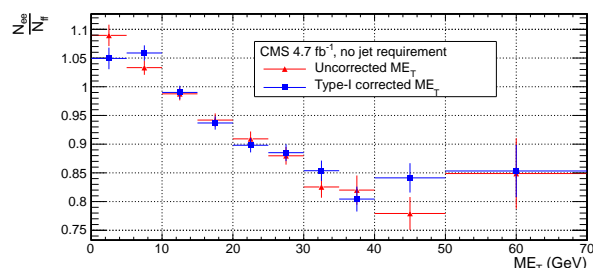
(a) Ratio of $\gamma\gamma$ to ee \cancel{E}_T distributions.(b) Ratio of $\gamma\gamma$ to ff \cancel{E}_T distributions.(c) Ratio of ee to ff \cancel{E}_T distributions.

Figure 7.27: Agreement between $\gamma\gamma$, ee , and ff samples for uncorrected (red triangles) and corrected (blue squares) \cancel{E}_T .

2537 electroweak background prediction. Finally, Table 7.7 shows the errors on the total
 2538 QCD + electroweak background prediction, broken down by origin (statistical or
 2539 systematic) and QCD background estimation sample (ee or ff). In the final result,
 2540 only the ff QCD estimate is used.

Table 7.4: Errors on the ee QCD background prediction as a fraction of the ee prediction.

Source of error	Fractional uncertainty (%)				
	[50, 60)	[60, 70)	[70, 80)	[80, 100)	≥ 100
Total	3.9	8.1	16	25	25
Statistics	3.6	7.8	16	24	22
No. events	3.6	7.7	15	24	20
In norm. region	0.43	0.44	0.46	0.55	0.51
In this E_T bin	3.5	7.7	15	24	20
Reweighting	0.73	1.2	3.5	4.3	7.7
In norm. region	0.19	0.19	0.2	0.24	0.23
In this E_T bin	0.71	1.2	3.5	4.3	7.7
Systematics	2.6	4.4	1.2	7.5	14
$f_{e \rightarrow \gamma}$ (in norm. region)	0.0012	0.0012	0.0013	0.0015	0.0014
m_{ee} background shape	1.4	2	0.72	5.5	12
Jet energy scale	2.2	3.9	0.96	5.1	6.9

2541 7.5 Results

2542 Figure 7.28(7.29) shows the E_T distribution of the inclusive(≥ 1 -jet) $\gamma\gamma$ search sample
 2543 along with the predicted E_T distributions of the QCD and electroweak backgrounds.
 2544 The observed number of two-photon events, ee and ff background estimates and
 2545 their errors, and expected number of inclusive(≥ 1 -jet) two-photon events from two
 2546 representative GGM SUSY models are listed in Table 7.8(7.9). (Details of the SUSY
 2547 MC production are given in Chapter 8.) The ee estimate is shown for comparison;
 2548 the ff estimate is the official result used in the interpretation. No deviation from the
 2549 Standard Model prediction is observed in the $\gamma\gamma$ search sample.

Table 7.5: Errors on the ff QCD background prediction as a fraction of the ff prediction.

Source of error	Fractional uncertainty (%)				
	[50, 60)	[60, 70)	[70, 80)	[80, 100)	≥ 100
Total	15	25	61	34	64
Statistics	7.2	14	30	33	38
No. events	7.1	14	29	33	36
In norm. region	0.64	0.64	0.64	0.64	0.64
In this E_T bin	7.1	14	29	33	36
Reweighting	0.85	2.7	5.1	6.9	13
In norm. region	0.27	0.27	0.27	0.27	0.27
In this E_T bin	0.81	2.6	5.1	6.9	13
Systematics	13	21	53	6.6	52
ee/ff difference	13	21	53	5.5	52
$f_{e \rightarrow \gamma}$ (in norm. region)	0.0012	0.0012	0.0012	0.0012	0.0012
Jet energy scale	0.099	1.7	1.8	3.5	1.8

Table 7.6: Errors on the $e\gamma$ electroweak background prediction as a fraction of the $e\gamma$ prediction.

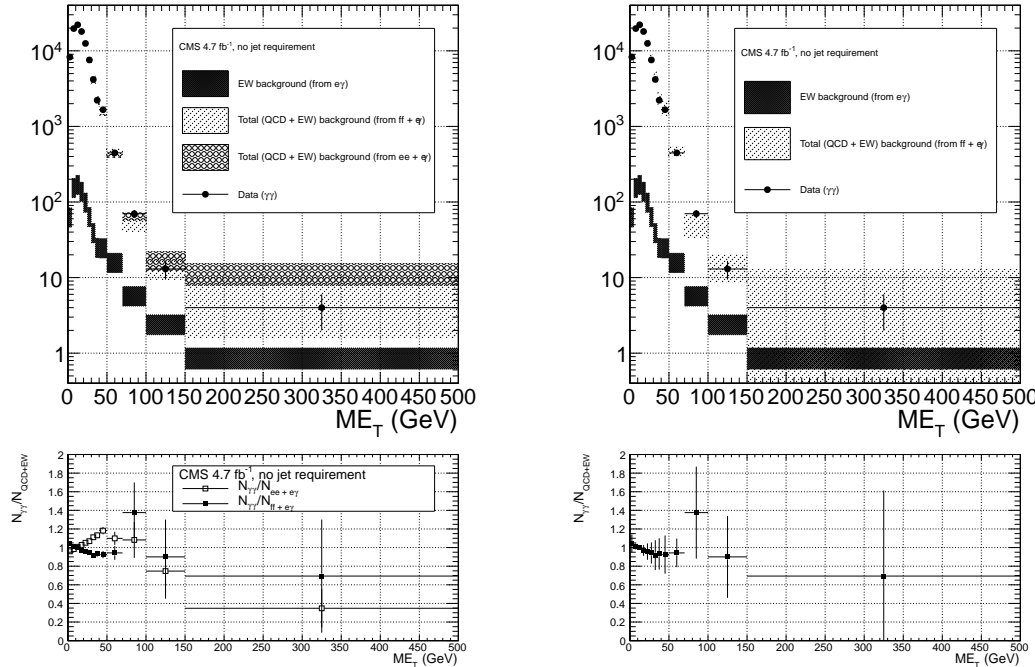
Source of error	Fractional uncertainty (%)				
	[50, 60)	[60, 70)	[70, 80)	[80, 100)	≥ 100
Total	29	29	30	30	30
Statistics	3.6	5.2	6.7	7.2	6.5
Systematics ($f_{e \rightarrow \gamma}$)	29	29	29	29	29

Table 7.7: Errors on the total QCD + electroweak background prediction as a fraction of the total prediction.

Source of error	Fractional uncertainty (%)				
	[50, 60)	[60, 70)	[70, 80)	[80, 100)	≥ 100
Total ($ee + e\gamma$)	3.9	7.8	15	22	22
Statistics	3.4	7.3	14	21	18
QCD	3.4	7.3	14	21	18
Electroweak	0.13	0.3	0.53	0.79	0.76
Systematics	2.7	4.5	2.6	7.4	13
QCD	2.5	4.1	1.1	6.7	12
Electroweak	1	1.7	2.3	3.2	3.4
Total ($ff + e\gamma$)	14	24	54	30	54
Statistics	6.9	13	26	29	30
QCD	6.9	13	26	29	30
Electroweak	0.11	0.24	0.79	0.83	1.1
Systematics	12	20	47	6.7	43
QCD	12	20	47	5.8	43
Electroweak	0.9	1.3	3.4	3.4	4.8

Table 7.8: Observed numbers of two-photon events, ee and ff background estimates and their errors, and expected numbers of two-photon events from two representative GGM SUSY models (details of MC simulation given in Chapter 8) for the E_T bins used in the search. The ee estimate is shown for comparison; the ff estimate is the official result used in the interpretation. Errors on the background estimates are detailed in Tables 7.4, 7.5, 7.6, and 7.7. Errors on the expected numbers of GGM events are purely statistical.

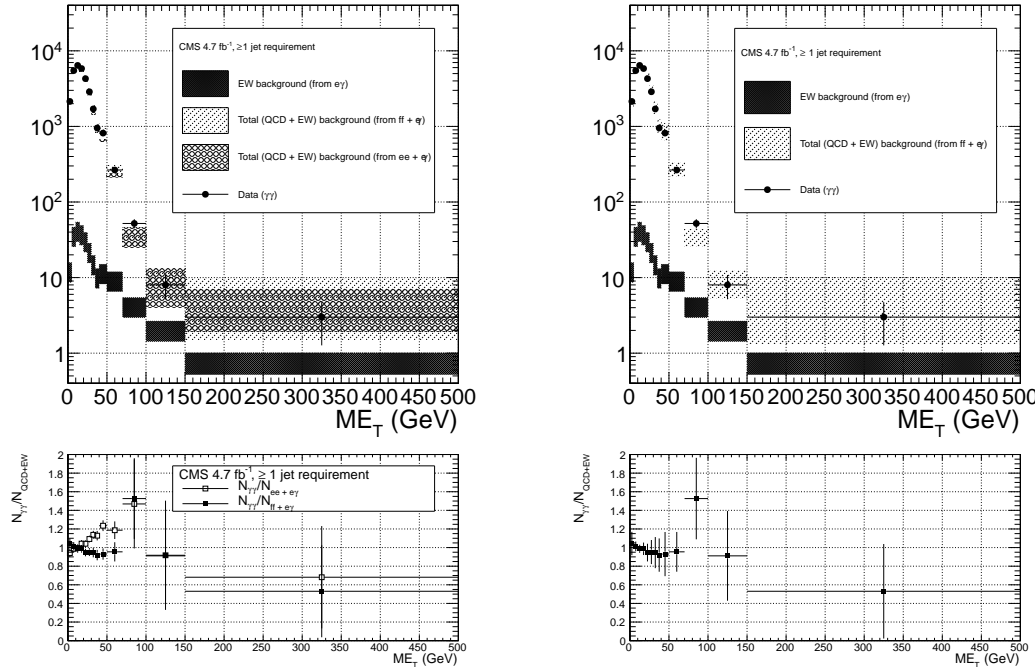
Source	No. events				
	[50, 60)	[60, 70)	[70, 80)	[80, 100)	≥ 100
Observation ($\gamma\gamma$)	354	93	37	33	17
Predicted background ($ff + e\gamma$)	361 ± 51.5	113 ± 27.1	26.9 ± 14.5	23.9 ± 7.23	20.2 ± 10.9
Predicted background ($ee + e\gamma$)	317 ± 14.1	90.2 ± 7.77	39.6 ± 5.75	25.1 ± 5.66	28.9 ± 6.70
$m_{\tilde{q}} = 720$ GeV $M_3 = 720$ GeV $M_1 = 375$ GeV	13.3 ± 2.13	17.7 ± 2.46	15.3 ± 2.33	42.9 ± 3.82	966 ± 18.3
$m_{\tilde{q}} = 1440$ GeV $M_3 = 1440$ GeV $M_1 = 375$ GeV	0.008 ± 0.003	0.009 ± 0.003	0.012 ± 0.003	0.030 ± 0.005	1.92 ± 0.04



(a) $ee + e\gamma$ and $ff + e\gamma$. The widths of the bands correspond to the errors given in Table 7.7, excluding the error associated with the difference between the ee and ff QCD estimates for the $ff + e\gamma$ E_T distribution.

(b) $ff + e\gamma$. The widths of the bands correspond to the errors given in Table 7.7, including the error associated with the difference between the ee and ff QCD estimates.

Figure 7.28: E_T distribution of the $\gamma\gamma$ search sample (black circles) along with the predicted E_T distributions of the QCD and electroweak backgrounds (small circle band for ee QCD prediction + electroweak prediction, slanted dashed band for ff QCD prediction + electroweak prediction). The electroweak background prediction is shown in the crosshatched band. The bottom plots show the ratio of the $\gamma\gamma$ E_T distribution to the $ee + e\gamma$ background distribution (open squares) and $ff + e\gamma$ background distribution (filled squares).



(a) $ee + e\gamma$ and $ff + e\gamma$. The widths of the bands correspond to the errors given in Table 7.7, excluding the error associated with the difference between the ee and ff QCD estimates for the $ff + e\gamma$ E_T distribution.

(b) $ff + e\gamma$. The widths of the bands correspond to the errors given in Table 7.7, including the error associated with the difference between the ee and ff QCD estimates.

Figure 7.29: E_T distribution of the $\gamma\gamma + \geq 1$ jet search sample (black circles) along with the predicted E_T distributions of the QCD and electroweak backgrounds (small circle band for ee QCD prediction + electroweak prediction, slanted dashed band for ff QCD prediction + electroweak prediction). The electroweak background prediction is shown in the crosshatched band. The bottom plots show the ratio of the $\gamma\gamma E_T$ distribution to the $ee + e\gamma$ background distribution (open squares) and $ff + e\gamma$ background distribution (filled squares).

Table 7.9: Observed numbers of two-photon + ≥ 1 -jet events, ee and ff background estimates and their errors, and expected numbers of two-photon + ≥ 1 -jet events from two representative GGM SUSY models (details of MC simulation given in Chapter 8) for the E_T bins used in the search. The ee estimate is shown for comparison; the ff estimate is the official result used in the interpretation. Errors on the background estimates are detailed in Tables 7.4, 7.5, 7.6, and 7.7. Errors on the expected numbers of GGM events are purely statistical.

Source	No. events				
	[50, 60)	[60, 70)	[70, 80)	[80, 100)	≥ 100
Observation ($\gamma\gamma + \geq 1$ jet)	202	63	27	25	11
Predicted background ($ff + e\gamma$)	200 ± 35.4	77.7 ± 28.1	19.4 ± 8.55	14.7 ± 7.04	14.4 ± 5.59
Predicted background ($ee + e\gamma$)	171 ± 10.2	52.7 ± 5.74	25.1 ± 4.76	10.2 ± 5.04	13.1 ± 5.74
$m_{\tilde{q}} = 720$ GeV $M_3 = 720$ GeV $M_1 = 375$ GeV	13.3 ± 2.13	17.7 ± 2.46	15.3 ± 2.33	42.9 ± 3.82	965 ± 18.3
$m_{\tilde{q}} = 1440$ GeV $M_3 = 1440$ GeV $M_1 = 375$ GeV	0.008 ± 0.003	0.009 ± 0.003	0.012 ± 0.003	0.031 ± 0.004	1.92 ± 0.04

2550 **Chapter 8**

2551 **Interpretation of Results in Terms**
2552 **of GMSB Models**

2553 As shown in Figs. 7.28 and 7.29 and Tables 7.8 and 7.9, no excess of events above
2554 the Standard Model expectation is found in either the ≥ 0 - or ≥ 1 -jet analyses for the
2555 GMSB-sensitive region $\cancel{E}_T \geq 50$ GeV. Therefore, upper limits on the production cross
2556 sections of various GMSB models are calculated and then translated into statements of
2557 exclusion. Section 8.1 describes the GMSB models that were generated with MC and
2558 tested for exclusion. The upper limit calculation and translation to model exclusions
2559 is laid out in Section 8.2. The upper limits themselves are presented in Section 8.3,
2560 and, finally, the exclusions are presented in Section 8.4.

2561 **8.1 Simplified Models**

2562 The exclusion reach of the two-photon search is presented for three different two-
2563 dimensional scans in GMSB parameter space. The first scan covers the bino NLSP
2564 scenario of Sec. 3.5. In this scan, M_2 , which controls the amount of wino mixing, is
2565 set to 3.5 TeV. M_1 , which controls the amount of bino mixing, is set to 375 GeV.
2566 This insures that all gauginos except the lightest neutralino are too heavy to be pro-

2567 duced in significant numbers at the LHC. All other mass parameters except for M_3
 2568 (\sim gluino mass) and $m_{\tilde{q}}$ (\sim first- and second-generation squark mass) are set to 3.5
 2569 TeV, which insures that squark/gluino decay to intermediate states such as third-
 2570 generation squarks or any flavor of lepton is strongly suppressed. Every mass param-
 2571 eter except for M_1 , M_3 , and $m_{\tilde{q}}$ is set so large that it has essentially no effect on
 2572 the sparticle dynamics that can be observed in LHC collisions, which are completely
 2573 determined by M_1 , M_3 , and $m_{\tilde{q}}$. The high-mass parameters are decoupled from the
 2574 relevant part of the spectrum. M_3 and $m_{\tilde{q}}$ are scanned over from $M_3 = m_{\tilde{q}} = 400$ GeV
 2575 to $M_3 = m_{\tilde{q}} = 2$ TeV in 80-GeV steps. The resulting simplified model consists only
 2576 of a gluino, first- and second-generation squarks, and the lightest neutralino and its
 2577 decay products (the gravitino is forced to be the LSP). The scan in M_3 - $m_{\tilde{q}}$ space illu-
 2578 minates the sensitivity of the two-photon search to different levels of signal hadronic
 2579 activity.

2580 The second scan is identical to the first except that the values of M_1 and M_2 are
 2581 inverted ($M_1 = 3.5$ TeV and $M_2 = 375$ GeV). In this case, M_1 is decoupled from
 2582 the relevant part of the spectrum. This corresponds to the wino NLSP scenario of
 2583 Sec. 3.5. Now, both the lightest neutralino and the lightest chargino have masses of
 2584 order 375 GeV, and are therefore produced with approximately equal frequency in
 2585 the gluino and squark decays. The chargino decays to $W + \tilde{G}$, so final states in this
 2586 scan often include leptons or large jet multiplicity. Since there is no guarantee that
 2587 two neutralinos will be produced and will decay to two photons, this search is not
 2588 well optimized for the wino NLSP scenario. However, a related CMS search with one
 2589 photon and ≥ 3 jets has an exclusion reach of ~ 1 TeV in M_3 and $m_{\tilde{q}}$ for this scenario
 2590 [59].

2591 The third scan is M_3 vs. M_1 for $m_{\tilde{q}}$, M_2 , and all other mass parameters equal to
 2592 2.5 TeV (decoupled). M_3 is scanned from 160 GeV to 2 TeV in 80-GeV steps, while
 2593 M_1 is scanned from 150 GeV to 1050 GeV in 100-GeV steps. $M_3 < M_1$ is not allowed,

as this would imply that the gluino, not the lightest neutralino, is the NLSP. This scan highlights the performance of the two-photon search as a function of M_1 (i.e. as a function of decays open to the neutralino), whereas the previous two scans keep M_1 fixed.

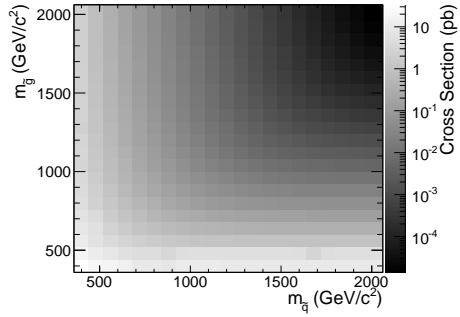
For each scan, the sparticle mass spectrum is generated with SuSpect 2.41 [141] and the decay widths with SDECAY 1.3 [142]. The event data (including production, unstable particle decay, parton showering, and hadronization) is generated with Pythia 6.422 [143], using the sparticle mass spectra and decay widths as inputs. The gravitino is always forced to be the LSP. The simulated data are reconstructed with CMSSWv4.2.2, which uses a detector simulation based on GEANT 4 [144]. Next to leading order cross sections are calculated with PROSPINO 2.1 [145], and shown in Figure 8.1 for the three signal MC scenarios.

8.2 Upper Limit Calculation and Model Exclusion

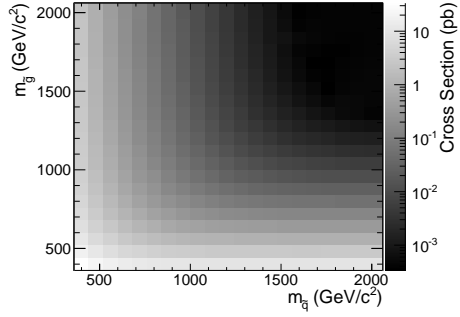
The upper limits are calculated according to the prescription followed for the 2011 ATLAS + CMS Higgs limit combination [146]. This prescription utilizes the frequentist CL_s method [147] with profile likelihood test statistic [148]. The CL_s method and the profile likelihood are explained in Section 8.2.2, using specific signal MC points to illustrate the procedure. First, however, the signal MC acceptance \times efficiency, which is an input to the limit setting procedure, is presented in Section 8.2.1.

8.2.1 Signal Acceptance \times Efficiency

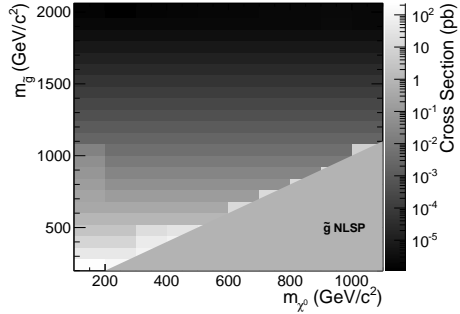
The signal acceptance \times efficiency (denoted $\mathcal{A} \times \epsilon$), defined for each signal point as the number of $\gamma\gamma$ events selected with $\cancel{E}_T \geq 50$ GeV divided by the total number of events generated, is shown in Figure 8.2 for the three different scenarios described in Sec. 8.1. Acceptance refers to the fraction of true events that can be detected given



(a) M_2 decoupled ($M_2 = 3.5$ TeV), $M_1 = 375$ GeV, M_3 vs. $m_{\tilde{q}}$.



(b) M_1 decoupled ($M_1 = 3.5$ TeV), $M_2 = 375$ GeV, M_3 vs. $m_{\tilde{q}}$.



(c) $m_{\tilde{q}}$ decoupled ($m_{\tilde{q}} = 2.5$ TeV), M_3 vs. M_1 .

Figure 8.1: Next to leading order cross sections for the three different MC scenarios described in the text.

2618 the fiducial extent of the detector and the E_T cuts on the photons. Efficiency denotes
 2619 the fraction of accepted events (i.e. those events passing the E_T and η cuts) that have
 2620 two photons passing the photon identification criteria.

2621 In Figs. 8.2(a) and 8.2(b), the large drop in $\mathcal{A} \times \epsilon$ for $m_{\tilde{q}} > M_3$ is due to an increase
 2622 in the number of jets produced per event and a consequent reduction in the number
 2623 of photons that pass the $I_{\text{comb}} < 6$ GeV cut. For $m_{\tilde{q}} > M_3$, there is more phase space
 2624 available to produce gluinos in the hard scatter than squarks. However, since gluinos
 2625 must decay via squarks, and in these models all squarks are heavier than the gluino,
 2626 only the two-jet decay $\tilde{g} \rightarrow q\tilde{q}\chi^0$ is available. Conversely, when $m_{\tilde{q}} < M_3$, there is
 2627 more phase space available to produce squarks, which may then decay via one jet as
 2628 $\tilde{q} \rightarrow q\tilde{\chi}^0$. Jets in SUSY events may be very close to the neutralino decay photons,
 2629 and as a result the photons may fail the strict isolation requirements, leading to lower
 2630 $\mathcal{A} \times \epsilon$ for jet-rich events. The worsened acceptance along $M_3 = 400$ GeV and $m_{\tilde{q}} = 400$
 2631 GeV in Fig. 8.2(b) is due to efficiency of the jet cut, which decreases drastically as
 2632 M_3 and $m_{\tilde{q}}$ approach M_1 because of shrinking phase space to produce hard jets in
 2633 the squark and gluino decays to neutralinos.

2634 The broad peak in $\mathcal{A} \times \epsilon$ shown in Fig. 8.2(a) for $m_{\tilde{q}} < M_3$ and ~ 600 GeV $<$
 2635 $m_{\tilde{q}} < \sim 1600$ GeV is due to the $E_T > 50$ GeV cut. The efficiency of the cut
 2636 decreases as $m_{\tilde{q}}$ decreases because of the fixed M_1 of 375 GeV. If the squark-neutralino
 2637 mass splitting gets too small, the likelihood of producing an energetic enough gravitino
 2638 to pass the \cancel{E}_T cut decreases.

2639 $\mathcal{A} \times \epsilon$ is generally much lower for the $M_2 = 375$ GeV grid (Figs. 8.2(c) and 8.2(d))
 2640 due to the larger contribution from chargino decays to $W + \tilde{G}$, which do not give rise
 2641 to photons in the final state. The increased acceptance for $M_3 > m_{\tilde{q}}$ is due to the
 2642 same jet multiplicity issue affecting the $M_1 = 375$ GeV grid. As M_3 and $m_{\tilde{q}}$ increase
 2643 relative to the fixed M_2 , the jets from squark and gluino decay get more energetic,
 2644 increasing the chance that they will overlap with the neutralino decay photon and

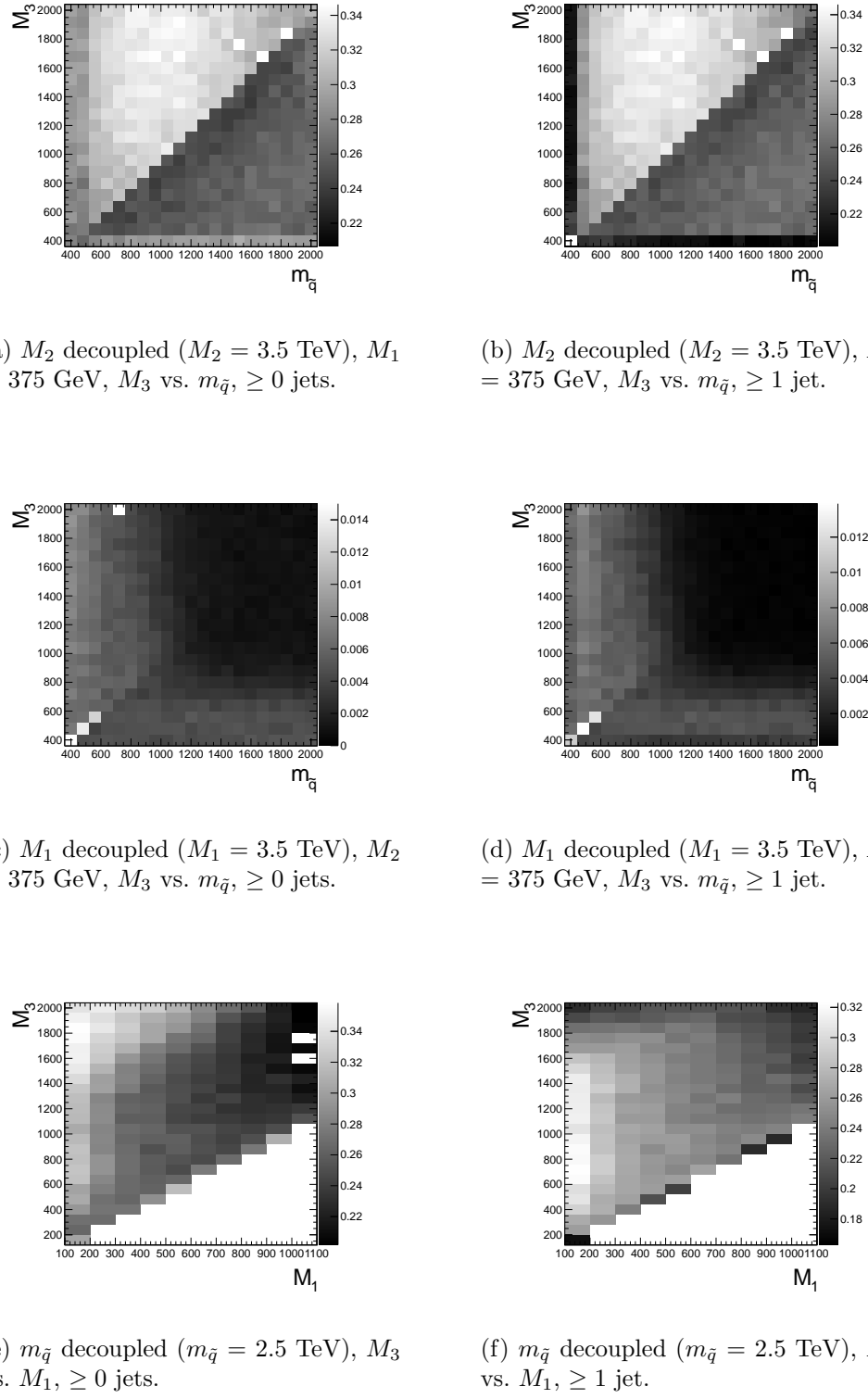


Figure 8.2: Signal acceptance \times efficiency (defined in the text) for the three different scenarios described in Sec. 8.1.

cause it to fail the isolation cut. For $m_{\tilde{q}} \gtrsim 1$ TeV and $M_3 \gtrsim 800$ GeV, the acceptance is so low that not enough events were simulated to see the acceptance decrease over the statistical error.

In Fig. 8.2(e), the neutralino is always heavy enough to guarantee decay to a photon that can pass the 40 GeV p_T cut. $\mathcal{A} \times \epsilon$ increases as M_3 increases because the larger gluino-neutralino mass splitting gives the neutralino a larger kinetic energy, increasing the chance that it will decay to a photon with 40 GeV p_T or higher. After the bino mass increases beyond the threshold needed to produce high p_T photons, $\mathcal{A} \times \epsilon$ decreases with increasing M_1 , independent of gluino mass, because higher M_1 means more phase space is open to decays of the form $\tilde{\chi}_1^0 \rightarrow Z\tilde{G}$ and $\tilde{\chi}_1^0 \rightarrow H\tilde{G}$. The two-photon search is naturally not as efficient for these decays.

There is a small chance that some real GMSB signal events could be reconstructed as ff events in the data. To correct the signal acceptance for this effect, the number of signal events reconstructed as ff events is subtracted from the number of signal $\gamma\gamma$ events, effectively reducing the signal acceptance. This is generally a small correction ($\sim 5\%$).

8.2.2 CL_s and the Profile Likelihood Test Statistic

The process of setting a cross section upper limit entails (1) defining a test statistic, (2) generating a distribution for that test statistic under the signal + background and background-only hypotheses, and (3) deciding whether or not the observed value of the test statistic is more compatible with the signal + background (i.e. weaker upper limit) or background-only (i.e. stronger upper limit) hypotheses by considering where it falls within the test statistic distributions. An important requirement on the choice of test statistic is that it be able to effectively discriminate between the signal + background and background-only hypotheses, i.e. the shape of its distribution for these two hypotheses should be different. The procedure for determining the exclud-

ability of a particular model given the value of the test statistic observed should not give rise to pathological behavior in the presence of small signals, low statistics, or weak sensitivity to models, as is commonly the case in high energy physics. These demands on the test statistic and the limit setting procedure itself dictate the choice of the profile likelihood test statistic and CL_s procedure.

In the remainder of this section, the notation is taken from ref. [146].

Profile Likelihood

For a specific model of GMSB, the limit setting procedure concerns the question of whether to reject the signal + background hypothesis $\mu s+b$ in favor of the background-only (Standard Model) hypothesis of b ($\mu = 0$). μ is a dimensionless signal strength parameter. s is the expected number of signal events, calculated from MC simulated signal events as in Secs. 8.1 and 8.2.1. b is the expected number of background events, estimated in Chap. 7. By the Neyman-Pearson lemma [149], the ratio of the likelihood of $\mu s+b$ to the likelihood of b is the test statistic with the highest power to reject $\mu s+b$ at whatever confidence level is desired. In practice, this means that the likelihood ratio is the best discriminator between the GMSB and Standard Model hypotheses.

The likelihood of the signal + background hypothesis as a function of the data (either real or generated) is defined as

$$\mathcal{L}(\text{data}|\mu, \theta) = \prod_{i=1}^N \frac{(\mu s_i(\theta) + b_i(\theta))^{n_i}}{n_i!} e^{-\mu s_i(\theta) - b_i(\theta)} p(\tilde{\theta}|\theta) \quad (8.1)$$

where $N = 5$ is the number of E_T bins used in the analysis ([50, 60) GeV, [60, 70) GeV, [70, 80) GeV, [80, 100) GeV, and [100, ∞) GeV); $s_i(\theta)$ and $b_i(\theta)$ are the expected number of signal and background events in E_T bin i , respectively; n_i is the number of events observed in E_T bin i ; and θ represents all the nuisance parameters

(uncertainties). $p(\tilde{\theta}|\theta)$ represents the product of probability distribution functions (PDFs) for the nuisance parameters, where $\tilde{\theta}$ is the default value of the nuisance parameter. In this analysis, there are eight experimental nuisance parameters per E_T bin, given here as relative errors on the expected number of signal events:

- Uncertainty on the measured integrated luminosity (4.5% in all bins) [150]
- Uncertainty on the signal acceptance due to $\epsilon_e^{\text{data}}/\epsilon_e^{\text{MC}}$ and the pixel veto efficiency error (cf. Sec. 6.4.2) (8% in all bins)
- Uncertainty on the signal acceptance due to imperfect pileup simulation (2.6% in all bins)
- Systematic uncertainty on QCD background prediction due to difference between ff and ee estimates (5.5%-53% of the QCD background depending on bin)
- Systematic uncertainty on electroweak background prediction due to p_T dependence of $f_{e \rightarrow \gamma}$ (29%-30% of the electroweak background depending on bin)
- Statistical uncertainty on the signal acceptance (1.8%-100% depending on model and bin)
- Statistical uncertainty on the QCD background prediction (7.2%-38% of the QCD background depending on bin)
- Statistical uncertainty on the electroweak background prediction (3.6%-7.2% of the electroweak background depending on bin)

and one very small theoretical nuisance parameter: the uncertainty on the signal acceptance due to underlying parton distribution function (PDF) uncertainties. In the limit-setting code, the uncertainties on signal acceptance due to photon efficiency and PDF errors are added in quadrature and treated as one. The uncertainty on the

2717 signal acceptance due to jet energy correction uncertainties is negligible, due to the
 2718 presence of many hard jets in GMSB signal events. The uncertainties on integrated
 2719 luminosity and pileup are 100% correlated between \cancel{E}_T bins, and the uncertainty on
 2720 signal acceptance can usually be treated similarly because the error on $\epsilon_e^{\text{data}}/\epsilon_e^{\text{MC}}$ often
 2721 dominates the PDF error on acceptance (although these three uncertainties are 0%
 2722 correlated with each other).

2723 To estimate the uncertainty due to imperfect simulation of LHC pileup, the square
 2724 of the average data efficiency for photons over the range 1-15 reconstructed primary
 2725 vertices (see Fig. 6.18(a)), weighted by the number of $\gamma\gamma$ events per primary vertex
 2726 bin, is calculated. The efficiency per primary vertex bin is estimated from a linear
 2727 fit to Fig. 6.18(a). The process is repeated for MC using the entire range of primary
 2728 vertices in Fig. 6.18(a) (all MC signal points have the same pileup simulation). The
 2729 error is taken as $2 \times |\text{avg. data efficiency squared} - \text{avg. MC efficiency squared}| / (\text{avg.}$
 2730 data efficiency squared + avg. MC efficiency squared).

2731 Each nuisance parameter PDF is modeled by a log-normal distribution:

$$p(\tilde{\theta}|\theta) = \frac{1}{\sqrt{2\pi} \ln \kappa} \exp\left(-\frac{(\ln \tilde{\theta}/\theta)^2}{2(\ln \kappa)^2}\right) \frac{1}{\tilde{\theta}} \quad (8.2)$$

2732 where $\tilde{\theta} = 1$ and $\kappa = 1 + \text{the one-standard-deviation relative error on the nuisance}$
 2733 parameter (e.g. for the 4.5% error due to integrated luminosity, $\kappa = 1.045$).

2734 Similarly, the likelihood of the background-only hypothesis as a function of the
 2735 data (either real or generated) is defined as

$$\mathcal{L}(\text{data}|0, \theta) = \prod_{i=1}^N \frac{b_i(\theta)^{n_i}}{n_i!} e^{-b_i(\theta)} p(\tilde{\theta}|\theta) \quad (8.3)$$

2736 The profile likelihood test statistic is defined as

$$\tilde{q}_\mu = -2 \ln \frac{\mathcal{L}(\text{data}|\mu, \hat{\theta}_\mu)}{\mathcal{L}(\text{data}|\hat{\mu}, \hat{\theta})}, 0 \leq \hat{\mu} \leq \mu \quad (8.4)$$

where the $\hat{\theta}_\mu$ maximize $\mathcal{L}(\text{data}|\mu, \hat{\theta}_\mu)$ when it is evaluated at a particular μ , and $\hat{\mu}$ and $\hat{\theta}$ are the global maximum likelihood estimators of μ and θ . The condition $\hat{\mu} \leq \mu$ insures that the obtained cross section upper limit is one-sided, i.e. there is no possibility to find a lower limit on the cross section. The profile likelihood test statistic has the nice property that in the asymptotic (large statistics) limit its PDF can be approximated by analytic formulae, eliminating the need to generate multiple toy experiments to get the PDF. However, the approximation breaks down for small numbers of observed events, so in practice the asymptotic limit is only used as a first guess at the location of the true limit.

The PDFs $f(\tilde{q}_\mu|\mu, \hat{\theta}_\mu^{\text{obs}})$ and $f(\tilde{q}_\mu|0, \hat{\theta}_0^{\text{obs}})$ for the profile likelihood test statistic under the signal + background and background-only hypotheses, respectively, are obtained by generating toy MC pseudo-experiments. $\hat{\theta}_\mu^{\text{obs}}$ and $\hat{\theta}_0^{\text{obs}}$ maximize Eqs. 8.1 and 8.3, respectively, when they are evaluated for the observed data. For each μ (and the background-only hypothesis $\mu = 0$), the pseudo-experiments are generated by picking random values of s and b from a Poisson distribution with the θ fixed as just described.

CL_s

In the classical frequentist approach, a signal model may be excluded at the 95% confidence level (CL) if the probability of any measurement of the test statistic to be greater than or equal to the observed value given the signal + background hypothesis is 5%. This means that the observed value of the test statistic is so incompatible with what one would expect to observe if the signal model were true that, under the

2759 assumption that the signal model *is* true, the chance of observing a test statistic even
 2760 further afield from the signal expectation is only 5%. Mathematically,

$$\begin{aligned} p_\mu &\equiv P(\tilde{q}_\mu \geq \tilde{q}_\mu^{\text{obs}} | \mu s + b) = \int_{\tilde{q}_\mu^{\text{obs}}}^{\infty} f(\tilde{q}_\mu | \mu, \hat{\theta}_\mu^{\text{obs}}) d\tilde{q}_\mu \\ p_\mu &\leq 0.05 \Rightarrow \text{exclude } \mu \end{aligned} \quad (8.5)$$

2761 where $\tilde{q}_\mu^{\text{obs}}$ is the observed value of the test statistic and p_μ is the p-value. As indicated
 2762 in Eq. 8.5, the p-value is simply the integral of the PDF of \tilde{q}_μ from $\tilde{q}_\mu^{\text{obs}}$ to infinity.

2763 By construction, the classical 95% CL frequentist approach described above will
 2764 reject a true signal + background hypothesis 5% of the time. This can happen if the
 2765 experiment gets “unlucky” and the observation fluctuates low, causing $\tilde{q}_\mu^{\text{obs}}$ to fall in
 2766 the tail of the \tilde{q}_μ distribution. This poses a problem for the case of very weak signals
 2767 ($\mu \sim 0$), because it will lead to spurious exclusions of models to which the experiment
 2768 has little sensitivity. To avoid this pitfall, the CL_s limit setting method is used.

2769 In the CL_s method, the classical frequentist p-value of Eq. 8.5 is simply divided by
 2770 one minus the p-value of the background-only hypothesis, and it is this ratio, rather
 2771 than the p-value of the signal + background hypothesis alone, that is required to be
 2772 ≤ 0.05 . Mathematically,

$$1 - p_0 \equiv P(\tilde{q}_\mu \geq \tilde{q}_\mu^{\text{obs}} | b) = \int_{\tilde{q}_\mu^{\text{obs}}}^{\infty} f(\tilde{q}_\mu | 0, \hat{\theta}_0^{\text{obs}}) d\tilde{q}_\mu \quad (8.6)$$

$$\text{CL}_s(\mu) \equiv \frac{p_\mu}{1 - p_0} \quad (8.7)$$

$$\text{CL}_s(\mu) \leq 0.05 \Rightarrow \text{exclude } \mu$$

2773 where p_0 is the p-value for the background-only hypothesis ($\mu = 0$). In the case of
 2774 low sensitivity to μ , $p_\mu \lesssim 1 - p_0$, so $\text{CL}_s(\mu) \lesssim 1$ and μ will not be excluded. On the

contrary, for high sensitivity to μ ($\mu s \gg \sigma_b$), $p_\mu \ll 1 - p_0$, so models that can be excluded by the criterion $p_\mu \leq 0.05$ will also be excluded by the criterion $\text{CL}_s \leq 0.05$. Compared to the classical frequentist method, CL_s limits can be a little stronger in the case of low signal sensitivity [146].

To determine the upper limit on the cross section of a particular model, the lowest value of μ for which $\text{CL}_s(\mu) \leq 0.05$, denoted $\mu^{95\% \text{ CL}}$, is found. The cross section upper limit of that model is then simply $\mu^{95\% \text{ CL}}$ multiplied by the expected cross section of the model (cf. Fig. 8.1).

In contrast to the observed upper limit, the expected upper limit is calculated from an ensemble of background-only MC pseudo-experiments. The distribution $f(\mu_{\text{pseudo}}^{95\% \text{ CL}})$ is plotted (one entry per pseudo-experiment). The median expected upper limits and $\pm 1\sigma$ and $\pm 2\sigma$ bands are defined as

$$0.5 = \int_0^{\mu_{\text{exp}}^{95\% \text{ CL}}} f(\mu_{\text{pseudo}}^{95\% \text{ CL}}) d\mu_{\text{pseudo}}^{95\% \text{ CL}} \quad (8.8)$$

$$0.16 = \int_0^{\mu_{-1\sigma,\text{exp}}^{95\% \text{ CL}}} f(\mu_{\text{pseudo}}^{95\% \text{ CL}}) d\mu_{\text{pseudo}}^{95\% \text{ CL}} \quad (8.9)$$

$$0.84 = \int_0^{\mu_{+1\sigma,\text{exp}}^{95\% \text{ CL}}} f(\mu_{\text{pseudo}}^{95\% \text{ CL}}) d\mu_{\text{pseudo}}^{95\% \text{ CL}} \quad (8.10)$$

$$0.025 = \int_0^{\mu_{-2\sigma,\text{exp}}^{95\% \text{ CL}}} f(\mu_{\text{pseudo}}^{95\% \text{ CL}}) d\mu_{\text{pseudo}}^{95\% \text{ CL}} \quad (8.11)$$

$$0.975 = \int_0^{\mu_{+2\sigma,\text{exp}}^{95\% \text{ CL}}} f(\mu_{\text{pseudo}}^{95\% \text{ CL}}) d\mu_{\text{pseudo}}^{95\% \text{ CL}} \quad (8.12)$$

The technical procedure followed to calculate the 95% CL cross section upper limits for each GMSB model tested is given below.

1. Calculate a guess for the median expected limit and $\pm 2\sigma$ error bands ($\mu_{\pm 2\sigma, \text{guess}}^{95\% \text{ CL}}$) using the asymptotic formulae for $f(\tilde{q}_\mu | 0, \hat{\theta}_0^{\text{obs}})$.

2. Calculate observed ($\mu_{\text{obs,asym}}^{95\% \text{ CL}}$), median expected ($\mu_{\text{exp,asym}}^{95\% \text{ CL}}$), and $\pm 1\sigma$ ($\mu_{\pm 1\sigma, \text{asym}}^{95\% \text{ CL}}$)

2792 and $\pm 2\sigma$ ($\mu_{\pm 2\sigma, \text{asym}}^{95\% \text{CL}}$) expected CL_s limits using the asymptotic formulae for
 2793 $f(\tilde{q}_\mu | \mu, \hat{\theta}_\mu^{\text{obs}})$ and $f(\tilde{q}_\mu | 0, \hat{\theta}_0^{\text{obs}})$. Restrict the range of $\mu_{\text{obs}, \text{asym}}^{95\% \text{CL}}$ and $\mu_{\text{exp}, \text{asym}}^{95\% \text{CL}}$ to
 2794 $[0, 5 \times \mu_{\pm 2\sigma, \text{guess}}^{95\% \text{CL}}]$ (this avoids pathological behavior of the limit-setting code
 2795 when the expected number of signal events is much greater than the observed
 2796 number of events and only introduces a $\sim 5\%$ upward bias in the observed limit,
 2797 well within the $\pm 1\sigma$ error bands).

- 2798 3. Calculate median expected ($\mu_{\text{exp}}^{95\% \text{CL}}$) and $\pm 1\sigma$ ($\mu_{\pm 1\sigma}^{95\% \text{CL}}$) and $\pm 2\sigma$ ($\mu_{\pm 2\sigma}^{95\% \text{CL}}$) ex-
 2799 pected CL_s limits using 100 toy MC pseudo-experiments to generate $f(\tilde{q}_\mu | \mu, \hat{\theta}_\mu^{\text{obs}})$
 2800 and $f(\tilde{q}_\mu | 0, \hat{\theta}_0^{\text{obs}})$. Restrict the range of $\mu_{\text{exp}}^{95\% \text{CL}}$ to $[0, 5 \times \mu_{\pm 2\sigma, \text{guess}}^{95\% \text{CL}}]$.
- 2801 4. If $\mu_{\pm 2\sigma}^{95\% \text{CL}}$ could not be calculated, set $\mu_{\pm 2\sigma}^{95\% \text{CL}} = \mu_{\pm 2\sigma, \text{asym}}^{95\% \text{CL}}$ instead.
- 2802 5. If $\mu_{+2\sigma}^{95\% \text{CL}} \neq \mu_{-2\sigma}^{95\% \text{CL}}$ and $\mu_{\text{obs}, \text{asym}}^{95\% \text{CL}} > 0.0001$:
 - 2803 • If $\mu_{\text{obs}, \text{asym}}^{95\% \text{CL}} > \mu_{+2\sigma}^{95\% \text{CL}}$, set $\mu_{+2\sigma}^{95\% \text{CL}} = 1.3 \times \mu_{\text{obs}, \text{asym}}^{95\% \text{CL}}$.
 - 2804 • If $\mu_{\text{obs}, \text{asym}}^{95\% \text{CL}} < \mu_{-2\sigma}^{95\% \text{CL}}$, set $\mu_{-2\sigma}^{95\% \text{CL}} = 0.7 \times \mu_{\text{obs}, \text{asym}}^{95\% \text{CL}}$.
- 2805 6. If $\mu_{+2\sigma}^{95\% \text{CL}} = \mu_{-2\sigma}^{95\% \text{CL}}$, set $\mu_{\pm 2\sigma}^{95\% \text{CL}} = \mu_{\pm 2\sigma, \text{asym}}^{95\% \text{CL}}$ instead.
- 2806 7. Scan over 100 equally spaced test values of μ between $\mu_{-2\sigma}^{95\% \text{CL}}$ and $\mu_{+2\sigma}^{95\% \text{CL}}$ and,
 2807 if $\mu > 0.0001$, calculate the CL_s p-value (p_μ) for this test value of μ to 10^{-6}
 2808 precision using a minimum of 500 toy experiments to generate $f(\tilde{q}_\mu | \mu, \hat{\theta}_\mu^{\text{obs}})$ and
 2809 $f(\tilde{q}_\mu | 0, \hat{\theta}_0^{\text{obs}})$.
- 2810 8. Determine the observed ($\mu_{\text{obs}, \text{scan}}^{95\% \text{CL}}$), median expected ($\mu_{\text{exp}, \text{scan}}^{95\% \text{CL}}$), and $\pm 1\sigma$ ($\mu_{\pm 1\sigma, \text{scan}}^{95\% \text{CL}}$)
 2811 and $\pm 2\sigma$ ($\mu_{\pm 2\sigma, \text{scan}}^{95\% \text{CL}}$) expected CL_s limits from the scan p-values for the signal
 2812 + background and background-only pseudo-experiments.

2813 Finally, a particular GMSB model is excluded if the upper limit on the cross
 2814 section for that model is less than the expected theoretical cross section.

2815 8.3 Cross Section Upper Limits

2816 Figure 8.3 shows the observed upper limits on the cross sections for the models de-
 2817 scribed in Sec. 8.1. In some ($\mathcal{O}(10^{-3})$) cases, the upper limit is zero due to a compu-
 2818 tational failure. The upper limit for these points is estimated from the average of the
 2819 upper limits of the four neighboring points, as shown in Figure 8.4. If any of the four
 2820 points is also missing a valid upper limit, it is dropped from the average. The errors
 2821 on the individual upper limits used in the estimate are propagated to the error on
 2822 the average.

2823 8.4 Exclusion Contours

2824 Exclusion contours for the GMSB models discussed above are shown in Figure 8.5. The
 2825 contours are derived from plots of predicted cross section minus cross section upper
 2826 limit ($\sigma \times (1 - \mu^{95\%CL})$), where σ is the nominal value of the predicted cross section
 2827 for a given GMSB model) vs. the two model parameters of interest, so the values are
 2828 either negative (not excluded) or positive (excluded). Sometimes, a particular point
 2829 may have a different sign than its four same-sign neighbors (cf. Fig. 8.4) due to a
 2830 fluctuation. In these cases, $\sigma \times (1 - \mu^{95\%CL})$ for the anomalous point is estimated
 2831 as the average $\sigma \times (1 - \mu^{95\%CL})$ of the four neighboring points. The errors on the
 2832 individual values of $\sigma \times (1 - \mu^{95\%CL})$ used in the estimate are propagated to the error
 2833 on the average.

2834 In the plots in Fig. 8.5, the expected limit (i.e. the contour derived from $\sigma \times (1 -$
 2835 $\mu_{\text{exp,scan}}^{95\%CL})$) is drawn in dark orange and the 1σ experimental band around the expected
 2836 limit (i.e. the shaded region between the contours derived from $\sigma \times (1 - \mu_{\pm 1\sigma, \text{scan}}^{95\%CL})$) is
 2837 drawn in light orange. The values of $\mu_{\text{exp,scan}}^{95\%CL}$ and $\mu_{\pm 1\sigma, \text{scan}}^{95\%CL}$ only reflect the experimental
 2838 uncertainties given in Sec. 8.2.2.

2839 The observed limits (derived from $\sigma \times (1 - \mu_{\text{obs,scan}}^{95\%CL})$) and 1σ theoretical error

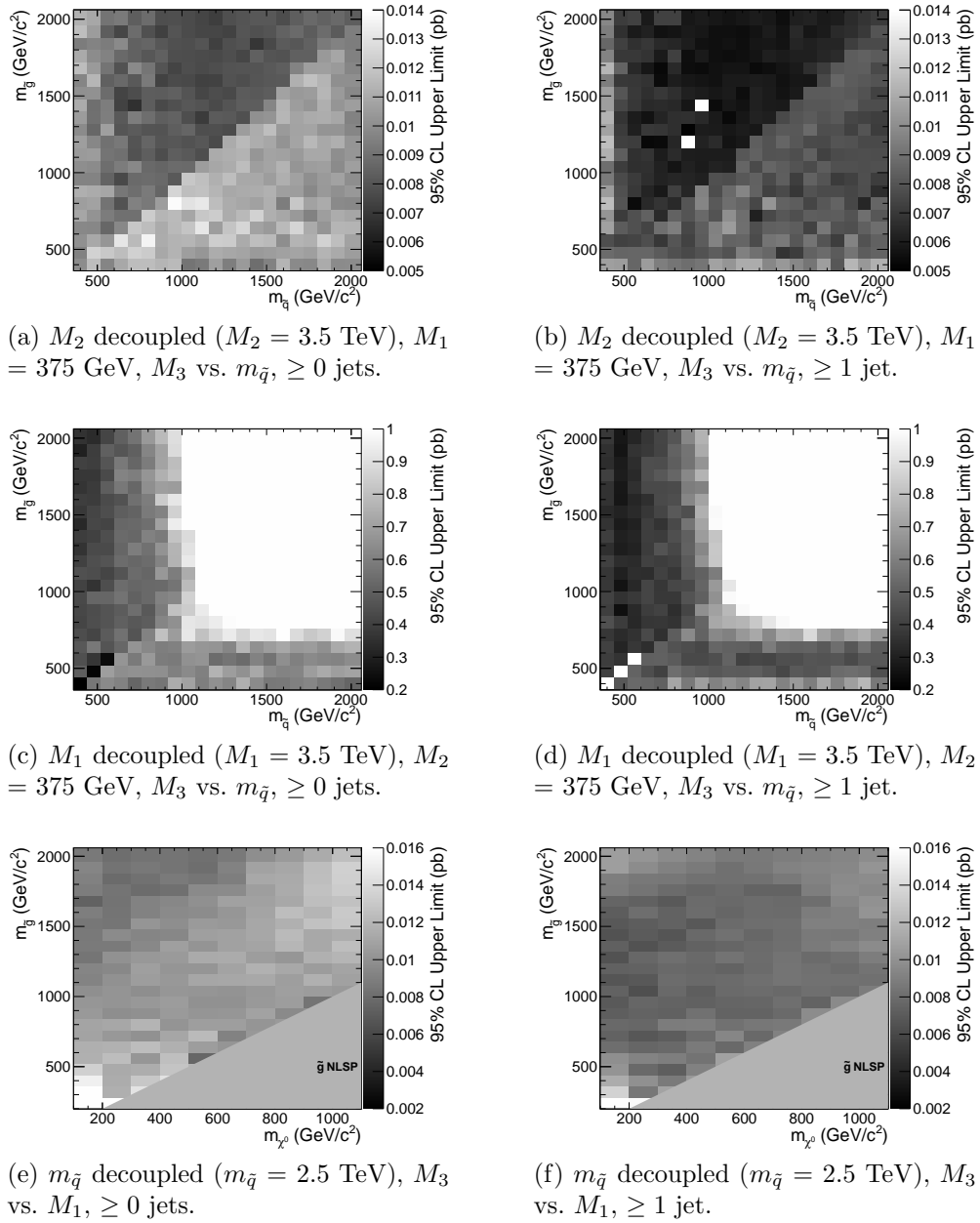


Figure 8.3: Cross section upper limits for the three different scenarios described in Sec. 8.1.

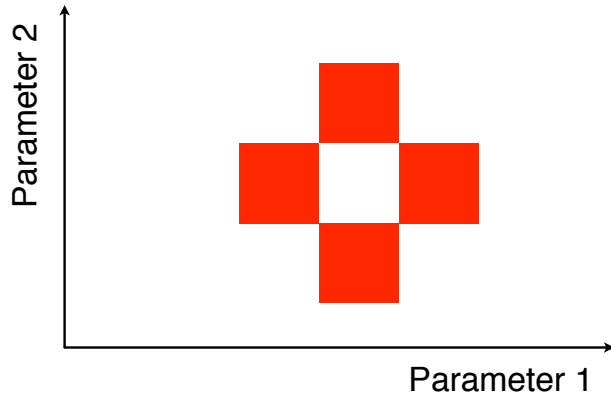


Figure 8.4: Diagram of the points (red squares) used in the estimation of an upper limit when a computational failure occurs (middle white square).

2840 bands around the observed limits in Fig. 8.5 are drawn in blue. The contours that
 2841 define this band are derived from $\pm(\sigma_{\pm 1\sigma} - \sigma\mu_{\text{obs,scan}}^{95\% \text{CL}})$, where $\sigma_{\pm 1\sigma}$ is the nominal
 2842 value of the predicted cross section \pm the one-standard-deviation theoretical error on
 2843 the predicted cross section. In this way, the experimental and theoretical errors, the
 2844 latter due to imperfect knowledge of the predicted cross section, are shown separately.
 2845 Comparing with Fig. 8.1, one can easily see that the shapes of the exclusion curves
 2846 are driven by the contours in the expected cross section plane. In all the plots, the
 2847 observed limit is slightly higher than the expected limit, reflecting the fact that the
 2848 background prediction is slightly higher than the observation.

2849 The dominant theoretical uncertainties on the GMSB cross sections are due to:
 2850

- PDF uncertainty (4%-100% depending on model)
- Renormalization scale uncertainty (0.036%-25% depending on model)

2852 The PDF4LHC [151–153] recommendations are used to calculate the effect of these
 2853 uncertainties on the GMSB cross sections. The recommendations state that PDF sets

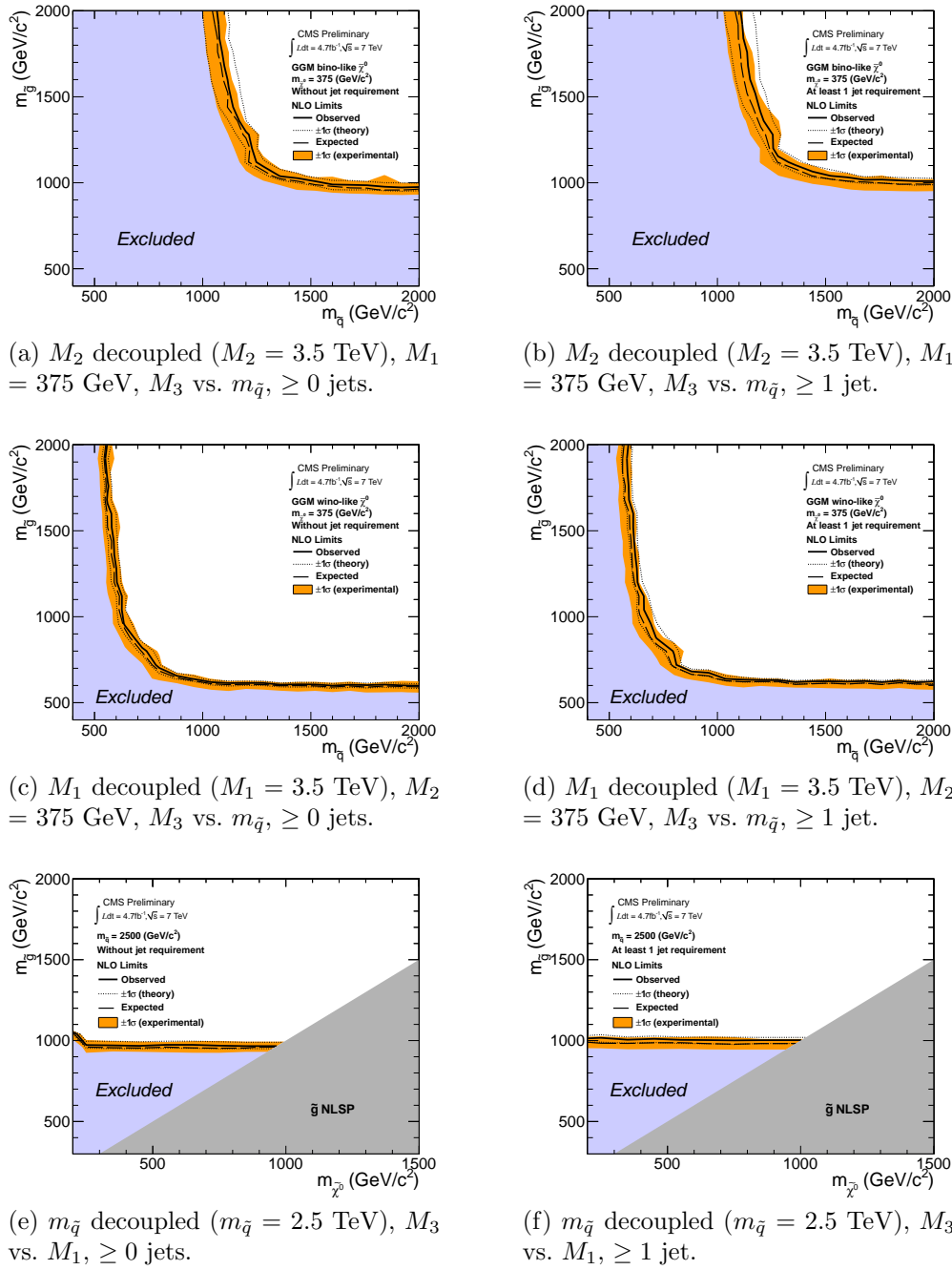


Figure 8.5: Exclusion contours for the three different scenarios described in Sec. 8.1.

2854 from MSTW08 [154], CTEQ6.6 [155], and NNPDF2.0 [156] should be considered in
 2855 the determination of the PDF uncertainties, because these three PDF sets include
 2856 constraints from the Tevatron and from fixed target experiments, as well as from
 2857 HERA [157], and are thus the most complete.

2858 Each collaboration's PDF prediction comes from a global fit to experimental data
 2859 with a certain number of free parameters. The best fit parameters come from minimiz-
 2860 ing the χ^2 ; increasing the χ^2 by one from its minimum can be written in terms of the
 2861 N -dimensional Hessian error matrix [158] where N is the number of free parameters.
 2862 To form the i^{th} pair of members of the PDF set, the PDF is evaluated once at the
 2863 parameter values given by the i^{th} eigenvector of the Hessian matrix, and then again
 2864 at the parameter values given by the negative of the i^{th} eigenvector. Each PDF set
 2865 therefore contains $2N$ members, corresponding to the positive and negative values of
 2866 the N eigenvectors [159].

2867 To calculate the PDF uncertainties for a given GMSB model, the leading order
 2868 Pythia cross section is reweighted by a factor of the error PDF divided by the leading
 2869 order PDF with which the model was generated. This is repeated for each error PDF
 2870 in a given PDF set. The $\pm 1\sigma$ deviations are proportional to the maximum difference
 2871 between cross sections obtained this way. The actual equation for the $\pm 1\sigma$ errors is
 2872 Eq. (43) of ref. [159]. In the same way, the $\pm 1\sigma$ errors are calculated for the CTEQ6.6,
 2873 MSTW08, and NNPDF2.0 PDF sets. The total error is given by the half the difference
 2874 between the largest $+1\sigma$ deviation and the smallest -1σ deviation [151–153].

2875 The uncertainties on the signal cross sections due to the choice of renormaliza-
 2876 tion/factorization scale ($\alpha_S(M_Z)$) are evaluated by calculating the PROSPINO next
 2877 to leading order cross section once with $\alpha_S(M_Z)$ halved, then once with $\alpha_S(M_Z)$ dou-
 2878 bled. The lower error on the cross section is taken as the absolute difference between
 2879 the nominal and halved-scale values of the cross section, while the upper error is taken
 2880 as the absolute difference between the nominal and doubled-scale values. The PDF

2881 and α_S uncertainties are added in quadrature to give the total PDF uncertainty.

2882 Note that the quoted GMSB cross sections are evaluated at next to leading order
2883 using PROSPINO, but it is the leading order Pythia cross sections that are reweighted
2884 to the next to leading order MSTW08, CTEQ6.6, and NNPDF2.0 PDFs to get the
2885 error bands. In addition, since to a good approximation the GMSB production cross
2886 sections for the M_3 - $m_{\tilde{q}}$ scans only depend on M_3 and $m_{\tilde{q}}$, the same PDF errors per
2887 point are used for the \tilde{B} -like and \tilde{W} -like grids.

2888 **Chapter 9**

2889 **Conclusion**

2890 The results of a search for evidence of new particle production via final states with
2891 2 photons, large \cancel{E}_T , and ≥ 0 or ≥ 1 jet in pp collisions at $\sqrt{s} = 7$ TeV have been
2892 presented. No deviation in the production rate from that predicted by the Standard
2893 Model has been found. The null results were used to constrain general models of
2894 gauge mediated supersymmetry breaking. In these types of models, gluinos and first-
2895 and second-generation squarks are restricted to masses above ~ 1 TeV.

2896 These bounds do not exclude supersymmetry. The gluinos and first- and second-
2897 generation squarks can be a little bit heavier (but not too much heavier than a few
2898 TeV) and still imply an elegant supersymmetric solution to the hierarchy problem.
2899 More importantly, the bounds on the first- and second-generation squarks say nothing
2900 about the stop squark, which is intimately connected to the Higgs mass. At one loop
2901 order in the supersymmetric Standard Model, the lightest Higgs mass is given by
2902 [160]

$$m_h^2 \lesssim m_Z^2 + \frac{3g^2 m_t^4}{8\pi^2 m_W^2} \left[\ln \frac{M_S^2}{m_t^2} + \frac{X_t^2}{M_S^2} \left(1 - \frac{X_t^2}{12M_S^2}\right) \right] \quad (9.1)$$

2903 where g is the $SU(2)_L$ coupling constant, M_S^2 is the average of the two observable

2904 stop squared masses, and X_t is a parameter that characterizes stop mixing. The Higgs
 2905 mass is directly sensitive to the stop mass, for which the only current lower bound of
 2906 330 GeV [161] is much weaker than for the first- and second-generation squarks (and
 2907 highly model dependent). The current hints of a Higgs with mass ~ 125 GeV [22, 23]
 2908 point to a stop mass below 2 TeV if SUSY is really a symmetry of nature, depending
 2909 on model.

2910 Future searches for GMSB could look for either direct pair production of stops
 2911 decaying via top quarks to neutralinos that then decay to photons, or for stops pro-
 2912 duced in the decay of a heavier pair-produced particle like the gluino. Looking for a
 2913 final state containing a top, antitop, and ≥ 1 photon may be advantageous because
 2914 the expected SM background should be small.

2915 Top quark reconstruction depends heavily on b jet identification. The same b tag-
 2916 ging techniques needed to find stops could also be applied to a search for a Higgsino-
 2917 like neutralino decaying primarily to $b\bar{b}$. If gaugino mixing were in a certain corner of
 2918 parameter space, then photon + $b\bar{b}$ events might provide a window onto GMSB.

2919 There are a number of interesting possibilities for future GMSB searches in ad-
 2920 dition to those just outlined. SUSY searches will likely remain a fruitful avenue of
 2921 investigation throughout the lifetime of the LHC.

²⁹²² **Appendix A**

²⁹²³ **Monte Carlo Samples**

²⁹²⁴ A number of MC samples are utilized in this analysis and referred to throughout the
²⁹²⁵ text. Below is a list of the MC samples used and an explanation of what the sample
²⁹²⁶ names mean.

²⁹²⁷ **A.1 List of Samples**

²⁹²⁸ 1. Drell-Yan + up to 2 hard jets:

²⁹²⁹ /DYJetsToLL_TuneZ2_M-50_7TeV-madgraph-tauola/
²⁹³⁰ Fall11-PU_S6_START42_V14B-v1/AODSIM

²⁹³¹ 2. QCD enriched with B and D meson decays to electrons:

²⁹³² /QCD_Pt-20to30_BCtoE_TuneZ2_7TeV-pythia6/
²⁹³³ Fall11-PU_S6_START42_V14B-v1/AODSIM,
²⁹³⁴ /QCD_Pt-30to80_BCtoE_TuneZ2_7TeV-pythia6/
²⁹³⁵ Fall11-PU_S6_START42_V14B-v1/AODSIM,
²⁹³⁶ /QCD_Pt-80to170_BCtoE_TuneZ2_7TeV-pythia6/
²⁹³⁷ Fall11-PU_S6_START42_V14B-v1/AODSIM

²⁹³⁸ 3. Photon + jet doubly enriched with jets passing an EM filter:

2939 /GJet_Pt-20_doubleEMEnriched_TuneZ2_7TeV-pythia6/
 2940 Fall11-PU_S6_START42_V14B-v1/AODSIM

2941 4. W leptonic decays + up to 2 hard jets:

2942 /WJetsToLNu_TuneZ2_7TeV-madgraph-tauola/
 2943 Fall11-PU_S6_START42_V14B-v1/AODSIM

2944 5. $t\bar{t}$ + up to 2 hard jets:

2945 /TTJets_TuneZ2_7TeV-madgraph-tauola/
 2946 Fall11-PU_S6_START42_V14B-v2/AODSIM

2947 A.2 Explanation of Naming Conventions

2948 • L: charged lepton

2949 • B: B hadron

2950 • C: D , or charmed, hadron

2951 • E: electron or positron

2952 • G: photon

2953 • W: W boson

2954 • Nu: neutrino

2955 • T: top quark

2956 • TuneZ2: Pythia tune incorporating 2010 LHC data with CTEQ6L1 [155] PDFs
 2957 [162]

2958 • M-50: Generated l^+l^- invariant mass threshold of 50 GeV

2959 • 7TeV: Generated center-of-mass energy 7 TeV

- 2960 ● **pythia6**: Parton showering and hadronization simulated with Pythia v6.424
- 2961 [143]
- 2962 ● **madgraph**: Hard interaction generated with MadGraph 5 [163]
- 2963 ● **tauola**: τ decays generated with Tauola [164]
- 2964 ● **PU_S6**: Generated with S6 pileup scenario, which has a mean between 6 and
- 2965 7 interactions per crossing, and includes pileup from the neighboring bunch
- 2966 crossings according to a Poisson distribution with mean equal to the number of
- 2967 interactions in the in-time crossing [165]
- 2968 ● **START42_V14B**: Reconstructed with best alignment and calibration constants
- 2969 and magnetic field conditions as of August 3, 2011
- 2970 ● **Pt_XtoY**: $X \leq$ generated $\hat{p}_T < Y$
- 2971 ● **BCToE**: Only keeps events if they contain at least one electron with $E_T > 10$
- 2972 GeV in $|\eta| < 2.5$ that came from a b or c quark
- 2973 ● **doubleEMEnriched**: Enriched in photons, electrons, electrons from b/c decay,
- 2974 and electromagnetic jets [166]
- 2975 ● **AODSIM**: Run through full CMS reconstruction algorithm based on a GEANT 4
- 2976 [144] detector simulation; AOD data tier, including generator-level information

2977 Bibliography

- 2978 [1] URL <http://cms.web.cern.ch/news/cms-detector-design>.
- 2979 [2] S. L. Glashow, Nucl. Phys. **22**, 579 (1961), URL <http://www.sciencedirect.com/science/article/pii/0029558261904692>.
- 2980 [3] S. L. Glashow, J. Iliopoulos, and L. Maiani, Phys. Rev. D **2**, 1285 (1970), URL <http://link.aps.org/doi/10.1103/PhysRevD.2.1285>.
- 2981 [4] J. Goldstone, A. Salam, and S. Weinberg, Phys. Rev. **127**, 965 (1962), URL <http://link.aps.org/doi/10.1103/PhysRev.127.965>.
- 2982 [5] S. Weinberg, Phys. Rev. Lett. **19**, 1264 (1967), URL <http://link.aps.org/doi/10.1103/PhysRevLett.19.1264>.
- 2983 [6] A. Salam and J. Ward, Phys. Lett. **13**, 168 (1964), URL <http://www.sciencedirect.com/science/article/pii/0031916364907115>.
- 2984 [7] M. Gell-Mann, Phys. Lett. **8**, 214 (1964), URL <http://www.sciencedirect.com/science/article/pii/S0031916364920013>.
- 2985 [8] G. Zweig, in *Developments in the Quark Theory of Hadrons*, edited by D. B. Lichtenberg and S. P. Rosen (Hadronic Press, Nonantum, MA, 1980), pp. 22–101.
- 2986 [9] J. Drees, Int. J. Mod. Phys. A **17**, 3259 (2002), URL <http://www.worldscinet.com/ijmpa/17/1723/S0217751X02012727.html>.

- 2996 [10] P. Higgs, Physics Letters **12**, 132 (1964), URL <http://www.sciencedirect.com/science/article/pii/0031916364911369>.
- 2997
- 2998 [11] P. W. Higgs, Phys. Rev. Lett. **13**, 508 (1964), URL <http://link.aps.org/doi/10.1103/PhysRevLett.13.508>.
- 2999
- 3000 [12] P. W. Higgs, Phys. Rev. **145**, 1156 (1966), URL <http://link.aps.org/doi/10.1103/PhysRev.145.1156>.
- 3001
- 3002 [13] I. Aitchison, *Supersymmetry in Particle Physics: An Elementary Introduction* (Cambridge Univ. Press, Cambridge, 2007).
- 3003
- 3004 [14] C. Quigg, in *Flavor Physics for the Millennium: TASI 2000 : Boulder, Colorado, US, 2000*, edited by J. L. Rosner (World Scientific, Singapore, 2001), p. 3, URL <http://arxiv.org/abs/hep-ph/0204104>.
- 3005
- 3006
- 3007 [15] L. Álvarez Gaumé and J. Ellis, Nat. Phys. **7**, 2 (2011), URL <http://dx.doi.org/10.1038/nphys1874>.
- 3008
- 3009 [16] G. Arnison et al. (UA1 Collaboration), Phys. Lett. B **122**, 103 (1983), URL <http://www.sciencedirect.com/science/article/pii/0370269383911772>.
- 3010
- 3011
- 3012 [17] G. Arnison et al. (UA1 Collaboration), Phys. Lett. B **126**, 398 (1983), URL <http://www.sciencedirect.com/science/article/pii/0370269383901880>.
- 3013
- 3014
- 3015 [18] J. F. Gunion, S. Dawson, H. E. Haber, and G. L. Kane, *The Higgs Hunter's Guide* (Westview, Boulder, CO, 1990).
- 3016
- 3017 [19] K. Nakamura et al. (Particle Data Group), J. Phys. G **37**, 075021 (2010), URL <http://stacks.iop.org/0954-3899/37/i=7A/a=075021>.
- 3018

- 3019 [20] S. P. Martin (2006), unpublished, arXiv:hep-ph/9709356, URL <http://arxiv.org/abs/hep-ph/9709356v6>.
- 3020
- 3021 [21] G. Jungman, M. Kamionkowski, and K. Griest, Phys. Rept. **267**,
3022 195 (1996), URL <http://www.sciencedirect.com/science/article/pii/0370157395000585>.
- 3023
- 3024 [22] S. Chatrchyan et al. (CMS Collaboration), Phys. Lett. B **710**, 26
3025 (2012), URL <http://www.sciencedirect.com/science/article/pii/S0370269312002055>.
- 3026
- 3027 [23] G. Aad et al., Phys. Lett. B **710**, 49 (2012), URL <http://www.sciencedirect.com/science/article/pii/S0370269312001852>.
- 3028
- 3029 [24] M. Dine and W. Fischler, Phys. Lett. B **110**, 227 (1982), URL <http://www.sciencedirect.com/science/article/pii/0370269382912412>.
- 3030
- 3031 [25] C. R. Nappi and B. A. Ovrut, Phys. Lett. B **113**, 175 (1982), URL <http://www.sciencedirect.com/science/article/pii/037026938290418X>.
- 3032
- 3033 [26] L. Alvarez-Gaumé, M. Claudson, and M. B. Wise, Nucl. Phys. B **207**,
3034 96 (1982), URL <http://www.sciencedirect.com/science/article/pii/0550321382901389>.
- 3035
- 3036 [27] M. Dine and A. E. Nelson, Phys. Rev. D **48**, 1277 (1993), URL <http://link.aps.org/doi/10.1103/PhysRevD.48.1277>.
- 3037
- 3038 [28] M. Dine, A. E. Nelson, and Y. Shirman, Phys. Rev. D **51**, 1362 (1995), URL
<http://link.aps.org/doi/10.1103/PhysRevD.51.1362>.
- 3039
- 3040 [29] M. Dine, A. E. Nelson, Y. Nir, and Y. Shirman, Phys. Rev. D **53**, 2658 (1996),
3041 URL <http://link.aps.org/doi/10.1103/PhysRevD.53.2658>.

- 3042 [30] A. H. Chamseddine, R. Arnowitt, and P. Nath, Phys. Rev. Lett. **49**, 970 (1982),
 3043 URL <http://link.aps.org/doi/10.1103/PhysRevLett.49.970>.
- 3044 [31] R. Barbieri, S. Ferrara, and C. Savoy, Phys. Lett. B **119**, 343 (1982), URL <http://www.sciencedirect.com/science/article/pii/0370269382906852>.
- 3046 [32] L. Ibáñez, Phys. Lett. B **118**, 73 (1982), URL <http://www.sciencedirect.com/science/article/pii/0370269382906049>.
- 3048 [33] L. Hall, J. Lykken, and S. Weinberg, Phys. Rev. D **27**, 2359 (1983), URL <http://link.aps.org/doi/10.1103/PhysRevD.27.2359>.
- 3050 [34] N. Ohta, Prog. Theor. Phys. **70**, 542 (1983), URL <http://ptp.ipap.jp/link?PTP/70/542/>.
- 3052 [35] J. Ellis, D. Nanopoulos, and K. Tamvakis, Phys. Lett. B **121**, 123
 3053 (1983), URL <http://www.sciencedirect.com/science/article/pii/0370269383909000>.
- 3055 [36] L. Alvarez-Gaumé, J. Polchinski, and M. B. Wise, Nucl. Phys. B **221**,
 3056 495 (1983), URL <http://www.sciencedirect.com/science/article/pii/0550321383905916>.
- 3058 [37] P. Meade, N. Seiberg, and D. Shih, Prog. Theor. Phys. Suppl. **177**, 143 (2009),
 3059 URL <http://ptp.ipap.jp/link?PTPS/177/143/>.
- 3060 [38] G. Aad et al., Phys. Lett. B **710**, 519 (2012), URL <http://www.sciencedirect.com/science/article/pii/S0370269312001955>.
- 3062 [39] T. Aaltonen et al. (CDF Collaboration), Phys. Rev. Lett. **104**, 011801 (2010),
 3063 URL <http://link.aps.org/doi/10.1103/PhysRevLett.104.011801>.
- 3064 [40] S. Chatrchyan et al. (CMS Collaboration) (2011), unpublished,
 3065 CMS-PAS-SUS-11-009, URL <https://cdsweb.cern.ch/record/1377324>.

- 3066 [41] URL <http://en.wikipedia.org/wiki/Tevatron>.
- 3067 [42] E. Fernandez, W. T. Ford, N. Qi, A. L. Read, J. G. Smith, T. Camporesi,
3068 R. De Sangro, A. Marini, I. Peruzzi, M. Piccolo, et al., Phys. Rev. Lett. **54**, 1118
3069 (1985), URL <http://link.aps.org/doi/10.1103/PhysRevLett.54.1118>.
- 3070 [43] E. W. Fernandez, W. T. Ford, N. Qi, A. L. Read, J. G. Smith, T. Camporesi,
3071 I. Peruzzi, M. Piccolo, R. B. Hurst, K. H. Lau, et al., Phys. Rev. D **35**, 374
3072 (1987), URL <http://link.aps.org/doi/10.1103/PhysRevD.35.374>.
- 3073 [44] D. Decamp et al. (ALEPH Collaboration), Phys. Lett. B **237**, 291
3074 (1990), URL <http://www.sciencedirect.com/science/article/pii/037026939091447J>.
- 3076 [45] F. Abe et al. (CDF Collaboration), Phys. Rev. Lett. **75**, 613 (1995), URL
3077 <http://link.aps.org/doi/10.1103/PhysRevLett.75.613>.
- 3078 [46] S. Abachi et al. (D0 Collaboration), Phys. Rev. Lett. **75**, 618 (1995), URL
3079 <http://link.aps.org/doi/10.1103/PhysRevLett.75.618>.
- 3080 [47] G. Alexander et al. (OPAL Collaboration), Phys. Lett. B **377**, 273
3081 (1996), URL <http://www.sciencedirect.com/science/article/pii/0370269396005023>.
- 3083 [48] S. Aid et al. (H1 Collaboration), Z. Phys. C **71**, 211 (1996),
3084 10.1007/BF02906978, URL <http://dx.doi.org/10.1007/BF02906978>.
- 3085 [49] S. Aid et al. (H1 Collaboration), Phys. Lett. B **380**, 461 (1996), URL <http://www.sciencedirect.com/science/article/pii/0370269396006405>.
- 3087 [50] B. Aubert et al. (BABAR Collaboration), Phys. Rev. Lett. **95**, 041802 (2005),
3088 URL <http://link.aps.org/doi/10.1103/PhysRevLett.95.041802>.

- 3089 [51] O. Buchmueller, R. Cavanaugh, A. De Roeck, M. J. Dolan, J. R. Ellis,
 3090 H. Flacher, S. Heinemeyer, G. Isidori, D. Martinez Santos, K. A. Olive, et al.,
 3091 Report No. CERN-PH-TH-2011-220, CERN (2011), URL [https://cdsweb.
 3092 cern.ch/record/1391061](https://cdsweb.cern.ch/record/1391061).
- 3093 [52] URL <https://twiki.cern.ch/twiki/pub/CMSPublic/PhysicsResultsSUS/>
 3094 CMS_SUSY_2011Limits_tanb10.pdf.
- 3095 [53] B. Allanach, M. Battaglia, G. Blair, M. Carena, A. De Roeck, A. Dedes,
 3096 A. Djouadi, D. Gerdes, N. Ghodbane, J. Gunion, et al., Eur. Phys. J. C **25**, 113
 3097 (2002), URL <http://dx.doi.org/10.1007/s10052-002-0949-3>.
- 3098 [54] G. Aad et al. (ATLAS Collaboration), J. Instr. **3**, S08003 (2008), URL <http://stacks.iop.org/1748-0221/3/i=08/a=S08003>.
- 3100 [55] A. Boyarsky, J. Lesgourgues, O. Ruchayskiy, and M. Viel, J. Cosmol. Astropart.
 3101 Phys. **2009**, 012 (2009), URL <http://stacks.iop.org/1475-7516/2009/i=05/a=012>.
- 3103 [56] E. Komatsu, J. Dunkley, M. R. Nolta, C. L. Bennett, B. Gold, G. Hinshaw,
 3104 N. Jarosik, D. Larson, M. Limon, L. Page, et al., Astrophys. J. Suppl. Ser. **180**,
 3105 330 (2009), URL <http://stacks.iop.org/0067-0049/180/i=2/a=330>.
- 3106 [57] C.-H. Chen and J. F. Gunion, Phys. Rev. D **58**, 075005 (1998), URL <http://link.aps.org/doi/10.1103/PhysRevD.58.075005>.
- 3108 [58] F. Staub, J. Niemeyer, and W. Porod, JHEP **2010**, 1 (2010), URL [http://dx.doi.org/10.1007/JHEP01\(2010\)058](http://dx.doi.org/10.1007/JHEP01(2010)058).
- 3110 [59] S. Chatrchyan et al. (CMS Collaboration) (2012), unpublished,
 3111 CMS-PAS-SUS-12-001, URL <https://cdsweb.cern.ch/record/1436111>.

- 3112 [60] L. Evans and P. Bryant, J. Instr. **3**, S08001 (2008), URL <http://stacks.iop.org/1748-0221/3/i=08/a=S08001>.
- 3113
- 3114 [61] URL <http://cms.web.cern.ch/news/summary-2011-p-p-running>.
- 3115 [62] URL <http://public.web.cern.ch/public/en/lhc/Facts-en.html>.
- 3116 [63] URL <http://cdsweb.cern.ch/record/833187>.
- 3117 [64] URL <http://www.rgbstock.com/photo/n7EsabW/Airplane>.
- 3118 [65] R. Flükiger, S. Y. Hariharan, R. Küntzler, H. L. Luo, F. Weiss, T. Wolf, and
3119 J. Q. Xu, in *SpringerMaterials - The Landolt-Börnstein Database: Nb-Ti*, edited
3120 by R. Flükiger and W. Klose (<http://www.springermaterials.com>, 2012), URL
3121 http://www.springermaterials.com/docs/info/10423690_53.html.
- 3122 [66] Y. Sun, F. Zimmermann, and R. Tomás, in *Proceedings of the 23rd Particle
3123 Accelerator Conference, Vancouver, 2009* (2009), URL <https://cdsweb.cern.ch/record/1235160>.
- 3124
- 3125 [67] O. S. Brüning, P. Collier, P. Lebrun, S. Myers, R. Ostojic, J. Poole, and
3126 P. Proudlock, *LHC Design Report* (CERN, Geneva, 2004).
- 3127 [68] URL <http://cdsweb.cern.ch/record/841568/files/>.
- 3128 [69] P. Komorowski and D. Tommasini, IEEE Trans. Appl. Supercond. **10**,
3129 166 (2000), URL <http://ieeexplore.ieee.org/xpl/articleDetails.jsp?arnumber=828202>.
- 3130
- 3131 [70] URL <http://lhc-machine-outreach.web.cern.ch/lhc-machine-outreach/components/magnets.htm>.
- 3132
- 3133 [71] S. Chatrchyan et al. (CMS Collaboration), J. Instr. **3**, S08004 (2008), URL
3134 <http://stacks.iop.org/1748-0221/3/i=08/a=S08004>.

- 3135 [72] G. L. Bayatian et al. (CMS Collaboration), *CMS Physics Technical Design*
 3136 *Report Volume I: Detector Performance and Software*, Technical Design Report
 3137 CMS (CERN, Geneva, 2006).
- 3138 [73] M. Ivova (2010), talk given at the Swiss Ph.D. School on Parti-
 3139 cle and Astroparticle Physics (CHIPP), Monte Verita', URL <https://indico.cern.ch/getFile.py/access?contribId=11&sessionId=14&resId=0&materialId=0&confId=80223>
- 3140
- 3141
- 3142 [74] G. Bolla, D. Bortoletto, C. Rott, A. Roy, S. Kwan, C. Chien, H. Cho,
 3143 B. Gobbi, R. Horisberger, and R. Kaufmann, Nucl. Instr. Meth. A **461**,
 3144 182 (2001), URL <http://www.sciencedirect.com/science/article/pii/S0168900200012018>.
- 3145
- 3146 [75] URL https://twiki.cern.ch/twiki/pub/CMSPublic/DPGResultsTRK/_imgf9e0ee48ebca770d7774454532b4b4ee.png.
- 3147
- 3148 [76] URL https://twiki.cern.ch/twiki/pub/CMSPublic/DPGResultsTRK/_img7569b7652b3f7c15030a11a4223e631c.png.
- 3149
- 3150 [77] URL https://twiki.cern.ch/twiki/pub//CMSPublic/DPGResultsTRK/hv11_d1.png.
- 3151
- 3152 [78] URL https://twiki.cern.ch/twiki/pub/CMSPublic/DPGResultsTRK/_imga571742cbcd3a14a9e2581ae95efa54c.gif.
- 3153
- 3154 [79] URL <https://twiki.cern.ch/twiki/pub//CMSPublic/DPGResultsTRK/StripHitRes2.gif>.
- 3155
- 3156 [80] URL https://twiki.cern.ch/twiki/pub//CMSPublic/EcalDPGResults/history2_laser.png.
- 3157

- 3158 [81] G. Akopdzhianov, A. Inyakin, and P. Shuvalov, Nucl. Instr. Meth. **161**,
 3159 247 (1979), URL <http://www.sciencedirect.com/science/article/pii/0029554X79903914>.
- 3160
 3161 [82] J. Wood, work in progress at the University of Virginia high energy physics
 3162 laboratory.
- 3163 [83] URL https://twiki.cern.ch/twiki/pub//CMSPublic/EcalDPGResults/electronres_eb_inclusive.png.
- 3164
 3165 [84] URL https://twiki.cern.ch/twiki/pub//CMSPublic/EcalDPGResults/electronres_ee_inclusive.png.
- 3166
 3167 [85] S. Chatrchyan et al. (CMS Collaboration) (2011), unpublished,
 3168 CMS-PAS-EXO-11-067, URL <https://cdsweb.cern.ch/record/1394286>.
- 3169 [86] URL <https://twiki.cern.ch/twiki/pub//CMSPublic/EcalDPGResults/seed-time.EEEE.png>.
- 3170
 3171 [87] N. Akchurin and R. Wigmans, Rev. Sci. Instr. **74**, 2955 (2003), URL http://rsi.aip.org/resource/1/rsinak/v74/i6/p2955_s1.
- 3172
 3173 [88] S. Chatrchyan et al. (CMS Collaboration) (2010), unpublished,
 3174 CMS-DP-2010-025, URL <https://cdsweb.cern.ch/record/1364222>.
- 3175 [89] S. Chatrchyan et al. (CMS Collaboration), J. Instr. **5**, T03014 (2010), URL
 3176 <http://stacks.iop.org/1748-0221/5/i=03/a=T03014>.
- 3177 [90] URL https://twiki.cern.ch/twiki/pub//CMSPublic/PhysicsResultsMU0/dimuMass_2011Run_1fb_20July2011.pdf.
- 3178
 3179 [91] S. Chatrchyan et al., JHEP **2012**, 1 (2012), URL [http://dx.doi.org/10.1007/JHEP04\(2012\)033](http://dx.doi.org/10.1007/JHEP04(2012)033).
- 3180

- 3181 [92] R. Alemany, C. Almeida, N. Almeida, M. Bercher, R. Benetta, V. Bexiga,
 3182 J. Bourotte, P. Busson, N. Cardoso, M. Cerrutti, et al., IEEE Trans. Nucl. Sci.
 3183 **52**, 1918 (2005), URL <http://ieeexplore.ieee.org/xpl/articleDetails.jsp?arnumber=1546528>.
- 3184
- 3185 [93] W. Smith, P. Chumney, S. Dasu, F. D. Lodovico, M. Jaworski, J. Lackey, and
 3186 P. Robl, in *Proceedings of the 7th Workshop on Electronics for LHC Experiments, Stockholm, 2001*, edited by C. Isabella (CERN, Geneva, 2001), pp.
 3187 238–242, URL <https://cdsweb.cern.ch/record/529417>.
- 3188
- 3189 [94] R. Brun and F. Rademakers, Nucl. Instr. Meth. A **389**, 81 (1997), URL <http://www.sciencedirect.com/science/article/pii/S016890029700048X>.
- 3190
- 3191 [95] J. Guteleber and L. Orsini, Clus. Comput. **5**, 55 (2002), URL <http://dx.doi.org/10.1023/A:1012744721976>.
- 3192
- 3193 [96] D. Box, D. Ehnebuske, G. Kakivaya, A. Layman, N. Mendelsohn, H. Nielsen,
 3194 S. Thatte, and D. Winer, Report No. W3C Note 08, W3C (2000), URL <http://www.w3.org/TR/2000/NOTE-SOAP-20000508/>.
- 3195
- 3196 [97] R. Arcidiacono et al. (2005), talk given at the 10th ICAL-EPCS International Conference on Accelerator and Large Experiment Physics Control Systems, Geneva, URL http://accelconf.web.cern.ch/accelconf/ica05/proceedings/pdf/o5_004.pdf.
- 3197
- 3198
- 3199
- 3200 [98] C. Eck, J. Knobloch, L. Robertson, I. Bird, K. Bos, N. Brook, D. Dillmann,
 3201 I. Fisk, D. Foster, B. Gibbard, et al., *LHC computing Grid: Technical Design Report. Version 1.06 (20 Jun 2005)*, Technical Design Report LCG (CERN,
 3202 Geneva, 2005).
- 3203
- 3204 [99] R. Brunelière, Nucl. Instr. Meth. A **572**, 33 (2007), URL <http://www.sciencedirect.com/science/article/pii/S0168900206019711>.
- 3205

- 3206 [100] S. Chatrchyan et al. (CMS Collaboration), J. Instr. **5**, T03011 (2010), URL
3207 <http://stacks.iop.org/1748-0221/5/i=03/a=T03011>.
- 3208 [101] S. Chatrchyan et al. (CMS Collaboration) (2010), unpublished,
3209 CMS-NOTE-2010-012, URL <https://cdsweb.cern.ch/record/1278160>.
- 3210 [102] P. Meridiani and C. Seez, Report No. CMS IN-2011/002, CERN
3211 (2011), URL http://cms.cern.ch/iCMS/jsp/openfile.jsp?type=IN&year=2011&files=IN2011_002.pdf.
- 3212 [103] P. Adzic et al. (CMS Electromagnetic Calorimeter Group), Eur. Phys. J. C **44**,
3213 1 (2006), URL <http://dx.doi.org/10.1140/epjcd/s2005-02-011-3>.
- 3214 [104] P. Adzic et al. (CMS Electromagnetic Calorimeter Group), J. Instr. **3**, P10007
3215 (2008), URL <http://stacks.iop.org/1748-0221/3/i=10/a=P10007>.
- 3216 [105] M. Malberti, in *Nuclear Science Symposium Conference Record (NSS/MIC)*,
3217 2009 IEEE (2009), p. 2264, URL http://ieeexplore.ieee.org/xpls/abs_all.jsp?arnumber=5402068.
- 3218 [106] S. Chatrchyan et al. (CMS Collaboration), J. Instr. **5**, T03010 (2010), URL
3219 <http://stacks.iop.org/1748-0221/5/i=03/a=T03010>.
- 3220 [107] R. Paramatti, J. Phys.: Conf. Ser. **293**, 012045 (2011), URL <http://stacks.iop.org/1742-6596/293/i=1/a=012045>.
- 3221 [108] Y. Yang (2011), poster presented at the Achievement Awards session of CMS
3222 Week, CERN, Geneva, URL http://www.hep.caltech.edu/cms/posters/PiOPoster_CMSWeekDec2011.pdf.
- 3223 [109] M. Anderson, A. Askew, A. Barfuss, D. Evans, F. Ferri, K. Kaadze, Y. Mar-
3224 avin, P. Meridiani, and C. Seez, Report No. CMS IN-2010/008, CERN
3225

- 3229 (2010), URL http://cms.cern.ch/iCMS/jsp/openfile.jsp?type=IN&year=2010&files=IN2010_008.pdf.
- 3230
- 3231 [110] A. David, M. Donega, M. Gataullin, et al. ($H \rightarrow \gamma\gamma$ working group), Report
3232 No. CMS AN-2011/426, CERN (2011), URL http://cms.cern.ch/iCMS/jsp/openfile.jsp?tp=draft&files=AN2011_426_v5.pdf.
- 3233
- 3234 [111] URL <https://twiki.cern.ch/twiki/bin/view/CMS/ECALEnergyScaleCorrections>.
- 3235
- 3236 [112] M. Cacciari, Report No. LPTHE-P06-04, LPTHE, Université P. et M. Curie
3237 (2006), URL <http://arxiv.org/abs/hep-ph/0607071>.
- 3238
- 3239 [113] M. Cacciari, G. Salam, and G. Soyez, Report No. CERN-PH-TH-2011-297,
CERN (2011), URL <https://cdsweb.cern.ch/record/1402449>.
- 3240
- 3241 [114] V. Khachatryan et al. (CMS Collaboration), Phys. Rev. Lett. **106**, 082001
(2011), URL <http://link.aps.org/doi/10.1103/PhysRevLett.106.082001>.
- 3242
- 3243 [115] A. Askew, B. Cox, D. Elvira, Y. Gershtein, M. Hildreth, D. Jang, Y.-F.
Liu, D. Mason, D. Morse, U. Nauenberg, et al., Report No. CMS AN-
3244 2011/515, CERN (2011), URL http://cms.cern.ch/iCMS/jsp/openfile.jsp?tp=draft&files=AN2011_515_v6.pdf.
- 3245
- 3246
- 3247 [116] W. Adam, R. Frühwirth, A. Strandlie, and T. Todorov, J. Phys. G **31**, N9
(2005), URL <http://stacks.iop.org/0954-3899/31/i=9/a=N01>.
- 3248
- 3249 [117] S. Chatrchyan et al. (CMS Collaboration) (2009), unpublished,
CMS-PAS-PFT-09-001, URL <https://cdsweb.cern.ch/record/1194487>.
- 3250
- 3251 [118] S. Chatrchyan et al. (CMS Collaboration) (2010), unpublished,
CMS-PAS-PFT-10-002, URL <https://cdsweb.cern.ch/record/1279341>.

- 3252 [119] S. Chatrchyan et al. (CMS collaboration), J. Instr. **6**, P11002 (2011), URL
 3253 <http://stacks.iop.org/1748-0221/6/i=11/a=P11002>.
- 3254 [120] M. Cacciari, G. P. Salam, and G. Soyez, JHEP **2008**, 063 (2008), URL <http://stacks.iop.org/1126-6708/2008/i=04/a=063>.
- 3256 [121] G. Salam (2009), talk given at CERN Theory Institute: SM and BSM Physics
 3257 at the LHC, CERN, Geneva, URL <https://indico.cern.ch/getFile.py/access?contribId=1&sessionId=9&resId=0&materialId=slides&confId=43022>.
- 3260 [122] C. W. Fabjan and R. Wigmans, Rep. Prog. Phys. **52**, 1519 (1989), URL <http://stacks.iop.org/0034-4885/52/i=12/a=002>.
- 3262 [123] URL <http://www-cdf.fnal.gov/physics/new/top/2004/jets/cdfpublic.html>.
- 3264 [124] S. Chatrchyan et al. (CMS collaboration), J. Instr. **6**, P09001 (2011), URL
 3265 <http://stacks.iop.org/1748-0221/6/i=09/a=P09001>.
- 3266 [125] S. Chatrchyan et al. (CMS Collaboration) (2009), unpublished,
 3267 CMS-PAS-JME-09-002, URL <https://cdsweb.cern.ch/record/1190234>.
- 3268 [126] F. Beaudette, D. Benedetti, P. Janot, and M. Pioppi, Report No. CMS AN-
 3269 2010/034, CERN (2010), URL http://cms.cern.ch/iCMS/jsp/openfile.jsp?tp=draft&files=AN2010_034_v2.pdf.
- 3271 [127] M. Konecki, in *Proceedings of the European Physical Society Europhysics Conference on High Energy Physics, EPS-HEP 2009, Krakow, Poland* (Proc. Sci.,
 3272 2009), p. 131, URL <http://inspirehep.net/record/861487>.
- 3274 [128] T. Sjöstrand, S. Mrenna, and P. Skands, Comput. Phys. Commun. **178**,

- 3275 852 (2008), URL <http://www.sciencedirect.com/science/article/pii/S0010465508000441>.
- 3276
- 3277 [129] URL <https://twiki.cern.ch/twiki/bin/view/CMS/PVTMain>.
- 3278 [130] J. P. Chou, S. Eno, S. Kunori, S. Sharma, and J. Wang, Report No. IN-
- 3279 2010/006, CERN (2010), URL http://cms.cern.ch/iCMS/jsp/openfile.jsp?type=IN&year=2010&files=IN2010_006.pdf.
- 3280
- 3281 [131] R. Korzekwa, F. Lehr, H. Krompholz, and M. Kristiansen, IEEE Trans.
- 3282 Elec. Dev. **38**, 745 (1991), URL <http://ieeexplore.ieee.org/xpl/articleDetails.jsp?arnumber=75200>.
- 3283
- 3284 [132] Y. Chen (2011), talk given at a meeting of the CMS JetMET group, CERN,
- 3285 Geneva, URL <https://indico.cern.ch/getFile.py/access?contribId=1&resId=0&materialId=slides&confId=129896>.
- 3286
- 3287 [133] W. Adam, B. Mangano, T. Speer, and T. Todorov, Report No. CMS-NOTE-
- 3288 2006-041, CERN, Geneva (2006), URL <https://cdsweb.cern.ch/record/934067>.
- 3289
- 3290 [134] G. Daskalakis, D. Evans, C. Hill, J. Jackson, P. Vanlaer, J. Berryhill,
- 3291 J. Haupt, D. Futyan, C. Seez, C. Timlin, et al., Report No. CMS AN-
- 3292 2007/019, CERN (2007), URL http://cms.cern.ch/iCMS/jsp/openfile.jsp?tp=draft&files=AN2007_019_v3.pdf.
- 3293
- 3294 [135] F. James and M. Roos, Comput. Phys. Commun. **10**, 343 (1975), URL <http://www.sciencedirect.com/science/article/pii/0010465575900399>.
- 3295
- 3296 [136] W. Verkerke and D. P. Kirkby, in *Proceedings of the Conference on Statistical*
- 3297 *Problems in Particle Physics, Astrophysics, and Cosmology: PHYSTAT 2005*,

- 3298 *Oxford, England, United Kingdom*, edited by L. Lyons and M. K. Unel (Impe-
 3299 rial Coll. Press, London, 2006), p. 186, URL <http://inspirehep.net/record/621398>.
 3300
- 3301 [137] J. E. Gaiser, Ph.D. thesis, Stanford University, 450 Serra Mall, Stanford,
 3302 CA 94305 (1982), URL <http://www.slac.stanford.edu/cgi-wrap/getdoc/slac-r-255.pdf>.
 3303
- 3304 [138] A. Askew, S. Arora, Y. Gershtein, S. Thomas, G. Hanson, R. Stringer, W. Flana-
 3305 gan, B. Heyburn, U. Nauenberg, S. Zang, et al., Report No. CMS AN-
 3306 2010/271, CERN (2010), URL http://cms.cern.ch/iCMS/jsp/openfile.jsp?tp=draft&files=AN2010_271_v8.pdf.
 3307
- 3308 [139] URL <https://cmsweb.cern.ch/das/>.
- 3309 [140] S. Chatrchyan et al. (CMS Collaboration), Phys. Rev. Lett. **106**, 211802 (2011),
 3310 URL <http://link.aps.org/doi/10.1103/PhysRevLett.106.211802>.
- 3311 [141] A. Djouadi, J.-L. Kneur, and G. Mourtaka (2005), unpublished,
 3312 arXiv:hep-ph/0211331, URL <http://arxiv.org/abs/hep-ph/0211331>.
- 3313 [142] M. Mühlleitner, A. Djouadi, and Y. Mambrini, Comp. Phys. Commun.
 3314 **168**, 46 (2005), URL <http://www.sciencedirect.com/science/article/pii/S0010465505000822>.
 3315
- 3316 [143] T. Sjöstrand, S. Mrenna, and P. Skands, JHEP **2006**, 026 (2006), URL <http://stacks.iop.org/1126-6708/2006/i=05/a=026>.
 3317
- 3318 [144] J. Allison, K. Amako, J. Apostolakis, H. Araujo, P. Dubois, M. Asai, G. Bar-
 3319 rand, R. Capra, S. Chauvie, R. Chytracek, et al., IEEE Trans. Nucl. Sci. **53**,
 3320 270 (2006), URL <http://ieeexplore.ieee.org/xpl/articleDetails.jsp?arnumber=1610988>.
 3321

- 3322 [145] W. Beenakker, R. Hoepker, and M. Spira (1996), unpublished,
 3323 arXiv:hep-ph/9611232, URL <http://arxiv.org/abs/hep-ph/9611232>.
- 3324 [146] G. Aad (ATLAS Collaboration), S. Chatrchyan (CMS Collaboration), and LHC
 3325 Higgs Combination Group, Report No. CMS-NOTE-2011-005, CERN, Geneva
 3326 (2011), URL <https://cdsweb.cern.ch/record/1379837>.
- 3327 [147] A. L. Read, in *Proceedings of the First Workshop on Confidence Limits, Geneva,*
 3328 2000, edited by L. Lyons, Y. Perrin, and F. James (CERN, Geneva, 2000), p. 81,
 3329 URL <https://cdsweb.cern.ch/record/411537>.
- 3330 [148] G. Cowan, K. Cranmer, E. Gross, and O. Vitells, Eur. Phys. J. C **71**, 1 (2011),
 3331 URL <http://dx.doi.org/10.1140/epjc/s10052-011-1554-0>.
- 3332 [149] J. Neyman and E. S. Pearson, Phil. Trans. R. Soc. London **231**,
 3333 289 (1933), URL <http://rsta.royalsocietypublishing.org/content/231/694-706/289.short>.
- 3335 [150] S. Chatrchyan et al. (CMS Collaboration) (2011), unpublished,
 3336 CMS-PAS-EWK-11-001, URL <https://cdsweb.cern.ch/record/1376102>.
- 3337 [151] S. Alekhin et al. (PDF4LHC Working Group) (2011), unpublished,
 3338 arXiv:1101.0536[hep-ph], URL <http://arxiv.org/abs/1101.0536>.
- 3339 [152] M. Botje et al. (PDF4LHC Working Group) (2011), unpublished,
 3340 arXiv:1101.0538[hep-ph], URL <http://arxiv.org/abs/1101.0538>.
- 3341 [153] URL <http://www.hep.ucl.ac.uk/pdf4lhc/index.html>.
- 3342 [154] A. Martin, W. Stirling, R. Thorne, and G. Watt, Eur. Phys. J. C **63**, 189 (2009),
 3343 URL <http://dx.doi.org/10.1140/epjc/s10052-009-1072-5>.

- 3344 [155] P. M. Nadolsky, H.-L. Lai, Q.-H. Cao, J. Huston, J. Pumplin, D. Stump, W.-K.
 3345 Tung, and C.-P. Yuan, Phys. Rev. D **78**, 013004 (2008), URL <http://link.aps.org/doi/10.1103/PhysRevD.78.013004>.
- 3347 [156] R. D. Ball, L. D. Debbio, S. Forte, A. Guffanti, J. I. Latorre, J. Rojo, and
 3348 M. Ubiali, Nucl. Phys. B **838**, 136 (2010), URL <http://www.sciencedirect.com/science/article/pii/S0550321310002853>.
- 3350 [157] A. Cooper-Sarkar (2012), unpublished, [arXiv:1206.0894\[hep-ph\]](https://arxiv.org/abs/arXiv:1206.0894), URL
 3351 <http://arxiv.org/abs/arXiv:1206.0894>.
- 3352 [158] D. Bourilkov, R. C. Group, and M. R. Whalley (2006), unpublished,
 3353 [arXiv:hep-ph/0605240](https://arxiv.org/abs/hep-ph/0605240), URL <http://arxiv.org/abs/hep-ph/0605240>.
- 3354 [159] J. M. Campbell, J. W. Huston, and W. J. Stirling, Rep. Prog. Phys. **70**, 89
 3355 (2007), URL <http://stacks.iop.org/0034-4885/70/i=1/a=R02>.
- 3356 [160] M. Carena, J. Conway, H. Haber, and J. Hobbs (2000), unpublished,
 3357 [arXiv:hep-ph/0010338](https://arxiv.org/abs/hep-ph/0010338), URL <http://arxiv.org/abs/hep-ph/0010338>.
- 3358 [161] G. Aad et al. (ATLAS Collaboration) (2012), unpublished,
 3359 ATLAS-CONF-2012-036, URL <https://cdsweb.cern.ch/record/1432203>.
- 3360 [162] R. Field (2011), talk given at LHC Physics Centre at CERN Mini-
 3361 mum Bias and Underlying Event Working Group Meeting, Geneva, URL
 3362 <https://indico.cern.ch/getFile.py/access?contribId=11&sessionId=2&resId=1&materialId=slides&confId=140054>.
- 3364 [163] J. Alwall, M. Herquet, F. Maltoni, O. Mattelaer, and T. Stelzer, JHEP **2011**,
 3365 1 (2011), URL [http://dx.doi.org/10.1007/JHEP06\(2011\)128](http://dx.doi.org/10.1007/JHEP06(2011)128).
- 3366 [164] Z. Wąs, Nucl. Phys. B - Proc. Suppl. **98**, 96 (2001), URL <http://www.sciencedirect.com/science/article/pii/S0920563201012002>.

3368 [165] URL http://cmsslxr.fnal.gov/lxr/source/SimGeneral/MixingModule/
3369 python/mix_E7TeV_Fall2011_Reprocess_50ns_PoissonOOTPU_cfi.py.

3370 [166] URL http://cmsslxr.fnal.gov/lxr/source/GeneratorInterface/
3371 GenFilters/src/doubleEMEnrichingFilterAlgo.cc.